Phénomènes de transfert dans des liquides réactifs à haute viscosité. Application au procédé d'élaboration du verre

Franck Pigeonneau

▶ **To cite this version:**

Franck Pigeonneau. Phénomènes de transfert dans des liquides réactifs à haute viscosité. Application au procédé d'élaboration du verre. Milieux fluides et réactifs. Université Pierre et Marie Curie (Paris), 2012. tel-01442971

HAL Id: tel-01442971
https://hal.science/tel-01442971

Submitted on 21 Jan 2017

HAL is a multi-disciplinary open access archive for the deposit and dissemination of scientific research documents, whether they are published or not. The documents may come from teaching and research institutions in France or abroad, or from public or private research centers.

L'archive ouverte pluridisciplinaire **HAL**, est destinée au dépôt et à la diffusion de documents scientifiques de niveau recherche, publiés ou non, émanant des établissements d'enseignement et de recherche français ou étrangers, des laboratoires publics ou privés.

MÉMOIRE
de synthèse des travaux scientifiques en vue de l'obtention du diplôme d'

HABILITATION à DIRIGER des RECHERCHES

Spécialité : Mécanique

Phénomènes de transfert dans des liquides réactifs à haute viscosité. Application au procédé d'élaboration du verre

présenté par
Franck PIGEONNEAU
Docteur de l'université de Pierre et Marie Curie

Soutenue le 25 mai 2012 à 10 h 30
devant le jury composé de :

M.	C. CLANET	Rapporteur
M.	C. GOURDON	Rapporteur
M.	L. LIMAT	Rapporteur
M.	A. AJDARI	Examinateur
M.	F. CHARRU	Président du jury
M.	H. A. STONE	Examinateur
M.	S. ZALESKI	Examinateur

Résumé

La synthèse de mes travaux de recherche concerne les phénomènes de transfert dans des liquides visqueux réactifs. L'application visée est l'élaboration des verres déclinée autour de trois grands sujets : les transferts de masse entre des bulles et un «verre» fondu, la stabilité des mousses de verre et les phénomènes de convection naturelle appliqués aux fours verriers.

Sur le premier thème, l'accent est mis sur la prise en compte des réactions chimiques d'oxydoréduction liées au fer contenu dans les verres industriels. Un modèle couplant advection-diffusion-réaction a été utilisé pour déterminer les coefficients de transferts de masse de l'oxygène. Ces résultats ont été appliqués à la résorption de bulles d'oxygène. Les évolutions de la taille des bulles au cours du temps obtenues expérimentalement sont comparées à celles issues des modèles numériques.

La stabilité des mousses a été abordée en étudiant le drainage et la stabilité de bulles à la surface libre d'un liquide et la stabilité de films verticaux. Un code numérique basé sur la formulation intégrale des équations de Stokes a été développé et appliqué au drainage des bulles. Les résultats montrent que les films entre une bulle et une surface libre drainent de façon exponentielle avec le temps et que la taille relative de la bulle comparée à l'échelle capillaire est un facteur important. Plus la bulle est grosse, plus le film draine lentement. Une expérience pour étudier le drainage de bulle dans un verre a été développée avec laquelle nous retrouvons les comportements théoriques indiqués ci-dessus. Des mécanismes de stabilisation des films de verre ont également été mis en avant reposant sur l'évaporation du sodium.

Les phénomènes de convection dans les fours verriers sont abordés en étudiant les distributions des temps de séjour. Une représentation minimale d'un bain de verre est faite à l'aide de deux réacteurs parfaitement agités avec un volume mort important mis en évidence. La convection naturelle est étudiée en focalisant sur un modèle simplifié à deux dimensions. Il ressort qu'un seul paramètre correspondant au produit du nombre de Rayleigh par le rapport d'aspect, hauteur sur longueur, au carré, contrôle l'écoulement et la thermique. Les lois de transferts sont établies à l'aide d'une analyse numérique.

Abstract

The synthesis of my works is on the transport phenomena occurring in high viscous reactive liquid. The industrial application is the glass melting for which three subjects appear: mass transfer between bubbles and molten glass, foam stability of glass and free convection applied to glass furnaces.

On the first subject, the oxidation-reduction reactions of iron contended in industrial glasses are investigated. An advection-diffusion-reaction model is solved to determine mass transfer coefficients of oxygen species. These solutions have been applied to the resorption of a pure oxygen bubble where comparisons between experimental and numerical results are done.

The foam stability is investigated by studying the drainage and the stability of bubbles at a free surface of a liquid and the stability of vertical liquid films. A numerical software based on the integral formulation of Stokes equations has been developed and applied to the bubble drainage. We point out that the liquid films between a bubble and a free surface drains exponentially with time. The relative bubble size compared of the capillary scale is an important factor. Larger the bubble is, smaller the liquid drainage is. Experiments of bubble drainage have been driven on molten glass where the same behaviors have been found. Mechanisms of film stability have been also identified driven by sodium volatilization.

The free convection in glass furnaces has been investigated by studying the residence time distribution. A reactor network of two ideal mixers is proposed where an useless volume is pointed out. The free convection is studied by emphasizing on a simple bidimensional configuration. Only one parameter drives the heat and mass transfer defined as the product of Rayleigh number by the aspect ratio, height over length, squared. The laws of heat and mass transfer are established from a numerical analysis.

Table des matières

Introduction

Les verres regroupent un très grand nombre d'applications dans l'habitat, l'automobile, l'audiovisuel, l'informatique et encore bien d'autres. Ceci est dû au fait que le verre possède trois propriétés essentielles [4] : la capacité de formage, la rigidité mécanique et la transparence. Il doit ces propriétés à sa structure moléculaire et au fait qu'un verre est un état bien particulier de la matière passant de l'état solide amorphe à l'état liquide sans transition de phase de première espèce (transition vitreuse). Selon Zarzycki [113], un verre est un solide amorphe possédant une température de transition vitreuse.

A l'échelle industrielle, le verre est élaboré et formé à une grande cadence. Par exemple, la production du verre plat peut atteindre plus de neuf cents tonnes par jour. Les procédés d'élaboration du verre sont déjà très optimisés avec des rendements énergétiques très importants, supérieurs à cinquante pour cent.

Aujourd'hui, l'industrie verrière comme bien d'autres industries est face à de nouveaux enjeux dans les domaines de l'énergie, de l'environnement, entre autres. De plus, le verre qui est un matériau réalisé depuis plusieurs millénaires laisse encore de nombreuses ombres sur les phénomènes physicochimiques mis en jeu lors de son élaboration.

Ceci renforce l'intérêt de développer une recherche à la fois fondamentale et appliquée sur l'élaboration des verres afin de mieux comprendre les phénomènes mis en jeu et pouvoir proposer à terme des innovations, voire des ruptures de procédés. Ainsi, l'unité mixte de recherche 125 CNRS/SAINT-GOBAIN, SURFACE DU VERRE ET INTERFACES, s'est vue attribuer une nouvelle mission ayant pour objectif de travailler sur les «matériaux hétérogènes réactifs» depuis 2007. L'élaboration du verre (procédé basé sur des réactions chimiques) fait appel à plusieurs disciplines scientifiques comme la chimie minérale, la mécanique des milieux granulaires, les transferts de chaleur à haute température, les transferts de masse, la mécanique des fluides monophasiques et polyphasiques, la combustion, l'électricité.

Il va de soi que tous les sujets ne peuvent être abordés dans le cadre de ce mémoire. L'accent sera mis sur les phénomènes de transferts qui ont lieu au cours de l'élaboration avec une forte dominance sur la mécanique des fluides. L'objectif de ce travail est d'approfondir les phénomènes qui ont lieu dans les procédés industriels afin de renforcer les moyens de modélisation des fours. La démarche globale est d'essayer de dégager des lois génériques à l'aide de principes premiers en se basant sur des méthodes d'analyse d'échelles. L'utilisation d'outils numériques permet de renforcer et d'affiner les lois préalablement établies. Par ailleurs, les difficultés à modéliser certains phénomènes rendent inéluctable l'expérimentation.

Avant d'aller plus loin dans l'exposé des résultats scientifiques, revenons sur les principes de

l'élaboration du verre ce qui permettra de structurer ce mémoire. Les procédés d'élaboration du verre fonctionnent en système ouvert : les matières premières sont introduites à une extrémité du four et le verre homogène, dépourvu dans la mesure du possible de toutes impuretés (bulles, infondus de silice) en sort à une autre extrémité. Ces fours peuvent être vus comme des réacteurs chimiques dans lesquels les matières premières, composées principalement de silice et de matières carbonatées qui y sont introduites réagissent entre elles grâce à un apport énergétique important. Ceci est réalisé soit par une combustion durant laquelle le combustible et le comburant (air ou oxygène) réagissent dans un espace de combustion situé au dessus du bain de verre, soit par effet Joule induit par le passage d'un courant au sein même du verre. Les transferts de chaleur entre l'espace de combustion et le verre sont principalement radiatifs et convectifs. L'écoulement des gaz dans l'espace de combustion sont turbulents.

La formation d'un verre fondu (silicate de calcium et de sodium) débute par des réactions en phase solide entre les grains de matière première puis d'autres dans les premiers liquides. L'utilisation de matières premières carbonatées entraîne une libération de gaz carbonique (CO_2). Une bonne partie de ce gaz s'échappe à travers le milieu granulaire que constitue la matière première. Malheureusement, le reste se retrouve à l'état dissous dans le verre. De par les faibles valeurs de solubilités du CO_2, une création importante de bulles a lieu.

Ainsi, le four doit dans un premier temps permettre que ces réactions chimiques s'effectuent, puis ensuite, que les bulles et autres impuretés s'éliminent. Cette deuxième étape est appelée affinage et est assez limitante dans le procédé. Le moyen pour faire partir les bulles est de laisser faire la gravité grâce à laquelle le contraste de masse volumique entre les gaz et le verre pousse les bulles vers la surface du bain de verre. Afin de rendre ce phénomène plus efficace, on joue sur deux leviers : l'un est la thermique et l'autre la chimie. En effet, l'augmentation de la température induit une diminution de la viscosité favorable à la remontée des bulles. De même, l'accroissement de la taille des bulles permet une remontée plus rapide : c'est pourquoi des agents affinants sont ajoutés aux matières premières, ce qui permet, par des réactions d'oxydoréduction, de libérer des gaz qui assureront un grossissement des bulles. Ces réactions d'oxydoréduction sont favorisées par la montée en température. Ainsi, les mécanismes de transferts de masse seront le premier thème de recherche abordé dans ce mémoire au cours du chapitre 1. L'accent sera mis sur l'impact des réactions d'oxydoréduction et plus particulièrement celle du fer qui se trouve sous deux états de valence dans le verre. Les méthodes utilisées ici seront basées sur le développement d'un modèle théorique et de sa résolution numérique. On cherchera à établir les lois de transfert de masse de façon unifiée, ce qui est très utile pour leur utilisation dans des logiciels de simulation numérique. Ces résultats numériques seront comparés à des données expérimentales. De plus, on cherchera à établir des relations permettant de quantifier simplement la variation de taille des bulles.

Lorsque les bulles arrivent en surface du bain de verre, il peut se former une couche de mousse qui reflète la compétition entre la quantité de bulles qui éclatent et celles qui arrivent du bain de verre. L'existence de ces mousses est nuisible au fonctionnement du four car elles sont un écran thermique très efficace conduisant à une diminution du transfert énergétique au bain de verre. Ces mousses sont de nature très différentes de celles que les physiciens étudient à l'échelle du laboratoire [19]. La stabilisation des mousses de verre fondu reste encore peu connue. Ainsi, le chapitre 2 sera dédié à l'étude de la stabilité des mousses de verre. On synthétisera ici un travail

expérimental effectué dans le cadre de la thèse d'H. Kočárková [53] au cours duquel un dispositif a été développé afin d'étudier le drainage d'un film de verre produit par une bulle se trouvant à proximité d'une surface libre. Par ailleurs, la simulation numérique de ce phénomène sera évoquée à l'aide du développement d'un code numérique que nous avons mis au point en nous basant sur la formulation d'intégrale des équations de Stokes. Nous étudirons la stabilité de films verticaux à l'aide d'expériences réalisées sur du verre fondu au cours desquelles des phénomènes d'évaporation engendrant des gradients de tension de surface stabilisent les films à des épaisseurs de l'ordre de la centaine de nanomètre. Nous présenterons un modèle de lubrification où ces effets seront pris en compte afin d'expliquer les résultats expérimentaux.

Le verre dans le four subit des grands courants de convection qui ont un impact sur son homogénéité et une signature sur les temps de séjour. Le dernier chapitre sera consacré aux phénomènes thermohydrodynamiques qui prennent naissance dans les bains de verre. La distribution des temps de séjour sera décrite où on cherchera à représenter le four comme un assemblage de réacteurs ideaux. Ensuite, la convection libre de nature assez particulière dans la mesure où les bains de verre sont chauffés en partie supérieure sera abordée. Cette configuration donnant des stratifications thermiques stables ne devraient pas nécessairement induire des mouvements de convection. Néanmoins, l'existence de gradient en surface à l'échelle du four conduit à des mouvements de convection. Ce type de convection également étudiée en océanographie [46] est communément désignée sous le nom de «convection horizontale». Nous chercherons à établir quels paramètres pilotent les phénomènes de transfert de masse et d'énergie.

Afin d'ouvrir sur de nouvelles perspectives de recherche, chaque fin de chapitre aura une section réservée aux nouvelles voies de recherche déjà initiées ou à développer.

Signalons pour finir cette introduction, que les travaux résumés ici se bornent uniquement à mes activités de recherches menées au sein du laboratoire SURFACE DU VERRE ET INTERFACES depuis 2007 en tant que chercheur associé à cette unité mixte recherche. Mes travaux antérieurs réalisés au sein du service ELABORATION DES VERRES de SAINT-GOBAIN RECHERCHE ayant une finalité industrielle ne peuvent pas figurer dans ce document public.

Outre les trois chapitres mentionnés ci-dessus, le document comporte quatre annexes : les trois premières sont une compilation d'articles relatifs aux trois chapitres développés dans ce manuscrit. La dernière annexe est une copie de mon *curriculum vitae*.

Chapitre 1

Transfert de masse autour des bulles

1.1 Principes de l'élaboration des verres

L'élaboration d'un verre consiste à réaliser la réaction suivante

$$\mathrm{SiO_2} + \mathrm{carbonates} \rightarrow \mathrm{silicate\ (verre)} + \mathrm{CO_2}, \tag{1.1}$$

donnant une forte quantité de CO_2. En règle générale, deux cents kilogrammes de CO_2 pour une tonne de verre sont produits. Bien qu'une grande partie de ce dioxyde de carbone s'échappe alors que les matières premières sont encore en phase solide, il en reste encore beaucoup après l'apparition des premiers liquides qui eux-mêmes deviennent de plus en plus visqueux à mesure de la dissolution de la silice. Ainsi, la formation de bulles est inéluctable et importante. Les expériences montrent que la quantité de bulles peut être grande, jusqu'à des valeurs supérieures à 10^8 bulles par mètre cube [70]. Les exigences en termes de qualité imposent moins d'une bulle supérieure à deux cents micromètres de diamètre par mètre cube pour les applications en verre plat. On voit à quel point l'étape d'«affinage», dont le but est de supprimer ces hétérogéités gazeuses, est importante.

L'affinage dans les installations industrielles est effectué à l'aide d'un processus chimique. On introduit dans les matières premières des éléments dits «affinants» qui par réduction à haute température produisent des gaz. Ceux-ci s'échangent avec les bulles existantes provoquant leur grossissement. Ensuite, la gravité permet l'évacuation de ces bulles à la surface libre du bain de verre. L'élément le plus utilisé est le sulfate qui produit la réaction suivante

$$\mathrm{SO_4^{2-}}(l) \rightleftharpoons \mathrm{SO_2}(g) + \frac{1}{2}\mathrm{O_2}(g) + \mathrm{O^{2-}}(l), \tag{1.2}$$

où l signifie les éléments en phase liquide et g ceux en phase gazeuse.

Dans les verres industriels, le fer est un élément qui se trouve à l'état de trace (généralement inférieur à 0,1 % en masse) dans les matériaux de carrière. Pour certaines applications, par exemple pour les verres automobiles, le fer est introduit en plus grande quantité. Au contraire, dans les applications photovoltaïques, le fer est fortement limité. En effet, le fer induit des changements de couleur et l'absorption du champ électromagnétique dans l'infrarouge dépendant de

la teneur en fer réduit, Fe^{2+}. Les deux états d'oxydoréduction, Fe^{2+} et Fe^{3+}, sont régis par la réaction suivante

$$Fe^{3+}(l) + \frac{1}{2}O^{2-}(l) \rightleftharpoons Fe^{2+}(l) + \frac{1}{4}O_2(g). \tag{1.3}$$

L'espèce réduite est favorisée à haute température.

La thermodynamique chimique permet de calculer les proportions des divers éléments moyennant la connaissance des constantes d'équilibres. Ces dernières sont obtenues à l'aide d'expériences mettant un verre en contact avec des mélanges de gaz à pressions partielles d'O_2 et de SO_2 contrôlées [8, 33]. Une autre technique utilise la voltamétrie [30].

Pour faire le calcul des concentrations des diverses espèces chimiques et des gaz affinants indispensables pour décrire les transferts de masse avec les bulles, la loi d'action de masse est utilisée. Afin de rendre la modélisation de ces calculs la plus souple possible, nous avons proposé une écriture où le nombre de réactions chimiques est quelconque avec un nombre quelconque de composés [75].

L'évolution des bulles est modélisée en suivant la composition de la bulle au cours du temps. Cinq gaz sont principalement impliqués [102] : O_2, SO_2 intervenant dans les réactions d'oxydoréduction vues précédemment ; CO_2 qui vient de la décarbonatation des matières premières et également de l'atmosphère de combustion ; H_2O et N_2 qui proviennent également de l'atmosphère. Si n_i correspond au nombre de mole dans la bulle de l'espèce gazeuse i où i varie de 1 à $N_g = 5$, sa variation temporelle est simplement donnée par

$$\frac{dn_i}{dt} = 2\pi a \,\mathrm{Sh}_i \,\mathcal{D}_i (C_i^\infty - C_i^S). \tag{1.4}$$

Dans cette dernière équation, t désigne le temps, a le rayon de la bulle et $\mathcal{D}_i$ le coefficient de diffusion. Les concentrations en gaz dissous dans le verre, C_i^∞, sont déterminées par les équilibres des réactions d'oxydoréduction comme évoquées ci-dessus. Pour les gaz dits «non affinants» comme H_2O, CO_2, N_2, les données expérimentales sont nécessaires. Pour les concentrations à la surface de la bulle, C_i^S, la loi d'Henry est utilisée sous la forme générale suivante

$$C_i^S = L_i P_i^{\beta_i}, \tag{1.5}$$

où ici le coefficient β_i prend en compte que certaines espèces sont chimiquement dissoutes entraînant une non-linéarité avec la pression partielle de cette espèce chimique, P_i. C'est le cas par exemple pour l'eau où l'exposant β_i est égal à $1/2$. Les solubilités, L_i, sont des fonctions de la température et de la composition des verres [56].

La quantité qui n'a pas encore été décrite dans (1.4) est Sh_i correspondant au nombre de Sherwood, fondamental dans la description des phénomènes de transfert sur lequel nous allons revenir en détail par la suite, §1.2. Ce nombre correspond au coefficient de transfert de masse sans dimension normalisé par le coefficient de masse en diffusion pure.

Lorsque les nombres de mole de chaque espèce sont connus, le rayon de la bulle est déterminé simplement en utilisant la loi des gaz parfaits sous la forme

$$\frac{3RT\sum_{i=1}^{N_g} n_i}{4\pi a^3} = P_0 + \rho g(H - z) + \frac{2\gamma}{a}, \tag{1.6}$$

où R est la constante absolue des gaz parfaits, T la température, P_0 la pression atmosphérique régnant au dessus du bain de verre, ρ la masse volumique du verre, H la hauteur totale de verre, z la position du centre de la bulle et γ la tension de surface entre le verre et la phase gazeuse.

Comme il est bien connu en génie chimique [58, 109], les réactions chimiques peuvent exacerber les transferts de masse. Pour autant, la plupart des contributions sur la modélisation de l'évolution des bulles dans les verres fondus ne tiennent pas compte de cet aspect [7]. Les recherches que nous avons menées sur le sujet ont porté sur l'étude des transferts de masse autour d'une bulle unique avec la prise en compte des réactions chimiques. Elles sont décrites dans la prochaine section.

L'annexe A reproduit trois articles sur ce thème dont les références sont les suivantes [76, 81, 77].

1.2 Transfert de masse autour d'une bulle

Dans ce travail, nous allons insister sur l'effet de la réaction d'oxydoréduction du fer. Il est également possible de faire la même étude en utilisant d'autres éléments polyvalents comme l'arsenic ou l'antimoine. Les travaux de Greene et Platts [39] ont montré que la résorption de bulles initialement composées d'oxygène est plus importante lorsque la quantité d'arsenic ou de fer est plus grande. Greene et Platts [39] expliquent ce phénomène par la présence de la réaction d'oxydoréduction de l'arsenic.

A SAINT-GOBAIN RECHERCHE, une expérience a été mise au point où le suivi de bulle se fait grâce à l'utilisation de creuset en silice transparente. Afin de simplifier l'étude, ces verres sont dépourvus de sulfate limitant à une seule réaction et à un seul gaz (O_2). On étudie deux verres, l'un ayant une faible quantité de fer, 0,03 % en masse et le deuxième ayant 0,1 % en masse de Fe. Les détails de l'expérience sont décrites dans la référence [81]. La FIGURE 1.1 présente un exemple de résultats très parlant où la résorption d'une bulle initialement composée d'oxygène est plus importante dans le verre à plus forte teneur en fer. Remarquons que les deux bulles ont des tailles initialement très proches.

Pour étudier ces phénomènes de transfert de masse, nous sommes amenés à décrire des mécanismes d'oxydation des verres qui restent encore incomplétement connus. Trois phénomènes sont principalement envisagés [26, 25, 68] : le premier est la diffusion de l'oxygène libre, le deuxième est la diffusion des ions d'oxygène. Le dernier mécanisme d'oxydation ne fait plus intervenir la diffusion de l'oxygène mais implique la diffusion des cations libres dans le verre, comme Na^+ par exemple. La neutralité électrique conduit à avoir des contre-diffusions d'électrons.

Ces recherches ouvrent le débat sur la nature des réactions chimiques lorsque des espèces gazeuses sont impliquées. Si ces dernières peuvent être dissoutes, les réactions peuvent avoir lieu de façon homogène dans le verre fondu. D'un autre coté, si le verre n'est pas perméable à certaines espèces gazeuses, les réactions ne peuvent avoir lieu qu'aux interfaces, on parle alors de réactions hétérogènes [17].

Pour ce qui est de l'oxygène, nous considérons que cette espèce diffuse dans le verre tout en étant influencée par la réaction d'oxydoréduction, éq. (1.3). Ainsi, le transport de l'oxygène peut

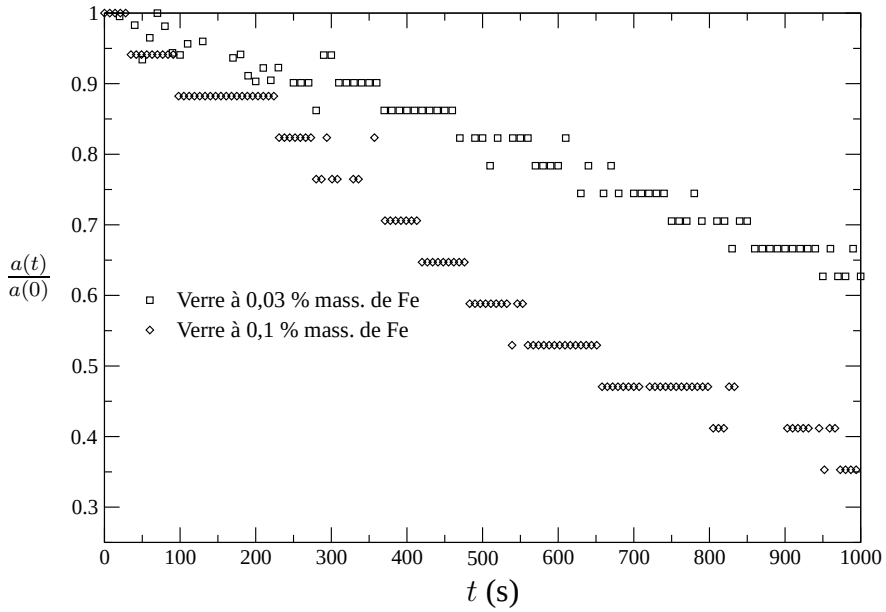

FIGURE 1.1 – Evolution de $a(t)/a(0)$ en fonction du temps pour deux verres, l'un ayant 0,03 % et l'autre 0,1 % de Fe en masse.

être décrit théoriquement à l'aide de l'équation suivante :

$$\frac{DC_{O_2}}{Dt} = \mathrm{div}\left(\mathcal{D}_{O_2}\mathbf{grad}C_{O_2}\right) + \dot{r}_{O_2}, \tag{1.7}$$

où C_{O_2} désigne la concentration molaire de l'oxygène dans le verre, $\mathcal{D}_{O_2}$ le coefficient de diffusion et $\dot{r}_{O_2}$ le taux de réaction chimique due à l'oxydoréduction du fer. Le membre de gauche correspond à la dérivée particulaire de C_{O_2}.

Dans la mesure où la réaction (1.3) peut être supposée instantanée, le taux de réaction, $\dot{r}_{O_2}$, s'exprime simplement en fonction de la dérivée matérielle de C_{O_2} [9, 76]. Les autres hypothèses faites sont de nature hydrodynamique : la première considère que l'écoulement est dans le régime de Stokes ce qui est facilement justifié par les faibles valeurs du nombre de Reynolds (de l'ordre de 10^{-2} voire moins). La deuxième est liée à la mobilité de l'interface bulle/verre. Nous avons supposé que celle-ci était totalement mobile en nous appuyant sur les résultats expérimentaux de [48, 43, 60]. Les auteurs y montrent que la vitesse d'ascension de bulles dans différents verres est prédite par la loi d'Hadamard-Rybczynski [40, 95] ce qui signifie que les interfaces bulle/verre sont totalement mobiles. Cette deuxième hypothèse, qui n'apporte qu'une correction mineure sur la vitesse d'ascension, a des effets bien plus importants sur les transferts de masse [59, 24].

La résolution numérique de ce problème a été publiée dans l'article [76] à l'aide d'une méthode par éléments finis : on y détermine le coefficient de transfert de masse autour d'une bulle en ascension dans un fluide au repos. Ce problème dépend des quatre nombres sans dimension

suivants

$$\mathrm{Pe} = \frac{2aV_T}{\mathcal{D}_{\mathrm{O}_2}}, \tag{1.8}$$

$$N_{\mathrm{Fe}} = \frac{C^{\infty}_{\mathrm{Fe}^{2+}}(1-\mathcal{R}^{\infty})Sa^{1/4}}{16C^{S}_{\mathrm{O}_2}}, \tag{1.9}$$

$$\mathrm{Sa} = \frac{C^{\infty}_{\mathrm{O}_2}}{C^{S}_{\mathrm{O}_2}}, \tag{1.10}$$

$$\mathcal{R}^{\infty} = \frac{C^{\infty}_{\mathrm{Fe}^{2+}}}{C^{\infty}_{\mathrm{Fe}^{2+}} + C^{\infty}_{\mathrm{Fe}^{3+}}}. \tag{1.11}$$

Le premier nombre est de celui de Péclet où a est le rayon de la bulle et V_T est la vitesse d'ascension de la bulle donnée par

$$V_T = \frac{ga^2}{3\nu}, \tag{1.12}$$

où g est l'accélération de la pesanteur et ν est la viscosité cinématique.

Le deuxième nombre sans dimension est très spécifique de la réaction d'oxydoréduction du fer. $C^{\infty}_{\mathrm{Fe}^{2+}}$ correspond à la concentration molaire en Fe^{2+} loin de la bulle et $C^{S}_{\mathrm{O}_2}$ désigne la concentration en oxygène à la surface de la bulle connue grâce à la loi d'Henry :

$$C^{S}_{\mathrm{O}_2} = L_{\mathrm{O}_2} P_{\mathrm{O}_2}, \tag{1.13}$$

où L_{O_2} est la solubilité et P_{O_2} la pression partielle dans la bulle d'oxygène.

Sa est la saturation en oxygène définie comme le rapport de la concentration en oxygène dans le verre à celle définie à la surface de la bulle. Finalement, $\mathcal{R}^{\infty}$ correspond à l'état de réduction du verre.

La résolution de l'équation (1.7) permet de calculer le coefficient de transfert de masse exprimé à l'aide du nombre de Sherwood défini par

$$\mathrm{Sh} = \frac{\displaystyle\int_{\mathcal{S}} \left.\frac{\partial C_{\mathrm{O}_2}}{\partial n}\right|_{\mathcal{S}} dS}{2\pi a \left(C^{\infty}_{\mathrm{O}_2} - C^{S}_{\mathrm{O}_2}\right)}, \tag{1.14}$$

où $\mathcal{S}$ est la surface de la bulle. La FIGURE 1.2 résume les résultats de tests trouvés sur les effets de la concentration en fer, de la température et de l'état de réduction. Le nombre de Sherwood est exprimé en fonction du nombre de Péclet. En parallèle de la solution numérique, une approximation de type couche limite lorsque le nombre de Péclet est grand a été développée (cf. détails dans [76]), également représentée sur la FIGURE 1.2. Cette solution de couche limite indique que le nombre de Sherwood suit une loi qui dépend de la racine carrée du nombre de Péclet.

On montre que plus la quantité de fer est importante, plus les coefficients de transfert de masse sont grands. L'augmentation de la quantité de fer entraîne des profils de concentration en oxygène plus raides. Ce qui veut dire que l'effet de la réaction chimique peut être vu comme une

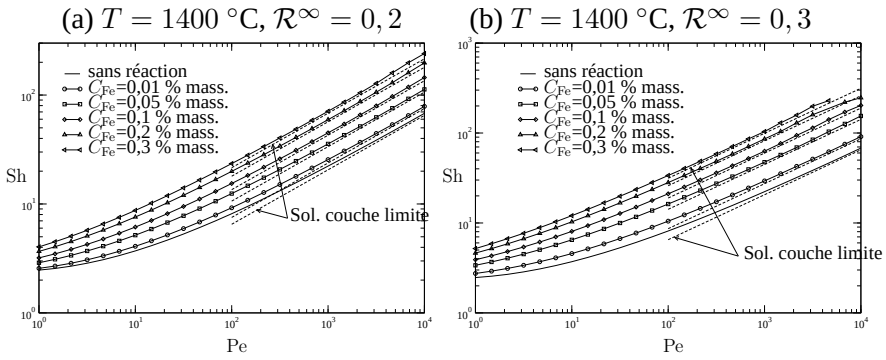

FIGURE 1.2 – Nombre de Sherwood en fonction du nombre de Péclet à $T = 1400$ °C et $\mathcal{R}^\infty = 0,2$ et $0,3$ où la concentration en fer total change dans la gamme $0,01$-$0,3$ % massique.

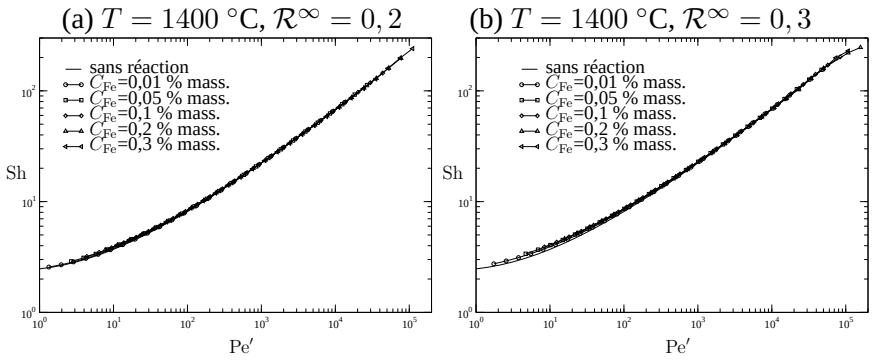

FIGURE 1.3 – Nombre de Sherwood en fonction du nombre de Péclet modifié à $T = 1400$ °C et $\mathcal{R}^\infty = 0,2$ et $0,3$ où la concentration en fer total change dans la gamme $0,01$-$0,3$ % massique.

diminution apparente du coefficient de diffusion ce qui produit une augmentation apparente du nombre de Péclet. En effet, on peut construire le nombre de Péclet suivant

$$\mathrm{Pe}' = \mathrm{Pe}\left[1 + \alpha(\mathrm{Sa}) N_{\mathrm{Fe}}\right], \tag{1.15}$$

où $\alpha(\mathrm{Sa})$ est la fonction obtenue en exploitant la solution de couche limite [76]

$$\frac{1}{\alpha} = \frac{1}{3,05\,\mathrm{Sa}^{-0,375}} + \frac{1}{1,28\,\mathrm{Sa}^{-1}}. \tag{1.16}$$

On constate alors que le nombre de Péclet modifié est toujours plus grand que Pe. L'introduction de ce nombre modifié a beaucoup d'intérêt car il permet de mettre l'ensemble des résultats de simulations numériques sur une courbe maîtresse comme il est possible de le voir sur la FIGURE 1.3 où le nombre de Sherwood a été représenté en fonction de Pe' pour les mêmes conditions que la FIGURE 1.2.

La courbe maîtresse correspond au cas où la réaction chimique n'a pas lieu et peut être décrite à l'aide de la corrélation bien connue [24] :

$$\mathrm{Sh} = 1 + \left(1 + 0,564\,\mathrm{Pe}'^{2/3}\right)^{3/4}, \tag{1.17}$$

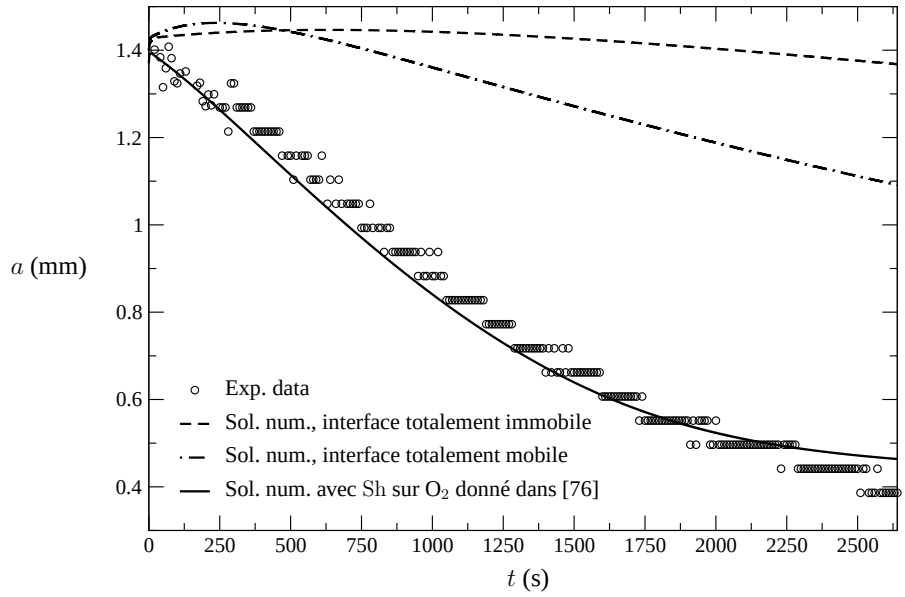

FIGURE 1.4 – Evolution temporelle d'une bulle dans un verre à 0,03 % en masse de fer à $T = 1400$ °C. Comparaison entre données expérimentales et résultats numériques.

où la seule modification apportée ici est l'utilisation du nombre de Péclet modifié. Ce résultat est fort intéressant car il permet d'utiliser une corrélation qui est facilement programmable dans un logiciel de mécanique des fluides numérique dans lequel on veut suivre l'évolution de bulles subissant des transferts de masse.

Dans la section 1.1, le modèle résumé par les équations (1.4-1.6) a été présenté et peut être utilisé pour l'étude des expériences de résorption de bulles d'oxygène. Bien que les verres utilisés aient une concentration en sulfate très faible (due aux pollutions que l'on trouve dans les matières permières), l'effet du SO_2 dissous peut avoir un effet pris en compte dans nos modélisations.

Les bulles évoluant dans des espaces confinés, l'hydrodynamique de l'ascension des bulles a été modifiée pour tenir compte des parois (cf. pour plus de détails [81]). Afin de voir l'importance de la modification du coefficient de transfert de masse de l'oxygène et de l'effet de la mobilité de l'interface, l'évolution temporelle de la taille d'une bulle obtenue expérimentalement est représentée sur la FIGURE 1.4. Nous comparons ces données expérimentales à diverses façons de prendre en compte le transfert de masse. La courbe en tirets correspond à une situation où l'interface de la bulle a été considérée comme immobile. Ceci conduit à des nombres de Sherwood en $\mathrm{Pe}^{1/3}$ [59, 24] prévoyant de moindres transferts comme on le voit clairement sur la FIGURE 1.4 d'où une résorption très fortement sous-estimée. L'utilisation de nombres de Sherwood pour des interfaces mobiles donne l'évolution représentée par la courbe en tiret point. Bien que plus grande, la résorption est encore largement sous-évaluée. Finalement, en utilisant le nombre de Sherwood pour l'oxygène obtenu à l'aide des développements présentés ci-dessus, la courbe en ligne continue reproduit de façon assez fidèle les résultats expérimentaux.

Grâce à ces nouveaux développements, l'effet du fer sur la résorption peut être reproduit théoriquement comme il est montré sur la FIGURE 1.5. Ces résultats ont été obtenus sans à avoir

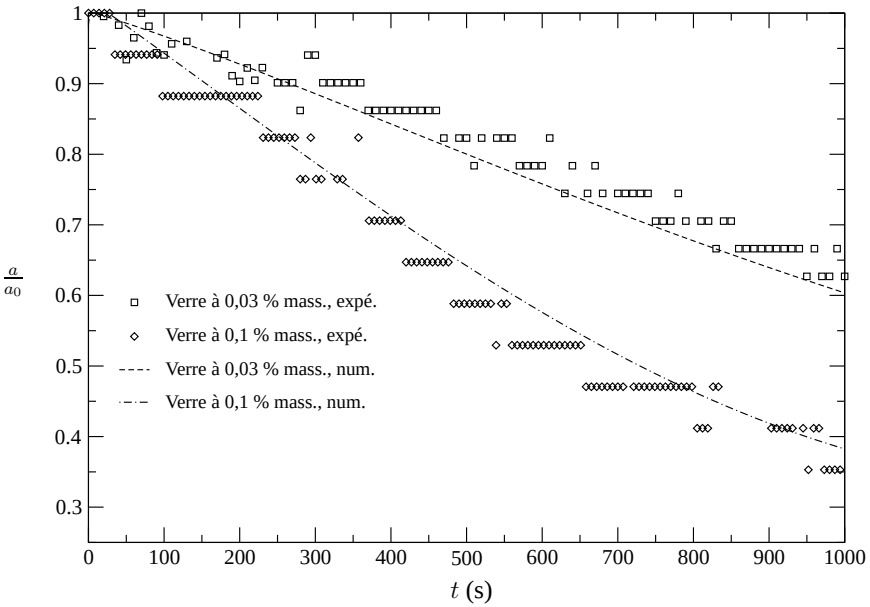

FIGURE 1.5 – $a(t)/a(0)$ en fonction du temps pour les deux verres ayant deux concentrations en fer différentes à $T = 1400$ °C. Comparaison entre les données expérimentales et le modèle numérique utilisant le nombre de Sherwood d'O_2 donné dans [76].

à caller des coefficients de diffusion ou autres paramètres. En fait, il est possible d'aller un peu plus loin dans l'analyse de la résorption des bulles d'oxygène. En effet, on a vu que plusieurs gaz sont impliqués dans l'évolution de la taille de la bulle. Néanmoins, ces gaz ne s'échangent pas tous à la même vitesse. En utilisant une analyse d'échelle, il est montré dans [77] que le temps caractéristique associé à une espèce chimique quelconque, indice i, est donné par

$$\tau_i = \frac{2a_0^2 P_0^{1-\beta_i}}{\mathrm{Sh}_{i,0}\,\mathcal{D}_i L_i RT}, \tag{1.18}$$

où a_0 est le rayon initial de la bulle et $\mathrm{Sh}_{i,0}$ est le nombre de Sherwood basé sur a_0. L'introduction du nombre de Sherwood permet de prendre en compte les phénomènes d'advection dans ce temps caractéristique. De plus, dans le cas de l'oxygène, l'effet de la réaction est également pris en compte.

Remarquons que, dans cette dernière relation, la quantité $L_i RT/P_0^{1-\beta_i}$ est sans dimension. Cette dernière correspond à la solubilité pour les concentrations écrites en massique.

L'utilisation des données sur les solubilités et les coefficients de diffusion résumées dans [7] permet de faire une estimation des temps caractéristiques donnés par (1.18) compte-tenu des conditions expérimentales publiées dans [81]. Ces temps sont résumés dans la TABLE 1.1 : le temps caractéristique le plus petit est celui associé à l'eau car la solubilité de l'eau est beaucoup plus grande que celles des autres espèces chimiques. L'eau s'échange très vite et atteint très rapidement une concentration d'équilibre facilement calculée à l'aide de la relation suivante

$$x_{\mathrm{H_2O}} = \mathrm{Sa}^2_{\mathrm{H_2O},0}, \tag{1.19}$$

Verre à 0,03 % mass. de Fe, $a_0 = 1,35$ mm, $T = 1400$ °C					
gaz	O_2	SO_2	CO_2	N_2	H_2O
τ_i (s)	1379	464	8686	78536	10
Verre à 0,03 % mass. de Fe, $a_0 = 1,7$ mm, $T = 1450$ °C					
gaz	O_2	SO_2	CO_2	N_2	H_2O
τ_i (s)	1007	423	6914	53898	8
Verre à 0,1 % mass. de Fe, $a_0 = 2,3$ mm, $T = 1300$ °C					
gaz	O_2	SO_2	CO_2	N_2	H_2O
τ_i (s)	3322	977	24630	310707	31
Verre à 0,1 % mass. de Fe, $a_0 = 1$ mm, $T = 1400$ °C					
gaz	O_2	SO_2	CO_2	N_2	H_2O
τ_i (s)	850	398	7445	67056	9

TABLE 1.1 – Temps caractéristique de transfert de masse pour chaque espèce chimique pour un verre à 0,03 et un autre à 0,1 % en masse de fer.

où $\mathrm{Sa}_{\mathrm{H_2O},0}$ correspond à la saturation en eau définie par

$$\mathrm{Sa}_{\mathrm{H_2O},0} = \frac{C^{\infty}_{\mathrm{H_2O}}}{L_{\mathrm{H_2O}}\sqrt{P_0}}. \tag{1.20}$$

Les deux autres gaz qui s'échangent sur des temps caractéristiques de plusieurs centaines de secondes sont l'oxygène et le dioxyde de soufre. Finalement, les deux gaz les plus lents sont le CO_2 et N_2. L'azote est particulièrement lent : son temps caractéristique d'échange peut atteindre plusieurs jours.

Ces résultats sont fortement liés aux solubilités. De façon plus précise, la quantité très importante est le produit $\mathcal{D}_i L_i RT/P_0^{1-\beta_i}$ qui fait intervenir le produit $\mathcal{D}_i L_i$ connu sous le nom de perméabilité [102]. Néanmoins, il est préférable d'utiliser le premier produit car il a pour dimension celui d'un coefficient de diffusion alors que $\mathcal{D}_i L_i$ n'a pas de dimension physique remarquable.

Finalement, compte-tenu de ces temps caractéristiques, on constate que pour la résorption d'une bulle d'oxygène les deux gaz les plus importants sont l'oxygène et le dioxyde de soufre. En considérant qu'initialement la bulle est composée uniquement d'oxygène mais est très vite compensée par l'eau, il est possible d'avoir une expression approchée de l'évolution temporelle du rayon de la bulle donnée par la relation suivante [77] :

$$\bar{a}(\bar{t}) = \left[1 - \frac{1}{2}\bar{t}\right]^2, \tag{1.21}$$

où $\bar{a} = a(\bar{t})/a(0)$ et $\bar{t}$ est un temps normalisé à l'aide de

$$\tau_{\mathrm{éch},\mathrm{O_2}} = \frac{\tau_{\mathrm{O_2}}}{(1 - x_{\mathrm{H_2O}} - Sa_{\mathrm{O_2},0} - \tau_{\mathrm{O_2}} Sa_{\mathrm{SO_2},0}/\tau_{\mathrm{SO_2}})}, \tag{1.22}$$

où $Sa_{\mathrm{O_2},0}$ et $Sa_{\mathrm{SO_2},0}$ sont données par

$$Sa_{\mathrm{O_2},0} = \frac{C^{\infty}_{\mathrm{O_2}}}{L_{\mathrm{O_2}} P_0},\ Sa_{\mathrm{SO_2},0} = \frac{C^{\infty}_{\mathrm{SO_2}}}{L_{\mathrm{SO_2}} P_0}. \tag{1.23}$$

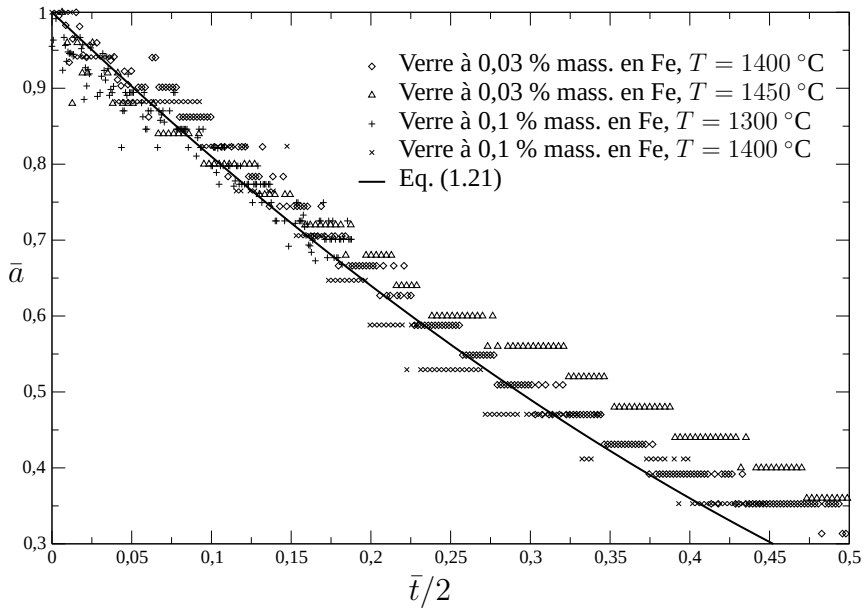

FIGURE 1.6 – $\bar{a}$ en fonction de $\bar{t}/2$ pour les deux verres ayant des concentrations en fer différentes. Comparaison entre les résultats expérimentaux et théorique.

Les quantités, τ_{O_2} et τ_{SO_2}, sont les temps caractéristiques d'échange liés respectivement à l'oxygène et au dioxyde de soufre donnés par l'équation (1.18).

Les données expérimentales obtenues sur les deux verres pour deux températures permettent d'obtenir l'évolution de $\bar{a}$ en fonction du temps normalisé selon l'équation (1.22) sur la FIGURE 1.6. Avec deux types de verre différents et différentes températures, les résultats se regroupent très bien sur une courbe maîtresse où l'équation (1.21) prédit de façon fidèle la résorption au cours des premiers instants.

1.3 Perspectives

Les résultats présentés ci-dessus ont été réalisés sur des verres où la quantité de sulfate a été réduite à son maximum. Néanmoins, le sulfate qui est très important dans le processus d'affinage nécessite d'être analysé de façon plus approfondie. La méthode employée pour faire le calcul des nombres de Sherwood sur l'oxygène peut être étendue à la réaction du sulfate donnée par l'équation (1.2). Ici, la difficulté est liée à la présence des deux gaz SO_2 et O_2. Ainsi, le transfert de masse de l'oxygène est influencé par plusieurs réactions. Une autre voie à étudier est de considérer que la réaction du sulfate n'intervient qu'à la surface des bulles (réaction hétérogène). Cette approche a l'avantage de simplifier les processus à décrire dans le liquide : seuls les phénomènes de diffusion et d'advection sont à prendre en compte. En contrepartie, les flux de masse des espèces SO_2 et O_2 doivent être écrits proprement compte-tenu des stœchiométries des réactions impliquées. La travail consiste à écrire proprement ces transferts de masse. En parallèle, des expériences sur l'évolution de bulles dans des verres ayant différents taux de sulfate sont à faire.

L'affinage des verres est un processus chimique mettant en jeu les deux phases, verre et gaz. Néanmoins, la modélisation numérique ne prend pratiquement jamais en compte le couplage chimique, hydrodynamique et thermique entre les deux phases. Pourtant, lorsque la quantité de bulles est grande comme aux premiers instants de l'élaboration des verres, les transferts de masse entre les bulles et le liquide induisent des changements d'équilibre chimique du verre. Rares sont les contributions où le couplage entre les bulles et le verre a été introduit. Citons néanmoins les travaux de Kloužek and Němec [52] où un premier modèle de ce genre a été proposé. Nous avons, dans la référence [75], décrit un modèle où le couplage chimique est réalisé en prenant un nombre quelconque de réactions chimiques. Ce modèle repose une nouvelle fois sur une hypothèse d'équilibre chimique instantané. Comme déjà évoqué, on sépare les gaz intervenant dans les réactions chimiques (gaz affinants) et les autres (gaz non-affinants). Le modèle repose sur l'écriture d'un système d'équations décrivant les degrés d'avancement des réactions en fonction de la consommation des gaz par les bulles, de la température ou encore la pression. Les détails du modèle sont décrits dans la référence [75]. Une étude sur la désulfatation a également été menée dans laquelle des expériences ont été comparées à ce modèle [66]. Néanmoins, ce dernier a été décrit pour un domaine spatialement homogène. L'évolution d'un nuage de bulles peut être décrit formellement par un bilan de population [90] où la conservation du nombre de bulles est écrite dans un espace des phases de dimension plus ou moins grand en fonction du nombre de degrés de liberté à prendre en compte pour décrire chaque inclusion. L'étape suivante consiste à trouver une méthode numérique fiable et robuste pour résoudre le problème complet. Pilon et Viskanta [84] ont proposé une méthode de caractéristique pour résoudre l'équation de bilan de population. Ils ont appliqué leur méthode à l'affinage du verre [83, 86]. Néanmoins, leurs travaux ont été faits à l'aide d'un code de mécanique des fluides structuré (*i.e.* fonctionnant sur une grille cartésienne). Nous voulons étendre ces travaux sur des logiciels basés soit sur la méthode des éléments finis ou des volumes finis.

Les interactions hydrodynamiques doivent être étudiées également précisément en axant les travaux sur la rhéologie des liquides très visqueux à bulles, qui restent encore peu étudiés. Citons, néanmoins les contributions expérimentales de Llewellin *et al.* [63] et celle de Rust et Manga [94] où le comportement non newtonien du milieu dû à la déformation des bulles lorsque le cisaillement local devient important est souligné. Les écoulements des bulles dans le verre présentant un faible nombre de Reynolds, les équations de Stokes peuvent être utilisés avantageusement. Le travail, qui doit être entrepris dans le cadre de la thèse de M. Guémas débuté en octobre 2011, est d'utiliser la modélisation à l'aide de la formulation intégrale des équations de Stokes [88] pour étudier les comportements rhéologiques d'un liquide visqueux ayant une fraction volumique non négligeable de bulles déformables.

Chapitre 2

Stabilité des mousses de «verre» fondu

Dans le chapitre précédent, nous avons vu que l'élimination des bulles est favorisée par l'ajout d'éléments chimiques dits affinants. Il est souvent fait usage du sulfate qui, à haute température, produit du SO_2 et O_2 par réaction d'oxydoréduction [8]. Ces deux dernières espèces gazeuses migrent de la fonte verrière vers les bulles, provoquant ainsi leur croissance. Avec l'augmentation de taille, les inclusions montent de façon plus rapide vers la surface du four. Ce mécanisme thermiquement activé se produit généralement dans une gamme de température assez faible (typiquement entre 1400 et 1450 °C) [50] avec un taux de production suffisamment grand pouvant conduire à la formation d'une mousse en surface du four.

La présence de cette mousse nuit fortement à l'efficacité du procédé à la fois sur le plan énergétique et sur la qualité du produit. En effet, la mousse isole thermiquement le bain de verre de l'atmosphère où se développe la combustion servant à chauffer le verre. L'isolation du bain de verre par la couche de mousse entraîne également une montée des températures dans la chambre de combustion, conduisant à une augmentation des émissions de polluants.

L'optimisation de plus en plus importante du procédé rend nécessaire de bien maîtriser les mécanismes de formation et de stabilisation des mousses de verre. Actuellement, les concepteurs de four ne disposent pas d'éléments fiables pour prédire l'apparition, la taille et l'étendue des couches de mousse présentes à la surface d'un four. Il devient alors difficile de maîtriser sous quelles conditions ces mousses existent.

Les recherches que nous avons menées dans le domaine se sont focalisées sur une approche mésoscopique où le drainage d'une bulle à la surface libre d'un verre a été étudié ainsi que la stabilité de films verticaux de verre. Ces deux points sont abordés successivement au cours des deux premières sections. Les perspectives sur ce thème seront ensuite présentées.

La synthèse faite dans ce chapitre correspond à trois articles [82, 55, 80] reproduits dans l'annexe B.

2.1 Drainage de bulles à la surface libre d'un liquide

Avant d'étudier le drainage et la stabilité d'une mousse, il est souvent fait usage d'investigations sur une bulle [100, 31] ou une goutte dans le cas d'émulsions [89, 41, 42]. Lorsqu'une

inclusion se dirige vers une interface, on peut identifier trois étapes.

La première est la montée de l'inclusion pilotée par les forces de flottabilité et les interactions hydrodynamiques. Lorsque les interfaces sont peu déformées, ces interactions hydrodynamiques peuvent être calculées précisément où la force de traînée augmente à mesure que l'inclusion est proche de l'interface, entraînant la diminution de la vitesse d'ascension [51]. La déformation des interfaces rend plus difficile la prédiction de ces interactions hydrodynamiques : cela nécessite des résolutions numériques telles que celles effectuées dans [82] dans la mesure où les écoulements sont supposés à faible nombre de Reynolds.

La deuxième étape est la stabilisation de l'inclusion au niveau de la surface libre où deux forces s'opposent : celle de flottabilité poussant la particule vers l'interface et celle de tension de surface résistant à la déformation de l'interface. Ceci entraîne une pression sur le film liquide qui draine en fonction du rapport des viscosités des deux fluides constituant l'inclusion et le liquide de la phase continue et du comportement des interfaces entre ces deux liquides. Pour des inclusions sans aucunes impuretés aux interfaces où la condition de continuité des contraintes tangentielles est satisfaite, Chi et Leal [22] ont montré que le rapport de viscosité avait de l'importance sur le drainage du film ainsi que sur les profils d'épaisseur de ces films. Yiantsios et Davis [112] ont procédé à une étude théorique de cette étape à la fois pour une goutte approchant d'une paroi solide ou d'une interface fluide. Ils indiquent que les épaisseurs des films varient de façon algébrique avec le temps. Néanmoins, ce travail n'est valide que pour des faibles déformations des interfaces et des rapports de viscosités finis. Pour les bulles, le rapport de viscosité ne joue plus aucun rôle, seuls les comportements des interfaces sont importants. Debrégeas *et al.* [31] ont montré que l'épaisseur d'un film de liquide très visqueux produit entre une bulle et une surface libre draine de façon exponentielle en fonction du temps.

La dernière étape correspond à l'éclatement de l'inclusion au niveau de la surface libre ou à sa traversée de l'interface entre les deux fluides. C'est de loin l'étape la plus difficile à appréhender car elle fait intervenir des forces à courte portée. Lorsque seules les forces de van der Waals agissent, les théories de Vrij [111] ou celle de Ruckenstein et Jain [93] peuvent être utilisées pour évaluer les épaisseurs critiques en deçà desquelles les films se rompent. La rupture est ensuite accompagnée d'une rétraction du film dont la physique dépend fortement de l'épaisseur de rupture et des propriétés physiques du liquide. Dans le cas des bulles, cette rétraction peut également s'accompagner de formation d'autres bulles [16].

2.1.1 Simulation numérique du drainage de bulles en présence de surface libre

La situation étudiée numériquement est celle de la FIGURE 2.1 où N bulles montent en direction d'une surface libre notée S_0. Le liquide dans lequel se trouvent les bulles a une viscosité dynamique μ et une masse volumique ρ constantes. Le champ de gravité dont la direction est indiquée sur FIGURE 2.1 a pour valeur absolue g. La tension de surface entre les deux fluides, supposée uniforme, est notée γ. La normale unitaire, $\boldsymbol{n}$, est par convention dirigée vers le liquide.

Le nombre de Reynolds basé sur la bulle de plus grande taille et sur une vitesse typique de montée de bulle donnée par $g4a^2/\nu$ où $a = \max(a_n)$ avec n variant de 1 à N et $\nu = \mu/\rho$, est sup-

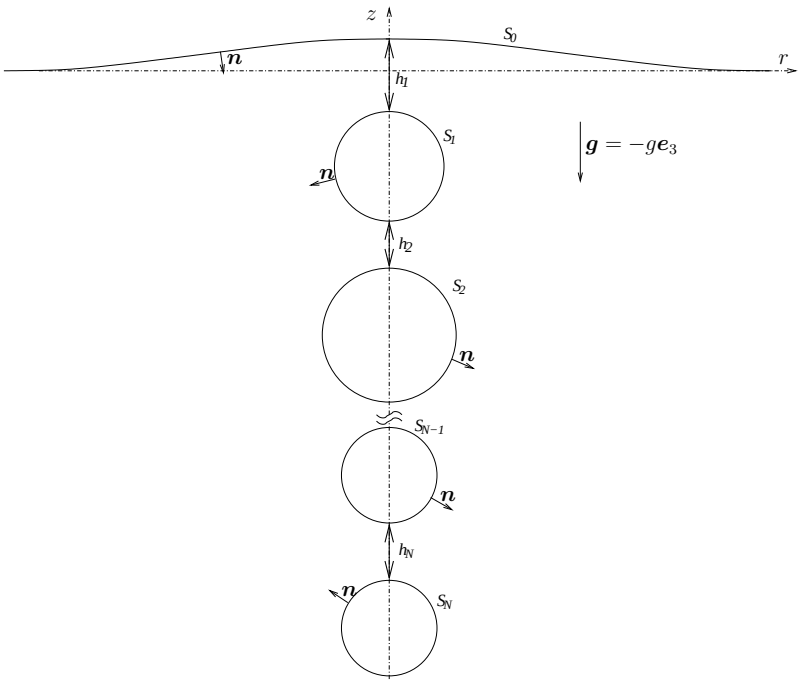

FIGURE 2.1 – Configuration axisymétrique de la montée de $N \geq 1$ bulle(s).

posé très faible pour utiliser l'approximation des équations de Stokes. Afin de traiter le transport de l'interface, une méthode d'intégrale de frontière a été utilisée dans laquelle seule la vitesse à l'interface demeure l'inconnue. La forme générale sans dimension de cette équation intégrale dite de Fredholm de deuxième espèce (cf. pour plus de détails sur les équations intégrales [27]) est la suivante [88] :

$$\boldsymbol{u}(\boldsymbol{x}_0) = -\frac{1}{4\pi}\int_S \boldsymbol{f}(\boldsymbol{x})\cdot\boldsymbol{G}(\boldsymbol{x},\boldsymbol{x}_0)dS(\boldsymbol{x}) + \frac{1}{4\pi}\fint_S \boldsymbol{u}(\boldsymbol{x})\cdot\boldsymbol{T}(\boldsymbol{x},\boldsymbol{x}_0)\cdot\boldsymbol{n}(\boldsymbol{x})dS(\boldsymbol{x}), \qquad (2.1)$$

où $\boldsymbol{x}_0$ est un point pris sur $S = \bigcup_{n=0}^{N} S_n$. Le symbole $\fint$ correspond à l'intégrale prise au sens de la valeur principale de Cauchy [73]. $\boldsymbol{f}(\boldsymbol{x})$ correspond au saut de contrainte donné par [1]

$$\boldsymbol{f}(\boldsymbol{x}) = \left(\frac{\boldsymbol{\nabla}_S\cdot\boldsymbol{n}}{\mathrm{Bo}} - z\right)\boldsymbol{n}. \qquad (2.2)$$

Bo est le nombre de Bond donné par

$$\mathrm{Bo} = \frac{\rho g 4a^2}{\gamma}. \qquad (2.3)$$

Le premier terme du membre de droite de (2.2) correspond au saut de contrainte lié à la tension de surface (force de Laplace). L'opérateur $\boldsymbol{\nabla}_S\cdot\boldsymbol{n}$ correspond à un facteur -2 près à la courbure

1. Dans l'article [82], nous avons utilisé une autre normalisation entraînant l'apparition d'un facteur 12. L'adimensionnement a été adaptée ici par souci d'uniformité de ce chapitre.

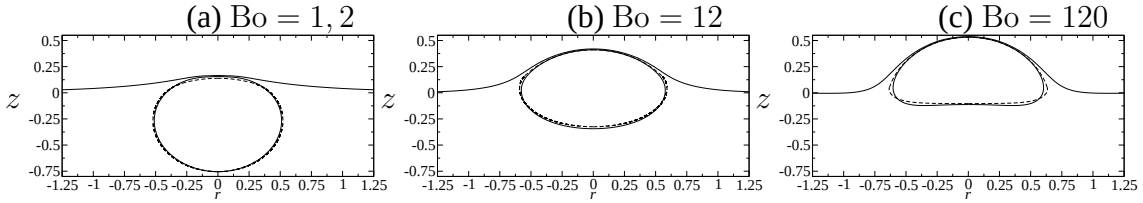

FIGURE 2.2 – Bulle proche d'une surface libre pour (a) $\mathrm{Bo} = 1, 2$, (b) $\mathrm{Bo} = 12$ et (c) $\mathrm{Bo} = 120$. Les lignes discontinues correspondent aux formes de bulle prédites par Princen [89].

moyenne de l'interface [1]. Le deuxième terme est lié à la contribution de la gravité dans la mesure où les équations de Stokes sont écrites sans force de volume.

Les deux quantités $\boldsymbol{G}(\boldsymbol{x}, \boldsymbol{x}_0)$ et $\boldsymbol{T}(\boldsymbol{x}, \boldsymbol{x}_0)$ sont les fonctions de Green associées à la solution fondamentale des équations de Stokes correspondant respectivement à des potentiels de simple et double couches. Leur forme exacte peuvent être trouvée dans le livre de Pozrikidis [88].

Une fois que la vitesse des interfaces est connue, leur transport est représenté par

$$\frac{d\boldsymbol{x}}{dt} = \boldsymbol{u}(\boldsymbol{x}, t). \tag{2.4}$$

Equation dans laquelle le temps est normalisé à l'aide de la quantité $\nu/(2ga)$.

La résolution numérique de ce problème met en œuvre une méthode d'éléments de frontière où les interfaces sont découpées en N_e éléments. Ensuite, une méthode de collocation est utilisée, consistant à placer N_c points de collocation sur chaque élément et à imposer l'équation intégrale sur l'ensemble de ces points. Seule la configuration bidimensionnelle axisymétrique a été retenue ce qui limite la discrétisation à des lignes de contour. Le problème s'avère singulier car le spectre de valeurs propres de la partie liée au potentiel de double couche, deuxième intégrale du membre de droite de l'équation (2.1), est compris dans le segment $[-1; 1]$. Afin de permettre la résolution numérique, nous avons utilisé une méthode de déflation de Wielandt supprimant les valeurs propres égales à un. Plus de détails sur la méthode peuvent être trouvés dans la référence [82] où nous avons recherché la technique la plus précise possible.

Les résultats numériques sur la montée d'une bulle vers une surface libre sont illustrés sur la FIGURE 2.2 où la forme d'une bulle proche de la surface libre est présentée pour trois nombres de Bond. Lorsque le nombre de Bond augmente, indiquant que la contribution liée à la flottabilité augmente, la bulle déforme fortement la surface libre et devient de plus en plus proche d'une demi-sphère. Princen [89] a déterminé par un simple calcul hydrostatique la forme prise par une inclusion proche d'une interface en supposant que le film entre les deux liquides est d'épaisseur négligeable. A partir de ce modèle nous avons déterminé les formes de bulles statiques. Elles sont indiquées en lignes discontinues sur la FIGURE 2.2 : l'accord avec nos résultats numériques est bon.

Le drainage peut être suivi en étudiant l'évolution de l'épaisseur du film au niveau de l'axe de symétrie en fonction du temps. La FIGURE 2.3 représente h, épaisseur du film, en fonction de t pour différent nombre de Bond. Le premier point important à noter est que l'épaisseur du film décroît exponentiellement avec le temps comme l'ont vu expérimentalement Debrégeas *et al.* [31]. En utilisant un modèle de lubrification où les conditions de contraintes de cisaillement

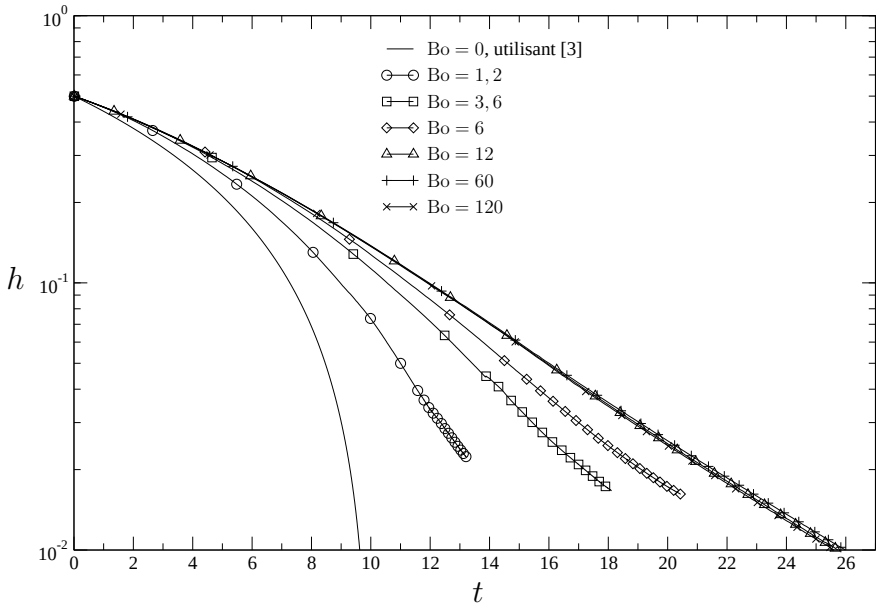

FIGURE 2.3 – h versus t pour $\mathrm{Bo} = 1,2\,;\ 3,6\,;\ 6\,;\ 12\,;\ 60\,;\ 120$. La courbe pour $\mathrm{Bo} = 0$ est obtenue grâce à la solution de Bart [3].

libres sont imposées aux interfaces, on peut établir que la décroissance de l'épaisseur du film est bien exponentielle comme nous le préciserons plus loin.

L'autre point important à noter sur la FIGURE 2.3 est que le taux de drainage, défini comme l'opposé de la dérivée logarithmique de h :

$$\tau_d^{-1} = -\frac{1}{h}\frac{dh}{dt}, \tag{2.5}$$

change en fonction du nombre de Bond. Plus Bo est petit, plus τ_d^{-1} est grand : le drainage est plus rapide. A la limite, lorsque le nombre de Bond tend vers zéro, les solutions exactes obtenues à l'aide des systèmes de coordonnées bisphériques par Bart [3] peuvent être utilisées pour trouver h en fonction du temps. Cette solution a été représentée sur la FIGURE 2.3 : la rupture du film se fait en temps fini du fait de la faible singularité des forces de lubrification (cf. pour plus de détails [82]). Un modèle permettant d'expliquer la dépendance avec le nombre de Bond est donné dans la prochaine sous-section.

Des configurations à deux et trois bulles ont été étudiées dans l'article [82] : les décroissances exponentielles sont également retrouvées. L'ajout d'une bulle accroît le drainage sur la bulle de tête (proche de la surface libre). L'effet est plus marqué à faible nombre de Bond. L'ajout de deux bulles ne change pas notablement le processus.

2.1.2 Expérience sur le drainage de bulles

Les études expérimentales sur le drainage de bulles ne sont pas nouvelles, à en juger par les références citées au début de ce chapitre. Par contre, développer ce type d'expériences sur du

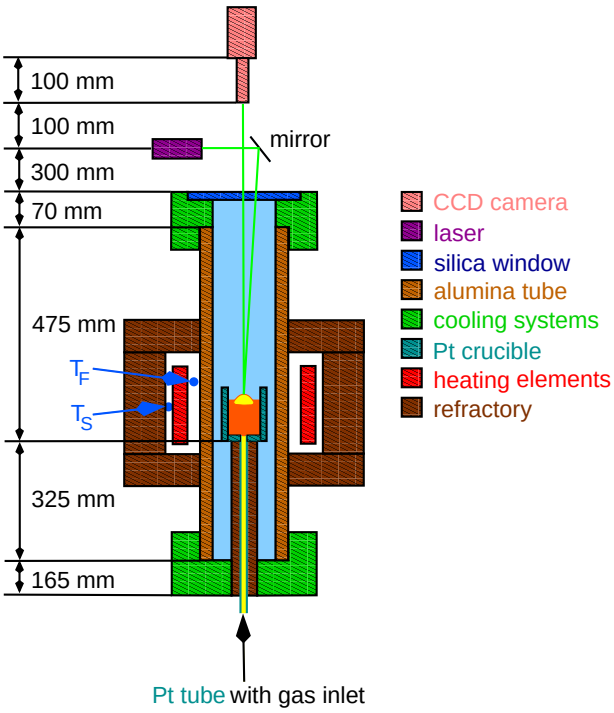

FIGURE 2.4 – Schéma de l'expérience réalisée sur le verre fondu dans un four tubulaire.

verre fondu reste un défi. Citons les travaux de Kappel *et al.* [49] où des études expérimentales ont été faites à la fois sur des films verticaux et sur des bulles. Néanmoins, si le drainage des films verticaux a été évalué, seuls les temps de vie des bulles ont été étudiés dans ce travail. Laimböck [57] a également repris l'expérience des films verticaux dans laquelle l'épaisseur est estimée par une mesure de résistivité électrique.

Kočárková [53, 55] a développé un dispositif expérimental pour étudier le drainage de film produit par une bulle à proximité d'une surface libre dans un verre fondu. Le dispositif, représenté sur la FIGURE 2.4, est constitué d'un four nécessaire à la chauffe du verre, réalisé à l'aide de résistances chauffantes. La température est régulée à l'aide d'un thermocouple noté T_F sur la FIGURE 2.4. Le verre est introduit dans un creuset platine-rhodium. Le fond du creuset dispose d'un trou de 100 μm de diamètre afin de permettre la création des bulles. Un tube en platine-rhodium fait la connexion avec une bouteille de gaz d'azote. Les bulles sont créées à la demande grâce à une électrovanne avec un temps d'ouverture contrôlé par un générateur d'impulsion. Le rayonnement du four étant très important, un filtre thermique est ajouté à la caméra, de même qu'un filtre de bande passante de 1 nm centré sur la longueur d'onde du laser.

La mesure de l'épaisseur du film à l'apex de la bulle se fait à l'aide d'un laser (longueur d'onde 532 nm) et d'une caméra CCD en utilisant une technique d'interférométrie. Nous ne sommes pas sûrs rigoureusement de l'ordre d'interférence ce qui induit que les épaisseurs des films ne peuvent être qu'étudiées qu'en relatif. Les mesures en absolue ne sont pas fiables.

Afin d'étendre cette étude à des liquides autre que le verre, cette expérience a été déclinée sur un montage à température ambiante réalisée à l'université Paris-Est, Marne la Vallée lors du

	μ (Pa·s)	ρ (kg·m^{-3})	γ (mN·m^{-1})	n (–)
Huile de ricin	0.75 ± 0.05	957	33.8	1.46
Huile UCON$^{\mathrm{TM}}$ oil	42 ± 5	1095	40.8	1.46
Verre 1	64 ± 7	2344	322	1.52
Verre 2	154 ± 13	2318	303	1.5

TABLE 2.1 – Viscosité dynamique, masse volumique, tension de surface et indice de réfraction des quatre liquides. Les propriétés du verre sont déterminées pour une température de fonctionnement de $1227°$C.

	SiO_2	Na_2O	CaO	K_2O	MgO	Al_2O_3
Verre 1	72.3	13.5	9.6	-	4	0.6
Verre 2	61.8	12.6	0.5	9.4	7.6	8.1

TABLE 2.2 – Composition des deux verres en pourcentage masique.

stage de Master 1 de Metallaoui [67] (cf. également [55]).

Quatre liquides ont été étudiés, deux à température ambiante : l'huide de ricin et une autre de synthèse (UCON$^{\mathrm{TM}}$) et deux verres à haute température. La TABLE 2.1 résume les propriétés physiques utiles de ces liquides pour l'étude du drainage. Les expériences sur les verres ont été réalisées à une température de $1227°$C. Les compositions des verres sont données dans la TABLE 2.2. La première composition est un verre sodocalcique classique alors que la deuxième est un verre pour des applications aéronautiques caractérisé par une plus forte teneur en alumine ce qui lui donne une plus grande viscosité. La détermination des propriétés physiques de ces verres est détaillée dans la thèse de Kočárková [53].

Les épaisseurs des films en fonction du temps sont données pour ces quatre liquides sur la FIGURE 2.5 : l'épaisseur y est normalisée par celle correspondant à l'ordre d'interférence la plus grande. Le temps est également normalisé de la même façon que celui utilisé dans les simulations numériques. A l'image de ce que nous avons vu à l'aide des simulations numériques, les épaisseurs de film décroissent de façon exponentielle avec le temps. Ceci témoigne que les interfaces des quatre liquides peuvent être considérées comme mobile. L'augmentation du nombre de Bond provoque aussi un ralentissement du drainage.

L'effet du nombre de Bond souligne le fait que la déformation de l'interface joue un rôle non négligeable dans le drainage. Comme Princen [89] l'a montré, la partie de la bulle se trouvant au dessus de la surface libre est une calotte sphérique caractérisée par son rayon de courbure, R_{cap}, sa hauteur émergée, h_{cap}. La surface de cette calotte sphérique est donnée simplement par la relation $S_{\mathrm{cap}} = 2\pi R_{\mathrm{cap}} h_{\mathrm{cap}}$. Un exemple de forme de bulle est donné sur la FIGURE 2.6 sur laquelle les dimensions R_{cap} et h_{cap} sont indiquées. Les trois parties remarquables de la bulle sont repérées.

A partir de ces données géométriques, il est possible de rendre compte de la dépendance en fonction du nombre de Bond du drainage du film. Pour cela, nous devons supposer que l'écoulement dans le film est de nature purement extensionnelle ce qui est justifié dans la mesure où

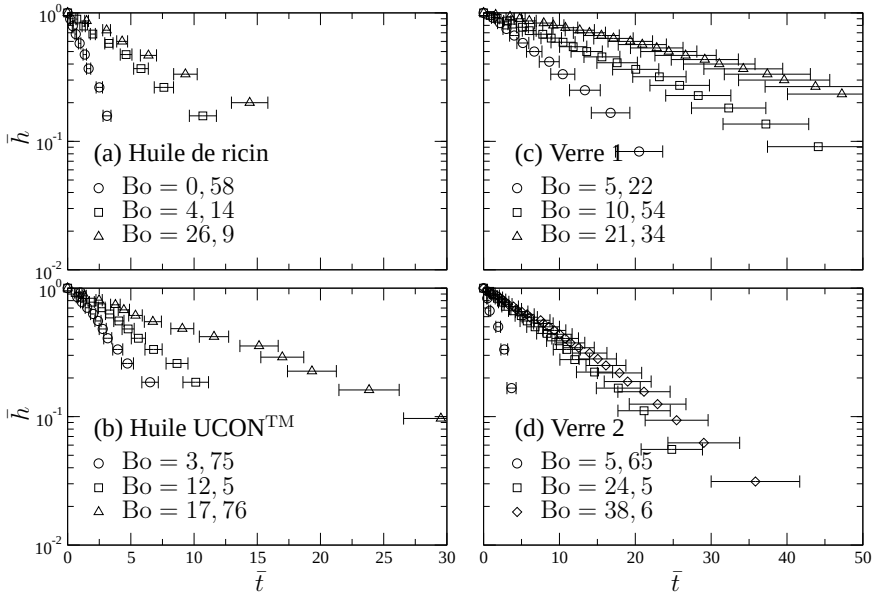

FIGURE 2.5 – Epaisseur normalisée des films à l'apex des bulles en fonction du temps normalisé pour les quatre liquides et pour différents nombre de Bond.

les interfaces sont libres de contraintes. En utilisant le modèle proposé par Petrie [74], la dérivée logarithmique de l'épaisseur normalisée prend la forme suivante

$$\frac{1}{h}\frac{dh}{dt} = -\frac{4\pi}{9S_{\mathrm{cap}}}, \tag{2.6}$$

où S_{cap} a été normalisée par le rayon de la bulle au carré et le temps normalisé de la même façon que dans la précédente section. L'évaluation de S_{cap} est donc cruciale pour estimer l'équation ci-dessus. En reprenant la formulation de Princen [89], les formes des bulles ont été recalculées ce qui permet la détermination de la surface de la calotte. La FIGURE 2.7 représente l'évolution de S_{cap} en fonction du nombre de Bond. L'augmentation de Bo entraîne une élévation de S_{cap}. Il est possible de montrer qu'à faible nombre de Bond, la surface de la calotte croît de façon linéaire avec Bo. De façon plus exacte, on a l'évolution suivante

$$S_{\mathrm{cap}} = \frac{\pi\,\mathrm{Bo}}{3}, \tag{2.7}$$

(cf. la courbe en ligne continue sur la FIGURE 2.7). A grand nombre de Bond, S_{cap} doit tendre vers l'aire d'une calotte hémisphérique. Ce qui, compte-tenu de la normalisation, donne la limite

$$\lim_{\mathrm{Bo}\to\infty} S_{\mathrm{cap}} = 2^{5/3}\pi. \tag{2.8}$$

Pour des valeurs intermédiaires, il est nécessaire d'avoir recours soit à la solution complète soit à une approximation. Nous avons cherché une solution approchée permettant de retrouver les deux régimes limites. Cette approximation est donnée sur la FIGURE 2.7 en ligne tiretée. Il s'agit

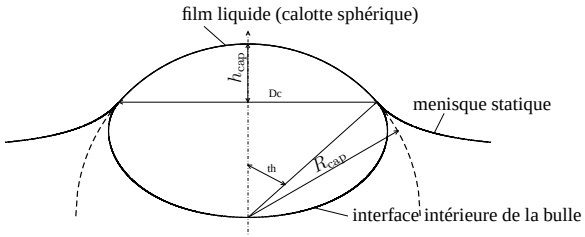

FIGURE 2.6 – Forme de bulle prédite par le modèle de Princen [89] pour $\mathrm{Bo} = 1$.

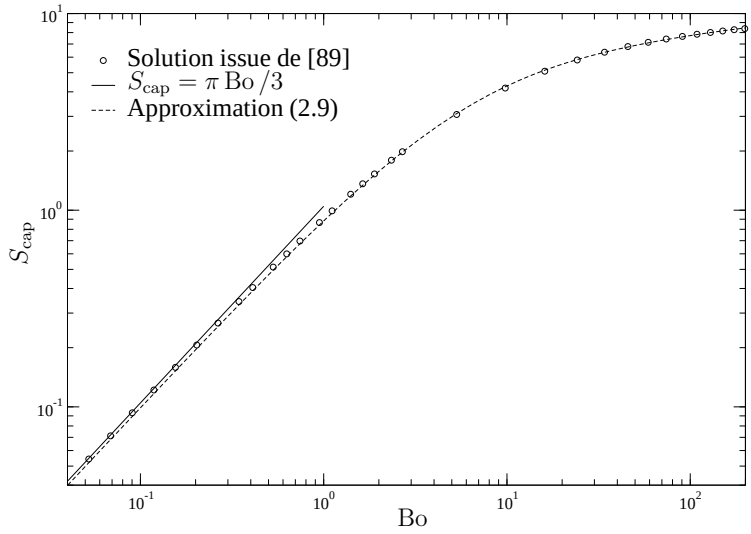

FIGURE 2.7 – S_{cap} en fonction de Bo obtenue en utilisant le modèle de Princen.

d'une régression obtenue en prenant une fonction rationnelle de la forme suivante

$$S_{\mathrm{cap}} = 2^{5/3}\pi \frac{94.7\,\mathrm{Bo} + \mathrm{Bo}^2}{902 + 142.5\,\mathrm{Bo} + \mathrm{Bo}^2}. \tag{2.9}$$

Le taux de drainage défini par (2.5) a été déterminé en utilisant les données expérimentales, par régression non linéaire de h en fonction de t. La FIGURE 2.8 donne l'évolution de τ_d^{-1} en fonction du nombre de Bond pour les quatre liquides. Le taux de drainage décroît bien pour l'ensemble des quatre liquides lorsque Bo augmente. Les résultats numériques de la précédente section ont été utilisés afin de déterminer τ_d^{-1}. Dans l'ensemble, les données numériques permettent de retrouver la tendance. Les meilleures comparaisons sont obtenues avec l'huile UCON$^{\mathrm{TM}}$. Pour les deux verres, les taux de drainage à grand nombre de Bond sont en assez bon accord. Par contre, les taux de drainage obtenus expérimentalement à faible Bo sont plus grands que ce que donne le calcul.

L'équation (2.6) a été utilisée pour déterminer τ_d^{-1} compte-tenu de (2.9). Cette solution est représentée sur la FIGURE 2.8 en ligne interrompue. Bien que ce modèle soit très simple, on reproduit de façon satisfaisante l'effet du nombre de Bond. On remarque néanmoins qu'à grand nombre de Bond, le modèle sous-estime le taux de drainage.

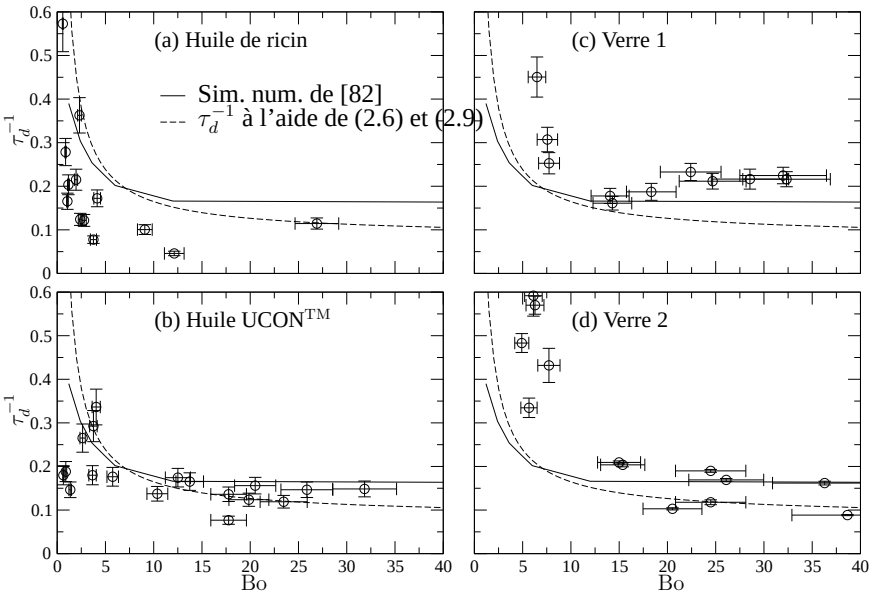

FIGURE 2.8 – Taux de drainage, τ_d^{-1}, en fonction du nombre de Bond pour les quatre liquides.

Les quatre liquides se comportent sensiblement de la même façon. Par contre, des expériences similaires ont été faite sur de l'huile de silicone [54] où nous avons trouvé que le taux de drainage est insensible au changement du nombre de Bond. A ce stade, aucune explication pertinente n'a pu être établie.

Concernant les expériences à haute température, en plus des deux verres déjà évoqués, d'autres formulations ont été examinées tels que des verres riches en oxyde de bore. Ces verres présentent des taux de drainage bien plus faibles que tous les autres. La stabilité des bulles a été étudiée sous l'angle du temps de vie. Nous avons séparé ce temps de vie en un temps de drainage observable grâce aux mesures interférométriques puis un temps où la bulle ne présente plus de franges d'interférences jusqu'à sa rupture. La synthèse des résultats montrent que le temps de vie des bulles commence par décroître lorsque la température augmente [53]. Par contre, le temps de vie s'accroît pour les plus fortes températures. Comme il est difficile de prélever les films issus des bulles afin de les analyser et de trouver une explication aux phénomènes décrits ici une expérience complémentaire a été réalisée et qui fait l'objet de la prochaine section.

2.2 Stabilité de films verticaux

L'expérience sur les films verticaux est également détaillée dans la thèse [53] de même que dans la référence [80]. Elle consiste à créer un film de verre en plongeant une structure en alliage platine-rhodium dans un creuset et à le ressortir. Ceci est effectué dans un four disposant d'un hublot par lequel le film est observé à l'aide d'une caméra. Seul un verre dont la composition est identique au verre 1 (cf. TABLE 2.2) a été étudié. Les temps de vie ont été enregistrés en fonction de la température. Sur la FIGURE 2.9, les résultats apparaissent en temps physique sur le graphe

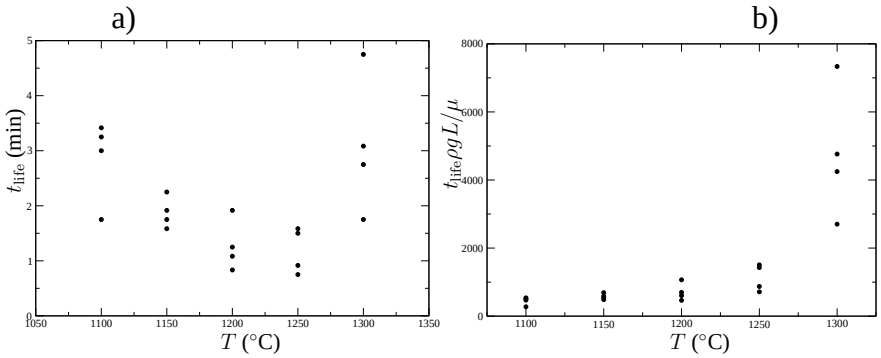

FIGURE 2.9 – a) Temps de vie des films verticaux de verre fondu en fonction de la température. b) Temps de vie normalisé des films verticaux en fonction de la température.

de gauche. Sur celui de droite, les temps ont été normalisés par la quantité $\rho g L/\mu$ où L est la hauteur de la boucle de platine-rhodium. Ce temps caractéristique du drainage a été proposé par Schwartz et Roy [99]. On constate bien qu'à basse température le temps de vie est très bien corrélé au drainage alors qu'à plus haute température (au dessus de 1250°C) le temps de vie est accru.

Ceci est dont la manifestation d'un phénomène stabilisant les films. Ce point avait d'ailleurs été souligné par Kappel *et al.* [49] et par Laimböck [57] qui indiquaient des épaisseurs de film stabilisé de l'ordre de la centaine de nanomètres.

Des films ont été prélevés après drainage ce qui permet de faire des analyses chimiques sur l'épaisseur du film. Les concentrations en oxydes sont déterminées à l'aide d'une technique de "Secondary Ion Mass Spectrometry" (SIMS). On observe une diminution de l'oxyde de sodium sur une dizaine de nanomètres : sur la FIGURE 2.10, deux profils sont donnés pour deux températures différentes. A 1400° C, l'échelle, notée δ, sur laquelle l'oxyde de sodium change est plus importante qu'à 1200° C. Les films ayant été prélevés après un même temps dans le four, on voit ici un effet thermique.

La volatilisation de l'oxyde de sodium est bien connue dans le verre [96, 6]. Cette évaporation s'explique par une réaction hétérogène entre la vapeur d'eau et l'oxyde de sodium produisant l'hydroxyde de sodium, NaOH. Cette évaporation contribue à changer la composition du verre dans le film. Or, ces modifications ont des conséquences sur la tension de surface. En effet, une diminution en Na_2O compensée par une augmentation de SiO_2 contribue à une augmentation de la tension de surface [98]. On peut y voir ici l'analogie avec la formation des larmes de vin où l'évaporation de l'alcool provoque une augmentation de la tension de surface [35, 44].

En utilisant une analogie avec les phénomènes de désorption, un modèle pour décrire la variation de tension de surface en fonction de l'épaisseur du film a été construit [80] : il repose sur le fait que l'évaporation de sodium est compensée par une augmentation de la silice et de l'oxyde de calcium qui constituent les trois oxydes principaux du verre.

Cette tension de surface a été employée dans un modèle de lubrification décrivant l'épaisseur et la vitesse du film à deux dimensions. Ce modèle est établi sur les bases théoriques proposées entre autres par Oron *et al.* [71], Howell [45] et Breward [18] dans lesquelles les effets de forces de viscosité élongationelle, de capillarité, de gravité et de gradient de tension de surface (Ma-

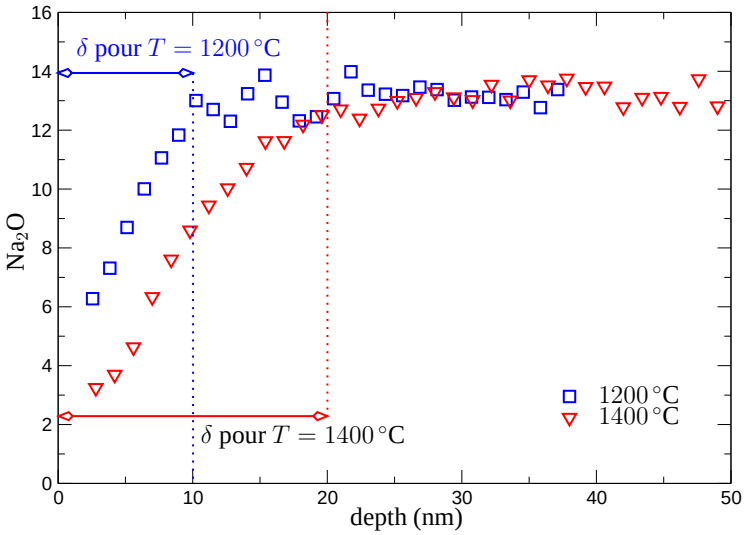

FIGURE 2.10 – Concentration en Na_2O en fonction de la profondeur d'un film pour deux températures.

rangoni) sont pris en compte. Les deux équations aux dérivées partielles non linéaires traduisant les conservations de la masse et de la quantité de mouvement sont résolues numériquement à l'aide d'une méthode aux différences finies impliquant une résolution numérique à l'aide d'une méthode de Newton-Raphson (cf. pour plus de détails [80]).

La FIGURE 2.11 présente l'évolution du minimum de l'épaisseur du film normalisé par l'épaisseur initiale du film en fonction du temps adimensionné par le temps caractéristique déjà indiqué précédemment, soit $\rho g L/\mu$. La couche sur laquelle l'évaporation a lieu varie de 0 à 10^{-6} m. Pour δ inférieure à 10^{-9} m, les variations de compositions ne sont pas assez importantes pour provoquer une stabilisation du film. Par contre, lorsque δ est égale à 10^{-8} m, l'évolution de l'épaisseur du film change de façon significative. L'ordre de grandeur de δ est bien celle que l'on observe expérimentalement. De plus, l'épaisseur à laquelle le film se stabilise trouvée à l'aide de ce modèle est sensiblement égale à 200 nm qui est en assez bon accord avec les évaluations faites par Laimböck [57]. Le film peut donc être stabilisé grâce à une augmentation de la tension de surface de $0,5$ % sur une étendue de l'ordre du centimètre.

Les calculs effectués pour des valeurs de δ supérieurs à 10^{-8} m montrent que la stabilisation a lieu à des épaisseurs plus élevées.

2.3 Perspectives

Les travaux sur la mousse de verre ont été focalisés à petite échelle : le drainage et la stabilité ont été étudiés soit sur des bulles soit sur des films verticaux. Des questions fondamentales sur l'hydrodynamique de bulles à proximité d'une surface libre restent ouvertes. Lorsque le nombre de Bond est faible, Berdan et Leal [11] ont étudié le comportement d'une particule solide à proximité d'une interface fluide. A l'aide d'une méthode de perturbation, ces auteurs ont pu établir la

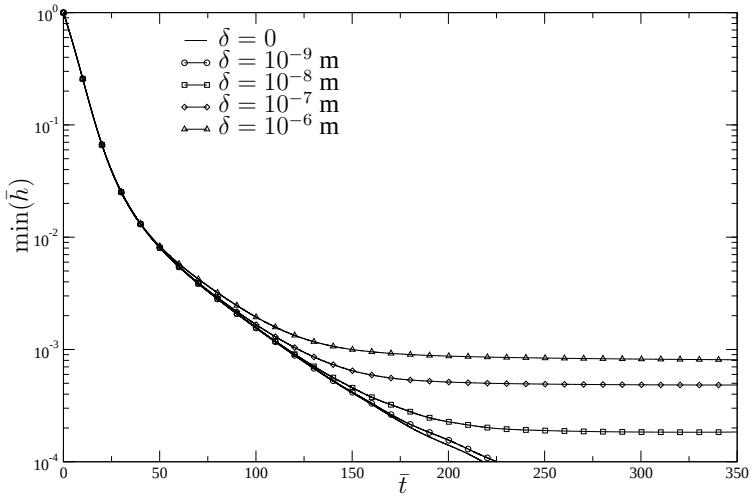

FIGURE 2.11 – Minimum de $\bar{h}$ dand le film liquide en fonction du temps pour $\delta = 0$, 10^{-9}, 10^{-8}, 10^{-7} et 10^{-6} m.

correction sur la force de traînée due à la déformation de l'interface. Par ailleurs, Chervenivanova et Zapryanov [21] ont étudié la déformation d'inclusions à proximité d'une interface fluide en utilisant des solutions déterminées à l'aide du système de coordonnées bisphériques. Ils n'ont pas cherché à déterminer les forces d'interaction hydrodynamique. La situation d'une bulle et d'une surface libre n'a fait l'objet d'aucune étude, à notre connaissance. Nous avons commencé à étudier cette situation pour laquelle la clé de voûte est le principe de réciprocité de Lorentz [64] dans le cadre de la thèse de M. Guémas, débutée en octobre 2011 en collaboration avec le laboratoire d'hydrodynamique de l'école Polytechnique.

Nos études sur le drainage de bulles de verre sous-entendent que la tension de surface est uniforme. Or, il existe des évidences expérimentales montrant que la tension de surface change en fonction de la nature des gaz [69]. Les simulations numériques réalisées à l'aide de la méthode d'intégrale de frontière sont généralisables aux situations où les tensions de surface de chaque interface sont différentes. Ce travail a également débuté dans le cadre de la thèse citée ci-dessus.

L'évaporation du sodium a été soulignée comme moyen de stabilisation des films. Les verres au bore montrent également une plus forte résistance au drainage. L'évaporation du bore peut sans doute jouer un rôle. Ce point reste à vérifier en faisant des expériences complémentaires.

En physique des mousses, le passage d'un film liquide à une mousse reste toujours une question difficile à répondre. Si ces dernières années, des études ont montrées que des relations sont possibles à faire sur des liquides aqueux, le cas du verre ou plus généralement de liquide sans surfactant reste ouvert. Plus généralement, le vieillissement de ce type de mousse est encore très mal connu. Le mûrissement de la mousse à l'aide de la diffusion de gaz perméables reste à évaluer. Comment les bulles coalescent ? Pour répondre à ces questions, des expériences sur des mousses de verre ou sur des liquides visqueux sans surfactants sont envisagées en collaboration avec le laboratoire Navier de l'école Nationale des Ponts et Chaussée. Ces travaux devront nous renseigner sur la modélisation du drainage de ces mousses de verre liquide.

D'un point de vue de la modélisation des fours verriers, il est important de mesurer l'im-

pact d'une couche de mousse sur les transferts thermiques. L'effet d'écrantage thermique d'une mousse est maintenant assez bien compris en fonction de la hauteur et de la morphologie de la couche de mousse [32, 85]. Néanmoins, il faut être en mesure, connaissant le flux de gaz dû au processus d'affinage, d'estimer la hauteur de mousse. Des modèles ont été proposés pour décrire la génération et la rupture de mousses aqueuses par Bhakta et Ruckeinstein [12, 13, 14]. Mais rien de tel n'a été proposé sur des mousses sans surfactants. Les travaux expérimentaux envisagés sur des mousses devraient nous permettre d'apporter des contributions sur cet aspect. On voit ici qu'il faut également avoir une bonne estimation des flux de gaz lié à l'affinage montrant la connection avec les travaux présentés dans le chapitre 1.

Outre ces applications orientées sur l'élaboration des verres, de nouveaux matériaux destinés à l'habitat voient le jour. Des milieux alvéolés sont obtenus à partir de verres recyclés [65] ou d'argile [20] broyés. Après mélange avec des agents nugléants, ils sont portés à haute température pour former une phase expansée dans laquelle la fraction volumique de gaz peut atteindre plus de 90 %. Ces milieux presentent souvent une double porosité dont les tailles caractéristiques sont séparées de deux ordres de grandeur. La présence ou non d'une forte connectivité et d'une porosité ouverte conditionne leurs applications. Nous envisageons d'étudier l'évolution de ces milieux en cours de formation en regardant à différents instants l'évolution morphologique de ces mousses.

Seuls le drainage et la stabilité ont été exposés dans le cadre de ces travaux. La rupture des films recèle des problèmes fondamentaux complémentaires. Par exemple, l'épaisseur à laquelle les films deviennent instables. Un autre sujet un peu étudié par Kočárková [53] est la formation de bulles parasites lors de l'éclatement de bulles plus grosses. Ce phénomène s'observe lorsque la viscosité est suffisamment faible (pour les expériences dans le verre, inférieure à 5 Pa·s). Il est lié à une rétraction rapide du film qui subit un battement conduisant à emprisonner de l'air d'où la formation de petites bulles [16]. Lors du stage de Metallaoui [67], réalisé en collaboration avec F. Rouyer de l'université de Paris-Est, Marne la Vallée, cette formation de bulles filles a été étudiée. Nous avons cherché à mesurer les vitesses de rétraction. Néanmoins, ces travaux restent à poursuivre. L'objectif est de pouvoir établir le diagramme de stabilité donnant la présence ou non de bulles «filles» ce qui peut être important dans le cadre des applications.

Chapitre 3

Thermohydrodynamique des bains de verre

La FIGURE 3.1 représente un four utilisé pour produire du verre plat par flottage sur bain d'étain. Les matières premières sont introduites au niveau de l'enfournement. Le four correspond principalement aux zones de fusion et d'affinage qui mesure plus de vingt mètres de long pour une largeur de plus de dix mètres alors que la hauteur est de l'ordre du mètre. L'énergie est fournie dans l'espace de combustion situé au dessus du bain de verre dans lequel des flammes se développent. L'air arrive des veines d'air et le combustible, fioul ou gaz, par des brûleurs. Les chambres de régénération ont pour fonction de récupérer l'énergie des produits de combustion qui ensuite sert à préchauffer l'air à des températures de l'odre de 1300 °C. Le conditionnement thermique correspondant à la zone de braise où la température du verre passe de 1400 à 1100 °C est précédé par le corset servant à séparer la partie fusion de celle de conditionnement. Le canal est la dernière partie avant le déversement du verre sur le bain d'étain.

Les fours industriels fonctionnent en système ouvert, ce qui signifie que les matières premières sont introduites à une extrémité et un verre chimiquement et thermiquement homogène en sort apte au formage des produits (verre plat, fibres, bouteilles, $\cdots$) dans l'idéal. Il faut donc que la réaction chimique donnée par la relation (1.1) ait le temps de se faire totalement. Ceci lie deux concepts forts du génie chimique, la thermodynamique et la cinétique. D'un point de vue thermodynamique, il est nécessaire d'apporter de l'énergie pour que la réaction (1.1) se produise. Ainsi, le four est une machine thermique dont les transferts de chaleur doivent être optimisés. Pour que les hétérogénéités disparaissent totalement, il faut du temps d'où l'aspect cinétique. On a vu au cours du chapitre 1 que les temps caractéristiques de l'évolution des bulles peuvent être grands. L'autre point crucial est que le four doit permettre un brassage du verre ce qui n'est pas facile pour un milieu très visqueux. La distribution des temps de séjour renseigne sur la capacité du système à élaborer un produit homogène. Elle apporte également des informations sur la flexibilité de l'installation. On débutera ce chapitre par quelques résultats sur ce point, §3.1.

Les fours verriers sont conduits en imposant des points chauds. D'autre part, le mélange vitrifiable absorbe beaucoup d'énergie ce qui induit l'apparition d'un point froid dans la zone d'enfournement. Ceci provoque des gradients thermiques longitudinaux à grande échelle entraînant l'apparition de mouvement de convection naturelle. De nos jours, la conception des fours s'ap-

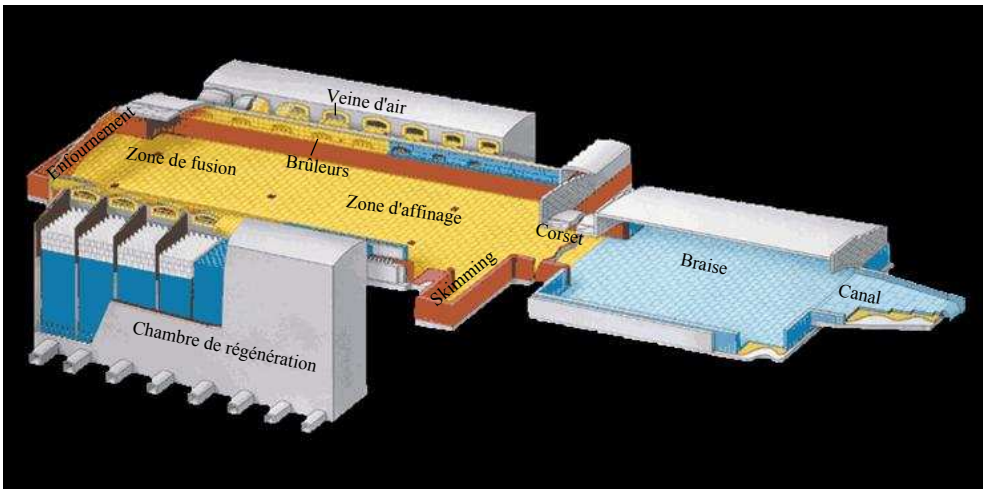

FIGURE 3.1 – Vue d'un four de verre plat obtenu par flottage sur bain d'étain.

puie fortement sur la simulation numérique. Néanmoins, bien que les puissances de calcul soient de plus en plus importantes, ces calculs restent encore assez longs et nécessitent des allers-retours entre les concepteurs et les modélisateurs. Il est donc indispensable d'avoir quelques outils pour guider le raisonnement des concepteurs limitant les cas à simuler. Dans le cas de la convection des fours, le problème consiste à savoir quels sont les paramètres essentiels qui pilotent les mouvements de convection et les coefficients de transfert thermique dans les fours. Ce problème sera abordé au cours de la section 3.2.

3.1 Distributions des temps de séjours dans les fours

Dans un système ouvert, les particules fluides ne subissent pas toutes la même histoire. Certaines y séjournent très peu et d'autre peuvent y rester indéfiniment. Une façon très courante de caractériser ces disparités est de déterminer la distribution des temps de séjour. C'est un élément essentiel pour caractériser le mélange [29]. Par définition, pour un système ouvert ayant un comportement stationnaire, la distribution des temps de séjour correspond à la réponse en sortie à un impulsion imposée (pic de Dirac) sur la zone d'entrée du système à un instant choisi de façon arbitraire. Néanmoins, à la fois expérimentalement et numériquement, il n'est pas facile de déterminer la réponse à une impulsion. Par contre, il est plus aisé de calculer la réponse à un échelon. Ensuite, la dérivée temporelle de la réponse à l'échelon correspond à la réponse à une impulsion, réponse qui est directement la distribution des temps de séjour. D'un point de vue pratique, cela revient à injecter un colorant à l'entrée du système et à déterminer sa concentration à la sortie. Numériquement, on le réalise en résolvant l'équation de transport non diffusive suivante

$$\frac{\partial C}{\partial t} + \boldsymbol{u} \cdot \mathbf{grad}\, C = 0, \tag{3.1}$$

où C est un colorant, t est le temps et $\boldsymbol{u}$ est le champ de vitesse. A l'entrée on impose $C = 1$ et sur l'ensemble des autres frontières, on prend des conditions de flux nul. Ce genre de procédure

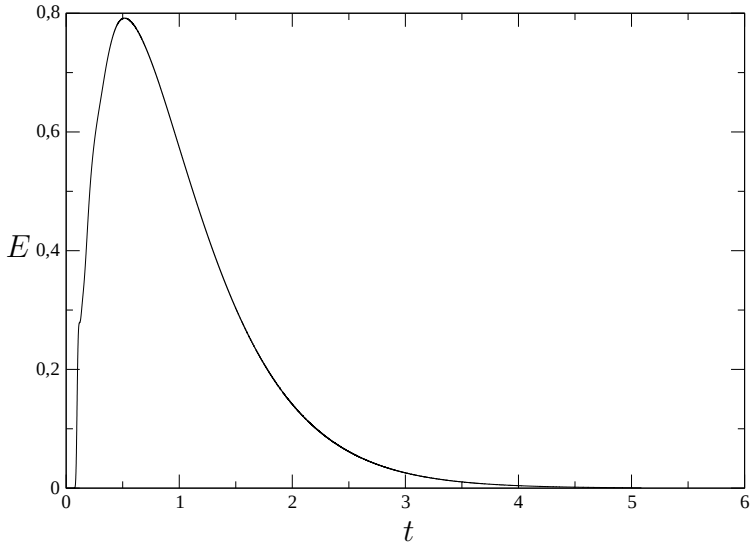

FIGURE 3.2 – Distribution des temps de séjour normalisée par $\langle t \rangle$ dans un four «float».

doit être faite avec précaution car il faut veiller à ce que la sortie ne subisse pas d'écoulement de retour sinon le résultat est entaché d'erreur.

Le flux à la sortie est déterminé à chaque instant, t, à l'aide de la relation suivante

$$F(t) = \frac{\rho \int_S C\boldsymbol{u} \cdot \boldsymbol{n} dS}{\dot{m}}, \tag{3.2}$$

où ρ est la masse volumique du liquide, S la surface matérialisant la sortie du système, $\boldsymbol{n}$ le vecteur normale unitaire sortant et $\dot{m}$ le débit massique.

La distribution des temps de séjour, $E(t)$, est donc donnée par

$$E(t) = \frac{dF(t)}{dt}. \tag{3.3}$$

Il est préférable de normaliser les distributions des temps de séjour à l'aide d'un temps caractéristique du système. Dans un système ayant une masse de matière égale à m et fonctionnant à un débit massique, $\dot{m}$, le temps moyen de séjour est estimé à l'aide de la relation suivante [110]

$$\langle t \rangle = \frac{m}{\dot{m}}. \tag{3.4}$$

Dans les fours produisant du verre plat par le procédé «float», la quantité de verre renfermé dans le four est de l'ordre de deux milles tonnes. Le débit massique étant de l'ordre de six cents tonnes de verre par jour, le temps moyen de séjour est de l'ordre de trois jours. La FIGURE 3.2 présente la distribution des temps de séjour normalisée par $\langle t \rangle$ en fonction du temps également adimensionné à l'aide de $\langle t \rangle$ pour un four «float».

La distribution s'avère être très large. Le temps minimum de séjour est de l'ordre de sept heures. Il est nécessaire d'attendre un temps égal à 2,3 fois le temps moyen, soit sept jours, pour que 95 % des particules fluides aient séjourné dans le four.

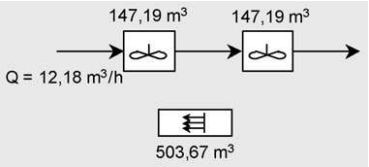

FIGURE 3.3 – Représentation en terme de réacteurs idéaux selon [87].

Le génie chimique tente de représenter le système en terme de réacteurs idéaux tels que des réacteurs parfaitement agités et pistons [58, 110]. Nous avons effectué une étude dans ce sens publiée dans la référence [87] à l'aide d'une méthode d'optimisation basée sur la minimisation de l'erreur quadratique entre la réponse obtenue par un assemblage de réacteurs et celle issue de nos simulations numériques. La configuration comportant un nombre minimum de réacteurs est illustrée sur la FIGURE 3.3 où deux réacteurs parfaitement agités caractérisés par leur volume sont placés en série. Le résultat essentiel ici est la présence d'un volume mort très important représentant pratiquement plus de 63 % du volume du four.

Ce volume mort reste encore difficile à relier à une description plus locale de l'écoulement. Pour répondre à cette interrogation, il est nécessaire d'introduire l'âge local dans les dispositifs étudiés. Ce type d'approche a déjà été envisagé par la résolution d'équations de transport de l'âge moyen par Baléo et Le Cloirec [2] et par Ghirelli et Leckner [36]. Si on définit $a(\boldsymbol{x})$ comme étant le temps moyen de résidence local et si le système a un fonctionnement stationnaire, l'équation régissant $a(\boldsymbol{x})$ est simplement l'équation de transport suivante

$$\frac{Da}{Dt} = \mathbf{grad}\, a \cdot \boldsymbol{u} = 1. \tag{3.5}$$

Le terme source décrit simplement que le point matériel a un temps de séjours local qui s'incrémente de façon uniforme par unité de temps le long des trajectoires des particules fluides. La résolution numérique de l'équation (3.5) a été faite à l'issue d'un calcul de four complet et est illustrée sur la FIGURE 3.4 où la trace de $a(\boldsymbol{x})$ sur les parois est représentée en heure. Deux zones très marquées se distinguent correspondant à deux grandes structures convectives.

Le four peut être vu comme l'assemblage en série de deux réacteurs parfaitement agités correspondant aux deux cellules de convection. En terme de répartition de temps de séjour, ces résultats montrent une équirépartition puisque le temps de séjour dans la première courroie est de l'ordre de 32 h correspondant sensiblement à la moitié du temps moyen de séjour obtenu à la sortie du four. Afin de vérifier ce point, la distribution des temps de séjour sans dimension de deux réacteurs parfaitement agités mis en série et ayant les mêmes temps moyens est donnée par la relation suivante

$$E(t) = 4t \exp\left(-2t\right). \tag{3.6}$$

La FIGURE 3.5 réprésente la comparaison de l'expression (3.6) avec la distribution des temps de séjour obtenue numériquement. L'absence de composante piston dans l'association des deux réacteurs ne permet pas de reproduire le temps minimum de séjour qui est pour un four float de l'ordre du dixième du temps moyen de séjour, soit 7 heures. Par contre, les deux distributions

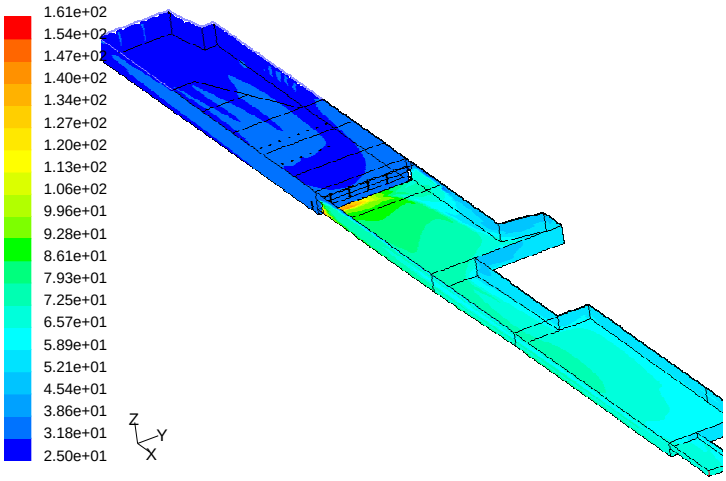

FIGURE 3.4 – Trace de $a(\boldsymbol{x})$ sur les parois d'un four «float» donnée en heure.

sont très similaires pour des temps de résidence supérieurs à une fois le temps géométrique. Ce point confirme que le four peut être vu comme la composition de deux réacteurs.

L'existence du volume mort trouvé dans le développement présenté plus haut n'est pas encore pleinement expliqué avec cette approche locale. Néanmoins, elle permet de confirmer que le four peut être vu comme deux réacteurs parfaitement agités placés en série.

3.2 Convection horizontale dans des cavités allongées

Comme vu au début de ce chapitre, les fours verriers ont des caractéristiques géométriques particulières : les profondeurs sont faibles comparées à leurs dimensions longitudinales et transversales. De plus, les simulations complètes des fours montrent qu'il y a peu de variation transversale dans les champs d'écoulement. Une façon d'aborder le problème théorique de la convection des fours verriers est d'étudier une situation plus simple. Il s'agit d'une configuration académique où l'écoulement est supposé bidimensionnel et dépourvu d'entrée et de sortie de matière. Le moteur de la convection doit être imposé : l'une des façons est d'appliquer une différence de température sur les parois verticales [15, 34] qui est une des configurations qui a été très étudiée [10]. Bien que cette situation permette de rendre compte de la physique, elle reste éloignée de la situation des fours qui sont chauffés depuis la surface. L'autre façon d'imposer un gradient de température est d'appliquer sur la partie supérieure du domaine un profil de température variable [78, 79].

Cette configuration beaucoup moins étudiée en génie thermique a néanmoins fait l'objet de nombreuses études en océanographie. L'apport de l'énergie solaire dépend de la latitude ce qui conduit à une chauffe non uniforme des océans. Les gradients de flux énergétiques sont à l'origine des mouvements océaniques [46, 91, 92]. L'étude de la convection dans une cavité où un profil de température non uniforme est imposé sur une des parois horizontales a fait l'objet de débats. Certains, comme Sandström [97] considérait qu'aucun d'écoulement ne pouvait naître si la

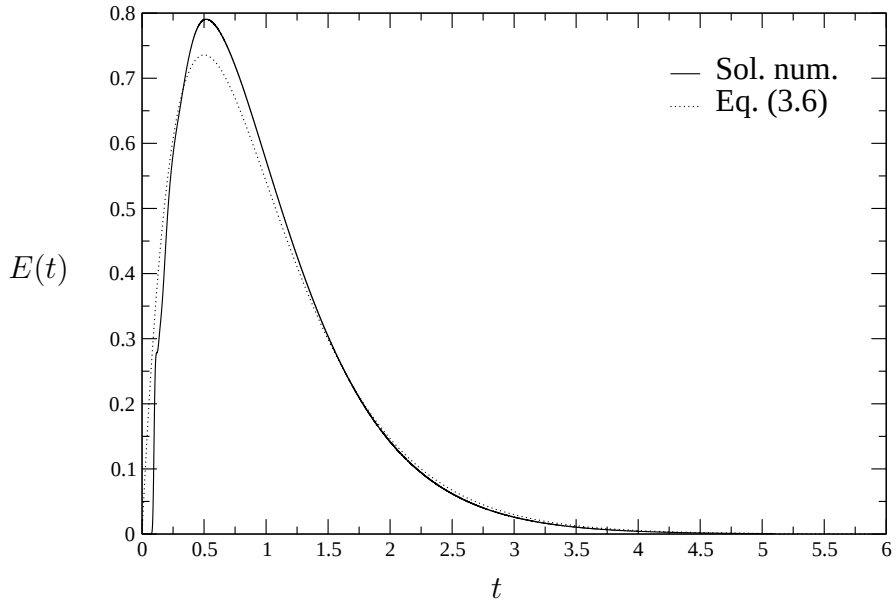

FIGURE 3.5 – Comparaison des distributions des temps de séjour obtenues à l'aide de la relation (3.6) et du calcul numérique.

température était imposée à la même hauteur. Il a fallu attendre les travaux de Jeffreys [47] pour avoir une première explication raisonnable sur l'existence des mouvements de convection. Les premiers travaux numériques prouvant l'existence des mouvements sont l'œuvre de Somerville [105] et de Rossby [91].

Quand bien même la température est appliquée sur une même horizontale, si le profil de température n'est pas uniforme, le champ de température dans la cavité admettra des gradients spatiaux dans toutes les directions. Ainsi, l'existence d'une composante horizontale du gradient thermique garantit la mise en mouvement du fluide. En effet, si le produit vectoriel entre le champ de gravité et le gradient thermique est non nul, la vorticité admet une valeur non nulle. On parle alors de convection naturelle sans seuil. A l'inverse, lorque les champs de gravité et du gradient thermique sont colinéaires, il est nécessaire d'atteindre un seuil si le champ de température est instable.

Dans l'article [34], nous avons pu établir les lois régissant l'intensité convective lorsque les températures sont appliquées sur les parois verticales. Le cas de la chauffe depuis la surface supérieure, représenté sur la FIGURE 3.6 a été traité dans l'article [79]. Les conditions aux limites cinématique et thermique sont également reportées sur cette figure. Des conditions d'adhérence ont été utilisées sur toutes les frontières bien que la surface du verre soit une surface libre. Néanmoins, notons que le mélange vitrifiable rigidifie la surface supérieure du four. De plus, la présence de mousse peut également changer les conditions aux limites. Chiu-Webster *et al.* [23] ont réalisé une étude numérique équivalente à la nôtre en utilisant à la fois des conditions d'adhérence ou de glissement montrant que cela ne change en rien les lois de transfert en dehors des facteurs multiplicatifs. Le profil de température a été choisi de sorte à garantir la continuité des flux thermiques aux coins supérieurs de la cavité. Il s'agit d'un profil sinusoïdal où $\Delta T = T_+ - T_-$ où

T_- est la température froide et T_+ la chaude. Ceci rend possible l'établissement de solutions approchées utilisant les méthodes de développement asymptotique comme décrit dans la référence [79].

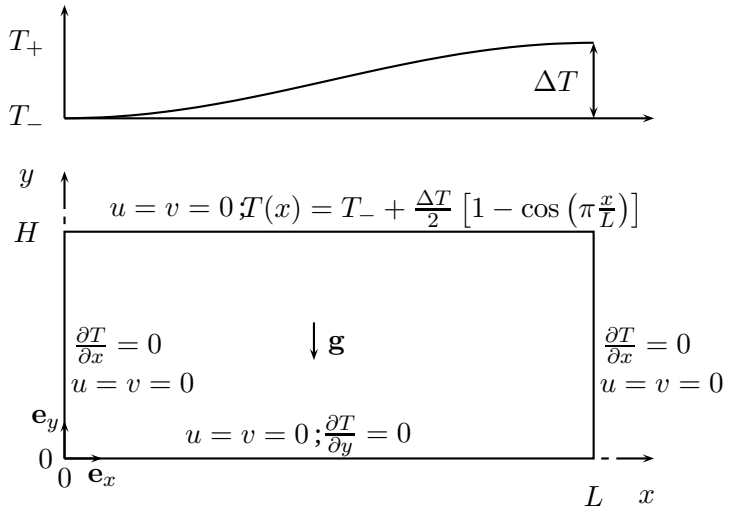

FIGURE 3.6 – Cavité rectangulaire où les conditions aux limites cinématique et thermique sont reportées.

Ce problème de convection est gouverné par les trois nombres sans dimension suivants [5] :

$$\mathrm{Pr} = \frac{\nu}{\kappa}, \tag{3.7}$$

$$A = \frac{H}{L}, \tag{3.8}$$

$$\mathrm{Ra} = \frac{g\beta\Delta T H^3}{\nu\kappa}, \tag{3.9}$$

où Pr est le nombre de Prandtl, rapport de la viscosité cinématique, ν, à la diffusivité thermique, κ. A est le rapport d'aspect hauteur sur longueur. Ra est le nombre de Rayleigh où g désigne l'accélération de la pesanteur, β le coefficient de dilatation volumique du fluide.

Cormack *et al.* [28] et Flesselles et Pigeonneau [34] ont montré que la vitesse caractéristique dans ce type de convection, dans la mesure où le rapport d'aspect A est petit, est $\mathrm{Ra}\,\kappa/L$. Ainsi, si les équations de bilan sont adimensionnées à l'aide de cette vitesse et par H, elles prennent la

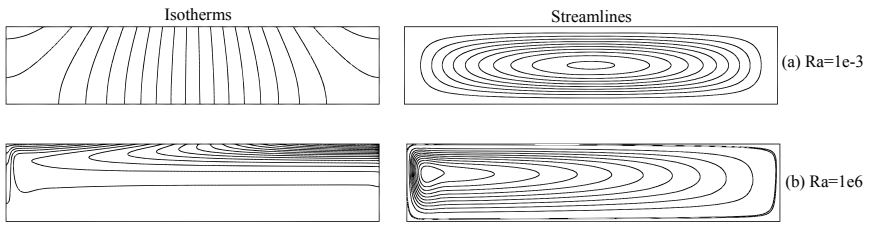

FIGURE 3.7 – Isothermes et lignes de courant dans une cavité de rapport d'aspect $1/5$ et pour $\mathrm{Ra} = 10^{-3}$ (première ligne) et $\mathrm{Ra} = 10^{6}$ (deuxième ligne).

forme suivante

$$\frac{\partial u}{\partial x} + \frac{\partial v}{\partial y} = 0, \tag{3.10a}$$

$$u\frac{\partial u}{\partial x} + v\frac{\partial u}{\partial y} = -\frac{\partial P}{\partial x} + \frac{\mathrm{Pr}}{\mathrm{Ra}\,A}\left(\frac{\partial^2 u}{\partial x^2} + \frac{\partial^2 u}{\partial y^2}\right), \tag{3.10b}$$

$$u\frac{\partial v}{\partial x} + v\frac{\partial v}{\partial y} = -\frac{\partial P}{\partial y} + \frac{\mathrm{Pr}}{\mathrm{Ra}\,A}\left(\frac{\partial^2 v}{\partial x^2} + \frac{\partial^2 v}{\partial y^2}\right) + \frac{\mathrm{Pr}}{\mathrm{Ra}\,A^2}\theta, \tag{3.10c}$$

$$u\frac{\partial \theta}{\partial x} + v\frac{\partial \theta}{\partial y} = \frac{1}{\mathrm{Ra}\,A}\left(\frac{\partial^2 \theta}{\partial x^2} + \frac{\partial^2 \theta}{\partial y^2}\right), \tag{3.10d}$$

où θ correspond à

$$\theta = \frac{T - T_-}{T_+ - T_-}. \tag{3.11}$$

Des recherches antérieures [92, 61, 38] montrent que le nombre de Prandtl ne jouait aucun rôle s'il est plus grand que un. Or, pour le verre, ce dernier est généralement supérieur à 10^2, voire à 10^3. Ainsi, l'étude numérique que nous avons menée a été faite en imposant le nombre de Prandtl égal à 10^3. Seuls, le rapport d'aspect et le nombre de Rayleigh sont variables.

Comme montré par Böhrer [15] dans la situation où la température est imposée sur les parois verticales, il existe deux grands régimes d'écoulement, l'un pour lequel les transferts thermiques sont gouvernés par les phénomènes de conduction et l'autre piloté par la convection. Ces deux régimes sont dits respectivement, conductif et convectif. Dans la situation représentée par la FIGURE 3.6, les isothermes et la fonction de courant sont données sur la FIGURE 3.7 pour $A = 1/5$ et $\mathrm{Ra} = 10^{-3}$ et $\mathrm{Ra} = 10^{6}$. A très faible nombre de Rayleigh, on trouve le régime conductif dans lequel la température suit la solution en absence d'écoulement qui est très facile à déterminer de façon exacte. On constate ici que ce champ de température admet bien un gradient longitudinal conduisant à l'apparition d'un champ de vitesse qui présente une symétrie par rapport au centre de la cavité.

Par contre, lorsque le nombre de Rayleigh est grand, les structures thermiques et cinématiques changent fortement et une importante dissymétrie apparaît. Le champ de température fait ressortir une couche limite juste en dessous de la frontière supérieure et une zone très homogène en dehors. Le centre de l'écoulement est complètement décalé vers la zone froide se trouvant à gauche de la cavité. Un jet pariétal dirigé vers le bas y apparaît.

Les questions importantes qui se posent maintenant sont les suivantes : quel paramètre régit le passage d'un régime à l'autre lorsque change le rapport d'aspect ? Quels sont les lois de transfert de masse et de chaleur dans chaque régime ? Pour répondre à ces questions nous avons fait à la fois une analyse d'échelle et une analyse numérique.

L'analyse d'échelle, esquissée dans [34], montre qu'un seul et unique paramètre contrôle les deux régimes : il s'agit du produit $\mathrm{Ra}\,A^2$. Cette quantité peut être interprétée comme le rapport du temps caractéristique de diffusion de la chaleur sur la hauteur H de la cavité au temps caractéristique d'advection suivant la longueur de la cavité. Les faibles $\mathrm{Ra}\,A^2$ correspondent donc à la situation où le transfert conductif domine. A l'inverse, les grandes valeurs de $\mathrm{Ra}\,A^2$ signifient que les échelles de temps les plus courtes sont liées à l'advection. L'analyse d'échelle permet d'établir que la vitesse caractéristique de l'écoulement, représentée sous forme normalisée par un nombre de Péclet défini par

$$\mathrm{Pe} = \frac{|u|_{\max} L}{\kappa}, \tag{3.12}$$

où $|u|_{\max}$ est la vitesse maximale longitudinale rencontrée dans la cavité, est donnée par

$$\mathrm{Pe}\,A^2 \sim \mathrm{Ra}\,A^2, \tag{3.13a}$$

dans le régime conductif et

$$\mathrm{Pe}\,A^2 \sim (\mathrm{Ra}\,A^2)^{2/5}, \tag{3.13b}$$

dans le régime convectif.

Quant au transfert thermique, généralement traduit en terme de nombre de Nusselt, correspondant au flux thermique normalisé par celui en absence d'écoulement, les comportements suivants sont obtenus

$$\mathrm{Nu} \sim A^2, \tag{3.14a}$$

dans le régime conductif et

$$\mathrm{Nu} \sim (\mathrm{Ra}\,A^2)^{1/5}, \tag{3.14b}$$

dans le régime convectif.

Nu correspond à un nombre de Nusselt soit local soit moyenné. La loi trouvée dans le régime convectif provient du fait que l'échelle typique de la couche limite est d'ordre $H/(\mathrm{Ra}\,A^2)^{1/5}$.

L'analyse numérique présentée dans la référence [79] permet de vérifier ces comportements. La FIGURE 3.8 donne $\mathrm{Pe}\,A^2$ en fonction de $\mathrm{Ra}\,A^2$ pour sept rapports d'aspect et une gamme de Ra allant de 1 à 10^9. Les deux régimes sont clairement identifiés. Nous avons établi des lois approchées qui pourront être consultées dans la référence [79].

Pour les transferts thermiques, comme l'intégrale du flux thermique sur la frontière doit être nulle par conservation de l'énergie, nous avons défini comme flux moyen la quantité suivante

$$\langle \mathrm{Nu} \rangle = \sqrt{A \int_0^{1/A} \left[\frac{\partial \theta(x)}{\partial y} \right]^2 dx}. \tag{3.15}$$

Cette dernière quantité est représentée en fonction de $\mathrm{Ra}\,A^2$ sur la FIGURE 3.9. L'évolution du nombre de Nusselt recèle quelques différences par rapport à l'évolution du nombre de Péclet. En

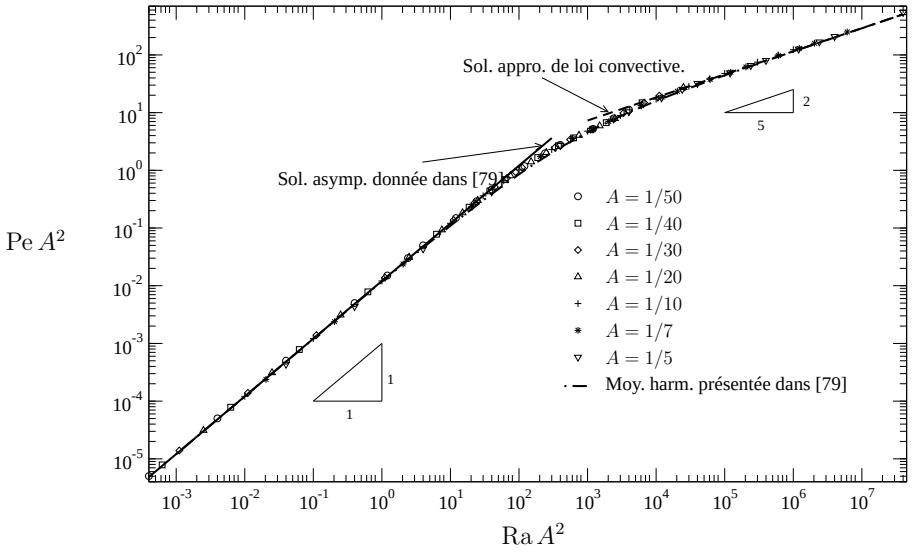

FIGURE 3.8 – $\mathrm{Pe}\,A^2$ en fonction de $\mathrm{Ra}\,A^2$ dans des cavités de rapports d'aspect $1/50$, $1/40$, $1/30$, $1/20$, $1/10$, $1/7$ et $1/5$.

effet, bien que les deux régimes asymptotiques soient bien retrouvés, un régime intermédiaire est clairement établi pour lequel le nombre de Nusselt croît très vite avec $\mathrm{Ra}\,A^2$. Ce régime transitoire dépend du rapport d'aspect. Dans la référence [79], des lois approchées ont également été proposées, non détaillées dans ce document.

Ces résultats sont un guide important pour les études plus pratiques menées sur des installations plus proches de la réalité. Par exemple, la prise en compte de la dépendance de la viscosité avec la température ne change pas les comportements asymptotiques. Des simulations sur des fours simplifiés avec entrée et sortie de matière montrent que le produit $\mathrm{Ra}\,A^2$ reste l'unique paramètre. Seuls les préfacteurs et les exposants sont un peu modifiés.

Compte-tenu des résultats trouvés au cours de ces travaux, nous pouvons établir que les fours verriers se trouvent dans le régime convectif, ce qui a des conséquences importantes sur leur fonctionnement. Ceci peut être vu simplement en examinant l'ordre de grandeur de la vitesse dans le four. Elle est donnée par la relation suivante

$$u_0 \sim \left(\frac{\beta \Delta T g}{\nu}\right)^{2/5} \kappa^{3/5} L^{1/5}. \tag{3.16}$$

Le premier point à noter est la disparition de la dépendance en H reflètant le fait que la hauteur n'est plus une échelle caractéristique. Le deuxième point à souligner est que la vitesse augmente avec la longueur de la cavité mais avec une dépendance faible : u_0 varie avec $L^{1/5}$. On remarque également que la vitesse dépend de la diffusivité thermique. Pour le verre et dans le cadre de l'approximation de Rosseland [103] où la conductivité thermique liée aux effets radiatifs est inversement proportionnelle au coefficient d'absorption radiatif du verre, l'intensité de la convection augmente avec la diminution du coefficient d'absorption. En d'autres termes,

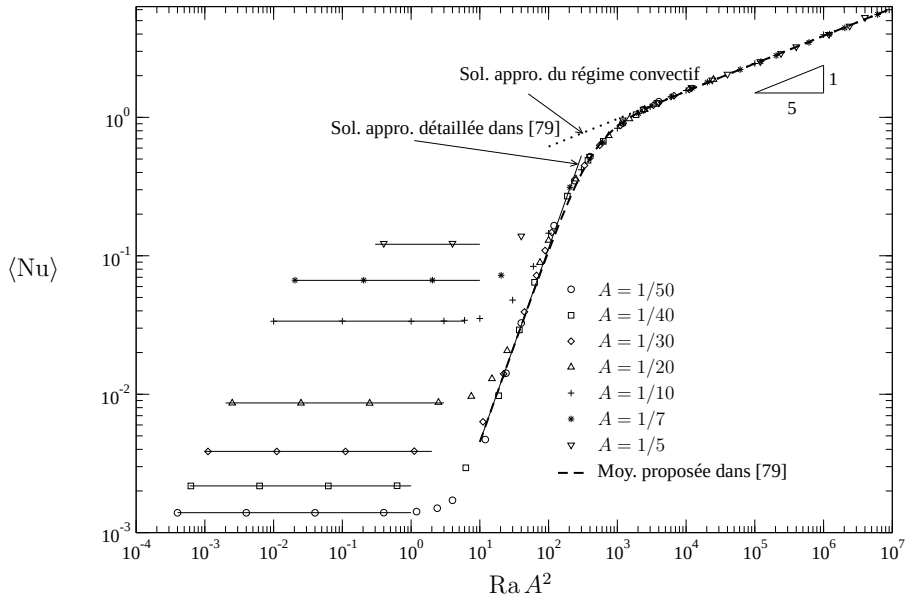

FIGURE 3.9 – $\langle \mathrm{Nu} \rangle$ en function de $\mathrm{Ra}\, A^2$ dans des cavités de rapports d'aspect $1/50$, $1/40$, $1/30$, $1/20$, $1/10$, $1/7$ et $1/5$.

plus le verre est clair plus la convection naturelle est activée. Ce résultat est en très bon accord avec ce qui est constaté en production.

3.3 Perspectives

La première section de ce chapitre a été consacrée aux distributions des temps de séjour et la deuxième à la convection naturelle. Or, l'écoulement dans le système a nécessairement un impact sur la distribution des temps de séjour ce qui a été peu étudié. Les fours verriers subissent régulièrement des changements de type de verre. Afin de mieux comprendre leur flexibilité, il serait intéressant de voir s'il est possible d'établir des modèles approchés décrivant les distributions des temps de séjour en fonction du produit $\mathrm{Ra}\, A^2$.

Le mélange de fluides visqueux a été abordé au cours de la thèse d'E. Gouillart [37] à l'aide de la théorie du chaos déterministe employée pour l'étude des systèmes dynamiques. Bien qu'il soit difficile de définir mathématiquement ce qu'est un «bon mélange», des indices de mélange ont été établis au cours de la thèse d'E. Gouillart pour des systèmes ouverts. Un lien important reste à faire entre les distributions des temps de séjour et le mélange, Danckwerts [29] et Zwietering [114] ont établi un degré de mélange basé sur les calculs de la variance du temps moyen local et sur celui du temps passé par le fluide dans le système. Liu [62] a très récemment été le premier à faire le calcul numérique de ce degré de mélange. Ce travail reste à faire dans le cadre de l'élaboration des verres.

Un point important souligné par beaucoup de groupes de recherche (cf. l'article de synthèse de Hughes et Griffiths [46]) est que la convection horizontale est très stable. Quand bien même

l'écoulement devient très stratifié, l'écoulement reste stationnaire pour des nombres de Rayleigh très grands. Certains auteurs comme Paparella et Young [72] y ont vu l'incapacité de ce type d'écoulement à devenir turbulent. Néanmoins, ces mêmes auteurs dans le même article montrent que l'écoulement peut devenir instable. Il a été confirmé depuis que ce type de configuration présente une bifurcation de Hopf où l'écoulement devient périodique en temps [108]. Nous avons entrepris d'étudier ce problème qui nécessite d'avoir des outils numériques précis. Ainsi, E. Uguz [1], étudiant en thèse à l'université de Floride (Gainesville,USA), a développé durant son passage dans notre laboratoire un solveur des équations de Navier-Stokes couplées à l'équation d'énergie à l'aide d'une méthode spectrale sur la base des polynômes de Tchébychev. L'apparition de la bifurcation de Hopf a pu être retrouvée pour quelques rapports d'aspect. Il reste à établir proprement le diagramme de stabilité pour voir quel paramètre contrôle ces instabilités.

Toujours dans le cadre de la convection horizontale, nous avons vu que le nombre de Nusselt suivait une loi en $(\mathrm{Ra}\,A^2)^{1/5}$ dans le régime convectif. Or, Siggers *et al.* [104] ont établi en se basant sur une approche variationelle que le nombre de Nusselt devait être en $(\mathrm{Ra}\,A^2)^{1/3}$. Or, cette limite n'a pour l'instant reçu aucune vérification convaincante. Seuls Sheard et King [101] ont vu un changement de pente sur leurs résultats de simulations numériques. Néanmoins, peu de cas ont été étudiés dans la référence [101]. Nous envisageons sur la base de notre solveur spectral de compléter la recherche du nombre de Nusselt sur une large gamme de nombres de Rayleigh et de rapports d'aspect.

Les applications ont été focalisées sur les fours à flammes. Néanmoins, les verres étant des milieux conducteurs de l'électricité, il est possible de leur appliquer des champs électriques. Par suite de la dissipation de l'énergie par effet Joule, ces champs électriques peuvent échauffer le verre. Ceci est utilisé de façon industrielle soit comme un appoint d'énergie soit comme un four à part entière [106]. Des études assez récentes menées par exemple par Sugilal *et al.* [107] montrent que ce type de configuration peut donner lieu à des instabilités qui dépendent du nombre de Prandtl. Plus le nombre de Prandtl est grand, plus les instabilités apparaissent pour des faibles valeurs de nombre de Rayleigh. Ceci peut avoir des conséquences sur la conduite des fours électriques. Ainsi, une meilleure connaissance de l'apparition de ces instabilités serait très utile d'un point de vue fondamental mais également appliqué.

1. E. Uguz a eu une bourse Chateaubriand lui permettant de venir durant cinq mois dans notre laboratoire en 2010. Cette collaboration a été menée grâce à l'appui du Prof. G. Labrosse de l'université d'Orsay.

Conclusion

Ce rapport qui synthétise mes recherches entreprises depuis juin 2007 au sein du laboratoire SURFACE DU VERRE ET INTERFACES permet de faire un bilan. Bien que partant d'une problèmatique purement industrielle, de nombreux sujets à connotation plus fondamentale ressortent. C'est d'ailleurs une des forces de notre laboratoire, situé à l'interface industriel-académique, de pourvoir prendre des sujets appliqués et d'en faire des sujets de recherche.

Un point sur lequel il est important d'appuyer est que le verre en tant que milieu fluide réactif reste encore difficile à étudier. Une des raisons est qu'il est difficile d'y faire des mesures à cause des hautes températures et de la forte corrosion. Les mesures sont souvent indirectes et faites à température ambiante. Ce manque de connaissance du milieu fait qu'il est difficile d'ébaucher des modèles théoriques étayés sur des observations.

Parmi les résultats exposés dans ce manuscrit, la chimie des verres se révèle très importante à comprendre. La difficulté essentielle est de l'inscrire dans une démarche de modélisation. Nous avons réussi à le faire par exemple sur l'étude portant sur la résorption des bulles d'oxygène pour laquelle l'effet de la concentration en fer a pu être mis en évidence théoriquement. D'autre part, l'étude sur la stabilité des mousses nous a fait prendre conscience de l'importance de l'évaporation du sodium. Une première tentative de modélisation théorique a d'ailleurs été proposée.

Une autre caractéristique de ces travaux est d'essayer de trouver des modèles d'étude plus simples que le dispositif industriel afin d'en tirer un maximum d'information. Le but est de dégager des lois, des comportements génériques qui seront des guides précieux pour ensuite revenir vers le système original. C'est ce que nous avons fait au cours de notre travail sur la convection naturelle appliquée aux fours verriers. L'autre exemple est l'étude du drainage des bulles à la surface libre des verres dont les résultats servent à interpréter certains phénomènes de moussage dans des fours.

Sur les trois grands sujets discutés dans ce document, nous avons évoqués des perspectives de recherche. Certaines sont d'ailleurs initiées comme celle portant sur la modélisation de l'hydrodynamique de bulles dans les liquides visqueux entreprise dans le cadre de la thèse de M. Guémas co-encadrée par A. Sellier (Laboratoire d'Hydrodynamique de l'école Polytechnique) et moi-même. Citons également les travaux d'E. Uguz travaillant à l'université de Floride sur les simulations numériques de la convection horizontale. D'autres perspectives ont été proposées à la fin de chaque chapitre sur lesquelles nous ne revenons pas. Néanmoins, l'une d'entre elles mérite d'être rappelée dans cette conclusion. Comme nous l'avons souligné à plusieurs reprises dans le texte, la modélisation des fours reste principalement fondée sur la thermohydrodynamique. Pourtant, les fours sont des réacteurs chimiques. Ainsi, il semble indispensable d'introduire des

aspects plus chimiques comme le couplage entre la phase gazeuse et le «verre» liquide. Les modèles déjà établis sur l'hydrodynamique des milieux diphasiques seront d'une aide précieuse sur ce point.

Signalons également les connections de ces travaux avec d'autres domaines scientifiques. Notamment, la géophysique traite de sujets portant sur des matériaux silicatés. La remontée des magmas dans les volcans entraîne l'apparition de bulles due à la décompression qui ont une importance cruciale sur les éruptions. Le manteau terrestre est le siège de mouvement de convection de fluide très visqueux qui partagent beaucoup de points communs avec les verres industriels. C'est pourquoi nous collaborons au sein de notre laboratoire avec des géophysiciens comme M. Toplis de l'observatoire Midi-Pyrénées.

La plupart des travaux évoqués dans ce manuscrit ont été réalisés en collaboration avec d'autres chercheurs avec lesquels nous allons continuer à travailler. Citons les travaux que nous conduisons actuellement avec A. Sellier. De même, la collaboration avec F. Rouyer et plus largement le laboratoire Navier de l'école des Ponts et Chausées se poursuit à l'aide de stages de master et de nouveaux projets de thèse. D'un point de vue international, nous faisons partir du programme d'interchance entre les Etats-Unis, le Japon et la France sur lequel nous nous sommes appuyés pour la venue d'E. Uguz.

Bibliographie

[1] R. Aris. *Vectors, Tensors and the basic equation of fluid mechanics*. Dover Publications, Inc, New York, 1962.

[2] J.-N. Baléo and P. Le Cloirec. Validating a prediction method of mean residence time spatial distributions. *AIChE Journal*, 46 :675–683, 2000.

[3] E. Bart. The slow unsteady settling of a fluid sphere toward a flat fluid interface. *Chem. Eng. Sci.*, 23 :193–210, 1968.

[4] J. Barton and C. Guillemet. *Le Verre, Science et Technologie*. EDP sciences, Paris, 2005.

[5] G. K. Batchelor. Heat tranfer by free convection across a closed cavity between vertical boundaries at different temperatures. *Quart. Appl. Math.*, 12 :209–233, 1954.

[6] R. G. C. Beerkens. Modeling the kinetics of volatilization from glass melts. *J. Am. Ceram. Soc.*, 84 :1952–1960, 2001.

[7] R. G. C. Beerkens. Analysis of advanced and fast fining processes for glass melts. In *Advances in Fusion and Processing of Glass III*, pages 3–24. American Ceramic Society, New York, 2003.

[8] R. G. C. Beerkens. Sulfate decomposition and sodium oxide activity in soda-lime-silica glass melts. *Journal of American Ceramic Society*, 86 :1893–1899, 2003.

[9] R. G. C. Beerkens and H. de Waal. Mechanism of oxygen diffusion in glassmelts containing variable-valence ions. *J. Am. Ceram. Soc.*, 73 :1857–1861, 1990.

[10] A. Bejan. *Convection heat transfer*. John Wiley & Sons, New York, 1995.

[11] C. Berdan and L. G. Leal. Motion of a sphere in the presence of a deformation interface. I. Perturbation of the interface from flat : The effects on drag and torque. *J. Colloid Interface Sci.*, 87 :62–80, 1982.

[12] A. Bhakta and E. Ruckenstein. Modeling of the generation and collapse of aqueous foams. *Langmuir*, 12 :3089–3099, 1996.

[13] A. Bhakta and E. Ruckenstein. Decay of standing foams : drainage, coalescence and collapse. *Adv. Colloid Interface Sci.*, 70 :1–124, 1997.

[14] A. Bhakta and E. Ruckenstein. Drainage and coalescence in standing foams. *J. Colloid Interface Sci.*, 191 :184–201, 1997.

[15] B. Böhrer. Convection in a long cavity with differentially heated end walls. *Int. J. Heat Mass Transfer*, 40 :4105–4114, 1997.

[16] J. C. Bird, R. de Ruiter, L. Courbin, and H. A. Stone. Daughter bubble cascades produced by folding of ruptured thin films. *Nature*, 465 :759–762, 2010.

[17] R. B. Bird, W. E. Steward, and E. N. Lightfoot. *Transport phenomena*. John Wiley and sons, New York, 1960.

[18] C. J. W. Breward. *The mathematics of foam*. PhD thesis, University of Oxford, 1999.

[19] I. Cantat, S. Cohen-Addad, F. Elias, F. Graner, R. Höhler, O. Pitois, F. Rouyer, and A. Saint-Jalmes. *Les mousses. Structure et dynamique*. Editions Belin, Paris, 2010.

[20] H. Chemani. Introduction d'un agent moussant dans une masse argileuse pour la fabrication de briques isolantes. *L'industrie Céramique et Verrière*, 988 :16–21, 2003.

[21] E. Chervenivanova and Z. Zapryanov. The slow motion of droplets perpendicular to a deformable flat fluid interface. *Q. J. Mech. Appl. Math.*, 41 :419–444, 1988.

[22] B. K. Chi and L. G. Leal. A theoretical study of the motion of a viscous drop toward a fluid interface at low Reynolds number. *J. Fluid Mech.*, 201 :123–146, 1989.

[23] S. Chiu-Webster, E. J. Hinch, and J. R. Lister. Very viscous horizontal convection. *J. Fluid Mech.*, 611 :395–426, 2008.

[24] R. Clift, J. R. Grace, and M. E. Weber. *Bubbles, Drops, and Particles*. Academic Press, New York, 1978.

[25] G. B. Cook and R. F. Cooper. Iron concentration and the physical processes of dynamic oxidation in an alkaline earth aluminosilicate glass. *Am. Mineral.*, 85 :397–406, 2000.

[26] G. B. Cook, R. F. Cooper, and T. Wu. Chemical diffusion and crystalline nucleation during oxidation of ferrous iron-bearing magnesium aluminosilicate glass. *J. Non-Cryst. Solids*, 120 :207–222, 1990.

[27] C. Corduneanu. *Integral equation and applications*. Cambridge University Press, Cambridge, 1991.

[28] D. E. Cormack, L. G. Leal, and J. Imberger. Natural convection in a shallow cavity differentially heated end walls. Part 1. Asymptotic theory. *J. Fluid Mech.*, 65 :209–229, 1974.

[29] P. V. Danckwerts. Continuous flow systems. Distribution of residence times. *Chem. Eng. Sci.*, 2 :1–13, 1953.

[30] A. Wondergem de Best. *Redox behaviour and fining of molten glass*. PhD thesis, Technische Universiteit Eindhoven, 1994.

[31] G. Debrégeas, P.-G. de Gennes, and F. Brochard-Wyart. The life and death of "bare" viscous bubbles. *Science*, 279 :1704–1707, 1998.

[32] A. G. Fedorov and L. Pilon. Glass foam : formation, transport properties, and heat, mass, and radiation transfer. *J. Non-Cryst. Solids*, 311 :154–173, 2002.

[33] C. J. B. Fincham and F. D. Richardson. The behaviour of sulphur in silicate and aluminate melts. *Prod. R. Soc. London A*, 223 :40–62, 1954.

[34] J.-M. Flesselles and F. Pigeonneau. Kinematic regimes of convection at hight Prandtl number in a shallow cavity. *C. R. Mécanique*, 332 :783–788, 2004.

[35] J. B. Fournier and A-M. Cazabat. Tears of wine. *Europhys. Lett.*, 20 :517–522, 1992.

[36] F. Ghirelli and B. Leckner. Transport equation for the local residence time of a fluid. *Chem. Eng. Sci.*, 59 :513–523, 2004.

[37] E. Gouillart. *Etude de l'advection chaotique dans les mélangeurs à tiges, en écoulements ouverts et fermés*. PhD thesis, Université Pierre et Marie Curie, 2007.

[38] H. J. J. Gramberg, P. D. Howell, and J. R. Ockendon. Convection by a horizontal thermal gradient. *J. Fluid Mech.*, 586 :41–57, 2007.

[39] C. H. Greene and D. R. Platts. Behavior of bubbles of oxygen and sulfur dioxide in soda-lime glass. *J. Amer. Ceram. Soc.*, 52 :106–109, 1969.

[40] J. Hadamard. Mouvement permanent lent d'une sphère liquide et visqueuse dans un liquide visqueux. *C. R. Acad. Sci. Paris*, 152 :1735–1738, 1911.

[41] S. Hartland. The coalescence of a liquid drop at a liquid-liquid interface. Part I : Drop shape. *Trans. Instn Chem. Engrs*, 45 :T97–T101, 1967.

[42] S. Hartland. The coalescence of a liquid drop at a liquid-liquid interface. Part II : Film thickness. *Trans. Instn Chem. Engrs*, 45 :T102–T108, 1967.

[43] E. J. Hornyak and M. C. Weinberg. Velocity of a freely rising gas bubble in a soda-lime silicate glass melt. *J. Amer. Ceram. Soc.*, 67 :C244–C246, 1984.

[44] A. E. Hosoi and J. W. M. Bush. Evaporative instabilities in climbing films. *J. Fluid Mech.*, 442 :217–239, 2001.

[45] P. D. Howell. Models for thin viscous sheets. *Eur. J. Appl. Math.*, 7 :321–346, 1996.

[46] G. O. Hughes and R. W. Griffiths. Horizontal convection. *Ann. Rev. Fluid Mech.*, 40 :185–208, 2008.

[47] H. Jeffreys. On fluid motions produced by differences of temperature and humidity. *Quart. J. Royal Meteor. Soc.*, 51 :356–1925, 1925.

[48] R. B. Jucha, D. Powers, T. McNeill, R. S. Subramanian, and R. Cole. Bubble rise in glassmelts. *J. Amer. Ceram. Soc.*, 65 :289–292, 1982.

[49] J. Kappel, R. Conradt, and H. Scholze. Foaming behaviour on glass melts. *Glastech. Ber.*, 60 :189–201, 1987.

[50] D.-S. Kim and P. Hrma. Foaming in glass melts produced by sodium sulfate decomposition under ramp heating conditions. *J. Am. Ceram. Soc.*, 75 :2959–2563, 1992.

[51] S. Kim and S. J. Karrila. *Microhydrodynamics. Principles and selected applications*. Dover Publications, Inc., New-York, 2005.

[52] J. Kloužek and L. Němec. Modelling of glass refining kinetics. Part 2 : Bubble distribution models and methods of measurement of refining properties. *Ceramics*, 47 :155–161, 2003.

[53] H. Kočárková. *Stabilité des mousses de verre : Expériences à l'échelle d'une bulle ou d'un film vertical (in English)*. PhD thesis, Université Paris-Est, Marne la Vallée, 2011.

[54] H. Kočárková, F. Pigeonneau, F. Rouyer, and M. Vignes-Adler. Film drainage between bubble and fluid interface. In *International Conference on Multiphase Flow 2010*, Tampa, Florida (USA), May 30-June 4 2010.

[55] H. Kočárková, F. Rouyer, and F. Pigeonneau. Film drainage of viscous liquid on top of bare bubble : Influence of the bond number. *Phys. Fluids*, under consideration, 2012.

[56] F. W. Kramer. Solubility of gases in glass melts. In *Properties of glass-forming melts*, pages 405–482. Taylor & Francis, 2005.

[57] P. Laimböck. *Foaming of glass melts*. PhD thesis, Technische Universiteit Eindhoven, 1998.

[58] O. Levenspiel. *Chemical reaction engineering*. John Wiley & Sons, New York, 1972.

[59] V. G. Levich. *Physicochemical hydrodynamics*. Prentice Hall, Englewood Cliffs, N.J., 1962.

[60] K.-W. K. Li and A. Schneider. Rise velocities of large bubbles in viscous Newtonian liquids. *J. Amer. Ceram. Soc.*, 76 :241–244, 1993.

[61] K.-O. Lim, T.-H. Song, and K.-S. Lee. Patterns of natural convection driven by the free surface temperature distribution in a glass melting furnace. *Glass Technol.*, 39 :27–31, 1998.

[62] M. Liu. Age distribution and the degree of mixing in continuous flow stirred tank reactors. *Chem. Eng. Sci.*, 69 :382–393, 2012.

[63] E. W. Llewellin, H. M. Mader, and S. D. R. Wilson. The rheology of a bubbly liquid. *Proc. R. Soc. Lond. A*, 458 :987–1016, 2002.

[64] H. A. Lorentz. Ein allgemeiner Satz, die Bewegung einer reibenden Flüssigkeit betreffend, nebst einigen Anwendungen desselben. In *Abhandlungen über Theoretische Physik*, pages 23–42. B. G. Teubner, Berlin, 1907.

[65] F. Méar, P. Yot, and M. Ribes. Effects of temperature, reaction time and reducing agent content on the synthesis of macroporous foam glasses from waste funnel glasses. *Mater. Lett.*, 60 :929–934, 2006.

[66] N. McDonald and F. Pigeonneau. In-situ measurements of the effect of sulphate on bubble growth rate and gas emissions during fining. In *XXIst International Congress on Glass*, Strasbourg, France, July, 1-6 2007.

[67] S. Metallaoui. Etude expérimentale du drainage et éclatement d'une bulle à la surface d'un liquide. Master 1 de sciences de l'ingénieur, Université Pierre et Marie Curie, 2011.

[68] B. O. Mysen and P. Richet. *Silicate Glasses and Melts : Properties and Structure*. Elsevier, Amsterdam, 2005.

[69] V. I. Nizhenko. V. N. Eremenko and the development of research into the surface properties of molten metals. *Powder Metall. Met. Ceram.*, 40 :315–336, 2001.

[70] L. Němec and J. Kloužek. Modelling of glass refining kinetics. Part 1 : single bubbles. *Ceramics*, 47 :81–87, 2003.

[71] A. Oron, S. H. Davis, and S. G. Bankoff. Long-scale evolution of thin liquid films. *Rev. Mod. Phys.*, 69 :931–980, 1997.

[72] F. Paparella and W. R. Young. Horizontal convection is non-turbulent. *J. Fluid Mech.*, 466 :205–214, 2002.

[73] R. Petit. *L'outil mathématique pour la physique*. Dunod Université, Paris, 5 edition, 1998.

[74] C. J. S. Petrie. Extensional viscosity : A critical discussion. *J. Non-Newtonian Fluid Mech.*, 137 :15–23, 2006.

[75] F. Pigeonneau. Coupled modelling of redox reactions and glass melt fining processes. *Glass Technol. : Eur. J. Glass Sci. Technol. A*, 48(2) :66–72, 2007.

[76] F. Pigeonneau. Mass transfer of rising bubble in molten glass with instantaneous oxidation-reduction reaction. *Chem. Eng. Sci.*, 64 :3120–3129, 2009.

[77] F. Pigeonneau. Mechanism of mass transfer between a bubble initially composed of oxygen and molten glass. *Int. J. Heat Mass Transfer*, 54 :1448–1455, 2011.

[78] F. Pigeonneau and J.-M. Flesselles. Convection laws for glass furnaces revisited. *Verre*, 9(2) :14–16, 2003.

[79] F. Pigeonneau and J.-M. Flesselles. Practical laws for natural convection of viscous fluids heated from above in a shallow cavity. *Int. J. Heat Mass Transfer*, 55 :436–442, 2012.

[80] F. Pigeonneau, H. Kočárková, and F. Rouyer. Stability of vertical films of molten glass due to evaporation. *Colloids Surf., A*, under consideration, 2012.

[81] F. Pigeonneau, D. Martin, and O. Mario. Shrinkage of oxygen bubble rising in a molten glass. *Chem. Eng. Sci.*, 65 :3158–3168, 2010.

[82] F. Pigeonneau and A. Sellier. Low-Reynolds-Number gravity-driven migration and deformation of bubbles near a free surface. *Phys. Fluids*, 23 :092102, 2011.

[83] L. Pilon, A. G. Fedorov, D. Ramkrishna, and R. Viskanta. Bubble transport in three-dimensional laminar gravity-driven flow – mathematical formulation. *J. Non-Cryst. Solids*, 336 :71–83, 2004.

[84] L. Pilon and R. Viskanta. Modified method of characteristics for solving population balance equations. *International Journal for Numerical Methods in Fluids*, 42 :1211–1236, 2003.

[85] L. Pilon and R. Viskanta. Radiation characteristics of glass containing gas bubbles. *J. Am. Ceram. Soc.*, 86 :1313–1320, 2003.

[86] L. Pilon and R. Viskanta. Bubble transport in three-dimensional laminar gravity-driven flow – numerical results. *Journal of Non-Crystalline Solids*, 336 :84–95, 2004.

[87] A. Ponsich, C. Azzaro-Pantel, S. Domenech, L. Pibouleau, and F. Pigeonneau. A systemic approach for glass manufacturing process modelling. *Chem. Eng. Process.*, 48 :1310–1320, 2009.

[88] C. Pozrikidis. *Boundary integral and singularity methods for linearized viscous flow*. Cambridge University Press, Cambridge, 1992.

[89] H. M. Princen. Shape of a fluid drop at a liquid-liquid interface. *J. Colloid Interface Sci.*, 18 :178–195, 1963.

[90] D. Ramkrishna. *Population balances. Theory and application to particulate systems in engineering*. Academic Press, San Diego, 2000.

[91] H. T. Rossby. On thermal convection driven by non-uniform heating from below : an experimental study. *Deep-Sea Res.*, 12 :9–16, 1965.

[92] H. T. Rossby. Numerical experiments with a fluid heated non-uniformly from below. *Tellus*, 50A :242–257, 1998.

[93] E. Ruckenstein and R. K. Jain. Spontaneous rupture of thin liquid films. *J. Chem. Soc., Faraday Trans. 2*, 70 :132–147, 1974.

[94] A. C. Rust and M. Manga. Effects of bubble deformation on the viscosity of dilute suspensions. *J. Non-Newtonian Fluid Mech.*, 104 :53–63, 2002.

[95] W. Rybczynski. Uber die fortschreitende bewegun einer flussingen kugel in einem zaben medium. *Bull. de l'Acad. des Sci. de Cracovie*, pages 40–46, 1911.

[96] D. M. Sanders and W. K. Haller. Effect of water vapor on sodium vaporization from two silica-based glasses. *J. Am. Ceram. Soc.*, 60 :138–141, 1977.

[97] J. W. Sandström. Meteorologishe studien im Schwedischen Hoghgebirge. *Göteb. Kungl. Vetensk. Vitterh. Handl.*, 17 :1–48, 1916.

[98] H. Scholze. *Glass. Nature, Structures and Properties*. Springer-Verlag, Berlin, 1990.

[99] L. W. Schwartz and R. V. Roy. Modeling draining flow in mobile and immobile soap films. *J. Colloid Interface Sci.*, 218 :309–323, 1999.

[100] J. Senée, B. Robillard, and M. Vignes-Adler. Films and foams of Champagne wines. *Food Hydrocolloids*, 13 :15–26, 1999.

[101] G. J. Sheard and M. P. King. The influence of height ratio on rayleigh-number scaling and stability of horizontal convection. In *Seventh International Conference on CFD in the Minerals and Process Industries*, Melbourne, Australia, 2009.

[102] J. E. Shelby. *Introduction to Glass Science and Technology*. The Royal Society of Chemistry, Cambridge, 1997.

[103] R. Siegel and J. Howell. *Thermal Radiation Heat Transfer*. Taylor & Francis, Levitown, 2002.

[104] J. H. Siggers, R. R. Kerswell, and N. J. Balmforth. Bounds on horizontal convection. *J. Fluid Mech.*, 517 :55–70, 2004.

[105] R. C. J. Somerville. A nonlinear spectral model of convection in a fluid unevenly heated from below. *J. Atmos. Sci.*, 24 :665–676, 1967.

[106] J. Stanek. *Electric melting of glass*. Elsevier, Paris, 1977.

[107] G. Sugilal, P. K. Wattal, and K. Iyer. Convective behaviour of a uniformly Joule-heated liquid pool in a rectangular cavity. *Int. J. Thermal Sci.*, 44 :915–925, 2005.

[108] L. Sun, D.-J. Ma, W. Zhang, and D.-J. Sun. Onset of unsteady horizontal convection in rectangular tank at $Pr = 1$. *Chin. Phys. Lett.*, 25 :2121–2124, 2008.

[109] P. Trambouze and J.-P. Euzen. *Les réacteurs chimiques. De la conception à la mise en œuvre*. Editions Technip, Paris, 2002.

[110] J. Villermaux. *Génie de la réaction chimique*. Tec & Doc Lavoisier, Paris, 1993.

[111] A. Vrij. Possible mechanism for the spontaneous rupture of thin, free liquid films. *Discuss. Faraday Soc.*, 42 :23–33, 1966.

[112] S. G. Yiantsios and R. H. Davis. On the buoyancy-driven motion of a drop towards a rigid surface or a deformable interface. *J. Fluid Mech.*, 217 :547–573, 1990.

[113] J. Zarzycki. *Le verre et l'état vitreux*. Masson, Paris, 1982.

[114] T. N. Zwietering. The degree of mixing in continuous flow systems. *Chem. Eng. Sci.*, 11 :1–15, 1959.

Annexe A

Reproduction d'articles relatifs au chapitre 1

Trois articles sur le sujet du transfert de masse dans les liquides silicatés sont reproduits ici dont les références sont les suivantes :

- F. Pigeonneau. Mass transfer of rising bubble in molten glass with instantaneous oxidation-reduction reaction. *Chem. Eng. Sci.*, 64 :3120-3219, 2009.
- F. Pigeonneau, D. Martin and O. Mario. Shrinkage of oxygen bubble rising in a molten glass. *Chem. Eng. Sci.*, 65 :3158-3168, 2010.
- F. Pigeonneau. Mechanism of mass transfer between a bubble initially composed of oxygen and molten glass. *Int. J. Heat Mass Transfer*, 54 :1448-1455, 2011.

Chemical Engineering Science 64 (2009) 3120 – 3129

Contents lists available at ScienceDirect

Chemical Engineering Science

journal homepage: www.elsevier.com/locate/ces

Mass transfer of a rising bubble in molten glass with instantaneous oxidation–reduction reaction

F. Pigeonneau*

Surface du Verre et Interfaces, UMR 125 CNRS/Saint-Gobain, 39 quai Lucien Lefranc – BP 135, 93303 Aubervilliers Cedex, France

ARTICLE INFO

Article history:
Received 19 June 2008
Received in revised form 23 March 2009
Accepted 25 March 2009
Available online 5 April 2009

Keywords:
Bubble
Chemical processes
Fluid mechanics
Mass transfer
Multiphase reactions
Numerical analysis

ABSTRACT

The mass transfer around a rising bubble has been studied within the field of glass melting processes. Due to the large value of liquid viscosity, creeping flow was used. The rising bubble is assumed to have a clean interface with a total mobility and the exact solution of Hadamard or Rybczynski was used to define the velocity field around the bubble. The mass transfer of oxygen in the soda–lime–silica glass melt where oxidation–reduction reactions of iron oxides occur is also described.

The dimensionless mass transfer coefficient, Sherwood number, was determined as a function of the Péclet number based on the terminal rise velocity of the bubble. Two different techniques have been used: the first based on the boundary layer theory and the second using a finite element method.

In order to take into account the oxidation–reduction reaction in a unified framework, a modified Péclet number has been defined as a function of two dimensionless numbers. The first is strongly linked to the equilibrium constant of the chemical reaction and the second is the glass saturation, defined as the ratio of oxygen concentration in the bulk to that at the bubble surface. The Sherwood number, taking into account the chemical reactions, increases with iron content as well as with glass reduction (i.e. small saturation level).

From an application point of view, the determination of a modified Péclet number is important because it is possible to use a similar expression (determined without the reaction) by replacing the classical Péclet number by the modified one proposed herewithin.

© 2009 Elsevier Ltd. All rights reserved.

1. Introduction

Mass transfer between dispersed bubbles and a continuous liquid phase occurs in many industrial chemical engineering applications such as liquid–liquid extraction, boiling, fermentation and other examples, some of which are listed by Clift et al. (1978) and Levenspiel (1972). The mass transfer efficiency of industrial plants is strongly dependent on the ratio of the contact surface of a dispersed phase to the reactor volume as well as on interphase mass transfer processes.

As is well known, mass transfer is strongly affected by the mobility of the interface between bubble and liquid. Many works have been devoted to the influence of the rigidity of this interface on both drag forces and mass transfer coefficients. Clift et al. (1978), Levich (1962) and more recently Sadhal et al. (1997) provide syntheses of this problem. The rigidity of the interface is mainly due to its contamination. An analogous effect occurs for bubbles in water as has been studied by McLaughlin (1996), Liao and McLaughlin (2000a, b) and Ponoth and McLaughlin (2000) where the dynamics of contamination was also investigated. Also, Dani et al. (2006) recently presented a numerical study where the effect of contamination was taken into account.

Glass melting is a relatively unique chemical process occurring in a highly viscous fluid. The "melting" process (in reality a series of chemical reactions involving SiO_2 and carbonates) leads to the abundant formation of bubbles dispersed in the molten glass and due to the high viscosity, removing these gaseous inclusions is a difficult task. A classical way to remove bubbles is to introduce small quantities of the so-called "fining" agents which work by increasing bubble size due to the mass transfer of "fining" gases dissolved in the molten glass toward the bubbles. In this particular process, mass transfer is related to the oxidation–reduction reactions which take place in molten glass. The fining process has been extensively studied in the past and an experimental device has been developed by Greene and Gaffney (1959) to study the shrinkage of an oxygen bubble kept spatially fixed though the rotation of the sample. Greene and Platts (1969) underlined that the shrinkage rate increases when metal oxides such as As_2O_3 or Fe_2O_3 are present in the molten glass.

* Tel.: +33 1 48 39 59 99; fax: +33 1 48 39 55 62.
E-mail address: franck.pigeonneau@saint-gobain.com.

0009-2509/$ - see front matter © 2009 Elsevier Ltd. All rights reserved.
doi:10.1016/j.ces.2009.03.045

As mentioned above, the dissolution of a bubble in molten glass requires taking into account the coupling of diffusion and chemical reactions. This subject has been treated by Crank (1956), in particular unidimensional and unsteady problems with instantaneous, irreversible, and reversible reactions for which he gave exact solutions. It is well established that a medium undergoing chemical reactions including diffusion shows an enhancement of mass transfer coefficients (Levenspiel, 1972)—see also French chemical engineering literature (Villermaux, 1993; Trambouze and Euzen, 2002). In spite of these works, few other studies have been carried out on the coupling of diffusion and chemical reactions with convection. Subramanian and Chi (1980) studied the enhancement produced by irreversible first order chemical reactions while taking into account the motion of the bubble interface due to dissolution. The coupling of diffusion and reaction for moving bubbles was investigated by Ruckenstein et al. (1971) using a first order irreversible reaction. The latter based their developments on an approximate solution of the velocity field close to the bubble interface and studied two limits: the first relevant to a viscous liquid and the second to an inviscid fluid.

The coupling of diffusion and equilibrium reactions for the case of oxygen diffusion in molten glass have been studied by Beerkens and de Waal (1990) and by Yoshikawa et al. (1998); however in these works, bubble motion is not taken into account. The aim of the present article is to study coupling between diffusion and instantaneous reaction for a rising bubble. The study will, in particular, focus on the problem of bubble shrinkage in molten glass where the bubble is initially filled with oxygen. This current work is devoted to the determination of the mass transfer coefficient.

In Section 2 of the present article, the theoretical model of mass transfer is presented and the oxidation–reduction reaction is detailed. The methods to determine mass transfer coefficients are presented in Section 3 using two means: the first prediction is done with boundary layer theory and the second by solving the advection–diffusion–reaction problem with a numerical method. The results are given in Section 4 and discussed in Section 5. Appendix A provides details about the determination of the boundary layer equation.

2. Theoretical model of mass transfer with an oxidation–reduction reaction

2.1. Oxidation–reduction reaction in molten glass

The diffusion of oxygen in molten glass has been studied by numerous authors—for more details see Doremus (2002). Oxygen diffusion is not only driven by molecular transport, the presence of other dissolved gases can lead to reactions with oxygen. The oxidation–reduction reactions of metal oxides can also influence oxygen diffusion. Cook et al. (1990) proposed a model of oxidation by cation transport. Beerkens and de Waal (1990) have already taken oxidation–reduction reactions into account for a unidimensional case without advection; Kawachi and Kawase (1998) and Yoshikawa et al. (1998) have done the same for a stationary bubble. In this work, only the influence of iron oxide oxidation–reduction reactions on oxygen diffusion is investigated.

Considering the case of a rising bubble, the molar concentration of oxygen, C_{O_2}, is described by the advection–diffusion–reaction equation as

$$\frac{DC_{O_2}}{Dt} = \operatorname{div}\left(\mathscr{D}_{O_2}\,\mathbf{grad}\,C_{O_2}\right) + \dot{r}_{O_2}, \tag{1}$$

where $\mathscr{D}_{O_2}$ is the diffusion coefficient of oxygen. The left-hand side of this equation represents the material derivative of molar concentration of oxygen. The reaction rate, $\dot{r}_{O_2}$, is due to the oxidation–reduction of iron given by

$$Fe^{3+} + \tfrac{1}{2}O^{2-} \leftrightarrow Fe^{2+} + \tfrac{1}{4}O_2, \tag{2}$$

where Fe^{3+} is the oxidized state and Fe^{2+} the reduced state. The overall oxidation state of the glass is generally measured as the ratio of the molar concentration of iron in its reduced state to the total concentration of iron:

$$\mathscr{R} = \frac{C_{Fe^{2+}}}{C_{Fe^{2+}} + C_{Fe^{3+}}}, \tag{3}$$

where $C_{Fe^{2+}}$ and $C_{Fe^{3+}}$ are, respectively, the molar concentrations of Fe^{2+} and Fe^{3+}. In the following, $C_{Fe} = C_{Fe^{2+}} + C_{Fe^{3+}}$ (corresponding to the total quantity of iron) remains constant due to the conservation of mass.

The determination of reaction rate, $\dot{r}_{O_2}$, has been already derived by Beerkens and de Waal (1990) and Yoshikawa et al. (1998) for unsteady diffusion equation. The situation where bubble motion occurs is studied here. Rüssel (1989) showed that the chemical relaxation time is in the microsecond range for $T \approx 1200\,^{\circ}C$ and goes down to nanoseconds at $T \approx 1500\,^{\circ}C$. The ratio of this time to the characteristic time of the rising bubble in a liquid, $2a/V_T$, defines the Damköhler number. In our problem, this number is always greater than 10^6. Consequently, chemical equilibrium is assumed to have been established at high temperature. The equilibrium constant of reaction (2) is given by

$$K_{Fe} = \frac{C_{Fe^{2+}} P_{O_2}^{1/4}}{C_{Fe^{3+}}}, \tag{4}$$

where P_{O_2} is the partial pressure of oxygen in the gas phase at equilibrium with the molten glass (Paul, 1990). In this latter equation, the concentration of O^{2-} is not taken into account since it is present in large quantities in a glass, thus making its activity constant. From Henry's law, the molar concentration of oxygen in the melt is related to the oxygen partial pressure through the equation

$$C_{O_2} = L_{O_2} P_{O_2}. \tag{5}$$

This equation expresses the balance of chemical potentials between the two phases (Kondepudi and Prigogine, 1998) where L_{O_2} is the solubility. From this equation, a modified equilibrium constant can be derived as follows:

$$K'_{Fe} = K_{Fe} L_{O_2}^{1/4} = \frac{C_{Fe^{2+}} C_{O_2}^{1/4}}{C_{Fe^{3+}}}. \tag{6}$$

For an instantaneous reaction and assuming that iron diffusion is very small, the production rate of oxygen can be written as (Crank, 1956)

$$\dot{r}_{O_2} = -\frac{1}{4}\frac{DC_{Fe^{3+}}}{Dt}. \tag{7}$$

The $-\frac{1}{4}$ factor comes from the stoichiometry of reaction (2). From the equilibrium constant, Eq. (6), $C_{Fe^{3+}}$ is thus given by

$$C_{Fe^{3+}} = \frac{C_{Fe} C_{O_2}^{1/4}}{K'_{Fe} + C_{O_2}^{1/4}}. \tag{8}$$

By taking the derivative of the last equation with respect to time, the reaction rate of oxygen is thus defined as

$$\dot{r}_{O_2} = -\frac{C_{Fe} K_{Fe}}{16 C_{O_2}^{3/4} (K_{Fe} + C_{O_2}^{1/4})^2}\frac{DC_{O_2}}{Dt}. \tag{9}$$

This expression depends exclusively on the molar concentration of oxygen. The reaction rate is, thus, directly proportional to the material derivative of C_{O_2} and not only to the partial derivative with respect to time as used by Yoshikawa et al. (1998).

2.2. Hydrodynamics and mass transfer around a bubble

As mentioned in the Introduction, the mobility of the interface strongly influences the hydrodynamics and mass transfer. Debrégeas et al. (1995) studied bursting bubbles in highly viscous liquids. They found that, for liquid polydimenthylsiloxane (PDMS), the bursting rate was exponential with time whereas for a soap film it was linear. In their next paper (Debrégeas et al., 1998), bubble lifetime was studied for a liquid without surface active elements and it was shown once again for PDMS and molten glass that film drainage presented an exponential feature with time. Moreover, experiments done on borate glass by Jucha et al. (1982), on soda–lime–silica glass by Hornyak and Weinberg (1984), and on nuclear waste glass by Li and Schneider (1993) showed that rise velocity is given by the Hadamard–Rybczynski formula (Hadamard, 1911; Rybczynski, 1911). These results cover a large range of bubble sizes (micrometers to centimeters). Consequently, the interface between the bubble and the liquid is considered as totally mobile. For a bubble whose dynamic viscosity tends to 0, the terminal velocity is therefore given by (Clift et al., 1978)

$$V_T = \frac{\Delta\rho g a^2}{3\mu}, \tag{10}$$

where $\Delta\rho$ is the difference in density between the inclusion and the continuous fluid, g the gravity constant, a the inclusion's radius and μ the dynamic viscosity of the surrounding fluid.

The terminal velocity given above has been established in Stokes' flow regime. In order to be within this approximation, the Reynolds number given by

$$Re = \frac{2aV_T}{\nu} \tag{11}$$

must be sufficiently small. Here, ν represents the kinematic viscosity equal to μ/ρ. Molten glass has a high dynamic viscosity even at temperatures close to 1500 °C where its value is approximatively equal to 6 Pa s for a classical soda–lime–silica glass. For a bubble with a radius equal to 1 mm rising in molten glass the order of magnitude of the Reynolds number is 10^{-3}. This number decreases to 10^{-5} when the temperature reaches 1200 °C. Consequently, the Stokes approximation to describe hydrodynamics is relevant. Moreover, the shape of the bubble is considered to be spherical since typical bubble sizes studied here are less than the capillary length, $\sqrt{\sigma/(\rho g)}$, equal to approximately 4 mm for molten glass where σ is the surface tension.

Mass transfer will be evaluated via the Sherwood number given by

$$Sh = \frac{2ak}{\mathscr{D}_{O_2}}, \tag{12}$$

where k is the average molar flux at the surface of a bubble defined by

$$k = \frac{\displaystyle\int_{\mathscr{S}} \mathscr{D}_{O_2} \left.\frac{\partial C_{O_2}}{\partial n}\right|_{\mathscr{S}} dS}{4\pi a^2 \Delta C_{O_2}}. \tag{13}$$

The bubble surface is $\mathscr{S}$ and, the difference in molar concentration between the bulk and the inclusion's surface is ΔC_{O_2}.

The Sherwood number is the ratio of the mass transfer coefficient with a relative motion between bubble and liquid to the mass transfer coefficient without motion. This dimensionless number is usually a function of the Péclet number defined by Clift et al. (1978) and Sadhal et al. (1997)

$$Pe = \frac{2aV_T}{\mathscr{D}_{O_2}}. \tag{14}$$

Even if the Reynolds number is small, mass transfer is mainly driven by the relative motion between bubble and liquid due to the small diffusion coefficient of oxygen. This point can be characterized by the determination of the Schmidt number

$$Sc = \frac{\nu}{\mathscr{D}_{O_2}}, \tag{15}$$

which varies between 10^6 at 1500 °C and 5×10^8 at 1200 °C for a classical soda–lime–silica glass. Therefore, the Péclet number's order of magnitude, $ReSc$, is 10^3 for a bubble radius equal to 10^{-3} m.

This problem is also assumed to occur under a steady-state regime. Any unsteadiness may come from the variation of the bubble size due to shrinkage. Taking into account the variation of bubble size over time has been done previously by Yoshikawa et al. (1998) without bubble motion. However, the ratio of the time scales for shrinkage to the mass transfer is sufficiently large to assume the mass transfer problem as quasi-steady state. This ratio is determined in Pigeonneau et al. (2009) where the typical value is 10^3.

Due to the revolution symmetry of the problem, the azimuthal component of velocity and all derivatives with respect to this direction are equal to 0. Finally, the problem is solved using a coordinate system relative to the bubble. The velocity field is normalized by the terminal velocity given by Eq. (10) and the spatial variables are written under dimensionless form with the characteristic length scale equal to $2a$. The velocity field is imposed as the exact solution given by Hadamard (1911). For a bubble in a liquid, the two components written in spherical coordinates are given by

$$u_r = -\left(1-\frac{1}{2r}\right)\cos\theta, \tag{16}$$

$$u_\theta = \left(1-\frac{1}{4r}\right)\sin\theta, \tag{17}$$

where u_r and u_θ are the velocity components along the radial and polar directions, respectively and r is the radius with θ the polar angle.

The oxygen concentration is normalized by the relationship

$$C = \frac{C_{O_2} - C^\infty_{O_2}}{C^S_{O_2} - C^\infty_{O_2}}, \tag{18}$$

where $C^S_{O_2}$ is the molar concentration of oxygen at the bubble surface given by Eq. (5). The concentration in the liquid far away from the bubble, $C^\infty_{O_2}$, can be determined with the equilibrium constant as follows:

$$C^\infty_{O_2} = \left[\frac{K_{Fe}(1-\mathscr{R}^\infty)}{\mathscr{R}^\infty}\right]^4, \tag{19}$$

where $\mathscr{R}^\infty$ is the oxidation state far away the bubble.

The dimensionless reaction rate, $\dot{r}_C$, is defined by the derivation presented at the beginning of this section. Its expression is given by

$$\dot{r}_C = -f(C)\frac{DC}{Dt}, \tag{20}$$

where $f(C)$ is

$$f(C) = \frac{N_{Fe}}{[Sa+(1-Sa)C]^{3/4}\{\mathscr{R}^\infty Sa^{1/4} + (1-\mathscr{R}^\infty)[Sa+(1-Sa)C]^{1/4}\}^2}. \tag{21}$$

The dimensionless group N_{Fe} is given by

$$N_{Fe} = \frac{C^\infty_{Fe^{2+}}(1-\mathscr{R}^\infty)Sa^{1/4}}{16C^S_{O_2}}, \tag{22}$$

where Sa represents the saturation of oxygen in molten glass

$$Sa = \frac{C^{\infty}_{O_2}}{C^{S}_{O_2}} \tag{23}$$

and $C^{\infty}_{Fe^{2+}}$ is the molar concentration of Fe^{2+} far away the bubble

$$C^{\infty}_{Fe^{2+}} = \mathscr{R}^{\infty} C_{Fe}. \tag{24}$$

Note that the dimensionless group, N_{Fe}, is a function of temperature and pressure and is linked to the nature of the glass though the equilibrium constant and the solubility of oxygen. This number is directly related to the iron content of the glass.

Therefore, the advection–diffusion reaction equation can be written as follows:

$$[1+f(C)]\frac{DC}{Dt} = \frac{1}{Pe}\mathrm{div}(\mathbf{grad}\, C). \tag{25}$$

This equation is used to determine the mass transfer coefficient via two numerical methods detailed in the next section.

3. Determination of Sherwood number

In this section, the determination of the Sherwood number is done in two ways. First, a boundary layer solution is proposed for large Péclet numbers. Secondly, a numerical solution using a finite element method is proposed when the Péclet number is in the range of $[1; 10^4]$.

3.1. Sherwood number for a large Péclet number

As mentioned in the preceding section, the Péclet number can be large even for the creeping flow of bubbles in a molten glass. To establish a solution when this is the case, boundary layer theory is used. This method has already been proposed by Levich (1962); however, the self-similar solution of Ruckenstein (1967) is used here. The solution given by Ruckenstein (1967) is also established for unsteady problem but only the steady-state regime is studied here.

When the Péclet number is large, a boundary layer develops around the bubble and it is possible to use classical boundary layer theory to find a simplified version of the equation which is easier to solve. The determination of a simplified version of the transport equation is briefly recalled below. Eq. (25) is written in spherical coordinates as

$$[1+f(C)]\left(u_r\frac{\partial C}{\partial r} + \frac{u_\theta}{r}\frac{\partial C}{\partial \theta}\right) = \frac{1}{Per^2}\left[\frac{\partial}{\partial r}\left(r^2\frac{\partial C}{\partial r}\right) + \frac{1}{\sin\theta}\frac{\partial}{\partial\theta}\left(\sin\theta\frac{\partial C}{\partial\theta}\right)\right]. \tag{26}$$

The boundary conditions for $C(r,\theta)$ are

$$C(1/2,\theta) = 1, \tag{27a}$$

$$\lim_{r\to\infty} C(r,\theta) = 0. \tag{27b}$$

The establishment of the boundary layer equation can be performed by following the perturbation method (Van Dyke, 1975) where here the perturbation parameter is the inverse of Pe. The problem is singular since if Pe tends to infinity, the right-hand side of the equation disappears. It is not possible to verify all boundary conditions. In order to overcome this problem, the typical solution is to define an inner expansion (Van Dyke, 1975). In order to do that, r is written as follows:

$$r = \frac{1+\delta(Pe)\zeta}{2}, \tag{28}$$

where ζ the normal coordinate to the bubble interface and $\delta(Pe)$ is a function of the Péclet number. This quantity defines the length scale of the boundary layer.

To fix the order of magnitude of δ, the convective and Laplacian terms in Eq. (26) are developed in Taylor series of δ. Using the principle of least degeneracy (Van Dyke, 1975), δ is equal to (more details are given in Appendix A):

$$\delta = \frac{1}{\sqrt{2Pe}}. \tag{29}$$

The boundary layer equation is obtained by developing C as a power series of δ. The first order gives the following equation:

$$[1+f(C)]\left(-\zeta\cos\theta\frac{\partial C}{\partial\zeta} + \frac{\sin\theta}{2}\frac{\partial C}{\partial\theta}\right) = \frac{\partial^2 C}{\partial\zeta^2}, \tag{30}$$

which is very similar to the equation given by Ruckenstein (1967) without the unsteady term (see Appendix A).

As with Ruckenstein (1967) and Ruckenstein et al. (1971), a self-similar solution can be determined where the self-similar coordinate is given by

$$\eta = \frac{\zeta}{g(\theta)} \tag{31}$$

and C becomes a function of η. The function g determined in Appendix A is given by

$$g(\theta) = 2\sqrt{\frac{2}{3}}\frac{\sqrt{2-3\cos\theta+\cos^3\theta}}{\sin^2\theta}. \tag{32}$$

The differential equation of C is given by

$$\frac{d^2C}{d\eta^2} + 2[1+f(C)]\eta\frac{dC}{d\eta} = 0, \tag{33}$$

where the boundary conditions are

$$C(0) = 1, \tag{34a}$$

$$\lim_{\eta\to\infty} C(\eta) = 0. \tag{34b}$$

If the function $f(C)$ is equal to 0, Eq. (33) is solved by $\mathrm{erfc}(\eta)$. When $f(C)$ is not equal to 0, it is necessary to solve Eq. (33) using a numerical method and a central finite-difference method has been used here. When the solution of C is known, the Sherwood number can be determined. The general expression of Sh is

$$Sh = \frac{1}{2}\int_0^{\pi}\left.\frac{\partial C}{\partial r}\right|_{r=1/2}\sin\theta\, d\theta. \tag{35}$$

After developing with the self-similar variable and integrating over θ, the Sherwood number is equal to

$$Sh = \frac{\sqrt{3}}{3}\left.\frac{dC}{d\eta}\right|_{\eta=0}\sqrt{Pe}. \tag{36}$$

In the limit of $f(C) = 0$, the derivative of C at $\eta = 0$ is equal to $2/\sqrt{\pi}$, the classical result of Levich (1962) is found, where

$$Sh_0 = 0.651\sqrt{Pe}. \tag{37}$$

The subscript 0 is added in order to specify that this expression is obtained without considering any reaction. In other cases, the derivative of C is determined by using a second order unsymmetrical scheme (Collatz, 1960).

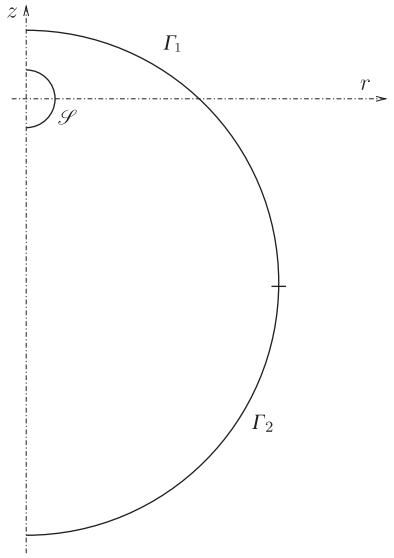

Fig. 1. Computation domain around a bubble in the meridian plane.

3.2. Sherwood number for a moderate Péclet number

In order to establish a solution for a large range of Péclet numbers, a numerical method has been used with the results presented in Section 4.2. The advection–diffusion reaction problem is solved in the domain represented by the meridian plane in Fig. 1. This figure is not to scale as the radius of the outside boundary is taken to be 20 times larger than the bubble size in the numerical computation. Due to the dominating advection problem, a large part of the bubble's wake is taken into account in the numerical simulation. The outside boundary is decomposed into two limits, Γ_1 in the downward part and Γ_2 in the upward one in the wake of the bubble. The bubble surface is denoted as $\mathscr{S}$ in Fig. 1.

The boundary conditions of Eq. (25) are

$$C = 1 \quad \text{on } \mathscr{S}, \tag{38a}$$

$$C = 0 \quad \text{on } \Gamma_1, \tag{38b}$$

$$\frac{\partial C}{\partial n} = 0 \quad \text{on } \Gamma_2. \tag{38c}$$

The last boundary condition for Γ_2 is due to the formation of a tail of concentration C in the bubble's wake. This condition assures the behavior of this tail far away from the bubble.

Eq. (25) with boundary conditions (38) is solved using finite element methods. The convection dominated transport problem requires a stabilization technique. Streamline diffusion is employed where only an artificial diffusion along the streamlines is added and, in order to minimize numerical error, the mesh is adapted with an estimation of *a posteriori* error. From the theoretical model presented above, the numerical solution of the dimensionless concentration C is determined and the mass transfer coefficient computed using Eq. (13) which, in its dimensionless form, is directly equal to the Sherwood number.

4. Results

After this presentation of the numerical methods utilized, the results are given below using the boundary layer solution and the finite element method, respectively.

The data required to determine the equilibrium constant of the iron oxide oxidation–reduction reaction as well as oxygen solubility can be found in Beerkens (2003).

4.1. Sherwood number for a large Péclet number

In order to control the influence of the chemical reaction, the Sherwood number is determined for three temperatures, four oxidation states and a range of iron contents equal to [0.01; 0.5] wt%. The mass transfer coefficient is given in Fig. 2 by plotting the ratio Sh^2/Sh_0^2 as a function of N_{Fe}. As expected, the Sherwood number increases with iron content due to the fact that the dimensionless group N_{Fe} is directly proportional to C_{Fe}. When the iron content approaches 0, the Sherwood number reaches the value without reaction, Eq. (37). The representation in terms of Sh^2/Sh_0^2 shows that Sh can be written as follows:

$$Sh = Sh_0\sqrt{1 + \alpha N_{Fe}}, \tag{39}$$

where α is a numerical coefficient depending on temperature and oxidation state.

The influence of the reaction is important at low temperatures and also for reduced glass (high $C_{Fe^{2+}}$). This effect can easily be understood due to the feature of $f(C)$ as a function of saturation state, Sa. Indeed, when both the temperature is low and the oxidation state is small (high value of $\mathscr{R}$), Sa can take small values. In this case, $f(C)$ becomes greater and greater. Consequently, mass transfer is greatly increased as it is possible to see in Fig. 2 where, for a glass at $\mathscr{R}^\infty = 0.4$ and $T = 1300\,^\circ$C, the Sherwood number can be 10 times greater than without reaction when the iron content reaches 0.5 wt%.

The enhancement of mass transfer with increasing $f(C)$ can be clearly seen by plotting the concentration C as a function of the self-similar variable η. Fig. 3 represents C versus η for various iron contents for (a) a glass with $\mathscr{R}^\infty = 0.2$ at $T = 1300\,^\circ$C and (b) for various oxidation states for a glass with $C_{Fe} = 0.1\%$ at $T = 1300\,^\circ$C. The concentration gradient increases with both iron content and reduction state. The scale of the boundary layer decreases when either iron content or $\mathscr{R}^\infty$ increases. The behavior of the Sherwood number as a function of N_{Fe} shown in Fig. 2 suggests that when the oxidation–reduction reaction is taken into account, boundary layer thickness is proportional to $1/\sqrt{Pe(1 + \alpha N_{Fe})}$.

In order to find the behavior of α, a large number of numerical simulations of the boundary layer solution were performed as a function of oxidation state and temperature. As already shown, the relevant parameter seems to be glass saturation. Thanks to this extensive analysis, α can be plotted as a function of Sa as is done here in Fig. 4. As expected, the values of α obtained for various temperatures and oxidation states match very well when these data are plotted as a function of saturation state. By using the numerical data, it is possible to find an approximate expression of α given by the relationship

$$\frac{1}{\alpha} = \frac{1}{3.05Sa^{-0.375}} + \frac{1}{1.28Sa^{-1}}. \tag{40}$$

This equation is represented by a solid line in Fig. 4 where good agreement with the numerical data is obtained. This relationship is determined by using a harmonic average of the two asymptotic trends observed both at small and large values of Sa. Indeed, when the glass is undersaturated and Sa is small, α is a function of $Sa^{-0.375}$ and for larger values of Sa, α is a function of Sa^{-1}.

The effect of the oxidation–reduction reaction of iron oxide can be seen as an enhancement of the advection term. Inversely, the reaction's effect may be seen as a reduction of the diffusion coefficient as already pointed out by Beerkens and de Waal (1990). Whatever the point of view, the effective Péclet number increases. From these developments, a modified Péclet number can be written as follows:

$$Pe' = Pe[1 + \alpha(Sa)N_{Fe}], \tag{41}$$

where $\alpha(Sa)$ is given by Eq. (40).

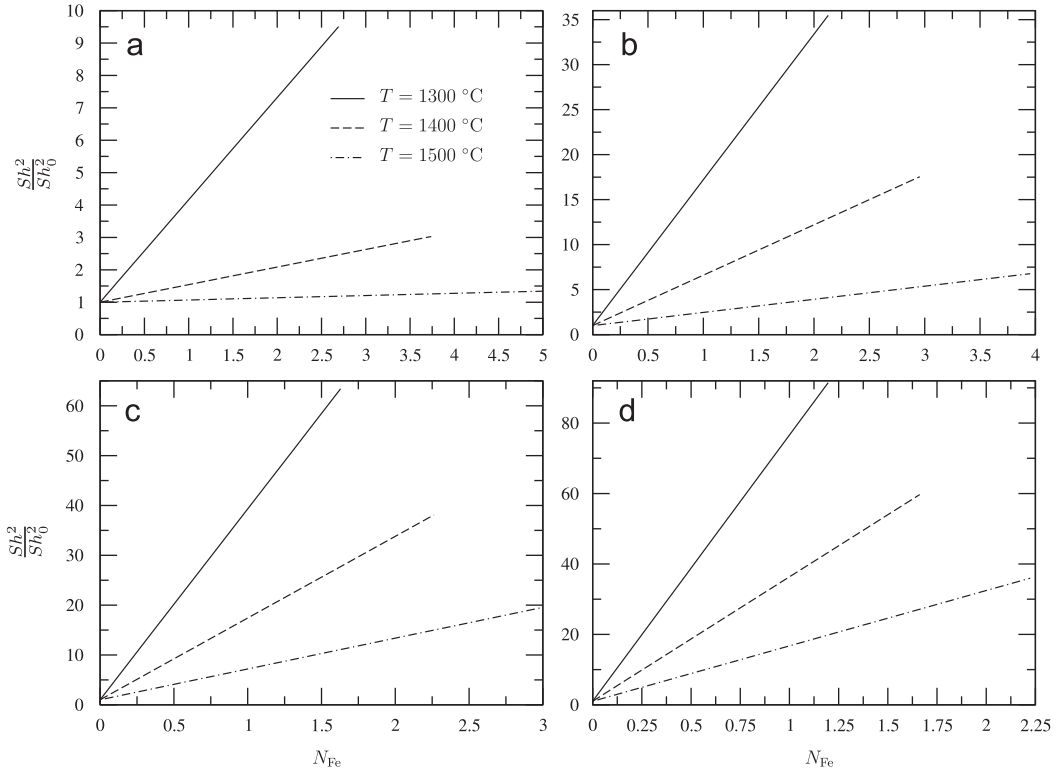

Fig. 2. Sh^2/Sh_0^2 as a function of N_{Fe} for $T = 1300$, 1400 and 1500 °C and (a) $\mathscr{R}^\infty = 0.1$, (b) $\mathscr{R}^\infty = 0.2$, (c) $\mathscr{R}^\infty = 0.3$ and (d) $\mathscr{R}^\infty = 0.4$.

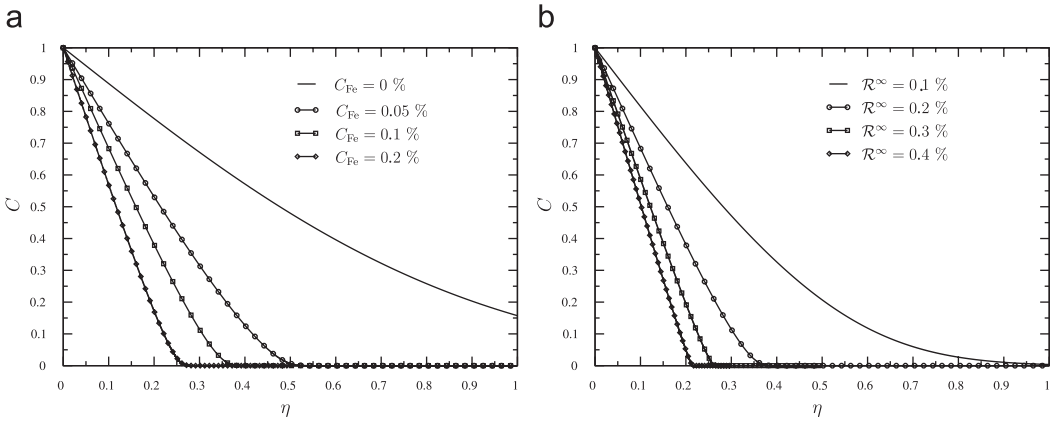

Fig. 3. C as a function of the self-similar variable η for (a) $\mathscr{R}^\infty = 0.2$ at $T = 1300$ °C and (b) $C_{\mathrm{Fe}} = 0.1\%$ at $T = 1300$ °C.

Finally, the Sherwood number can be written using the same expression independent of chemical reaction, Eq. (37), where Pe is replaced by Pe'.

4.2. Sherwood number for a moderate Péclet number

In order to verify the numerical method used in this subsection, a numerical computation has been performed without the reaction term. The Péclet number is taken to be in the range of $[1; 10^4]$. Fig. 5 presents the Sherwood number as a function of the Péclet number obtained using the present numerical method. The solid line is an approximate solution given by Clift et al. (1978). Over the whole range of Péclet numbers, the agreement between our solution and the prediction of Clift et al. (1978) is good wherein, for small Péclet numbers, the Sherwood number approaches 2 which is an asymptotic value when advection is equal to 0. Nevertheless, due to our choice of computational domain, we cannot determine the Sherwood number for very small Péclet numbers. We report also in Fig. 5 the limit solution, Eq. (37), obtained for large Péclet numbers.

After this preliminary result, the influence of the oxidation–reduction reaction is investigated where the advection–diffusion reaction equation is solved for various iron concentrations and at two temperatures. The oxidation state in the glass bulk is taken to be equal to 0.2 and 0.3. The Sherwood number features are given in Fig. 6 where C_{Fe} varies over the range of $[0.01; 0.3]$ wt% for $T = 1400$ and 1500 °C. In both situations, we compare the numerical solutions with that obtained without chemical reaction represented as a solid line in Fig. 6. The solution obtained from boundary layer theory presented in the preceding subsection is also given where the Sherwood numbers are plotted using dashed lines in Fig. 6.

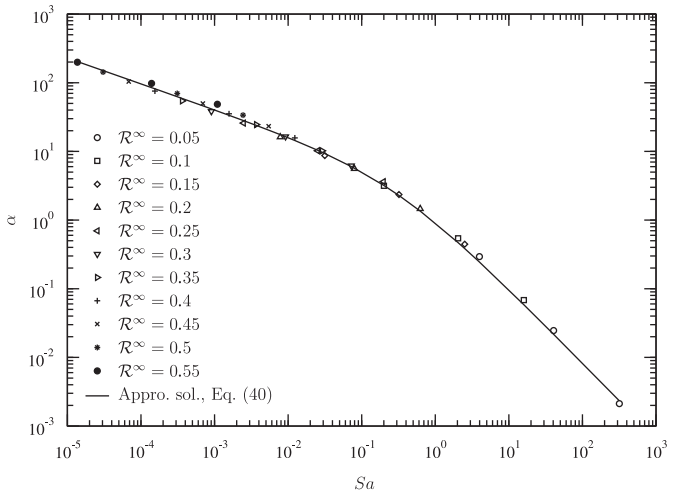

Fig. 4. α as a function of Sa for various oxidation states.

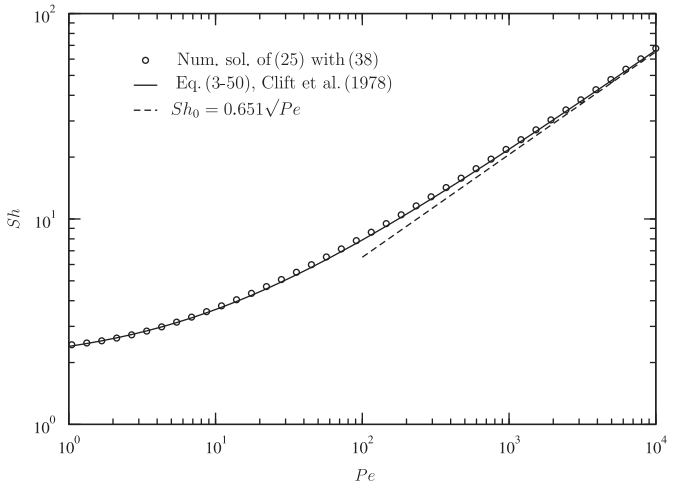

Fig. 5. Sherwood number as a function of Péclet number without oxidation–reduction reaction. Comparison with the solution given by Clift et al. (1978).

The oxidation–reduction reaction enhances the mass transfer coefficient over the whole range of Péclet numbers. For a glass with $\mathscr{R}^\infty = 0.3$ at $T = 1400\,^\circ$C, the Sherwood number is multiplied by 2 when the Péclet number is equal to 1. The increase in the Sherwood number is more important when the Péclet number is high since, for a glass with $\mathscr{R}^\infty = 0.3$ at $T = 1400\,^\circ$C, Sh is 3.8 times greater than the value without reaction for $Pe = 10^4$.

As already seen in the preceding subsection, the Sherwood number's increase is more important at small temperatures and for reduced glass. The concentration of reduced iron leads to an enhancement of the mass transfer coefficient. The comparison with boundary layer theory shows that the agreement between the two methods is relatively good. Nevertheless, a difference for larger Péclet numbers is observed. From the finite element method, it is difficult to obtain a good prediction for Sh when the Péclet number is large due to the limited size of the boundary layer around the bubble.

A modified Péclet number has been proposed above, leading to a unified Sherwood number. This modified Péclet number is a function of the dimensionless group N_{Fe} and the glass saturation, Sa. In order to validate that this modification can be extended to a large range of Péclet numbers, the Sherwood numbers obtained using finite element methods were plotted in Fig. 7 as function of Pe' given by Eq. (41). All numerical values of the Sherwood number correspond well to the master curve equivalent to that obtained without considering the chemical reaction. Consequently, the Sherwood number can be written as

$$Sh = 1 + (1 + 0.564Pe'^{2/3})^{3/4}, \tag{42}$$

which is the same correlation proposed by Clift et al. (1978) where the classical Péclet number is replaced by the modified Péclet number introduced in this work.

This result is, from an application point of view, very important since it is possible to use an approximate function to determine the Sherwood number as a function of the modified Péclet number. This type of equation can easily be implemented into software devoted to the study of bubbles.

5. Discussion

As expected, the oxidation–reduction reaction enhances the mass transfer coefficient. From the two methods employed in this work, the Sherwood number becomes a function of Pe and also of N_{Fe} and Sa. The enhancement of the Sherwood number can reach a factor of ten for reduced glass at low temperatures. The results obtained here agree with experimental data given by Greene and Platts (1969), where the role played by the oxidation–reduction reaction was underlined. These authors showed that when the iron content of glass increases, bubble shrinkage becomes more important and that this is a consequence of the increased mass transfer coefficient.

An expression of the Péclet number taking into account the chemical reaction has been established. This result does not vary greatly from that proposed by Beerkens and de Waal (1990) and by Itoh et al. (1997) who proposed modifying the mass transfer coefficient though a multiplication of the square root of the ratio of diffusion coefficient to effective diffusion coefficient taking into account the oxidation–reduction reaction. Itoh et al. (1997) generalized, correcting for a moving bubble but taking a Sherwood number used for a solid particle. Beerkens (2003) proposed the same correction but also with a Sherwood number function applicable for a solid particle. In fact, the correction in the case of a rigid interface should be proportional to the cubic root of the diffusion coefficient ratio since the concentration boundary layer is inversely proportional to the power of one-third of the Péclet number (Clift et al., 1978; Levich, 1962).

From this analysis, various consequences can be drawn. First, the oxygen diffusion coefficient in glass was generally determined regardless of the oxidation–reduction reaction; Doremus (1960), for example, used an exact solution obtained for a pure diffusion process. Secondly, the presence of other gases in a molten glass leads to a multicomponent diffusion process. The mass transfer mechanisms must be analyzed differently as a function of gas species whether or not the oxidation–reduction reactions are taken into account. This point suggests that the Sherwood numbers must be defined for species present in chemical reactions and other relationships for other species.

6. Conclusion

Mass transfer around a rising bubble in molten glass has been investigated. The first part of this work focused on coupling advection–diffusion to chemical reaction processes for oxygen in molten glass. The bubble/liquid interface was assumed to be completely mobile which is the case for a clean bubble, and chemical equilibrium of the iron oxide oxidation–reduction reaction has also been assumed. A model to describe the mass transfer around a bubble under a quasi-steady state regime was presented.

The dimensionless mass transfer coefficient, the Sherwood number, was determined via two methods: the first founded on

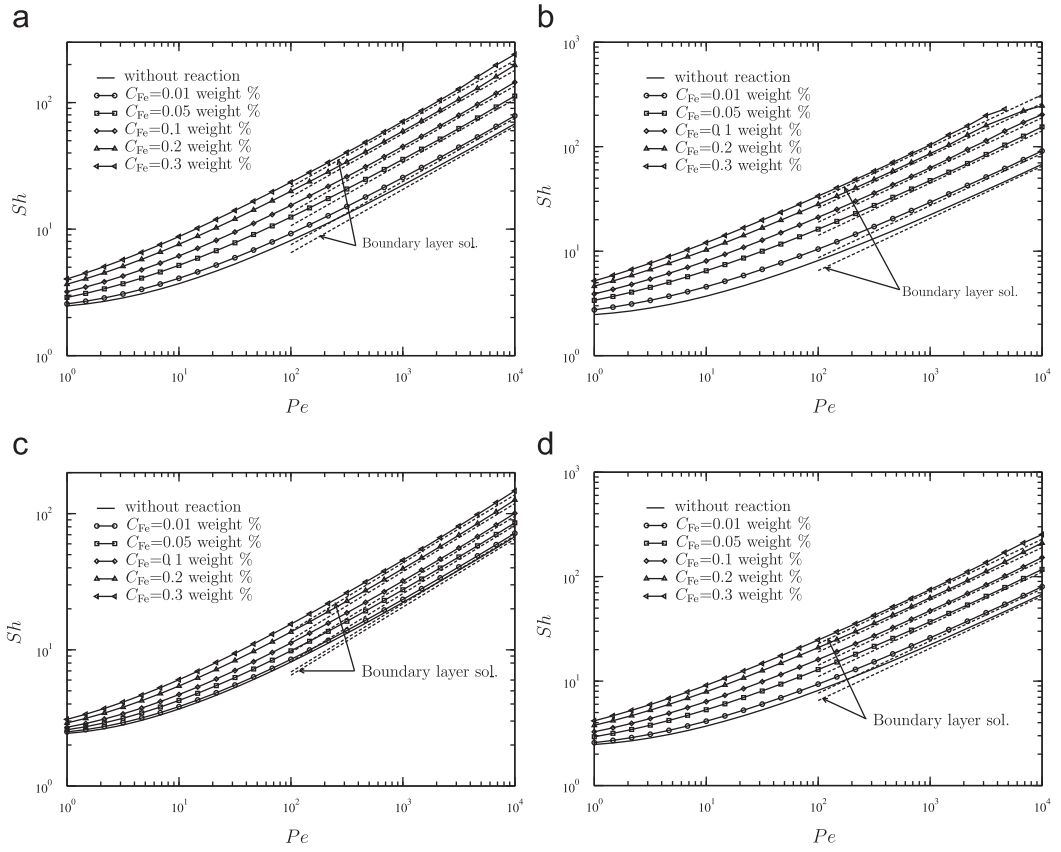

Fig. 6. Sherwood number as a function of Péclet number at $T = 1400$ and 1500 °C and $\mathscr{R}^{\infty} = 0.2$ and 0.3 where the total iron content varies in the range 0.01–0.3 wt%.

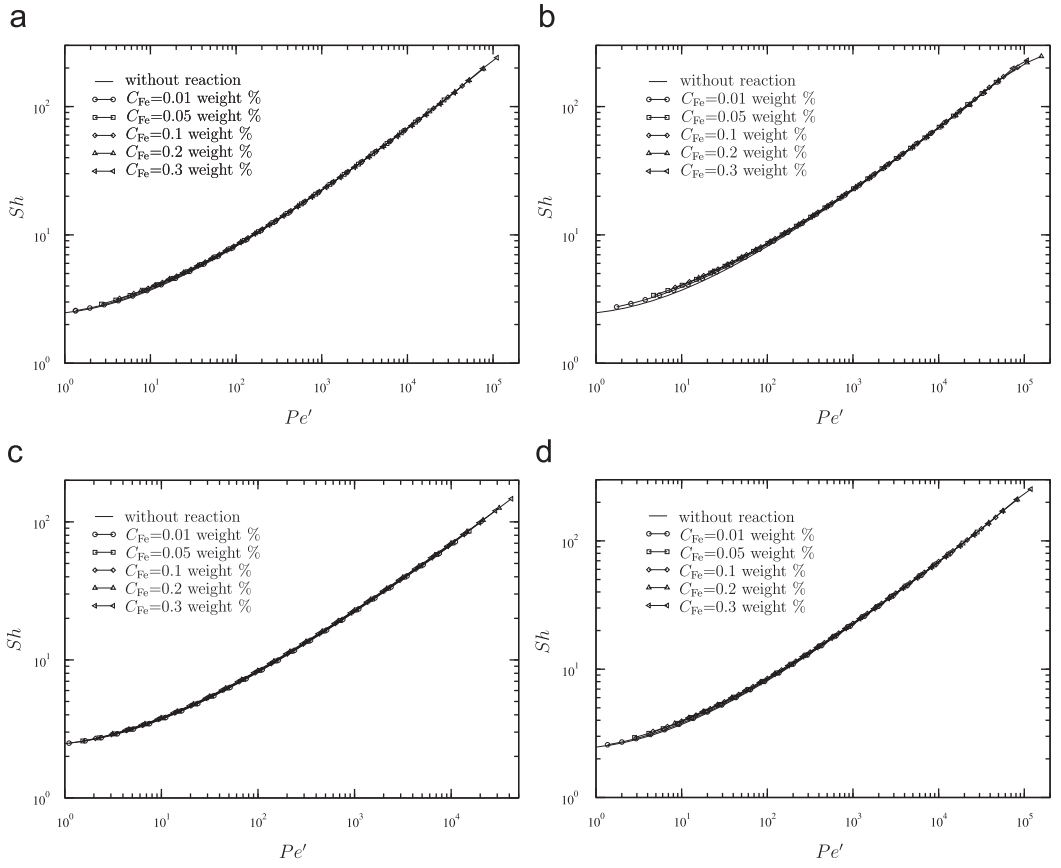

Fig. 7. Sherwood number as a function of a modified Péclet number at $T = 1400$ and 1500 °C and $\mathscr{R}^{\infty} = 0.2$ and 0.3 where the total iron content varies in the range 0.01–0.3 wt%.

boundary layer theory and the second on a numerical resolution of the full problem. The influence of increasing iron content was investigated and it was found that it increases the Sherwood number. This result can be explained by either an enhancement of the advection term or a decrease in the diffusion coefficient. A definition of a modified Péclet number taking into account the oxidation–reduction reaction has also been proposed, which leads to a unified relationship between the Sherwood number and the modified Péclet number. This latter is the product of the Péclet number with a function which depends only on a dimensionless group, N_{Fe}, proportional to the iron content, as well as the glass saturation.

The establishment of a unified expression of the Sherwood number taking into account the oxidation–reduction reaction has many consequences. It is, for example, possible to use the same equations in order to describe bubble shrinkage or growth as those which neglect the chemical reaction. The difference is to be found only in whether or not the definition of the Péclet number takes into account the chemical reactions as a function of the gas species.

Here, only one gas has been studied with one chemical reaction; however, in many applications and in particular the glass process, it is possible to have two gas species (i.e. O_2 and SO_2) with two oxidation–reduction reactions. This problem leads to the description of the advection–diffusion reaction processes of these two species and will be addressed in future work.

Appendix A. Development of the boundary layer equation on $C(r,\theta)$

In this appendix, the boundary layer equation on $C(r,\theta)$ is established from the perturbation method (Van Dyke, 1975). As already indicated in Section 3.1, r is written as

$$r=\frac{1+\delta\zeta}{2}, \tag{A.1}$$

where δ is an unknown function of the Péclet number which must be smaller than unity. The quantity ζ is the inner coordinate (Van Dyke, 1975).

First of all, Eq. (26) is rewritten as a function of ζ and θ:

$$[1+f(C)]\left(\frac{u_r}{\delta}\frac{\partial C}{\partial\zeta}+\frac{u_\theta}{1+\delta\zeta}\frac{\partial C}{\partial\theta}\right)=\frac{1}{2Pe\delta^2(1+\delta\zeta)^2}\left\{\frac{\partial}{\partial\zeta}\left[(1+\delta\zeta)^2\frac{\partial C}{\partial\zeta}\right]+\frac{4\delta^2}{\sin\theta}\frac{\partial}{\partial\theta}\left(\sin\theta\frac{\partial C}{\partial\theta}\right)\right\}. \tag{A.2}$$

Assuming that δ is a perturbation parameter, u_r/δ, $u_\theta/(1+\delta\zeta)$ and also the right-hand side of (A.2) are developed in Taylor series where the relationships (16) and (17) giving u_r and u_θ, respectively, are used. The preceding equation becomes

$$[1+f(C)]\left\{-[\zeta-\delta\zeta^2+\mathcal{O}(\delta^2)]\cos\theta\frac{\partial C}{\partial\zeta}+\frac{1}{2}[1+\mathcal{O}(\delta^2)]\sin\theta\frac{\partial C}{\partial\theta}\right\}=\frac{1}{2Pe\delta^2}[1-2\delta\zeta^2+\mathcal{O}(\delta^2)]\left[\frac{\partial^2 C}{\partial\zeta^2}+2\delta\frac{\partial}{\partial\zeta}\left(\zeta\frac{\partial C}{\partial\zeta}\right)+\mathcal{O}(\delta^2)\right]. \tag{A.3}$$

The order of magnitude of δ can now be specified. Indeed, the $Pe\delta^2$ product can be finite, infinite or zero when the Péclet number tends to infinity. However, the two last possibilities lead to degenerate solutions that cannot assure the boundary conditions. Consequently, the only possible solution is that the $Pe\delta^2$ product is a finite value. This choice is guided by the principle of least degeneracy (Van Dyke, 1975). Arbitrarily, $Pe\delta^2$ can be defined as follows:

$$Pe\delta^2=\tfrac{1}{2}. \tag{A.4}$$

Thus, δ is equal to

$$\delta=\frac{1}{\sqrt{2Pe}}. \tag{A.5}$$

From this result, it can be shown that the boundary layer thickness is proportional to $Pe^{-1/2}$ when the interface between the bubble and the liquid is assumed to be totally mobile.

Now, if all terms proportional to δ, δ^2 and so on in Eq. (A.3) are neglected, the first order approximation gives the boundary layer equation:

$$[1+f(C)]\left(-\zeta\cos\theta\frac{\partial C}{\partial\zeta}+\frac{\sin\theta}{2}\frac{\partial C}{\partial\theta}\right)=\frac{\partial^2 C}{\partial\zeta^2}. \tag{A.6}$$

Following Ruckenstein (1967) and Ruckenstein et al. (1971), a self-similar solution can be determined where the self-similar variable, η, is given by

$$\eta=\frac{\zeta}{g(\theta)}. \tag{A.7}$$

Eq. (A.6) is now written as function of η and θ as follows:

$$\frac{d^2C}{d\eta^2}+[1+f(C)]\left[g^2(\theta)\cos\theta+\frac{\sin\theta}{2}g(\theta)g'(\theta)\right]=0. \tag{A.8}$$

In order to have an equation with C uniquely a function of η, the whole term function of θ can be fixed and equal to an arbitrary constant:

$$g^2(\theta)\cos\theta+\frac{\sin\theta}{2}g(\theta)g'(\theta)=2. \tag{A.9}$$

Consequently, g is a solution of an ordinary differential equation of the first order where the general solution is given by

$$g(\theta)=2\sqrt{\frac{2}{3}}\frac{\sqrt{A-3\cos\theta+\cos^3\theta}}{\sin^2\theta}, \tag{A.10}$$

where A is an integration constant. To fix the value of A, it should be noted that the flux of C is proportional to $1/g(\theta)$. In order to have a finite value of the molar flux at $\theta=0$, A must be equal to 2.

Finally, C must be determined by a numerical method as presented in Section 3.1.

References

Beerkens, R.G.C., 2003. Analysis of advanced and fast fining processes for glass melts. In: Advances in Fusion and Processing of Glass III.American Ceramic Society, New York, pp. 3–24.

Beerkens, R.G.C., de Waal, H., 1990. Mechanism of oxygen diffusion in glassmelts containing variable-valence ions. J. Am. Ceram. Soc. 73, 1857–1861.

Clift, R., Grace, J.R., Weber, M.E., 1978. Bubbles, Drops, and Particles. Academic Press, New York.

Collatz, L., 1960. The Numerical Treatment of Differential Equations. Springer, Berlin.

Cook, G.B., Cooper, R.F., Wu, T., 1990. Chemical diffusion and crystalline nucleation during oxidation of ferrous iron-bearing magnesium aluminosilicate glass. J. Non-Cryst. Solids 120, 207–222.

Crank, J., 1956. The Mathematics of Diffusion. Clarendon Press, Oxford.

Dani, A., Cockx, A., Guiraud, P., 2006. Direct numerical simulation of mass transfer spherical bubbles: the effect of interface contamination at low Reynolds numbers. Int. J. Chem. Reactor Eng. 4, 1–21.

Debrégeas, G., de Gennes, P.-G., Brochard-Wyart, F., 1998. The life and death of "bare" viscous bubbles. Science 279, 1704–1707.

Debrégeas, G., Martin, P., Brochard-Wyart, F., 1995. Viscous bursting of suspended films. Phys. Rev. Lett. 75, 3886–3889.

Doremus, R.H., 1960. Diffusion of oxygen from contracting bubbles in molten glass. J. Am. Ceram. Soc. 43, 655–661.

Doremus, R.H., 2002. Diffusion of Reactive Molecules in Solids and Melts. Wiley, New York.

Greene, C.H., Gaffney, R.F., 1959. Apparatus for measuring the rate of absorption of a bubble in glass. J. Am. Ceram. Soc. 42, 271–275.

Greene, C.H., Platts, D.R., 1969. Behavior of bubbles of oxygen and sulfur dioxide in soda-lime glass. J. Am. Ceram. Soc. 52, 106–109.
Hadamard, J., 1911. Mouvement permanent lent d'une sphère liquide et visqueuse dans un liquide visqueux. C. R. Acad. Sci. Paris 152, 1735–1738.
Hornyak, E.J., Weinberg, M.C., 1984. Velocity of a freely rising gas bubble in a soda-lime silicate glass melt. J. Am. Ceram. Soc. 67, C244–C246.
Itoh, E., Yoshikawa, H., Miura, H., Kawase, Y., 1997. A quasi-stationary model for bubble behaviour in glass melts with refining reactions. Glass Technol. 38, 134–140.
Jucha, R.B., Powers, D., McNeill, T., Subramanian, R.S., Cole, R., 1982. Bubble rise in glassmelts. J. Am. Ceram. Soc. 65, 289–292.
Kawachi, S., Kawase, Y., 1998. Evaluation of bubble removing performance in a TV glass furnace. Part 1. Mathematical formulation. Glastech. Ber. 71, 83–91.
Kondepudi, D., Prigogine, I., 1998. Modern Thermodynamics: From Heat Engines to Dissipative Structures. Wiley, New York.
Levenspiel, O., 1972. Chemical Reaction Engineering. Wiley, New York.
Levich, V.G., 1962. Physicochemical Hydrodynamics. Prentice-Hall, Englewood Cliffs, NJ.
Li, K.-W.K., Schneider, A., 1993. Rise velocities of large bubbles in viscous Newtonian liquids. J. Am. Ceram. Soc. 76, 241–244.
Liao, Y., McLaughlin, J.B., 2000a. Bubble motion in aqueous surfactant solutions. J. Colloid Interface Sci. 224, 297–310.
Liao, Y., McLaughlin, J.B., 2000b. Dissolution of a freely rising bubble in aqueous surfactant solutions. Chem. Eng. Sci. 55, 5831–5850.
McLaughlin, J.B., 1996. Numerical simulation of bubble motion in water. J. Colloid Interface Sci. 184, 614–625.
Paul, A., 1990. Chemistry of Glasses. Chapman & Hall, London.
Pigeonneau, F., Martin, D., Mario, O., 2009. Shrinkage of oxygen bubble rising in a molten glass. Chem. Eng. Sci., submitted for publication.
Ponoth, S.S., McLaughlin, J.B., 2000. Numerical simulation of mass transfer for bubbles in water. Chem. Eng. Sci. 55, 1237–1255.
Rüssel, C., 1989. Redox reactions during cooling of glass melts—a theoretical consideration. Glass Sci. Technol. 62, 199–203.
Ruckenstein, E., 1967. Mass transfer between a single drop and a continuous phase. Int. J. Heat Mass Transfer 10, 1785–1792.
Ruckenstein, E., Dang, V.-D., Gill, W.N., 1971. Mass transfer with chemical reaction from spherical one or two components bubbles or drops. Chem. Eng. Sci. 26, 647–668.
Rybczynski, W., 1911. Uber die fortschreitende bewegun einer flussingen kugel in einem zaben medium. Bull. de l'Acad. des Sci. de Cracovie, 40–46.
Sadhal, S.S., Ayyaswamy, P.S., Chung, J.N., 1997. Transport Phenomena with Drops and Bubbles. Springer, New York.
Subramanian, R.S., Chi, B., 1980. Bubble dissolution with chemical reaction. Chem. Eng. Sci. 35, 2185–2194.
Trambouze, P., Euzen, J.-P., 2002. Les reacteurs chimiques. De la conception à la mise en œuvré, Editions Technip, Paris.
Van Dyke, M., 1975. Perturbation Methods in Fluid Mechanics. The Parabolic Press, Stanford.
Villermaux, J., 1993. Genie de la réaction chimiqué. Tec & Doc Lavoisier, Paris.
Yoshikawa, H., Miura, H., Kawase, Y., 1998. Dissolution of bubbles in glassmelts with equilibrium redox reactions: approximations for a moving bubble boundary. J. Mater. Sci. 33, 2701–2707.

Chemical Engineering Science 65 (2010) 3158–3168

Contents lists available at ScienceDirect

Chemical Engineering Science

journal homepage: www.elsevier.com/locate/ces

Shrinkage of an oxygen bubble rising in a molten glass

F. Pigeonneau [a,*], D. Martin [b], O. Mario [b]

[a] Surface du Verre et Interfaces, UMR 125 Unité mixte CNRS/Saint-Gobain, 39 quai Lucien Lefranc – BP 135, 93303 Aubervilliers Cedex, France
[b] Saint-Gobain Recherche, 39 quai Lucien Lefranc – BP 135, 93303 Aubervilliers Cedex, France

ARTICLE INFO

Article history:
Received 1 October 2009
Received in revised form
27 January 2010
Accepted 1 February 2010
Available online 6 February 2010

Keywords:
Bubble
Chemical processes
Fluid mechanics
Mass transfer
Multiphase reactions
Numerical analysis

ABSTRACT

The mechanisms controlling the evolution of a bubble surrounded by molten glass are important to understand in order to improve melting in glass furnaces, particularly during a change in composition. In order to provide insight into this phenomenon, the behavior of an isolated bubble rising in molten glass is examined both experimentally and numerically.

An experimental procedure developed specifically to observe, in situ, a rising bubble is described. Two soda-lime-silica compositions are tested, with low and high iron content, respectively.

The numerical model used to describe bubble shrinkage is based on the results recently proposed in Pigeonneau (2009). A specific mass transfer coefficient is used for oxygen where the oxidation–reduction reaction of iron oxides is taken into account.

A comparison between the experimental and numerical results shows the importance of the oxidation–reduction reaction of iron in the mass transfer of oxygen. The shrinkage rate of a pure O_2 bubble is enhanced with reduced molten glass iron content.

© 2010 Elsevier Ltd. All rights reserved.

1. Introduction

The removal of gas bubbles is of great interest for many industrial processes. This is especially true for the glass industry where bubbles are formed by the physical trapping, within a highly viscous fluid, of atmospheric gases and the decomposition of raw materials (Shelby, 1997). The elimination of gaseous inclusions is called "fining" and occurs by a combination of mass transfer processes and bubble migration to the free surface. Therefore, improved understanding of the shrinkage or growth of a bubble in a complex chemical environment is important in order to optimize the melting process.

A classical method used to remove bubbles during glass melting is to introduce "fining" agents such as arsenic, antimony oxides or sulfate in small quantities (Shelby, 1997). At high temperature, these agents are reduced releasing oxygen and/or sulfur dioxide into the glass. The bubbles already present increase in size due to the mass transfer of the dissolved gases towards them. Iron is present as an impurity in many mineral elements used as raw materials in glass melting (Mysen and Richet, 2005). The oxidation–reduction state of iron is carefully controlled in the glass melting process since it plays an important role in glass color, see Hirashima et al. (1988). The chemical equilibrium of molten glass is complex and includes the action of gaseous inclusions and chemical reactions occurring within. Gaseous species involved in this process are water vapor, H_2O, and nitrogen, N_2 coming from the atmosphere; carbon dioxide, CO_2, produced by the decomposition of raw materials; as well as sulfur dioxide, SO_2 and oxygen, O_2, originating from the fining agents.

Research on bubble features in molten glass has been ongoing for many years, both experimentally and theoretically. Among the first contributions, Greene and Gaffney (1959) developed a rotating experimental device to stabilize and observe a bubble. Greene and Kitano (1959), Greene and Lee (1965) and Greene and Platts (1969) used the same experimental set-up to study pure O_2 and SO_2 bubbles in soda-lime glasses. They demonstrated, for example, that a bubble shrinks faster in glasses containing As_2O_3. Němec (1980a, b) developed an experimental method where a single bubble is released in a transparent crucible containing molten glass and its size recorded *via* a camera. More recently, Kloužek and Němec (2003) proposed a method by transferring the former from the top to the bottom of the crucible when it approaches the free surface to increase interaction time between the bubble and the molten glass.

Doremus (1960) provides one of the first theoretical contributions studying the shrinkage of a bubble in molten glass. He determined the diffusion coefficient of oxygen for different glass compositions based on a diffusion-controlled process. Readey and Cooper (1966) studied, *via* a finite difference method, the mass transfer following a pure diffusion process where the temporal evolution of the bubble's radius was introduced into the numerical model. In order to take into account the effect of chemical reactions on the oxygen resorption pointed out by Greene and Lee (1965), Subramanian and Chi (1980) developed a model where a first-order irreversible reaction was introduced. The role of oxidation–reduction reactions of polyvalent cations

* Corresponding author. Tel.: +33 1 48 39 59 99; fax: +33 1 48 39 55 62.
E-mail address: franck.pigeonneau@saint-gobain.com (F. Pigeonneau).

0009-2509/$ - see front matter © 2010 Elsevier Ltd. All rights reserved.
doi:10.1016/j.ces.2010.02.003

has been studied by Yoshikawa and Kawase (1997) for an immobile bubble. The oxidation–reduction reaction was assumed to be very fast but limited by the diffusion of oxygen following a first development by Beerkens and de Waal (1990). It was pointed out by Yoshikawa and Kawase (1997) that bubble growth is enhanced by the oxidation–reduction reaction.

As indicated above, various species interact with a bubble in molten glass. A multicomponent bubble has been studied by Ramos (1986) where bubble motion was introduced using mass transfer coefficients taken from classical textbooks as Levich (1962), Clift et al. (1978), and Sadhal et al. (1997). Němec and Mühlbauer (1980) proposed an equivalent model, valid for bubbles considered as solid particles with the mass transfer dominated by advection. Moreover, the mass transfer coefficients are identical for all gases. Itoh et al. (1997a) also studied bubble modeling and tested various mass transfer coefficients. In order to take into account the oxidation–reduction reaction, Itoh et al. (1997b) changed the mass transfer coefficient by introducing an effective diffusion coefficient. An equivalent method has been recently proposed by Beerkens (2002, 2003).

Despite these contributions, the influence of oxidation–reduction reactions has not been studied carefully, especially in the case of a rising bubble. The mass transfer coefficient for O_2 must be established and, moreover, precise comparisons with experimental results are lacking. Consequently, this work is focused on experimentally quantifying evolution of bubbles initially filled with oxygen and rising in soda-lime-silica glass. The influence of oxygen on mass transfer is studied by taking two glass compositions with different iron contents and oxidation states. In order to focus on oxygen transfer, sulfate was not included in the raw materials apart from as an impurity. Recently, an equation for the mass transfer coefficient of O_2 taking into account the oxidation–reduction reaction of iron oxide was proposed (Pigeonneau, 2009). A model based on this result describing a multicomponent bubble is presented here.

The experimental method is detailed in Section 2. The theoretical model describing the shrinkage or growth of a bubble is presented in Section 3, and the results obtained numerically and experimentally are given in Section 4. Symbols and abbreviations are given in the Notation. The hydrodynamic interactions between a bubble and two parallel walls are described in Appendix A. The physical and chemical properties of the glass and the gases used for the numerical simulations are given in Appendix B.

2. Experimental set-up and glass samples

The observation of a bubble in molten glass requires special equipment working at high temperature. An experimental set-up based on the work of Kloužek and Němec (2003) was developed. A general view of the experiment is given in Fig. 1. A glass sample is heated and melted in a laboratory furnace. The thermal inhomogeneity does not exceed 10 K in the region of the crucible. To limit optical distortions and to allow for an easy determination of the bubble size, the glass sample is introduced into a flat silica crucible. The glass sample volume is a rectangular prism where the height, length, and width are equal to 10, 5, and 1 centimeters, respectively. The quantity of glass for one experiment is around 120 g.

A bubble is created by injecting gas from a bottle through a small silica tube where one of the extremities is immersed in the molten glass as shown in Fig. 1. The control of the nature of the gas in the silica tube allows the genesis of a bubble with a known initial composition. Fig. 2 shows two photographs of the crucible with glass inside. The formation of a bubble is shown in Fig. 2(a). To avoid interactions with the rising bubble, the silica tube is mounted close to the free surface.

After its inflation, the bubble rises under the buoyancy force in the crucible and a video camera records the bubble size as

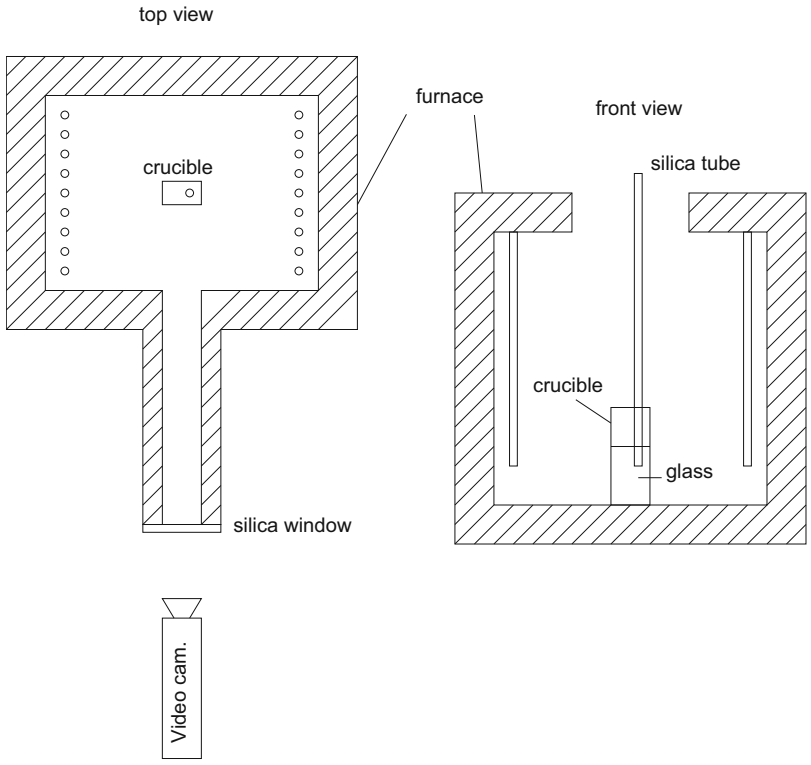

Fig. 1. Views of the laboratory furnace used to measure the bubble size at high temperature as a function of time.

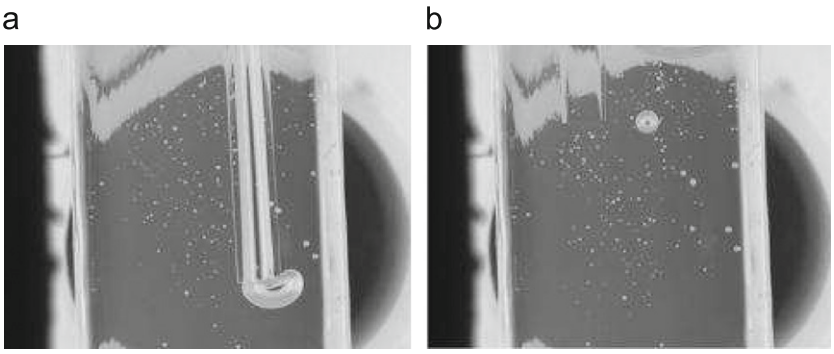

Fig. 2. Photographs of the experiment: (a) the bubble is created by blowing a gas through the silica tube; (b) the bubble is rising in the crucible nearby the free surface.

Table 1
Composition of glasses in wt% used in the experiments with the sulfate content and the reduction state.

Glass	SiO_2	Na_2O	CaO	MgO	Al_2O_3	Fe	S	$\mathcal{R}^\infty$
1	71.9	13.97	9.5	4	0.6	0.03	1×10^{-2}	0.57
2	71.8	13.99	9.5	4	0.6	0.11	1×10^{-2}	0.42

The iron content is the sum of the two polyvalent cations Fe^{2+}, and Fe^{3+}. The sulfur content is the sum of SO_4^{2-}, and SO_2.

a function of time (see Fig. 1). The photograph in Fig. 2(b) is taken when a bubble reaches the top of the crucible.

The method proposed by Kloužek and Němec (2003) is used in our work to increase the observation time of the bubble and to better simulate the industrial glass process. When the bubble approaches the free surface, it is manually trapped using the silica tube and is then transferred to the bottom of the crucible. The procedure can be repeated multiple times and, the experimental time can easily exceed 30 min.

The bubble radius is measured by counting the number of pixels representing the bubble with a calibration with an object of known dimension (for example, the silica tube). The uncertainties are equal to one pixel on the radius measurement. Consequently, with the typical resolution used with our video camera, the absolute uncertainty on the bubble radius is approximately $\pm 60\,\mu m$.

The transfer of the bubble from the top to the bottom of the crucible takes a few seconds. Therefore, we consider that it does not significantly affect the mass transfer process which occurs over a much longer time. No sharp change was observed in bubble size during the transfer operation.

The presence of the silica crucible can lead to a silica enrichment in the glass sample during the experiment. At 1450 °C, which is the highest temperature used in the experiment, the diffusion coefficient of silica is around $7\times10^{-11}\,m^2\,s^{-1}$ (Cable and Martlew, 1984). From a pure diffusion model, the diffusion layer, δ, can be estimated from the relationship

$$\delta = \sqrt{\mathcal{D}_{SiO_2} t}, \tag{1}$$

where $\mathcal{D}_{SiO_2}$ is the diffusivity of SiO_2 and t, the time. For the typical duration of the experiment (1 h), this layer is around 5×10^{-4} m. The rate of mass transfer of SiO_2, $\dot{m}_{SiO_2}$, can be evaluated from

$$\dot{m}_{SiO_2} = \frac{\mathcal{D}_{SiO_2}}{\delta}\Delta\rho_{SiO_2} S, \tag{2}$$

where $\Delta\rho_{SiO_2}$ is the difference of partial density of SiO_2 between the glass and the pure silica, and S is the total surface of the crucible wetted by the glass. So, from the geometry of the crucible and the glass composition given in Table 1, the total mass of SiO_2 diffused into the glass over 1 h is approximatively 2×10^{-6} kg.

Table 2
Estimation of molar concentrations of dissolved gases in the two glasses used in the experiments.

Glass	H_2O (mol m^{-3})	N_2 (mol m^{-3})	CO_2(mol m^{-3})
1	36.6	1×10^{-2}	5×10^{-2}
2	36.6	1×10^{-2}	5×10^{-2}

Consequently, from this simple estimation, the enrichment of silica from the crucible is too small to alter significantly the glass composition.

The experiments were performed on two compositions of soda-lime-silica glass as given in Table 1. As pointed out in the Introduction, the work is focused on the influence of iron content and oxidation state. Consequently, the first glass has a low iron content, and the second an iron content 3.6 times greater. Even if the sulfur content is very low, the quantity of SO_2 can be important compared to the oxygen concentration; therefore, the sulfur content is indicated in Table 1. The iron and sulfur contents are determined by chemical analysis while the quantity of reduced iron, Fe^{2+}, is obtained by optical spectrometry.

The numerical model presented in the next section requires the knowledge of molar concentrations of dissolved gases in the molten glass. As presented in Kloužek and Němec (2003), a mass spectroscopy analysis is used to determine molar concentrations of N_2 and CO_2. This measurement is based on the assumption of equilibrium between the bubble and the molten glass. A bubble, which has stayed a sufficiently long time in the molten glass to reach an equilibrium state, is trapped (along with the surrounding glass) in the silica tube and quenched. A mass spectroscopy analysis is then performed on the bubble at room temperature. Knowledge of the mass fractions of N_2 and CO_2 found in the bubble leads to the determination of molar concentrations thanks to the Henry's law. The uncertainties of this measurement are significant but difficult to estimate as mentioned by Kloužek and Němec (2003). The molar concentration of water dissolved in the glass is obtained with an infrared optical spectrometry. The molar concentrations of H_2O, N_2, and CO_2 in the bulk molten glass are given in Table 2.

3. Model of shrinkage or growth of a bubble in molten glass

As indicated in the Introduction, various gaseous species are dissolved in molten glass. Consequently, a bubble dispersed in this glass can be composed of all gaseous species present. A model for a multicomponent bubble with N_g gaseous species is presented here and has already been described in Pigeonneau (2007). After a general description of a bubble's temporal in molten glass, Section 3.1, the model currently used to determine the mass transfer coefficients is presented in Section 3.2. The previous model used for the same purpose is recalled in Section 3.3 and the terminal rise velocity of a bubble is presented in Section 3.4. Finally, the method employed to calculate the molar concentrations of various dissolved species is summarized in Section 3.5.

3.1. Temporal evolution of bubble composition

Due to mass transfer, the number of moles of each species in the bubble changes with time. The time derivative of the number of moles, n_i, of gaseous species i is determined by the relationship

$$\frac{dn_i}{dt} = 2\pi a Sh_i \mathcal{D}_i (C_i^{\infty} - C_i^S), \tag{3}$$

where a is the bubble radius, $\mathcal{D}_i$ the diffusion coefficient and C_i^{∞} the bulk molar concentration of gaseous species i. The quantity, Sh_i, is the Sherwood number which will be presented in detail in the next subsection. The molar concentration on the bubble's surface, C_i^S, is given by Henry's law:

$$C_i^S = L_i P_i^{\beta_i}, \tag{4}$$

where L_i is the solubility coefficient and P_i the partial pressure in the bubble of gaseous species i. The exponent, β_i, is equal to unity for most species but $\frac{1}{2}$ for water since it is chemically dissolved in molten glass (Scholze, 1968; Paul, 1990).

When the number of moles of each species is known, the bubble radius can be determined by solving the implicit equation

$$\frac{3RT\sum_{i=1}^{N_g} n_i}{4\pi a^3} = P_0 + \rho g(H-z) + \frac{2\sigma}{a}, \tag{5}$$

where R is the universal gas constant, T the temperature, P_0 the atmospheric pressure, H the liquid height, σ the surface tension and z the position of the bubble. Eq. (5) represents the equilibrium between the pressure obtained from the ideal gas law and the hydrostatic and Laplace pressures.

3.2. Present model to describe the mass transfer

The Sherwood number, Sh_i, of gaseous species i is defined as the ratio of the mass transfer coefficient with motion to the mass transfer coefficient without motion. This dimensionless number takes into account the main physical phenomena such as diffusion and advection. As presented in the textbooks of Clift et al. (1978) and Sadhal et al. (1997), interface mobility has an important effect on mass transfer.

Chemical reactions can also influence mass transfer. The main conclusion of Pigeonneau (2009) was the need to define a new mass transfer coefficient for gases taking part in oxidation–reduction reactions and a few details will be summarized below. For the other species, the usual Sherwood number is used (Clift et al., 1978; Sadhal et al., 1997).

As in Pigeonneau (2009), the bubble interface is assumed to be fully mobile. Consequently, the Sherwood number, Sh_i, of species not participating in the oxidation–reduction reaction of iron oxide is given by the relationship (Clift et al., 1978)

$$Sh_i = 1 + (1 + 0.564 Pe_i^{2/3})^{3/4}, \tag{6}$$

where the Péclet number, Pe_i, is defined as

$$Pe_i = \frac{2aV_T}{\mathcal{D}_i}. \tag{7}$$

In this last equation, V_T is the terminal rise velocity of the bubble which is detailed in Section 3.4. Eq. (6) behaves as $\sqrt{Pe_i}$ when the Péclet number is large which is a characteristic feature of a fully mobile interface (Levich, 1962).

The oxidation–reduction reaction of iron oxide taking place in molten glass is described by the following relationship (Paul, 1990)

$$Fe^{3+} + \tfrac{1}{2} O^{2-} \rightleftharpoons Fe^{2+} + \tfrac{1}{4} O_2, \tag{8}$$

where Fe^{3+} is the oxidized state and Fe^{2+} the reduced state, O^{2-} the free oxygen ion and O_2 the dioxygen. The equilibrium constant of this last reaction is given by

$$K_{Fe} = \frac{C^{\infty}_{Fe^{2+}} C^{\infty 1/4}_{O_2}}{C^{\infty}_{Fe^{3+}}} \tag{9}$$

in which $C^{\infty}_{Fe^{2+}}$ and $C^{\infty}_{Fe^{3+}}$ are the bulk molar concentrations of Fe^{2+} and Fe^{3+}, respectively, and $C^{\infty}_{O_2}$ the molar concentration of oxygen dissolved in molten glass. The equilibrium constant, K_{Fe} in Eq. (9) is related to concentration which means that K_{Fe} takes into account the activity coefficient of each species occurring in the reaction. The concentration O^{2-} is not taken into account since it is present in large quantities in glass, thus making its activity constant. Finally, it should be noted that from this definition of the equilibrium constant, K_{Fe} is expressed as the fourth root of molar concentration ($mol^{1/4}\,m^{-3/4}$). The equilibrium constant K_{Fe} is expressed as a function of temperature given in Appendix B for soda-lime-silica glass.

As shown in Pigeonneau (2009), this reaction enhances the mass transfer of oxygen. Consequently, the Sherwood number is written with the relationship given above, Eq. (6), but the Péclet number is replaced with the modified version proposed in Pigeonneau (2009), Pe'_{O_2}:

$$Pe'_{O_2} = Pe_{O_2}[1 + \alpha(Sa_{O_2}) N_{Fe}], \tag{10}$$

where $\alpha(Sa_{O_2})$ is

$$\frac{1}{\alpha} = \frac{1}{3.05 Sa_{O_2}^{-0.375}} + \frac{1}{1.28 Sa_{O_2}^{-1}}. \tag{11}$$

The oxygen saturation, Sa_{O_2}, is equal to

$$Sa_{O_2} = \frac{C^{\infty}_{O_2}}{C^S_{O_2}}, \tag{12}$$

where $C^{\infty}_{O_2}$ and $C^S_{O_2}$ are the bulk and surface oxygen concentrations, respectively.

The dimensionless number, N_{Fe}, is defined as follows (Pigeonneau, 2009):

$$N_{Fe} = \frac{C^{\infty}_{Fe^{2+}} (1 - \mathcal{R}^{\infty}) Sa_{O_2}^{1/4}}{16 C^S_{O_2}}, \tag{13}$$

where $\mathcal{R}^{\infty}$ is the reduction state of iron defined by

$$\mathcal{R}^{\infty} = \frac{C^{\infty}_{Fe^{2+}}}{C^{\infty}_{Fe}}. \tag{14}$$

The total iron content in the molten glass, C^{∞}_{Fe}, is given by $C^{\infty}_{Fe^{2+}} + C^{\infty}_{Fe^{3+}}$.

3.3. Previous model to describe mass transfer

Most authors working in glass science use a relationship to compute the Sherwood number under the assumption of a fully immobile interface. Beerkens (2002, 2003), Itoh et al. (1997a, b) and Ramos (1986) take the following relationship:

$$Sh_i = 1 + (1 + Pe_i)^{1/3}, \tag{15}$$

which behaves as $\sqrt[3]{Pe_i}$ for a large Péclet number. This behavior is also used in the work of Němec and Mühlbauer (1980) and Němec and Kloužek (2003).

3.4. Terminal rise velocity

The terminal rise velocity of a bubble, V_T, is defined based on equilibrium between drag and gravity forces applied on it. Assuming a fully mobile interface, the drag force is given by the solution of Hadamard (1911) and Rybczynski (1911). Consequently, the terminal rise velocity is

$$V_T = \frac{ga^2}{3\nu}, \tag{16}$$

where g is the gravity constant. The quantity, ν, is the kinematic viscosity of liquid equal to μ/ρ where μ is the dynamic viscosity and ρ the density.

Eq. (16) has been established for a bubble rising in an infinite medium. However, the experiments presented in the previous section are carried out in a finite domain. Since the bubble rises in a gap only 10 mm wide, wall effects can be important. Therefore, a wall correction is needed and is described briefly in Appendix A. For example, for a bubble with a radius of 2 mm, approximately the maximum size reached in the experiments, the terminal velocity is reduced by 30% compared to the case of an infinite medium. For a 1 mm radius bubble, the reduction is only 13%.

3.5. Determination of molar concentrations in the bulk

To solve Eq. (3), the molar concentration of each dissolved species in the glass bulk is required. For species not taking part in oxidation–reduction reactions, such as N_2, CO_2, and H_2O, the molar concentration is determined thanks to experimental data obtained using the set-up described in the preceding section. For species participating in oxidation–reduction reactions, such as O_2 and SO_2, molar concentrations are determined analytically assuming chemical equilibrium.

Knowing of the reduction state of iron, the molar concentration of O_2 is determined following the relationship (Pigeonneau, 2009):

$$C^{\infty}_{O_2} = \left[\frac{K_{Fe}(1-\mathcal{R}^{\infty})}{\mathcal{R}^{\infty}}\right]^4, \tag{17}$$

where K_{Fe} is the equilibrium constant of the reaction (8), which is a function of temperature, given in Appendix B.

The molar concentration of SO_2 is driven by the equilibrium of the chemical reaction

$$SO_4^{2-} \rightleftharpoons SO_2 + \frac{O_2}{2} + O^{2-}, \tag{18}$$

where the equilibrium constant is

$$K_S = \frac{C^{\infty}_{SO_2}\sqrt{C^{\infty}_{O_2}}}{C^{\infty}_{SO_4^{2-}}}, \tag{19}$$

in which, $C^{\infty}_{SO_2}$ is the molar concentration of SO_2 in the molten glass and $C^{\infty}_{SO_4^{2-}}$ the molar concentration of SO_4^{2-}. As already pointed out for the iron reaction's equilibrium, K_S is related to the concentrations meaning that it takes into account the activity coefficient of each species occurring in the reaction. Moreover, the concentration O^{2-} is not taken into account since it is present in such large quantities in glass: that its activity is constant. Finally, remark that from this definition of the equilibrium constant, K_S is expressed in square root of molar concentration ($mol^{1/2}\,m^{-3/2}$).

Then, knowing the total sulfur content, $C^{\infty}_S = C^{\infty}_{SO_2} + C^{\infty}_{SO_4^{2-}}$, and $C^{\infty}_{O_2}$, $C^{\infty}_{SO_2}$ can be computed by

$$C^{\infty}_{SO_2} = \frac{K_S C^{\infty}_S}{C^{\infty}_{O_2} + K_S}. \tag{20}$$

The total sulfur content is determined by chemical analysis applied on glass samples used in the experiments. The numerical coefficients used to determine K_S are given in Appendix B.

The ordinary differential equations (3) are solved numerically with a fourth-order Runge–Kutta method. The bubble radius is determined using a successive approximation method applied on Eq. (5). The numerical computations are carried out using solubilities, and diffusion coefficients of all species taken from the literature (Beerkens, 2003). Their values are listed in Appendix B along with the dynamic viscosity, density and surface tension.

4. Results and discussion

In this section, the results obtained both experimentally and numerically are presented for the two glass compositions used in the experiments at various temperatures between of 1300 and 1450 °C. We begin by comparing various numerical computations with the experimental results, in Section 4.1. The analysis is focused on the bubble size versus time in Sections 4.2 and 4.3 is devoted to discussing the results.

4.1. Comparison with different numerical solutions

In order to compare the current work against previous modeling efforts, the bubble size versus time obtained with the properties of glass 1 at 1400 °C is shown in Fig. 3. The numerical computations have been performed with three types of model. The first is achieved with the Sherwood number corresponding to a fully immobile interface, Eq. (15), for all species as used by Beerkens (2002, 2003), Itoh et al. (1997a, b), Němec and Mühlbauer (1980) and Němec and Kloužek (2003). For the second calculation, the Sherwood number assuming a fully mobile interface is tested for all species as done by Ramos (1986). Finally, the third computation is carried out using the new developments presented here where the Sherwood number is taken from Eq. (6) for species not occurring in the iron oxidation–reduction reaction. For O_2 species, the modified Péclet number which takes into account the chemical reaction of iron is used.

The circle symbols in Fig. 3 represent results obtained experimentally. As mentioned in Section 2, a bubble size is evaluated by counting the number of pixels, thus, the radius obtained is discrete since a change in size is measurable only when the number of pixels is modified by one unit. This explains the "steps" observed in the experimental data. As a result, the width of the steps represents the order of magnitude of uncertainties.

As clearly shown in Fig. 3, the assumption of a fully immobile interface largely underestimates the mass transfer process. Even if the shrinkage rate is faster with the Sherwood number taken from Eq. (6), the numerical results are still a poor fit to the experimental data. The introduction of a new Sherwood number for oxygen species completely changes the bubble behavior the numerical result obtained with the present model is very close to the experimental data. Consequently, the enhancement of the

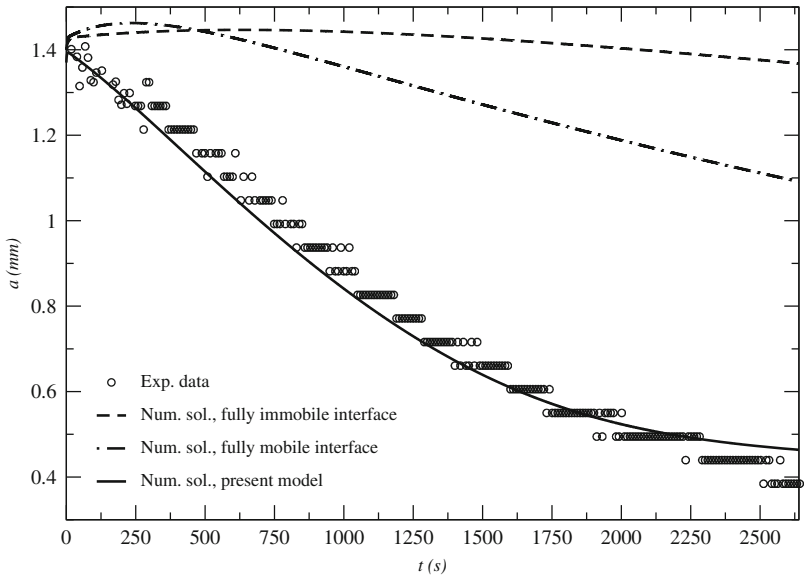

Fig. 3. Temporal evolution of bubble size obtained for the glass 1 (low iron content) at $T = 1400\,^{\circ}C$. Comparison between experimental and numerical results.

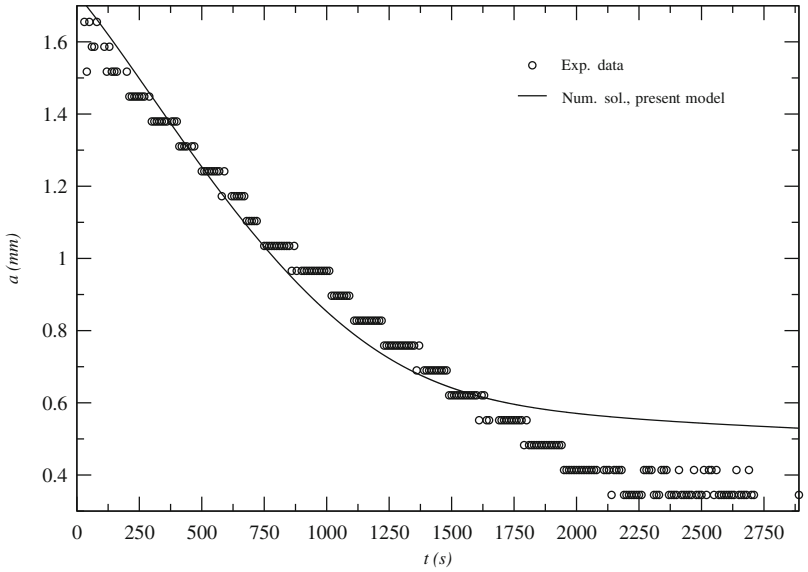

Fig. 4. Bubble size as a function of time for glass 1 at $T = 1450\,^{\circ}C$. Comparison between numerical model with a new mass transfer for O_2 and experimental results.

mass transfer coefficient due to oxidation–reduction is underlined in order to describe the behavior of a bubble dispersed in molten glass.

4.2. Bubble size versus time

In order to verify the relevance of this development, results obtained for the two glass compositions at various temperatures are presented considering only the new model.

The bubble size as a function of time at $T = 1450\,^{\circ}C$ for glass 1 is given in Fig. 4 and it can be seen that there is an adequate fit between experimental and numerical results. As already shown in Fig. 3, two distinct stages are observed: bubble shrinkage followed by a plateau where the bubble size does not change significantly. Remark, however, the bubble size is numerically overestimated.

Bubble radius versus time for glass 2 is given (for two temperatures) in Fig. 5. The numerical results show good agreement with the experimental data and the bubble sizes obtained numerically and experimentally at $T = 1450\,^{\circ}C$ are very close over the time period studied.

4.3. Discussion

The importance of oxidation–reduction on the shrinkage of oxygen bubbles in molten glass has previously been underlined by Greene and Platts (1969) who showed an enhanced shrinkage rate for a glass containing arsenic oxides. The present work has focused on glass containing iron oxides and not arsenic oxides, nevertheless, oxygen dissolution is of the same nature involving diffusion, advection, and reaction. The ability of molten glass to absorb oxygen is related to the quantity of reduced iron. The increase in Sherwood number coupled with the reduced state of iron and total iron content obtained in Pigeonneau (2009) expresses this ability.

The experimentally observed and numerically calculated temporal evolution of bubble size (normalized by its initial value)

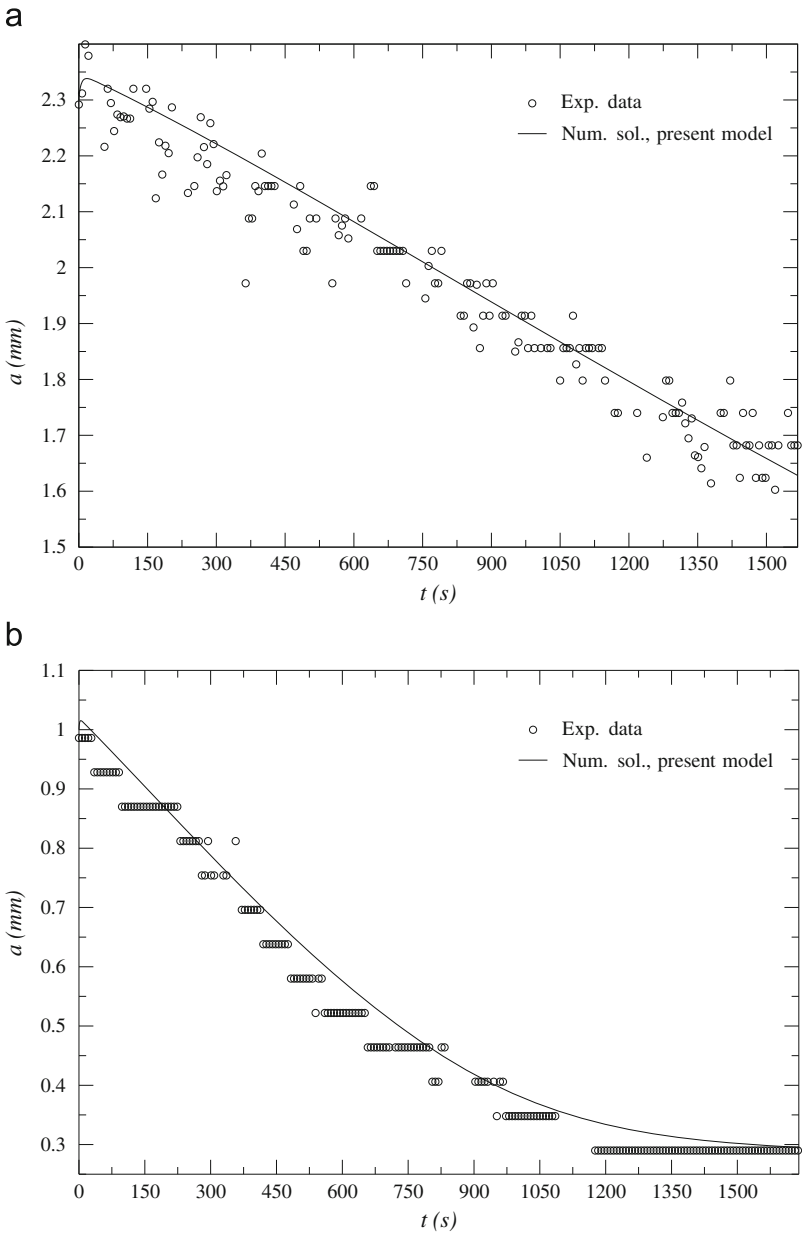

Fig. 5. Bubble size as a function of time for glass 2 at (a) $T = 1300\,^{\circ}C$, (b) $T = 1400\,^{\circ}C$. Comparison between numerical model with a new mass transfer for O_2 and experimental results.

is plotted as a function of time for the two glass compositions at $T = 1400\,^{\circ}C$ in Fig. 6. Even though the temperature is identical, meaning that the diffusion coefficients and dynamic viscosity are equal, the shrinkage rate changes from one glass to another. This trend can be described by the theoretical model used in the present work: the shrinkage rate of an oxygen bubble increases with the ferrous iron content.

The results obtained show a general trend concerning bubble size in molten glass. Each oxygen bubble shrinks during the first stage due to the unsaturated oxygen state of the glass and, therefore, oxygen moves from the bubble towards the melt. As highlighted by experimental observations at high temperatures, a second stage is observed where the bubble size seems to reach a steady-state. This is the consequence of the presence of other gases in the molten glass. Since the bubble initially contains only oxygen, the glass is comparatively over-saturated with other gaseous species (for example CO_2). The system made up of both the bubble and the glass tends towards an equilibrium, where the activities of species on the bubble surface and in the molten glass are equal.

5. Conclusion

A specially designed experiment has been used to determine the size of an oxygen bubble rising in a molten glass while undergoing a mass transfer process. The work has been focused on the role of iron on mass transfer where two glass compositions have been used: one with a low concentration of iron and the second with a larger one. The temporal evolution of a bubble is also described theoretically where the results obtained on mass transfer coefficients for O_2 in Pigeonneau (2009) have been applied.

Numerical simulations have been carried out using various mass transfer coefficients found in the literature. A comparison with the experimental results shows the relevance of the iron

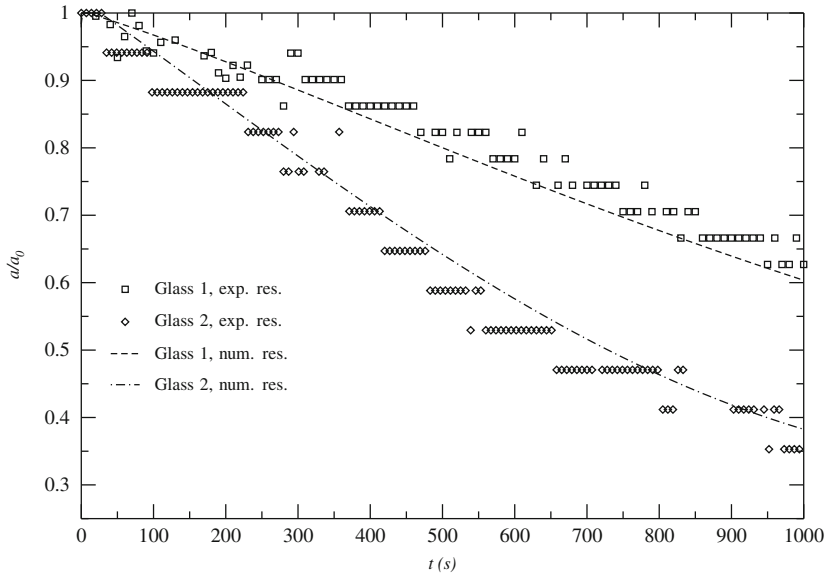

Fig. 6. Bubble size divided by its initial value as a function of time for the two glasses at $T = 1400\ ^{\circ}C$. Comparison between numerical model with mass transfer and experimental results.

oxidation–reduction reaction on O_2 mass transfer in the description of shrinkage for a pure oxygen bubble using Sherwood number proposed by Pigeonneau (2009) gives a good estimation of the shrinkage rate.

A full description of a bubble in molten glass requires a novel for gaseous species taking part in chemical reactions and another for those which do not. The mass transfer coefficient for non-reactive gaseous species can be taken from textbooks such as Clift et al. (1978) and Sadhal et al. (1997).

By comparing the two glass compositions studied in the current work, it was seen that the shrinkage rate of a pure oxygen bubble increases with reduced iron content in the molten glass. One critical conclusion for glass melting is that the oxidation–reduction of iron at high temperature is mainly driven by oxygen transfer.

Although this work has focused on shrinkage, the developments proposed are also applicable for bubble growth. However, the conclusions given here can be used as a guide for the study of fining processes in glass compositions where the iron content varies.

Notation

a	bubble radius, m
a_0	initial bubble radius, m
A_{Fe}	coefficient in the equilibrium constant of the iron oxidation–reduction reaction, $mol^{1/4}\,m^{-3/4}$
$A_i^{(D)}$	coefficient in the diffusion coefficient of gaseous species i, $m^2\,s^{-1}$
$A_i^{(S)}$	coefficient in the solubility of gaseous species i, $mol\,m^{-3}\,Pa^{-\beta_i}$
A_S	coefficient in the equilibrium constant of the sulfur oxidation–reduction reaction, $mol^{1/2}\,m^{-3/2}$
b	distance between the center of the particle and the right wall, m
B_{Fe}	coefficient in the equilibrium constant of the iron oxidation–reduction reaction, K
$B_i^{(D)}$	coefficient in the diffusion coefficient of gaseous species i, K
$B_i^{(S)}$	coefficient in the solubility of gaseous species i, K
B_S	coefficient in the equilibrium constant of the sulfur oxidation–reduction reaction, K
B_{VFT}	coefficient in the dynamic viscosity of molten glass following the Vogel–Fulcher–Tamman formula, K
c	distance between the center of the particle and the left wall, m
C_{Fe}^{∞}	total molar concentration of iron in the molten glass, $mol\,m^{-3}$
$C_{Fe^{2+}}^{\infty}$	bulk molar concentration of reduced iron in the molten glass, $mol\,m^{-3}$
$C_{Fe^{3+}}^{\infty}$	bulk molar concentration of oxidized iron in the molten glass, $mol\,m^{-3}$
C_i^{∞}	bulk molar concentration of gaseous species i, $mol\,m^{-3}$
C_i^{S}	molar concentration of gaseous species i on the bubble surface, $mol\,m^{-3}$
$C_{O_2}^{\infty}$	bulk molar concentration of oxygen, $mol\,m^{-3}$
$C_{O_2}^{S}$	molar concentration of oxygen on the bubble surface, $mol\,m^{-3}$
C_S^{∞}	total molar concentration of sulfur in the molten glass, $mol\,m^{-3}$
$C_{SO_2}^{\infty}$	bulk molar concentration of sulfur dioxide, $mol\,m^{-3}$
$C_{SO_4^{2-}}^{\infty}$	molar concentration of SO_4^{2-} in the molten glass, $mol\,m^{-3}$
$\mathcal{D}_i$	diffusion coefficient of gaseous species i in the molten glass, $m^2\,s^{-1}$
$\mathcal{D}_{SiO_2}$	diffusion coefficient of silica in the molten glass, $m^2\,s^{-1}$
F_d	drag force on a particle, N
g	gravity constant, $m\,s^{-2}$
H	liquid height, m
K_{Fe}	equilibrium constant of the iron oxidation–reduction reaction, $mol^{1/4}\,m^{-3/4}$
K_S	equilibrium constant of the sulfate oxidation–reduction reaction, $mol^{1/2}\,m^{-3/2}$
k_w	wall correction factor, dimensionless
L_i	solubility coefficient of gaseous species i, $mol\,m^{-3}\,Pa^{-\beta_i}$
$\dot{m}_{SiO_2}$	rate of mass of silica from the crucible to the molten glass, $kg\,s^{-1}$
n_i	number of moles in the bubble of gaseous species i, mol
N_g	total number of gaseous species, dimensionless

N_{Fe} dimensionless number related to the oxidation–reduction reaction of iron oxides, dimensionless
P_i partial pressure in the bubble of gaseous species i, Pa
P_0 atmospheric pressure, Pa
Pe_i Péclet number related to the gaseous species i, dimensionless
Pe_{O_2} Péclet number related to oxygen, dimensionless
Pe'_{O_2} modified Péclet number related to oxygen taking into account the iron oxidation–reduction reaction, dimensionless
R universal gas constant, $J\,K^{-1}\,mol^{-1}$
$\mathcal{R}^{\infty}$ iron reduction state of molten glass, dimensionless
s relative position of the particle between two parallel wall, dimensionless
S crucible surface wetted by the molten glass, m^2
Sh_i Sherwood number of gaseous species i, dimensionless
Sa_{O_2} saturation of oxygen defined at P_0, dimensionless
t time, s
T temperature, K
T_{VFT} coefficient in the dynamic viscosity of molten glass following the Vogel–Fulcher–Tamman formula, K
V velocity of a particle, $m\,s^{-1}$
V_T terminal rise velocity of the bubble, $m\,s^{-1}$
z local position of the bubble center, m

Greek letters

α function of oxygen saturation for the computation of the modified Péclet number, dimensionless
β_i characteristic exponent of gaseous species i in the Henry's law, dimensionless
δ diffusion layer of silica from the crucible to the molten glass, m
μ dynamic viscosity of liquid, Pa s
μ_{VFT} coefficient in the dynamic viscosity of molten glass following the Vogel–Fulcher–Tamman formula, Pa s
ν kinematic viscosity of liquid, equal to μ/ρ, $m^2\,s^{-1}$
ρ liquid density, $kg\,m^{-3}$
$\Delta\rho_{SiO_2}$ difference of partial density between the pure silica and the glass, $kg\,m^{-3}$
σ surface tension, $N\,m^{-1}$

Acknowledgements

The authors would like to thank A.-M. Billet, O. Masbernat of the Laboratoire de Génie Chimique of Toulouse (France) and E. Climent, and V. Sarrot of the Institut de Mécanique des Fluides of Toulouse (France) for many fruitful discussions concerning bubble physics in reactive liquids. Our acknowledgments are also addressed to E. Grignon who performed part of the experimental study during his internship at Saint-Gobain Recherche (France). We would like to thank E. Søndergård and N. McDonald for their help in the preparation of this paper.

Appendix A. Terminal velocity in a finite media

The experiment to follow the bubble is done in a finite domain. Consequently, as the bubble's volume is significant compared to the crucible's dimensions, the hydrodynamic interaction between the bubble and the walls is partially important. In order to estimate the modified drag force on the bubble in the crucible, we consider only the interactions with those vertical walls which are the closest to the bubble.

In order to take the wall effect into account, the drag force has been corrected using the results of Keh and Chen (2001) who proposed an exact solution of the Stokes equations for a spherical inclusion moving with constant velocity between two infinite parallel walls. The drag force depends on the ratio between the radius of the particle to the distance from the particle to the right wall and the position of the particle between the two walls as shown in Fig. 7. The radius of the particle is a while b and c represent the position of the particle center from the right and the left walls, respectively.

For a bubble moving parallel to the walls with a velocity V, the drag force, F_d, can be written as

$$F_d = 4\pi\mu a V k_w(a/b, s). \tag{21}$$

In this last equation, the wall correction factor, k_w, is always greater than unity. This coefficient is a function of the ratio a/b and s which is defined as follows:

$$s = \frac{b}{b+c}. \tag{22}$$

For a gaseous inclusion localized in the middle of the two walls, $s = \frac{1}{2}$ while k_w versus a/b is represented in Fig. 8.

If the drag force given by (21) is used, the terminal velocity can be modified as follows:

$$V_T = \frac{ga^2}{3\nu k_w}. \tag{23}$$

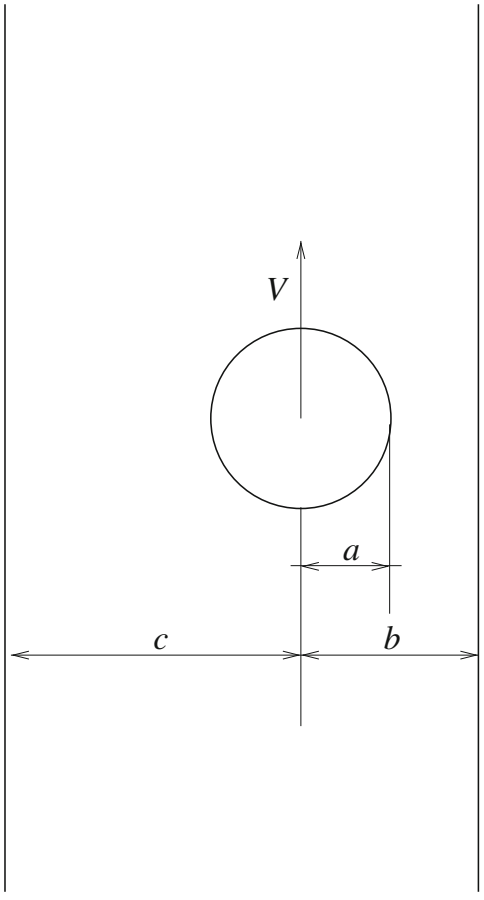

Fig. 7. Geometric sketch of a particle between two parallel walls.

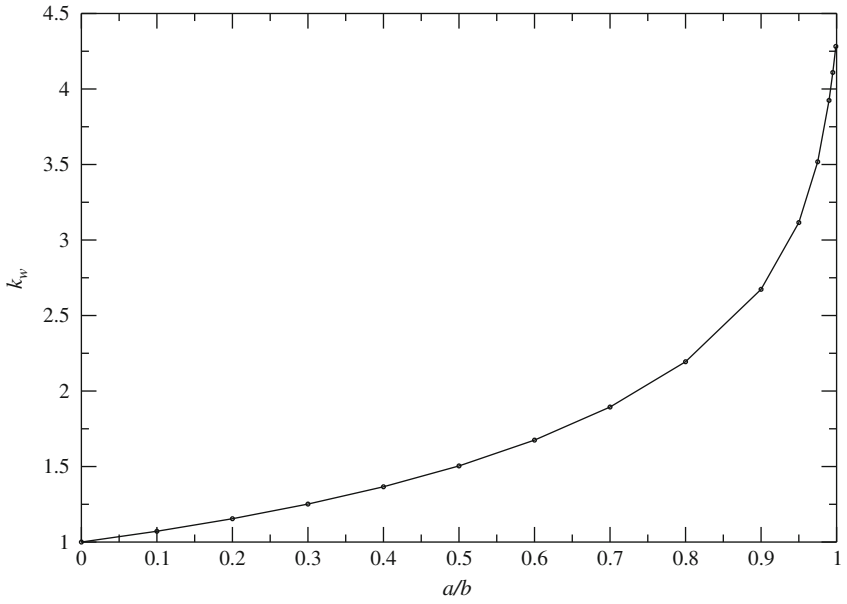

Fig. 8. Wall correction factor versus a/b for a bubble in the middle of the two walls, $s=\frac{1}{2}$. The data are taken from Keh and Chen (2001).

Table 3
Numerical values of $A_j^{(S)}$ and $B_j^{(S)}$ used to determine the solubilities of dissolved gaseous species in soda-lime-silica glass taken from Beerkens (2003).

Gas	O_2	SO_2	CO_2	N_2	H_2O
$A_j^{(S)}$	1.37×10^{-4}	6.44×10^{-7}	5.6×10^{-7}	1.1×10^{-5}	6.8×10^{-1}
$B_j^{(S)}$	-6633	7860	3120	-6633	-613

Table 4
Numerical values of $A_j^{(D)}$ and $B_j^{(D)}$ used to determine the diffusion coefficients of dissolved gaseous species in soda-lime-silica glass taken from Beerkens (2003).

Gas	O_2	SO_2	CO_2	N_2	H_2O
$A_j^{(D)}$	3×10^{-3}	4.45×10^{-7}	1.92×10^{-5}	4.3×10^{-5}	1.2×10^{-5}
$B_j^{(D)}$	$-26\,580$	$-15\,360$	$-21\,516$	$-19\,364$	$-18\,320$

For this computation, the bubble is assumed to rise in the middle of the crucible. The coefficient k_w is estimated from the results shown in Fig. 8.

Appendix B. Physical and chemical properties of soda-lime-silica glass

Numerical simulations have been carried out on the soda-lime-silica glass compositions given in Table 1. The aim of this appendix is to list the physical and chemical properties of these glasses. It is possible to obtain further details on the nature and the properties of glass in Paul (1990) and Scholze (1990).

The dynamic viscosity, μ, is defined by the Vogel–Fulcher–Tamman formula (Scholze, 1990):

$$\mu=\mu_{\mathrm{VFT}}\exp\left(\frac{B_{\mathrm{VFT}}}{T-T_{\mathrm{VFT}}}\right), \tag{24}$$

where μ_{VFT}, B_{VFT}, and T_{VFT} are

$$\mu_{\mathrm{VFT}}=1.95\times10^{-3}\ \mathrm{Pa\,s}, \tag{25a}$$

$$B_{\mathrm{VFT}}=9855\ \mathrm{K}, \tag{25b}$$

$$T_{\mathrm{VFT}}=539\ \mathrm{K}. \tag{25c}$$

The glass density, ρ, above the glass transition temperature is assumed to be constant and equal to $2340\ \mathrm{kg\,m^{-3}}$ for our numerical computations. The surface tension used in Section 4 is taken to be equal to $0.36\ \mathrm{N\,m^{-1}}$.

The equilibrium constant of the oxidation–reduction reaction of iron oxide, Eq. (8) is taken from Beerkens (2003) where K_{Fe} given by Eq. (9) is related to the molar concentration of iron oxide and oxygen. The quantity K_{Fe} is written as follows:

$$K_{\mathrm{Fe}}=A_{\mathrm{Fe}}\exp\left(-\frac{B_{\mathrm{Fe}}}{T}\right), \tag{26}$$

where A_{Fe} and B_{Fe} are given by

$$A_{\mathrm{Fe}}=2359.26\ \mathrm{mol^{1/4}\,m^{-3/4}}, \tag{27a}$$

$$B_{\mathrm{Fe}}=16958.66\ \mathrm{K}. \tag{27b}$$

For the reaction of sulfate following Eq. (18), the equilibrium constant, K_{S}, is given by

$$K_{\mathrm{S}}=A_{\mathrm{S}}\exp\left(-\frac{B_{\mathrm{S}}}{T}\right), \tag{28}$$

where A_{S} and B_{S} are

$$A_{\mathrm{S}}=1.21\times10^{5}\ \mathrm{mol^{1/2}\,m^{-3/2}}, \tag{29a}$$

$$B_S = 2.8 \times 10^4\ \mathrm{K}. \tag{29b}$$

Measuring solubility and diffusion coefficients is a difficult task in glass science and numerous studies have been devoted specifically to this work. Beerkens (2003) presented a compilation of solubilities and diffusion coefficients for many of the species dissolved in a classical soda-lime-silica glass based on an extensive literature review. These data are used in the present work.

The solubilities used in Section 4 are defined by the formula

$$L_j = A_j^{(S)} \exp\left(\frac{B_j^{(S)}}{T}\right). \tag{30}$$

The solubility is given in $\mathrm{mol\,m^{-3}\,Pa^{-1}}$ for most species and in $\mathrm{mol\,m^{-3}\,Pa^{-1/2}}$ for water vapor. The coefficients $A_j^{(S)}$ and $B_j^{(S)}$ for gases discussed in this work are listed in Table 3.

The diffusion coefficients of dissolved species are given in $\mathrm{m^2\,s^{-1}}$ and expressed as follows:

$$\mathcal{D}_j = A_j^{(D)} \exp\left(\frac{B_j^{(D)}}{T}\right), \tag{31}$$

where the coefficients $A_j^{(D)}$ and $B_j^{(D)}$ are summarized in Table 4.

References

Beerkens, R.G.C., 2002. Modeling of the melting process in industrial glass furnaces. In: Mathematical Simulation in Glass Technology. Springer, Berlin, pp. 17–73 (Chapter 2.1).

Beerkens, R.G.C., 2003. Analysis of advanced and fast fining processes for glass melts. In: Advances in Fusion and Processing of Glass III. American Ceramic Society, New York, pp. 3–24.

Beerkens, R.G.C., de Waal, H., 1990. Mechanism of oxygen diffusion in glassmelts containing variable-valence ions. J. Am. Ceram. Soc. 73, 1857–1861.

Cable, M., Martlew, D., 1984. The effective binary diffusivity of silica in sodium silicate melts: a review and recommendation. Glass Technol. 25, 270–276.

Clift, R., Grace, J.R., Weber, M.E., 1978. Bubbles Drops and Particles. Academic Press, New York.

Doremus, R.H., 1960. Diffusion of oxygen from contracting bubbles in molten glass. J. Am. Ceram. Soc. 43, 655–661.

Greene, C.H., Gaffney, R.F., 1959. Apparatus for measuring the rate of absorption of a bubble in glass. J. Am. Ceram. Soc. 42, 271–275.

Greene, C.H., Kitano, I., 1959. Rate of solution of oxygen bubbles in commercial glasses. Glastech. Ber. 32K (V), 44–48.

Greene, C.H., Lee, H.A., 1965. Effect of As_2O_3 and $NaNO_3$ on the solution of O_2 in soda-lime glass. J. Am. Ceram. Soc. 48, 528–533.

Greene, C.H., Platts, D.R., 1969. Behavior of bubbles of oxygen and sulfur dioxide in soda-lime glass. J. Am. Ceram. Soc. 52, 106–109.

Hadamard, J., 1911. Mouvement permanent lent d'une sphère liquide et visqueuse dans un liquide visqueux. C. R. Acad. Sci. Paris 152, 1735–1738.

Hirashima, H., Yoshida, T., Brückner, R., 1988. Redox equilibria and constitution of polyvalent ions in oxide melts and glasses. Glastech. Ber. 61, 283–292.

Itoh, E., Yoshikawa, H., Kawase, Y., 1997a. Modelling of bubble removal from glassmelts at fining temperatures. Glastechn. Ber. 70, 8–16.

Itoh, E., Yoshikawa, H., Miura, H., Kawase, Y., 1997b. A quasi-stationary model for bubble behaviour in glass melts with refining reactions. Glass Technol. 38, 134–140.

Keh, H.J., Chen, P.Y., 2001. Slow motion of a droplet between two parallel plane walls. Chem. Eng. Sci. 56, 6863–6871.

Kloužek, J., Němec, L., 2003. Modelling of glass refining kinetics. Part 2: bubble distribution models and methods of measurement of refining properties. Ceramics 47, 155–161.

Levich, V.G., 1962. Physicochemical Hydrodynamics. Prentice-Hall, Englewood Cliffs, NJ.

Mysen, B.O., Richet, P., 2005. Silicate Glasses and Melts: Properties and Structure. Elsevier, Amsterdam.

Němec, L., 1980a. The behaviour of bubbles in glass melts. Part 1: bubble size controlled by diffusion. Glass Technol. 21, 134–138.

Němec, L., 1980b. The behaviour of bubbles in glass melts. Part 2: bubble size controlled by diffusion and chemical reaction. Glass Technol. 21, 139–144.

Němec, L., Kloužek, J., 2003. Modelling of glass refining kinetics. Part 1: single bubbles. Ceramics 47, 81–87.

Němec, L., Mühlbauer, M., 1980. Mathematical model of bubble behaviour during refining of glass melts. J. Non-Cryst. Solids 38/39, 593–598.

Paul, A., 1990. Chemistry of Glasses. Chapman & Hall, London.

Pigeonneau, F., 2007. Coupled modelling of redox reactions and glass melt fining processes. Glass Technol. Eur. J. Glass Sci. Technol. A 48 (2), 66–72.

Pigeonneau, F., 2009. Mass transfer of rising bubble in molten glass with instantaneous oxidation–reduction reaction. Chem. Eng. Sci. 64, 3120–3129.

Ramos, J.I., 1986. Behavior of multicomponent gas bubbles in glass melts. J. Am. Ceram. Soc. 69, 149–154.

Readey, D.W., Cooper, A.R., 1966. Molecular diffusion with a moving boundary and spherical symmetry. Chem. Eng. Sci. 21, 917–922.

Rybczynski, W., 1911. Uber die fortschreitende bewegun einer flussingen kugel in einem zaben medium. Bull. de l'Acad. des Sci. de Cracovie, 40–46.

Sadhal, S.S., Ayyaswamy, P.S., Chung, J.N., 1997. Transport Phenomena with Drops and Bubbles. Springer, New York.

Scholze, H., 1968. Gases in glass. In: Proceedings of the 8th International Congres on Glass, Londres.

Scholze, H., 1990. Glass. Nature, Structures and Properties. Springer, Berlin.

Shelby, J.E., 1997. Introduction to Glass Science and Technology. The Royal Society of Chemistry, Cambridge.

Subramanian, R.S., Chi, B., 1980. Bubble dissolution with chemical reaction. Chem. Eng. Sci. 35, 2185–2194.

Yoshikawa, H., Kawase, Y., 1997. Significance of redox reactions in glass refining processes. Glass Sci. Technol. 70, 31–39.

Author's personal copy

International Journal of Heat and Mass Transfer 54 (2011) 1448–1455

Contents lists available at ScienceDirect

International Journal of Heat and Mass Transfer

journal homepage: www.elsevier.com/locate/ijhmt

Mechanism of mass transfer between a bubble initially composed of oxygen and molten glass

F. Pigeonneau *

Surface du Verre et Interfaces, UMR 125 Unité mixte CNRS/Saint-Gobain, 39 quai Lucien Lefranc, BP 135, 93303 Aubervilliers Cedex, France

ARTICLE INFO

Article history:
Available online 21 December 2010

Keywords:
Bubble
Chemical processes
Glass science
Mass transfer
Multiphase reactions
Dimension analysis

ABSTRACT

The bubble removal from molten glass is an important problem in glass melting process. In this paper, the mass transfer undergone by a bubble rising in molten glass is studied, the multicomponent feature being taken into account. In order to identify the time scaling of the bubble shrinkage, a careful dimension analysis is performed.

A characteristic time to describe the mass transfer for each gaseous species in a bubble is introduced with an alternative expression of the permeability. This new permeability has the dimension of a diffusion coefficient, which is useful to compare to other transport phenomena. From the physical data known for soda–lime–silica glasses, a fast equilibrium state of water between a bubble and molten glass is determined. The opposite situation is observed for nitrogen.

Experimental results giving the bubble size versus time with a dimensionless form leads to a good match at short time whatever the glass nature and the temperature. Finally, a simple equation to determine bubble size as a function of time is given, based on the dimension analysis previously established.
© 2010 Elsevier Ltd. All rights reserved.

1. Introduction

The dispersion of gaseous inclusions in a continuous liquid phase is an important problem in handling materials such as molten glass. During glass melting, bubble removal, achieved by buoyancy forces, is necessary but difficult due to the high dynamic viscosity even at high temperature: it is larger than 10 Pa·s at 1400 °C. Therefore, "fining" agents are added in raw materials, releasing gases at high temperature, Shelby [28]. The bubbles grow due to the migration of the "fining" gases from glass into the bubbles. Consequently, the mass transfer process concerning bubbles dispersed in a molten glass must be carefully studied in order to design new efficient furnaces.

The mass transfer around a bubble or a drop has been studied for many years and the state of knowledge can been found in the textbook of Sadhal et al. [26]. In the framework of molten glass, Shelby [28] summed up the key points. He underlined that apart from carbon dioxide coming from the decomposition of raw materials and oxygen, the presence of other dissolved gases in molten glass such as water vapor, sulfur dioxide and nitrogen is an important feature.

As underlined by Mysen and Richet [14], iron is a major polyvalent metal found in natural and industrial glasses. The oxidation–reduction state of iron is carefully controlled in the glass melting process because of its important role in glass color, see [11]. The bubble behavior in molten glass have been studying for many years with the first contributions by the group of Greene [7–10]. They developed an experimental device allowing the stabilization and the observation of a bubble. Later, Němec [15,16] developed an experimental method where a single bubble is released in a transparent crucible containing molten glass and its size is recorded *via* a camera. The aim of this experimental set-up is to follow a bubble undergoing a motion relative to molten glass. More recently, Kloužek and Němec [12] improved the experiment by transferring the bubble from the top to the bottom of the crucible when it approaches the free surface to increase the interaction time between the bubble and molten glass.

Doremus [6] provided one of the first theoretical contributions about the shrinkage of a bubble in molten glass. Readey and Cooper [25] studied, *via* a finite difference method, the mass transfer taking into account a pure diffusion process with the temporal evolution of the bubble's radius introduced into a numerical model. The modeling of multicomponent bubbles in molten glass had been done by Ramos [24] or more recently by Němec and Kloužek [17] and was summed up by Beerkens [1]. In order to take into account the effect of chemical reactions on the oxygen resorption pointed out by Greene and Lee [9], Subramanian and Chi [29] developed a model where a first-order irreversible reaction was introduced. The role of oxidation–reduction reactions of polyvalent cations had been studied by Yoshikawa and Kawase [30] for an immobile bubble. The oxidation–reduction reaction was assumed to be very fast but limited by the diffusion of oxygen according to the first

* Tel.: +33 1 48 39 59 99; fax: +33 1 48 39 55 62.
E-mail address: franck.pigeonneau@saint-gobain.com

0017-9310/$ - see front matter © 2010 Elsevier Ltd. All rights reserved.
doi:10.1016/j.ijheatmasstransfer.2010.11.049

Author's personal copy

Nomenclature

Roman symbols

a	bubble radius (m)
a_0	initial bubble radius (m)
$A_i^{(D)}$	coefficient in the diffusion coefficient of gaseous species i ($m^2\ s^{-1}$)
$B_i^{(D)}$	coefficient in the diffusion coefficient of gaseous species i (K)
$A_i^{(S)}$	coefficient in the solubility of gaseous species i ($mol\ m^{-3}\ Pa^{-\beta_i}$)
$B_i^{(S)}$	coefficient in the solubility of gaseous species i (K)
$C^{\infty}_{Fe^{2+}}$	molar concentration of reduced iron in molten glass ($mol\ m^{-3}$)
$C^{\infty}_{Fe^{3+}}$	molar concentration of oxidized iron in molten glass ($mol\ m^{-3}$)
C_i^{∞}	bulk molar concentration of gaseous species i($mol\ m^{-3}$)
$C^{\infty}_{O_2}$	bulk molar concentration of O_2($mol\ m^{-3}$)
C_i^S	molar concentration of gaseous species i on the bubble surface ($mol\ m^{-3}$)
$\mathscr{D}_i$	diffusion coefficient of gaseous species i in molten glass ($m^2\ s^{-1}$)
g	gravity constant ($m\ s^{-2}$)
H	liquid height (m)
K_{Fe}	equilibrium constant of the iron oxidation–reduction reaction ($mol^{1/4}\ m^{-3/4}$)
L_i	solubility coefficient of gaseous species i($mol\ m^{-3}\ Pa^{-\beta_i}$)
n_i	number of moles in the bubble of gaseous species i (mol)
N_{Fe}	Dimensionless number related to the oxidation–reduction reaction of iron oxides (–)
N_g	total number of gaseous species (–)
N_h	dimensionless number defined as $\rho gH/P_0$ (–)
N_σ	dimensionless number defined as $2\sigma/(P_0 a_0)$ (–)
P_i	partial pressure in the bubble of gaseous species i (Pa)
P_0	atmospheric pressure (Pa)
Pe_i	Péclet number related to the gaseous species i (–)
Pe_{O_2}	Péclet number related to O_2 (–)
Pe'_{O_2}	modified Péclet number related to O_2 taking into account the iron oxidation–reduction reaction (–)
R	universal gas constant ($J\ K^{-1}\ mol^{-1}$)
$\mathscr{R}^{\infty}$	iron reduction state of molten glass (–)
$Sa_{i,0}$	saturation of gaseous species i defined at P_0 (–)
$Sa_{H_2O,0}$	saturation of water defined at P_0 (–)
Sa_{O_2}	saturation of oxygen defined at the partial pressure P_{O_2} (–)
$Sa_{O_2,0}$	saturation of oxygen defined at P_0 (–)
$Sa_{SO_2,0}$	saturation of sulfur dioxide defined at P_0 (–)
Sh_i	Sherwood number of gaseous species i (–)
$\overline{Sh}_i$	ratio of the Sherwood number of gaseous species i for a bubble size a divided by the Sherwood number of gaseous species i for the initial bubble size a_0 (–)
t	time (s)
$\bar{t}$	reduced time (–)
T	temperature (K)
V_T	terminal rising velocity of the bubble ($m\ s^{-1}$)
x_i	molar fraction of gaseous species i in the bubble (–)
x_{H_2O}	molar fraction of water in the bubble (–)
z	local position of the bubble center (m)
$\bar{z}$	normalized local position of the bubble center (–)

Greek symbols

α	function of oxygen saturation Sa_{O_2} for the computation of the modified Péclet number (–)
β_i	characteristic exponent of gaseous species i in the Henry's law (–)
μ	dynamic viscosity of liquid (Pa s)
ν	kinematic viscosity of liquid, equal to μ/ρ ($m^2\ s^{-1}$)
ρ	liquid density ($kg\ m^{-3}$)
σ	surface tension ($N\ m^{-1}$)
τ	characteristic time of mass transfer (s)
τ_i	characteristic time of mass transfer of gaseous species i (s)
$\bar{\tau}_i$	reduced characteristic time of mass transfer of gaseous species i defined as τ_i/τ_{O_2} (–)
τ_{O_2}	characteristic time of mass transfer of oxygen (s)
τ_{Sh,O_2}	characteristic time of shrinkage of an oxygen bubble (s)
$\bar{\tau}_{SO_2}$	reduced characteristic time of mass transfer of SO_2 defined as τ_{SO_2}/τ_{O_2} (–)

developments of Beerkens and de Waal [3]. It was pointed out by Yoshikawa and Kawase [30] that the bubble growth is enhanced by the oxidation–reduction reaction. The chemical coupling between the two phases had been recently studied by Pilon et al. [23] where a population balance equation is used. Recently, the influence of oxidation–reduction reaction on mass transfer around a rising bubble in molten glass had been studied by Pigeonneau [21], and Pigeonneau et al. [22]. It was pointed out both experimentally and numerically that when the iron content increases the mass transfer of bubble is enhanced.

In spite of these many contributions, the role played by the various gases on the bubble size is seldom studied. Moreover, even if numerical simulations are applied to describe bubbles dispersed in molten glass, a scaling analysis is missing. From the point of view of the industrial process, it is very important to know the order of magnitude of shrinkage or growth rate of bubbles dispersed in a furnace as a function of the glass nature and the composition of each bubble. Therefore, the purpose of this article is to find the time scale of the mass transfer as a function of various species and glass nature. In order to describe the shrinkage of a bubble initially composed of 100% of oxygen, a dimension analysis is proposed. The work will be focused on soda–lime–silica glasses with two iron contents.

The model describing the temporal evolution of a bubble in molten glass is briefly recalled in Section 2. The dimension analysis is done in Section 3. Finally, a conclusion is given in Section 4. Appendix A presents the physical and chemical properties taken from the literature and used in this work.

2. Statement of problem

As mentioned above, a model for a multicomponent bubble with N_g gaseous species has already been described in detail in [20,22] and will be briefly recalled below.

2.1. Temporal evolution of bubble composition

The bubble radius, a, is determined by solving the implicit equation

$$\frac{3RT\sum_{i=1}^{N_g} n_i}{4\pi a^3} = P_0 + \rho g(H-z) + \frac{2\sigma}{a}, \tag{1}$$

where R is the universal gas constant, T the temperature, n_i the number of moles of gaseous species i, P_0 the atmospheric pressure, ρ the glass density, g the gravity, H the liquid height, z the local

Author's personal copy

position of the bubble and σ the surface tension. In this last equation, each gaseous species is assigned by the index i varying from 1 to N_g.

Eq. (1) represents the equilibrium between the pressure given by the ideal gas law and the pressure obtained from the summation of atmospheric, hydrostatic and Laplace pressures. In order to solve Eq. (1), the number of moles of each species and the local position, z must be determined.

The quantity n_i is evaluated by the following ordinary differential equation

$$\frac{dn_i}{dt} = 2\pi a Sh_i \mathscr{D}_i \left(C_i^{\infty} - C_i^{S}\right), \tag{2}$$

corresponding to the mass balance between the bubble and its surrounding. In Eq. (2), $\mathscr{D}_i$ is the diffusion coefficient, Sh_i the Sherwood number described below, C_i^{∞} the bulk molar concentration of gaseous species i. The molar concentration on the bubble surface, C_i^S, is given by Henry's law:

$$C_i^S = L_i P_i^{\beta_i}, \tag{3}$$

where L_i is the solubility coefficient, P_i the partial pressure in the bubble of species i. The exponent, β_i, is equal to unity for most species, but is 1/2 for water since it is chemically dissolved in molten glass [19].

The local position of the bubble is determined by

$$\frac{dz}{dt} = V_T, \tag{4}$$

with molten glass assumed to be static. As in [21], the bubble interface in molten glass is assumed fully mobile. Consequently, the terminal rising velocity of the bubble, V_T, is given for a "clean bubble" [5,26] by the relationship

$$V_T = \frac{ga^2}{3\nu}, \tag{5}$$

in which, ν is the kinematic viscosity defined as the ratio μ/ρ where μ is the dynamic viscosity of the liquid.

2.2. Mass transfer coefficients

The Sherwood number of gaseous species i,Sh_i in Eq. (2), represents the ratio of the mass transfer with diffusion and advection to the mass transfer without relative motion between the bubble and molten glass. As reported in classical textbooks of Clift et al. [5], and Sadhal et al. [26], the interface mobility plays an important role in mass transfer.

Chemical reactions can be also involved in the mass transfer process. The main conclusion of [21] was the need to define a new mass transfer coefficient for O_2 taking into account in the oxidation–reduction reaction of iron oxides defined by [19]

$$Fe^{3+} + \frac{1}{2}O^{2-} \rightleftharpoons Fe^{2+} + \frac{1}{4}O_2, \tag{6}$$

where, Fe^{3+} is the oxidized state and Fe^{2+} the reduced state, O^{2-} the free oxygen ion and O_2 the dioxygen.

2.2.1. Sherwood number without reaction

For the other species, the usual Sherwood number is used, [5,26]. The Sherwood number of species not participating in the oxidation–reduction reaction of iron oxides and for a fully mobile interface is given by the relationship [5]

$$Sh_i = 1 + \left(1 + 0.564 Pe_i^{2/3}\right)^{3/4}, \tag{7}$$

where the Péclet number, Pe_i, is defined as

$$Pe_i = \frac{2aV_T}{\mathscr{D}_i}. \tag{8}$$

2.2.2. Sherwood number with reaction

The reaction (6) enhances the mass transfer of oxygen where the Sherwood number for O_2 have been determined in [21] under assumptions of instantaneous chemical reaction limited by the diffusion of oxygen. As it has been pointed out in [21], the Sherwood number can be written with the same relationship (7) but the Péclet number is replaced by the modified version, Pe'_{O_2}, given by:

$$Pe'_{O_2} = Pe_{O_2}[1 + \alpha(Sa_{O_2})N_{Fe}], \tag{9}$$

where $\alpha(Sa_{O_2})$ is defined by

$$\frac{1}{\alpha} = \frac{1}{3.05 Sa_{O_2}^{-0.375}} + \frac{1}{1.28 Sa_{O_2}^{-1}}. \tag{10}$$

The oxygen saturation, Sa_{O_2}, is equal to

$$Sa_{O_2} = \frac{C_{O_2}^{\infty}}{C_{O_2}^{S}}, \tag{11}$$

where $C_{O_2}^{\infty}$, and $C_{O_2}^{S}$ are the bulk and surface oxygen concentrations, respectively.

The dimensionless number, N_{Fe}, is defined as follows

$$N_{Fe} = \frac{C_{Fe^{2+}}^{\infty}(1 - \mathscr{R}^{\infty})Sa_{O_2}^{1/4}}{16 C_{O_2}^{S}}, \tag{12}$$

where $\mathscr{R}^{\infty}$ is the reduction state of iron defined by

$$\mathscr{R}^{\infty} = \frac{C_{Fe^{2+}}^{\infty}}{C_{Fe^{2+}}^{\infty} + C_{Fe^{3+}}^{\infty}}. \tag{13}$$

In these two last equations, $C_{Fe^{2+}}^{\infty}$ and $C_{Fe^{3+}}^{\infty}$ are the bulk molar concentrations of Fe^{2+} and Fe^{3+} respectively.

Eqs. (1), (2), and (4) can been solved numerically to obtain the radius, the position, and the composition of the bubble as it is done in [20,22]. Here a scaling analysis is addressed to find the time scale occurring in the mass transfer of the bubble. The theoretical prediction will be compared with experimental results recently presented by Pigeonneau et al. [22] for two glasses with a set-up very close to the experiment presented by Kloužek and Němec [12]. A bubble is inflated thanks to a silica tube and observed through a transparent silica crucible with a video-camera. The bubble size is determined by a simple image analysis. The composition of glasses are given in Table 1. They are similar apart from the iron content and its reduction state defined by Eq. (13).

3. Scale analysis of the mass transfer of a O_2 bubble

The scale analysis requires to write the system of equations, Eqs. (1), (2), and (4), under a dimensionless form. These equations involve $N_g + 2$ unknowns: N_g gas species, bubble position, z, and radius, a. In order to simplify the analysis, the assumption about the pressure inside the bubble is presented in Section 3.1. After, the dimensionless equations describing the bubble composition is established in Section 3.2. A careful description of various time

Table 1
Composition of glasses in wt% used in the experiments with the sufate content and the oxidation state. The iron content is the sum of the two polyvalent cations Fe^{2+}, and Fe^{3+}. The sulfate content is the sum of SO_4^{2-}, and SO_2.

Glass	SiO_2	Na_2O	CaO	MgO	Al_2O_3	Fe	S	$\mathscr{R}^{\infty}$
1	71.9	13.97	9.5	4	0.6	0.03	$1 \cdot 10^{-2}$	0.57
2	71.8	13.99	9.5	4	0.6	0.11	$1 \cdot 10^{-2}$	0.42

Author's personal copy

scales and also a new definition of the gas permeability as a function of gaseous species are presented in Section 3.3. Finally, an approximate solution is proposed in Section 3.4. This scale analysis is based on precepts introduced by Bejan (see chap. 1 of [4]).

3.1. Pressure inside the bubble

If a_0 is the initial bubble radius, a is normalized by

$$\bar{a} = \frac{a}{a_0}. \tag{14}$$

The local position of the bubble, z, is normalized with H as

$$\bar{z} = \frac{z}{H}. \tag{15}$$

The pressure inside the bubble can be written as follows

$$P = P_0\left[1 + N_h(1-\bar{z}) + \frac{N_\sigma}{\bar{a}}\right], \tag{16}$$

where N_g and N_σ are given by

$$N_h = \frac{\rho g H}{P_0}, \tag{17a}$$

$$N_\sigma = \frac{2\sigma}{P_0 a_0}. \tag{17b}$$

For $P_0 = 1$ bar, N_h measuring the importance of hydrostatic pressure, is equal to 0.23 when H is equal to one meter. Nevertheless, in the experimental conditions reported in [22] where $H = 0.1$ m, N_h is equal to $2.3\,10^{-2}$. The dimensionless number N_σ is equal to $7\,10^{-3}$ for $a_0 = 1$ mm with $P_0 = 1$ bar. Consequently, to a first approximation, the hydrostatic and Laplace pressures are neglected in the following developments.

In the other words, the pressure inside the bubble is assumed constant meaning that during the bubble motion, the hydrostatic part is not enough important to change significantly the total pressure. It is the same conclusion regarding the effect of the surface tension as long as the bubble is larger than 70 μm corresponding to the bubble size obtaining when $N_\sigma = 0.1$. This hypothesis simplifies the analysis since in this case, the coupled problem between gaseous species, bubble radius and position can be separated. Indeed, the requirement of the bubble position is not needed to describe the total pressure. Consequently, Eq. (4) is excluded in the following of this work.

Nevertheless, remark that even if the bubble position is not taken into account, the bubble motion remains important on the mass transfer process due to the low value of the mass diffusivity as it was showed in [21,22].

3.2. Dimensionless equations of mole number

The total number of moles in a bubble can be estimated by the ideal gas law. The initial number of moles in the bubble is given by

$$n_0 = \frac{P_0 4\pi a_0^3}{3RT}. \tag{18}$$

If the dimensionless number of moles is written as follows

$$\bar{n} = \frac{n}{n_0}, \tag{19}$$

and since the pressure is assumed constant, we have

$$\bar{n} = \bar{a}^3. \tag{20}$$

The number of moles of species i is reduced as follows

$$\bar{n}_i = \frac{n_i}{n_0}, \tag{21}$$

giving from the Dalton's law the relationship

$$\bar{n}_i = x_i \bar{a}^3, \tag{22}$$

where x_i is the molar fraction of gaseous species i in the bubble. Since

$$\sum_{i=1}^{N_g} x_i = 1, \tag{23}$$

the sum of $\bar{n}_i$ over the N_g gaseous species is of course equal to $\bar{n}$.

So, Eq. (2), describing the time derivative of number of moles of gaseous species i, can be written under dimensionless form with the time reduced as follows

$$\bar{t} = \frac{t}{\tau}. \tag{24}$$

At this step, the characteristic time of the mass transfer, τ, is an unknown quantity which has to be determined as a function of relevant phenomena describing the bubble shrinkage. To clearly define τ, the various time scales involved in the mass transfer of a bubble have to be examined carefully.

From definition (22), the time derivative of the number of moles is given by

$$\frac{1}{\tau}\frac{d(x_i\bar{a}^3)}{d\bar{t}} = -\frac{3\overline{Sh}_i\bar{a}\left(x_i^{\beta_i} - Sa_{i,0}\right)}{\tau_i}. \tag{25}$$

In this last equation, $Sa_{i,0}$ is the saturation of gaseous species i defined by

$$Sa_{i,0} = \frac{C_i^\infty}{L_i P_0^{\beta_i}}. \tag{26}$$

This saturation is defined with the pressure P_0 as if the bubble was composed only of the gaseous species i. In order to remember this point, the symbol 0 is introduced on the lower index in $Sa_{i,0}$.

In Eq. (28), $\overline{Sh}_i$ is defined by

$$\overline{Sh}_i = \frac{Sh_i}{Sh_{i,0}}. \tag{27}$$

This quantity, resulting of the introduction of $Sh_{i,0}$ in τ_i (see the discussion below), is just the ratio of the Sherwood number for the bubble size a to the one for the bubble size a_0. This quantity will be larger than one if the bubble grows and lesser than one if the bubble shrinks. It represents the effect of advection for the bubble size a compared to the bubble size equal to a_0. It can be defined as a function of $\bar{a}$ as it will be done in the following.

The characteristic time for the mass transfer of gaseous species i,τ_i, is given by

$$\tau_i = \frac{2a_0^2 P_0^{1-\beta_i}}{Sh_{i,0}\mathscr{D}_i L_i RT}. \tag{28}$$

This quantity is easily derived by the introduction of the characteristic variables in Eq. (2) defined for the initial bubble size. The division by the Sherwood number is done in order to take into account the bubble motion in the mass transfer. As it can be easily evaluated, the typical value of the Péclet number can exceed 10^3 for which the Sherwood number is larger than 10. Consequently, without $Sh_{i,0}$, τ_i should be a diffusion time normalized with the bubble size which is irrelevant in the process mainly driven by the advection. Moreover, the oxidation–reduction reaction of iron oxides by oxygen is also taken into account when the Sherwood number is introduced in Eq. (28) with the definition of Sh_{O_2} and Pe'_{O_2} given in the previous section.

To establish (28), the molar concentration difference between the bubble surface and the bulk of molten glass is taken, leading

Author's personal copy

to the occurrence of the solubility in τ_i. Finally, it should be noted that the $L_iRT/P_0^{1-\beta_i}$ is a dimensionless number.

3.3. Permeability, and time scales, τ_i, versus gas species

To simplify again Eq. (25), it is important to have a clear idea about the time scale (28) as a function of gaseous species. Before to do that, the gas permeability is introduced.

The product $\mathscr{D}_iL_iRT/P_0^{1-\beta_i}$ in (28) depends on the diffusion but also on the solubility of gaseous species *i*. This quantity represents the rate of gas exchange between the two phases. So, for two species having the same diffusion coefficient, the respective characteristic time of mass transfer can be very different if their solubilities are very different. The product $\mathscr{D}_iL_i$ is usually defined as the permeability of gaseous species *i*, see for example [28]. However, we suggest to use the product $\mathscr{D}_iL_iRT/P_0^{1-\beta_i}$ since this quantity has the same unit as a diffusion coefficient, which is useful to compare with other relevant phenomena. Moreover, for water, the exponent β_i is equal to 1/2, and the permeability of water depends on the pressure: it is an important point for applications not present in the definition given by Shelby [28].

Consequently, the characteristic time, τ_i, being inversely proportional to the permeability decreases with the permeability. The quantity τ_i was calculated for O_2, SO_2, CO_2, N_2 and H_2O for temperatures and initial sizes presented in [22]. The diffusion coefficient and solubility of each species are taken from relationships depending on temperature summed up in Appendix A. The numerical values of τ_i are given in Table 2.

These characteristic times present a large range of values. Table 2 gives values of few seconds for water meaning that this gaseous species reaches very rapidly an equilibrium state. This result is mainly due to its large solubility. Water is chemically dissolved in molten glass [27]. Thus water solubility is a few order of magnitude larger than that of other species. At 1300 °C for example, the water solubility is 0.46 mol m^{-3} $Pa^{-1/2}$ while the value for N_2 is 1.6×10^{-7} mol m^{-3} Pa^{-1}. Consequently, the bubble is quickly filled with water with a molar fraction given by

$$x_{H_2O} = Sa^2_{H_2O,0}. \tag{29}$$

This last equation comes from the cancellation of the right hand side of (25).

The mass transfer process is relatively fast for SO_2 since the typical value is about three or four hundred seconds. The characteristic time of the mass transfer for oxygen is larger than the one obtained for sulfur dioxide. Moreover, note that the effect of the oxidation–reduction of iron is clearly established. The comparison of the time scale, τ_i, obtained at 1400 °C for the two glasses shows that the characteristic time for glass 2 is 1.6 times lesser than for glass 1. The difference is not due to the initial bubble sizes which are unlike between the two glasses. At $T = 1400$ °C, the Péclet number for the bubble is larger than 10^3 which means that the Sherwood number can be taken as a function of the square root of the Péclet number. In this limit, the Sherwood number scales as $a_0^{3/2}$. Consequently, the time scale τ_i for oxygen must be proportional to $\sqrt{a_0}$. Then, the ratio between the initial bubble size between the two glasses should give a time scale only 1.16 times lesser for the bubble observed in glass 2. The characteristic time taking into account the effect of the oxidation–reduction reaction is more important due to the larger value of the Sherwood number in a glass where the iron content is more important.

Table 2
Characteristic times of mass transfer of each gaseous species determined under experimental conditions (temperature and initial size of the observed bubble) for the two glasses.

Glass 1, a_0 = 1.35 mm, T = 1400°C					
gas	O_2	SO_2	CO_2	N_2	H_2O
τ_i (s)	1379	464	8686	78536	10
Glass 1, a_0 = 1.7 mm, T = 1450°C					
gas	O_2	SO_2	CO_2	N_2	H_2O
τ_i (s)	1007	423	6914	53898	8
Glass 2, a_0 = 2.3 mm, T = 1300°C					
gas	O_2	SO_2	CO_2	N_2	H_2O
τ_i (s)	3322	977	24630	310707	31
Glass 2, a_0 = 1 mm, T = 1400°C					
gas	O_2	SO_2	CO_2	N_2	H_2O
τ_i (s)	850	398	7445	67056	9

Mass transfer processes for CO_2, and N_2 are very slow. The characteristic time, τ_i, can reach a typical value larger than few thousand seconds for CO_2, and larger than few ten thousand seconds for N_2. Consequently, the filling-up of a bubble with CO_2, and N_2 can take a long time.

From the numerical simulation presented in [22], molar fractions in the bubble can be determined in order to verify the conclusions drawn above. Fig. 1 presents x_i as a function of time for the five species, SO_2, O_2, CO_2, N_2 and H_2O with the main figure, representing volume fraction after a time equal to one half of hour. The results were obtained with the properties of glass 2 at $T = 1400$ °C. Two inserts are introduced in Fig. 1 in order to focus on the behavior of a bubble after very short time (Insert 1) and on very long time (Insert 2). This numerical result confirms the dimension analysis: water is rapidly in equilibrium between the two phases as it is shown in Insert 1 of Fig. 1. While the volume fractions of N_2 and CO_2 are small during the first few minutes, they become larger when time increases. In Insert 2 of Fig. 1, the volume fractions of N_2 and CO_2 are significant in the bubble.

Consequently, from this simple analysis, it is possible to establish a hierarchy of gaseous species entering or exiting of a bubble. Comparing to the typical time scale in glass melting process where the average residence time in a glass bath can exceed one day, water can be considered in an equilibrium state quasi-instantaneously. At very short times, since the bubble is composed mainly of oxygen, the introduction of water in the bubble produces a fast decrease of molar fraction of O_2 as it can be seen in Fig 1. A bubble undergoes the introduction of CO_2 and N_2 over a typical time larger than few hours as a function of temperature.

This analysis can be useful in the feature of bubbles dispersed in an industrial plant, the composition of each bubble in a molten glass depending on its residence time. Consequently, gas analysis of bubble in a glass can give information about the origin of this defect.

3.4. An approximate solution of bubble radius

The time scale τ introduced in Eq. (25) can now be specified. From the previous analysis, the relevant species are O_2, and SO_2. The study is focused on oxygen bubble, so τ is taken equal to the characteristic time of mass transfer of oxygen, τ_{O_2}. The time derivative of the reduced bubble radius can be written as follows:

$$\frac{d\bar{a}}{dt} = -\frac{1}{\bar{a}}\sum_{i=1}^{N_g}\frac{\overline{Sh_i}}{\bar{\tau}_i}\left(x_i^{\beta_i} - Sa_{i,0}\right), \tag{30}$$

where $\bar{\tau}_i$ is the reduced time scale of gaseous species *i* defined by

$$\bar{\tau}_i = \frac{\tau_i}{\tau_{O_2}}. \tag{31}$$

From Eq. (30) given above and Eq. (25), the time derivative of molar fraction x_i in the bubble is given by

$$\frac{dx_i}{dt} = \frac{3}{\bar{a}^2}\sum_{j=1}^{N_g}\frac{\overline{Sh_j}}{\bar{\tau}_j}\left(x_j^{\beta_j} - Sa_{j,0}\right)(x_i - \delta_{ij}), \tag{32}$$

Author's personal copy

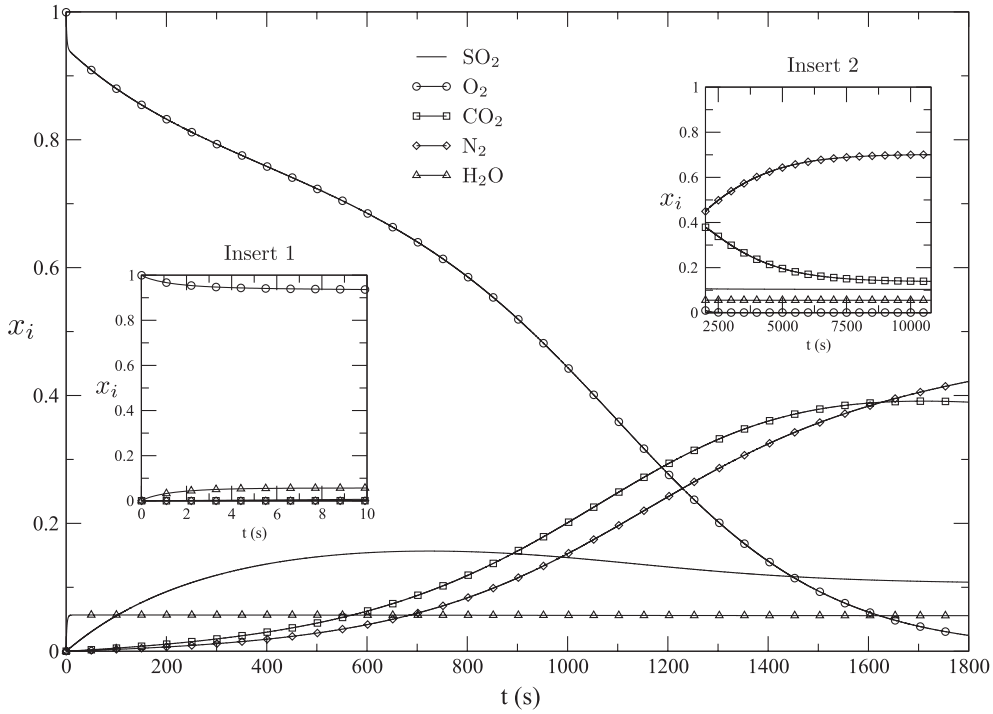

Fig. 1. Molar fraction of gaseous species as a function of time in a bubble obtained from the numerical simulation with characteristics of glass 2 at $T = 1400°C$. Insert 1 gives molar fraction at very short time and Insert 2 at very long time.

where δ_{ij} is the Kronecker symbol, equal to 1 if $i = j$ and equal to 0 if $i \neq j$.

Using these equations, it is possible to find an approximate solution of $\bar{a}$ at short times. In order to do that and according to the analysis given in the previous subsection, the bubble is assumed to be composed mainly of oxygen and water. Sulfur dioxide is also taken into account since its kinetics has been shown sufficiently fast to reduce the shrinkage rate. Moreover, if the Sherwood numbers are taken in the limit of large Péclet numbers [5,13,21] (*i.e.* in the boundary layer regime), the ratio $\overline{Sh}_i$ is directly equal to $\bar{a}^{3/2}$ as it has been shown in the Section 3.3. In this limit, Eq. (30) can be easily integrated to give an explicit solution of bubble size variation:

$$\bar{a}(\bar{t}) = \left[1 - \frac{1}{2}\left(1 - x_{H_2O} - Sa_{O_2,0} - \frac{Sa_{SO_2,0}}{\bar{\tau}_{SO_2}}\right)\bar{t}\right]^2. \tag{33}$$

This relationship, one of the more important result of this paper is a generalized version of the solution already given by Onorato et al. [18], the multicomponent bubble being taken into account in the present work. Onorato et al. [18] derived their solution by taking into account the Laplace pressure which is not done here. Eq. (33) shows that the bubble radius is a quadratic function of time.

Table 3 summarizes the numerical values of quantities required to compute the solution (33) for the two specific glasses and for temperatures used in the experiments reported in [22]. Remark that from these data, both O_2, and SO_2 are under-saturated. Moreover, the molar fraction of water depends slightly on temperature.

In Fig. 2, the normalized bubble size is given as a function of dimensionless time, written as $(1 - x_{H_2O} - Sa_{O_2,0} - Sa_{SO_2,0}/\bar{\tau}_{SO_2})\bar{t}/2$, obtained from the experimental data for the two glasses used in this work. With this reduced form and with assumptions made above, all experimental data consist roughly of a master curve independent of temperature and the glass nature. In Fig. 2, the solution given by Eq. (33) is reported: at short times a good agreement is found between experimental results and this approximate solution for the two glasses.

When the time increases Eq. (33) underestimates the bubble size compared of experimental results meaning that the solution (33) becomes invalid. In fact, Eq. (33) has been established assuming that the bubble composition does not change significantly. This point is valid as long as oxygen is the most important species inside the bubble. Consequently, the approximate solution (33) is relevant over the time scale of τ_{O_2}. Beyond this time, the bubble size behavior can change deeply as it is pointed out in [22].

From this analysis, the characteristic time to describe the shrinkage of an oxygen bubble can be written as follows

$$\tau_{Sh,O_2} = \frac{2a_0^2}{Sh_{O_2,0}\mathscr{D}_{O_2}L_{O_2}RT\left(1 - x_{H_2O} - Sa_{O_2,0} - Sa_{SO_2,0}/\bar{\tau}_{SO_2}\right)}. \tag{34}$$

This time differs from τ_{O_2} by the division of $1 - x_{H_2O} - Sa_{O_2,0} - Sa_{SO_2,0}/\bar{\tau}_{SO_2}$ which is always lesser than one. The introduction of this last quantity in (34) enables to take into account the effects of water and sulfate dioxide. For the data reported in Tables 2 and 3, the time scale (34) is around 50% or 60% larger than τ_{O_2}. As already discussed in the last subsection, this characteristic time takes into account most of phenomena occurring around an oxygen bubble shrinking in molten glass. Therefore, this time can be computed easily as a function of the bubble size and the glass nature.

Table 3
$Sa_{O_2,0}, Sa_{SO_2,0}$, and x_{H_2O} at different temperatures for the two glasses used in the present work.

	T(°C)	$Sa_{O_2,0}$	$Sa_{SO_2,0}$	x_{H_2O}
Glass 1	1400	$9.3 \cdot 10^{-5}$	$1.1 \cdot 10^{-1}$	$6 \cdot 10^{-2}$
	1450	$2.68 \cdot 10^{-4}$	$1.3 \cdot 10^{-1}$	$6 \cdot 10^{-2}$
Glass 2	1300	$1.1 \cdot 10^{-4}$	$9.6 \cdot 10^{-2}$	$6.2 \cdot 10^{-2}$
	1400	$1.10 \cdot 10^{-3}$	$1.1 \cdot 10^{-1}$	$6 \cdot 10^{-2}$

Author's personal copy

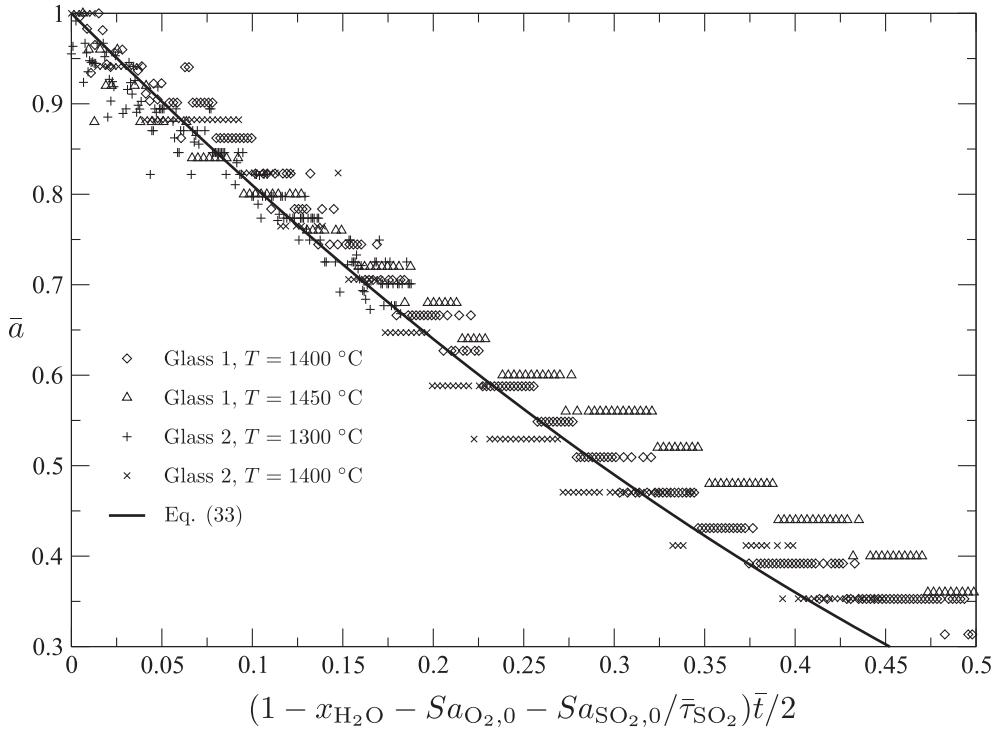

Fig. 2. Normalized bubble size as a function of dimensionless time for the two glasses. Comparison between theoretical solution and experimental results.

4. Conclusion

The mass transfer of a multicomponent bubble rising in molten glass has been studied in this work. The general model to describe the composition and the size of a bubble is presented. To describe more clearly the effect of each gaseous species, a dimension analysis is proposed with the pressure inside a bubble assumed to be constant. A characteristic time related to mass transfer process for each gaseous species is proposed showing that the rate of exchange depends strongly on the gas nature.

The fundamental quantity involved in the mass transfer of a specific gaseous species is related to the product of the diffusion coefficient by the solubility, known as the permeability (see [28]). Here, a new definition of the permeability is proposed having the same unit as a diffusion coefficient.

From this analysis, we show that the equilibrium state between a bubble and molten glass is quickly reached for water. This result is due to the large solubility of water in molten glass, generally, few order of magnitude larger than for the other species. A reverse situation is observed for carbon dioxide and nitrogen. Consequently, the composition of a bubble in molten glass changes over a very long time.

In spite of the multicomponent feature of a bubble in molten glass, it is possible to consider only two gases, O_2 and SO_2 for the first times of the bubble shrinkage. Consequently, for a bubble initially composed of oxygen, a simplified equation of bubble size can be deduced with a characteristic time based only on the oxygen transfer. The range of application of the simplified solution is related to the change of bubble composition. Since the analysis is based on bubbles initially composed of 100% of O_2, the bubble composition does not change over the characteristic time corresponding to the mass transfer of oxygen. Moreover, from this scaling analysis, experimental data giving the bubble size versus time (obtained for two glasses with different iron contents and various temperatures) match very well in a master curve. This calculation needs rescaling of the time with the proposed characteristic times based on the mass transfer of oxygen. Finally, the agreement between experimental data and the results given by this simplified equation of bubble size shows its relevance and that it can be useful to estimate quickly the bubble behavior without computing of the full problem.

Moreover, this analysis can give an important information about the residence time of a bubble in molten glass, the bubble composition changing as a function of its age in molten glass. Consequently, the experimental knowledge of a bubble composition could be used to determine the origin of a bubble defect in a furnace though the experimental determination of the bubble composition remains a difficult task in glass science.

The work has been focused on bubbles initially filled with 100% of oxygen. A similar analysis has to be done when a bubble is composed with another gas species.

Acknowledgments

The author is indebted to an anonymous referee form the various suggestions in the structure of this article and for the fruitful discussions.

Appendix A. Physical and chemical properties of soda–lime–silica glass

The solubilities used in Section 3 are defined by the formula [2]

$$L_j = A_j^{(S)} \exp\left(\frac{B_j^{(S)}}{T}\right). \tag{35}$$

The solubility is given in mol m^{-3} Pa^{-1} for most species and in mol m^{-3} Pa$^{-1/2}$ for water vapor. The coefficients $A_j^{(S)}$ and $B_j^{(S)}$ for gases discussed in this work are listed in Table A.1.

Author's personal copy

Table A.1
Numerical values of $A_j^{(S)}$ and $B_j^{(S)}$ used to determine the solubilities of dissolved gaseous species in soda–lime–silica glass taken from [2].

Gas	O_2	SO_2	CO_2	N_2	H_2O
$A_j^{(S)}$	$1.37 \cdots 10^{-4}$	$6.44 \cdots 10^{-7}$	5.6×10^{-7}	$1.1 \cdots 10^{-5}$	$6.8 \cdots 10^{-1}$
$B_j^{(S)}$	−6633	7860	3120	−6633	−613

Table A.2
Numerical values of $A_j^{(D)}$ and $B_j^{(D)}$ used to determine the diffusion coefficients of dissolved gaseous species in soda-lime-silica glass taken from [2].

Gas	O_2	SO_2	CO_2	N_2	H_2O
$A_j^{(D)}$	3×10^{-3}	$4.45 \cdots 10^{-7}$	$1.92 \cdots 10^{-5}$	$4.3 \cdots 10^{-5}$	$1.2 \cdots 10^{-5}$
$B_j^{(D)}$	−26580	−15360	−21516	−19364	−18320

The diffusion coefficients of dissolved species are given in $m^2\,s^{-1}$ and expressed as follows

$$\mathscr{D}_j = A_j^{(D)} \exp\left(\frac{B_j^{(D)}}{T}\right), \tag{36}$$

where the coefficients $A_j^{(D)}$ and $B_j^{(D)}$ are summarized in Table A.2.

References

[1] R.G.C. Beerkens, Modeling of the melting process in industrial glass furnaces, in: Mathematical Simulation in Glass Technology, Springer, Berlin, 2002, pp. 17–73. Chapter 2.1.
[2] R.G.C. Beerkens, Analysis of advanced and fast fining processes for glass melts, in: Advances in Fusion and Processing of Glass III, American Ceramic Society, New York, 2003, pp. 3–24.
[3] R.G.C. Beerkens, H. de Waal, Mechanism of oxygen diffusion in glassmelts containing variable-valence ions, J. Am. Ceram. Soc. 73 (1990) 1857–1861.
[4] A. Bejan, Convection Heat Transfer, John Wiley & Sons, New York, 1995.
[5] R. Clift, J.R. Grace, M.E. Weber, Bubbles, Drops, and Particles, Academic Press, New York, 1978.
[6] R.H. Doremus, Diffusion of oxygen from contracting bubbles in molten glass, J. Amer. Ceram. Soc. 43 (1960) 655–661.
[7] C.H. Greene, R.F. Gaffney, Apparatus for measuring the rate of absorption of a bubble in glass, J. Amer. Ceram. Soc. 42 (1959) 271–275.
[8] C.H. Greene, I. Kitano, Rate of solution of oxygen bubbles in commercial glasses, Glastech. Ber. 32K (V) (1959) 44–48.
[9] C.H. Greene, H.A. Lee, Effect of As_2O_3 and $NaNO_3$ on the solution of O_2 in soda–lime glass, J. Amer. Ceram. Soc. 48 (1965) 528–533.
[10] C.H. Greene, D.R. Platts, Behavior of bubbles of oxygen and sulfur dioxide in soda–lime glass, J. Amer. Ceram. Soc. 52 (1969) 106–109.
[11] H. Hirashima, T. Yoshida, R. Brückner, Redox equilibria and constitution of polyvalent ions in oxide melts and glasses, Glastech. Ber. 61 (1988) 283–292.
[12] J. Kloužek, L. Němec, Modelling of glass refining kinetics. Part 2: Bubble distribution models and methods of measurement of refining properties, Ceramics 47 (2003) 155–161.
[13] V.G. Levich, Physicochemical Hydrodynamics, Prentice Hall, Englewood Cliffs, N.J., 1962.
[14] B.O. Mysen, P. Richet, Silicate Glasses and Melts: Properties and Structure, Elsevier, Amsterdam, 2005.
[15] L. Němec, The behaviour of bubbles in glass melts. Part 1: Bubble size controlled by diffusion, Glass Technol. 21 (1980) 134–138.
[16] L. Němec, The behaviour of bubbles in glass melts. Part 2: Bubble size controlled by diffusion and chemical reaction, Glass Technol. 21 (1980) 139–144.
[17] L. Němec, J. Kloužek, Modelling of glass refining kinetics. Part 1: single bubbles, Ceramics 47 (2003) 81–87.
[18] P.I.K. Onorato, M.C. Weinberg, D.R. Uhlmann, Behavior of bulles in glassmelts: III, Dissolution and growth of a rising bubble containing a single gas, J. Am. Ceram. Soc. 64 (1981) 676–682.
[19] A. Paul, Chemistry of Glasses, Chapman and Hall, London, 1990.
[20] F. Pigeonneau, Coupled modelling of redox reactions and glass melt fining processes, Glass Technol. Eur. J. Glass Sci. Technol. A 48 (2) (2007) 66–72.
[21] F. Pigeonneau, Mass transfer of rising bubble in molten glass with instantaneous oxidation–reduction reaction, Chem. Eng. Sci. 64 (2009) 3120–3129.
[22] F. Pigeonneau, D. Martin, O. Mario, Shrinkage of oxygen bubble rising in a molten glass, Chem. Eng. Sci. 65 (2010) 3158–3168.
[23] L. Pilon, A.G. Fedorov, D. Ramkrishna, R. Viskanta, Bubble transport in three-dimensional laminar gravity-driven flow-mathematical formulation, J. Non-Cryst. Solids 336 (2004) 71–83.
[24] J.I. Ramos, Behavior of multicomponent gas bubbles in glass melts, J. Am. Ceram. Soc. 69 (1986) 149–154.
[25] D.W. Readey, A.R. Cooper, Molecular diffusion with a moving boundary and spherical symmetry, Chem. Eng. Sci. 21 (1966) 917–922.
[26] S.S. Sadhal, P.S. Ayyaswamy, J.N. Chung, Transport Phenomena with Drops and Bubbles, Springer-Verlag, New York, 1997.
[27] H. Scholze, Gases in glass. In Proceeding of the 8th International Congress on Glass, Londres, 1968.
[28] J.E. Shelby, Introduction to Glass Science and Technology, The Royal Society of Chemistry, Cambridge, 1997.
[29] R.S. Subramanian, B. Chi, Bubble dissolution with chemical reaction, Chem. Eng. Sci. 35 (1980) 2185–2194.
[30] H. Yoshikawa, Y. Kawase, Significance of redox reactions in glass refining processes, Glass Sci. Technol. 70 (1997) 31–39.

Annexe B

Reproduction d'articles relatifs au chapitre 2

Dans cette annexe, nous reproduisons deux articles traitant de la migration et du drainage de film sur des bulles à proximité d'une surface libre et un article sur l'étude de la stabilité et du drainage de films verticaux dont les références sont

- F. Pigeonneau and A. Sellier. Low-Reynolds-Number gravity-driven migration and deformation of bubbles near a free surface. *Phys. Fluids*, 23 :092102, 2011.
- H. Kočárková, F. Rouyer and F. Pigeonneau. Film drainage of viscous liquid on top of bare bubble : Influence of the Bond number. *Phys. Fluids*, under consideration.
- F. Pigeonneau, H. Kočárková and F. Rouyer. Stability of vertical films of molten glass due to evaporation. *Colloids Surf., A*, in press.

Low-Reynolds-number gravity-driven migration and deformation of bubbles near a free surface

Franck Pigeonneau[1] and Antoine Sellier[2]
[1]*Surface du Verre et Interfaces – UMR 125 CNRS/Saint-Gobain, 39 Quai Lucien Lefranc – BP 135, 93303 Aubervilliers Cedex, France*
[2]*Laboratoire d'Hydrodynamique (LadHyX), Ecole Polytechnique, 91128 Palaiseau Cedex, France*

(Received 18 January 2011; accepted 18 July 2011; published online 6 September 2011)

We investigate numerically the axisymmetric migration of bubbles toward a free surface, using a boundary-integral technique. Our careful numerical implementation allows to study the bubble(s) deformation and film drainage; it is benchmarked against several tests. The rise of one bubble toward a free surface is studied and the computed bubble shape compared with the results of Princen [J. Colloid Interface Sci. **18**, 178 (1963)]. The liquid film between the bubble and the free surface is found to drain exponentially in time in full agreement with the experimental work of Debrégeas *et al.* [Science **279**, 1704 (1998)]. Our numerical results also cast some light on the role played by the deformation of the fluid interfaces and it turns out that for weakly deformed interfaces (high surface tension or a tiny bubble) the film drainage is faster than for a large fluid deformation. By introducing one or two additional bubble(s) below the first one, we examine to which extent the previous trends are affected by bubble-bubble interactions. For instance, for a 2-bubble chain, decreasing the bubble-bubble separation increases the deformation of the last bubble in the chain. Finally, the exponential drainage of the film between the free surface and the closest bubble is preserved, yet the drainage is enhanced. © *2011 American Institute of Physics*. [doi:10.1063/1.3629815]

I. INTRODUCTION

Phase separation is involved in many chemical processes, such as flotation, liquid-liquid or gas-liquid extractions. The final stage of such processes, in which two phases have to be separated, is generally limited by the collapse of inclusions at the free surface. For instance, the coalescence of bubbles in highly viscous fluids is observed in various fields, such as geophysics[1] or the glass industry. For the latter application, the energetic efficiency of glass furnaces is deeply related to the occurrence of a foam layer on top of the molten glass bath.[2] Since the transition between frost and foam depends strongly upon the lifetime of a bubble in the vicinity of the free surface, more insights into the idealized problem of a drop or a bubble moving toward a free surface are needed in order to handle such basic and industrial issues.

Earlier basic studies in this direction include the work of Princen,[3] who approximated the drop shape at a liquid-liquid free interface by balancing the pressures driven by gravity with surface tension effects. Hartland[4] confirmed experimentally the theoretical predictions of Princen,[3] using a drop made of glycerol or golden syrup immersed in liquid paraffin (light fluid). Hartland[5] also determined the profile of the film thickness and observed a minimum film thickness near the edge of the film. He[6] later developed a theoretical model based on lubrication theory, in which faster drainage occurred for mobile interfaces. Jones and Wilson[7] developed a lubrication theory to determine the behavior of the liquid film where the settling of a solid particle and a drop were both studied. They demonstrated that the film thickness behaves as an algebraic function of time.

The special case of bubble drainage in a high viscous fluid was experimentally examined by Debrégeas *et al.*[8] using silicon oil. From an interferometry method, an exponential decrease of the film thickness with time was clearly established. This study was limited to large bubbles compared to the capillary scale. Howell[9] later studied the drainage of a bubble close to a free surface, using a lubrication model and restricting attention to a bidimensional bubble. Nevertheless, the case of axisymmetric bubble was reported in an appendix where Howell showed that the film thickness evolves as an algebraic function of time when the deformation is small, and the gravity is neglected.

One drawback of the lubrication theory is the poor knowledge of the initial conditions. Generally, the latter depend on the dynamics prior to the lubrication regime. With this idea in mind, Chi and Leal[10] developed a numerical method based on an integral formulation of Stokes equations in axisymmetric configuration. This work has been done for a viscous drop with a dynamic viscosity that is a multiple $\hat{\mu}$ of the viscosity of the continuous liquid, and computations were achieved mainly for $\hat{\mu}$ in the domain [0.1,10]. Chi and Leal[10] pointed out a fast drainage for small viscosity ratio $\hat{\mu}$, a neutral drainage for $\hat{\mu} = \mathcal{O}(1)$ and a low drainage for large $\hat{\mu}$. A boundary-integral equation approach has been also used by Manga[1] to study how a drop crosses a liquid-liquid interface.

Two-phase flows can be numerically studied by various techniques. The oldest one is the "Volume of Fluid" method pioneered by Hirt and Nichols,[11] where the two phases are seen as a single fluid with a concentration varying between 0 in a phase and 1 in another one. Interfaces are then tracked setting this concentration equal to 1/2. The "level set" approach is based on the description of a distance function from an interface where the interface is mathematically defined for the level set equal to zero. This method is for

 © 2011 American Institute of Physics

Author complimentary copy. Redistribution subject to AIP license or copyright, see http://phf.aip.org/phf/copyright.jsp

example used by Sussman *et al.*[12] Another method is the "front-tracking" technique in which the interfaces between the two phases are tracked using a discrete representation of the interfaces (see, for instance, Unverdi *et al.*[13]). The main advantage of these numerical methods is the ability to deal with arbitrary Reynolds numbers. Unfortunately, such techniques require to discretize the entire domain and also to consider interfaces with thickness of order of a few cells. Hence, interfaces that are too close can be merged depending on the spatial resolution. This prohibits the accurate simulation of film drainage at small scales.

The boundary-integral method is a powerful alternative method, in which the fluid interfaces are carefully described. The method is based on integral formulations exploiting[14] the existence of a fundamental solution (Green's functions) and of a reciprocity relationship. These requirements are fulfilled for Stokes equations, for which the reciprocity relationship is known since the pioneering work of Lorentz,[15] whereas the Green's functions has been obtained 80 years ago by Odqvist.[16] Theoretical issues for Stokes flows together with the associated boundary-integral equations have also been mathematically addressed by Ladyzhenskaya.[17] However, the first numerical resolutions of boundary integral equations for creeping flows were only first performed by Youngren and Acrivos[18] for a solid body and by Rallison and Acrivos[19] for a viscous drop. As this method is now widely employed, we refer the reader to the books of Pozrikidis[20] and Kim and Karrila[21] for further details.

This work examines the motion and deformation of bubbles moving toward a free surface in a highly viscous fluid when the inertial forces are negligible. Since arbitrary and fully three-dimensional geometries would result in very involved numerical implementation and computations, we restrict the study to axisymmetric geometries. This assumption therefore prevents us from tracking in time non-axisymmetric shapes disturbances that might be produced by non-axisymmetric instabilities. A boundary-integral approach of Stokes equations and a relevant well-posed boundary-integral equation specifically developed for axisymmetric geometries involving several bubbles and a free surface are obtained in Sec. III. Since we aim at investigating the film drainage between bubbles or bubble and a free surface, special efforts are made to solve accurately the boundary-integral equations, as detailed in Sec. IV. The implemented procedure then permits us to study the motion and drainage of one, two, and three bubbles in axisymmetric configuration in Sec. V.

II. GOVERNING EQUATIONS AND RELEVANT PROCEDURE

We consider a Newtonian liquid with uniform viscosity μ and density ρ, subject to the uniform vertical gravity field $\boldsymbol{g} = -g\boldsymbol{e}_3$ with magnitude $g > 0$. The ambient fluid above the $z = 0$ plane free surface is a gas with a uniform pressure p_a. Injecting $N \geq 1$ bubble(s) in the liquid results, by buoyancy effects, in a motion of each bubble toward the free surface, whereas the shape of the bubble(s) and the free surface both change with time. As outlined in the introduction, determining those time-dependent shapes exhibiting significant deformations

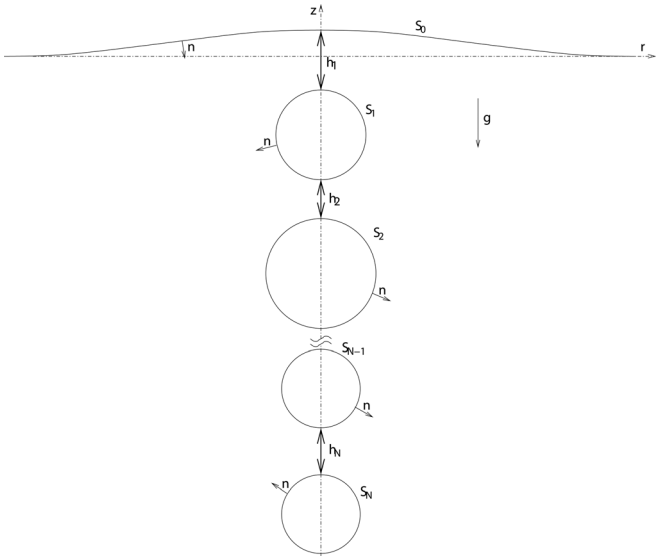

FIG. 1. Retained axisymmetric configurations for $N \geq 1$ bubble(s).

is a challenging issue of fundamental interest. The present work addresses such a task for axisymmetric configurations. As depicted in Fig. 1, one therefore assumes at each time a free surface and a single bubble or a N-bubble chain (for $N \geq 2$) that share an axis of revolution parallel to the gravity field $\boldsymbol{g}$. The different surfaces are numbered from the top to the bottom with bubble $\mathcal{B}_n$ having a smooth surface S_n, whereas S_0 denotes the disturbed free surface. Moreover, those boundaries are characterized by the same *constant* surface tension γ, and a unit normal vector $\boldsymbol{n}$ directed into the liquid.

Each bubble $\mathcal{B}_n$, made of a gas with *uniform* pressure p_n (for instance) and negligible density and viscosity, is spherical with radius a_n at initial time. In the time-dependent liquid domain $\mathcal{D}(t)$, the fluid has pressure $p + \rho\boldsymbol{g}\cdot\boldsymbol{x}$ and velocity $\boldsymbol{u}$ with typical magnitude $U = \rho g a^2/(3\mu)$, where $a = \max(a_n)$. Moreover, the resulting Reynolds number Re obeys

$$\mathrm{Re} = \rho U a/\mu \ll 1, \tag{1}$$

so that all inertial effects are neglected. Assuming quasi-steady changes for the bubble(s) and free surface shapes, the flow $(\boldsymbol{u}, p)$ therefore fulfills the steady Stokes equations

$$\mu\nabla^2\boldsymbol{u} = \mathbf{grad}p, \tag{2}$$

$$\nabla\cdot\boldsymbol{u} = 0, \tag{3}$$

in the liquid domain $\mathcal{D}(t)$, to be supplemented with the far-field behavior

$$(\boldsymbol{u}, p) \to (\boldsymbol{0}, 0), \quad \text{as } ||\boldsymbol{x}|| \to \infty, \tag{4}$$

and additional boundary conditions on each surface S_n for $n = 0, \ldots, N$. Setting $p_0 = p_a$ and denoting by $\boldsymbol{\sigma}$, the stress tensor of the flow $(\boldsymbol{u}, p)$, these relevant conditions consist of both the relation (because the surface tension γ is uniform)

$$\boldsymbol{\sigma}\cdot\boldsymbol{n} = (\rho\boldsymbol{g}\cdot\boldsymbol{x} - p_n + \gamma\nabla_S\cdot\boldsymbol{n})\boldsymbol{n}, \tag{5}$$

on S_n for $n = 0, \ldots, N$, and the usual zero-mass flux conditions (impermeable surfaces)

Author complimentary copy. Redistribution subject to AIP license or copyright, see http://phf.aip.org/phf/copyright.jsp

$$\boldsymbol{V}\cdot\boldsymbol{n}=\boldsymbol{u}\cdot\boldsymbol{n}, \tag{6}$$

on S_n for $n=0,\ldots,N$, where $\boldsymbol{V}$ is the material velocity on each surface S_n. In Eq. (5), the quantity $\nabla_S\cdot\boldsymbol{n}$ is the surface divergence of the unit normal $\boldsymbol{n}$, which is related to the local average curvature H as $\nabla_S\cdot\boldsymbol{n}=2H$ (see Aris[22]). Furthermore, we assume in practice that both the temperature and the pressure are uniform and time independent in each bubble, which its volume is therefore constant as time evolves. Under the boundary conditions (6), one then supplements Eqs. (2)–(5) with the additional relations

$$\int_{S_n}\boldsymbol{u}\cdot\boldsymbol{n}dS=0,\quad \text{for } n=1,\ldots,N. \tag{7}$$

Observe that Eq. (7) also holds on the free surface S_0 because $\boldsymbol{u}$ is divergence free, see Eq. (3), and Eq. (7) is valid for each bubble.

At that stage, it is worth highlighting the following steps when tracking in time the shapes of the bubble(s) and free surface:

(i) At a given time t, one first obtains the liquid flow $(\boldsymbol{u}, p)$ in the given fluid domain $\mathcal{D}(t)$ with boundaries S_n by solving the problem (2)–(5) in conjunction with Eq. (7). As explained in Sec. III B, one then actually gets a unique solution $(\boldsymbol{u}, p)$ for Eqs. (2)–(5) and (7).

(ii) Once $(\boldsymbol{u}, p)$ has been obtained, one gets at the same time t the normal component $\boldsymbol{V}\cdot\boldsymbol{n}$ by exploiting Eq. (6). The knowledge of this normal velocity $\boldsymbol{V}\cdot\boldsymbol{n}$ then permits one to move each bubble and the free surface for a given time step dt and then to determine the updated liquid domain $\mathcal{D}(t+dt)$.

The entire procedure (i)–(ii) is embedded in a Runge-Kutta algorithm to determine the time-dependent shapes of the bubble(s) and free surface. Such a scheme, quite simple by essence, however, deserves a few key remarks:

(i) It requires to efficiently solve at each time the well-posed problem (2)–(5) and (7). At a first glance, this might be numerically achieved by computing the flow $(\boldsymbol{u}, p)$ in the entire liquid domain using a standard finite element technique for instance. Unfortunately, this would first require to adequately truncate the unbounded liquid domain and it would also become very cpu-time consuming if a good accuracy is required. Another boundary approach, free from these important drawbacks, is therefore introduced and implemented in Secs. III and IV.

(ii) As previously noticed, the key boundary condition (5) involves the local curvature $H=\nabla_S\cdot\boldsymbol{n}/2$ on each boundary. Clearly, the accuracy level at which this quantity is numerically approximated directly dictates the accuracy of the whole method and one therefore needs to adequately discretize, as detailed in Sec. IV, each surface S_n.

(iii) In order to accurately track in time the drainage occurring for small bubble-bubble or/and bubble free-surface gap(s), one must resort to a careful numerical treatment of the boundary integrals and use as many nodal points as necessary.

III. BOUNDARY FORMULATION

We present in this section the advocated boundary approach to accurately solve the problem (2)–(5) and (7) for a given liquid domain $\mathcal{D}(t)$ and prescribed gravity field $\boldsymbol{g}$, *uniform* surface tension γ, *uniform* ambient pressure p_a, and *uniform* pressures p_n for $n=1,\ldots,N$.

A. Relevant integral representation and associated boundary-integral equation

Since the flow $(\boldsymbol{u}, p)$ obeys in the liquid domain the Stokes equations (2) and the far-field behavior (4), its velocity field $\boldsymbol{u}$ receives in the entire liquid domain the following widely employed integral representation:[20]

$$\boldsymbol{u}(\boldsymbol{x}_0)=-\frac{1}{8\pi\mu}\int_S\boldsymbol{f}(\boldsymbol{x})\cdot\boldsymbol{G}(\boldsymbol{x},\boldsymbol{x}_0)dS(\boldsymbol{x})+\frac{1}{8\pi}\int_S\boldsymbol{u}(\boldsymbol{x})\cdot\boldsymbol{T}(\boldsymbol{x},\boldsymbol{x}_0)\cdot\boldsymbol{n}(\boldsymbol{x})dS(\boldsymbol{x}), \tag{8}$$

with the entire surface $S=\bigcup_{n=0}^{N}S_n$ and $\boldsymbol{f}$ the surface traction defined as

$$\boldsymbol{f}(\boldsymbol{x})=\boldsymbol{\sigma}\cdot\boldsymbol{n}(\boldsymbol{x}), \tag{9}$$

and second- and third-rank tensors $\boldsymbol{G}$ and $\boldsymbol{T}$ the usual free-space Oseen-Burgers tensor and associated stress tensor admitting the Cartesian components G_{ij} and T_{ijk} given by

$$G_{ij}(\boldsymbol{x},\boldsymbol{x}_0)=\frac{\delta_{ij}}{||\boldsymbol{x}-\boldsymbol{x}_0||}+\frac{(x_i-x_{0,i})(x_j-x_{0,j})}{||\boldsymbol{x}-\boldsymbol{x}_0||^3}, \tag{10}$$

$$T_{ijk}(\boldsymbol{x},\boldsymbol{x}_0)=-6\frac{(x_i-x_{0,i})(x_j-x_{0,j})(x_k-x_{0,k})}{||\boldsymbol{x}-\boldsymbol{x}_0||^5}, \tag{11}$$

where δ_{ij} is the Kronecker symbol.

Because Eq. (8) holds for $\boldsymbol{x}_0$ located in the liquid domain, it permits one to compute the velocity field $\boldsymbol{u}$ in the liquid by solely appealing to two surface quantities: the velocity $\boldsymbol{u}$ and the traction $\boldsymbol{f}$ on surface S. For the flow $(\boldsymbol{u}, p)$ governed by Eqs. (2)–(5), the traction $\boldsymbol{f}$ is prescribed by the boundary condition (5), and one therefore solely needs to determine the velocity $\boldsymbol{u}$ on the entire liquid boundary S. This is achieved by letting $\boldsymbol{x}_0$ tend to S in Eq. (8). Curtailing the details which are available for instance in Pozrikidis,[20] one then arrives at the following key Fredholm boundary-integral equation of the second kind for the unknown velocity $\boldsymbol{u}$ on the liquid boundary S:

$$4\pi\boldsymbol{u}(\boldsymbol{x}_0)-\fint_S\boldsymbol{u}(\boldsymbol{x})\cdot\boldsymbol{T}(\boldsymbol{x},\boldsymbol{x}_0)\cdot\boldsymbol{n}(\boldsymbol{x})dS(\boldsymbol{x})=-\frac{1}{\mu}\int_S\boldsymbol{f}(\boldsymbol{x})\cdot\boldsymbol{G}(\boldsymbol{x},\boldsymbol{x}_0)dS(\boldsymbol{x}), \tag{12}$$

for $\boldsymbol{x}_0$ on S. In Eq. (12), the symbol $\fint$ means a weakly singular integration in the principal value sense of Cauchy (see Hadamard[23] and Kupradze[24]). It turns out that the resulting integral is actually a regular one, because of the scalar product with the unit normal $\boldsymbol{n}$. Noting that for $\boldsymbol{x}_0$ located on S (see Pozrikidis[20]),

Author complimentary copy. Redistribution subject to AIP license or copyright, see http://phf.aip.org/phf/copyright.jsp

$$\int_{S_n} \boldsymbol{n}(\boldsymbol{x}) \cdot \boldsymbol{G}(\boldsymbol{x}, \boldsymbol{x}_0) dS(\boldsymbol{x}) = \boldsymbol{0}, \tag{13}$$

for $n = 1, \ldots, N$ and injecting the boundary condition (5) in (12) with each pressure p_n being *uniform* then finally yields the boundary-integral equation

$$\boldsymbol{u}(\boldsymbol{x}_0) - \frac{1}{4\pi\mu} \fint_S \boldsymbol{u}(\boldsymbol{x}) \cdot \boldsymbol{T}(\boldsymbol{x}, \boldsymbol{x}_0) \cdot \boldsymbol{n}(\boldsymbol{x}) dS(\boldsymbol{x}) = \boldsymbol{S}(\boldsymbol{x}_0), \tag{14}$$

for $\boldsymbol{x}_0$ on S and $\boldsymbol{S}(\boldsymbol{x}_0)$ given by

$$\boldsymbol{S}(\boldsymbol{x}_0) = \frac{1}{4\pi} \int_S [(\rho \boldsymbol{g} \cdot \boldsymbol{x} + \gamma \nabla_S \cdot \boldsymbol{n}) \boldsymbol{n}](\boldsymbol{x}) \cdot \boldsymbol{G}(\boldsymbol{x}, \boldsymbol{x}_0) dS(\boldsymbol{x}). \tag{15}$$

Of course (5)–(15) is recovered by setting to zero the drop viscosity ratio in Rallison and Acrivos.[19] In summary, for the present work, one has to invert at each time the above boundary-integral equation (14) in conjunction with the relations (7) when the traction $\boldsymbol{f} = \boldsymbol{\sigma} \cdot \boldsymbol{n}$ is prescribed by Eq. (5). Once this is done numerically, the liquid domain is subsequently updated by employing (6) and, if necessary, the velocity field $\boldsymbol{u}$ is computed in the entire liquid domain by appealing to the integral representation (8). Since this approach only involves the surface quantities $\boldsymbol{u}$ and $\boldsymbol{\sigma} \cdot \boldsymbol{n}$, it is termed a boundary approach. It clearly solely requires to mesh the entire surface S and permits one to accurately obtain the velocity $\boldsymbol{u}$ on S without calculating the liquid flow $(\boldsymbol{u}, p)$ in the unbounded liquid domain.

B. Basic issues for the proposed boundary approach

Any solution $(\boldsymbol{u}, p)$ to Eqs. (2)–(5) obeys Eq. (14), but we also require $\boldsymbol{u}$ to satisfy Eq. (7). Actually, Eq. (14) does not admit a unique solution, i.e., is ill-posed. To clarify this issue, let us introduce for a given bubble $\mathcal{B}_n$ the eigenvalues λ and associated eigenfunctions $\boldsymbol{v}$ defined on the bubble boundary S_n such that

$$\frac{1}{4\pi} \fint_{S_n} \boldsymbol{v}(\boldsymbol{x}) \cdot \boldsymbol{T}(\boldsymbol{x}, \boldsymbol{x}_0) \cdot \boldsymbol{n}(\boldsymbol{x}) dS(\boldsymbol{x}) = \lambda \boldsymbol{v}(\boldsymbol{x}_0), \tag{16}$$

for $\boldsymbol{x}_0$ on S_n. Whatever the bubble $\mathcal{B}_n$, the set of eigenvalues (the so-called spectrum) is the segment $[-1, 1]$ with $\lambda = 1$ having multiplicity one (see, for instance, Pozrikidis[20]). The associated normalized eigenfunctions defined on S_n are denoted by $\boldsymbol{v}_n$ and such that $\int_{S_n} \boldsymbol{v}_n \cdot \boldsymbol{v}_n dS = 1$. Hence, for $N = 1$, it is clear that $\boldsymbol{v}$ obeys Eq. (12) for $\boldsymbol{f} = 0$ and therefore Eq. (14) does not have a unique solution if any. It is possible to draw similar conclusions for $N \geq 2$ with this time $\boldsymbol{v}$ solution of Eq. (12) for $\boldsymbol{f} = 0$. Consequently, the right-hand side of Eq. (14) must satisfy compatibility conditions for Eq. (14) to have at least one solution! To specify those conditions, we first recall (see Pozrikidis[20]) that for arbitrary surfaces S_n and S_m (with either $m = n$ or $m \neq n$)

$$\int_{S_0} n_k(\boldsymbol{x}_0) T_{ijk}(\boldsymbol{x}, \boldsymbol{x}_0) dS(\boldsymbol{x}_0) = 0, \tag{17}$$

for $\boldsymbol{x}$ on S_n and

$$\int_{S_m} n_k(\boldsymbol{x}_0) T_{ijk}(\boldsymbol{x}, \boldsymbol{x}_0) dS(\boldsymbol{x}_0) = 4\pi \delta_{ij} \delta_{mn}, \tag{18}$$

for $\boldsymbol{x}$ on S_n (when $m = n$, the integral (18) is a weakly singular integral in the principal value sense of Cauchy).

Multiplying Eq. (14) by the normal vector $\boldsymbol{n}(\boldsymbol{x}_0)$ and integrating over the surface S_n, one thus arrives at the following compatibility relations for the right-hand side $\boldsymbol{S}(\boldsymbol{x}_0)$ of Eq. (14):

$$\int_{S_n} \boldsymbol{S}(\boldsymbol{x}_0) \cdot \boldsymbol{n}(\boldsymbol{x}_0) dS(\boldsymbol{x}_0) = 0, \tag{19}$$

for $n = 1, \ldots, N$. Noting that $G_{ij}(\boldsymbol{x}, \boldsymbol{x}_0) = G_{ji}(\boldsymbol{x}_0, \boldsymbol{x})$, exploiting the identities (13) and the definition (15) of the right-hand side $\boldsymbol{S}$ immediately shows that the above conditions (19) are satisfied for the addressed boundary-integral equation (14). Accordingly, Eq. (14) has solutions $\boldsymbol{u}$, which read $\boldsymbol{u} = \boldsymbol{u}_0 + \boldsymbol{v}_{\beta_1, \ldots, \beta_N}$ with $\boldsymbol{u}_0$ any solution. For the present work, we require the selected solution $\boldsymbol{u}$ to comply with the relations (7). This is achieved by using Wielandt's deflation technique as performed, among others, by Loewenberg and Hinch,[25] Zinchenko *et al.*,[26] and explained in details in Kim and Karrila.[21] For $N \geq 1$ bubbles, it is then possible to prove that $\boldsymbol{u}$ solution to Eqs. (14) and (7) obeys the *modified, well-posed*, and *coupled* boundary-integral equations

$$\boldsymbol{u}(\boldsymbol{x}_0) - \frac{1}{4\pi} \fint_S \boldsymbol{u}(\boldsymbol{x}) \cdot \boldsymbol{T}(\boldsymbol{x}, \boldsymbol{x}_0) \cdot \boldsymbol{n}(\boldsymbol{x}) dS(\boldsymbol{x}) - \sum_{n=1}^{N} \left[\frac{\int_{S_n} \boldsymbol{u}(\boldsymbol{x}) \cdot \boldsymbol{n}(\boldsymbol{x}) dS(\boldsymbol{x})}{\int_{S_n} dS(\boldsymbol{x})} \right] \boldsymbol{n}(\boldsymbol{x}_0) = \boldsymbol{S}(\boldsymbol{x}_0), \tag{20}$$

for $\boldsymbol{x}_0$ on S_n, $n = 1, \ldots, N$.

Clearly, $\boldsymbol{u}$ solution to Eqs. (14) and (7) obeys Eq. (20). Conversely, multiplying Eq. (20) by $\boldsymbol{n}(\boldsymbol{x}_0)$ and integrating over the surface S_n this time shows that, using Eqs. (17), (18), and (19), a solution $\boldsymbol{u}$ to Eq. (20) also fulfils the relations (7) and thus obeys Eq. (14). Hence, the unique and required solution to both Eqs. (14) and (7) is the solution of the coupled boundary-integral equations (20), which is therefore well-posed. Moreover, as the reader may easily check, the homogeneous counterpart of Eq. (20), here obtained by selecting $\boldsymbol{S} = \boldsymbol{0}$, has spectrum $[-1, 1]$.

C. Case of the axisymmetric fluid domain

The entire material developed in Secs. III A and III B is actually valid for arbitrary three-dimensional N-bubble clusters. However, as previously mentioned in the Introduction, the numerical counterpart results in heavy implementation step and computations. Therefore, we confine the analysis to axisymmetric configurations, as the one depicted in Fig. 1, and non-axisymmetric instabilities are thus not treated here. For convenience, we further adopt cylindrical coordinates (r, ϕ, z) with $r = \sqrt{x^2 + y^2}$ and ϕ the azimuthal angle in the range $[0, 2\pi]$. In Eq. (14), we perform the integration in the azimuthal direction. Setting $\boldsymbol{u} = u_r \boldsymbol{e}_r + u_z \boldsymbol{e}_z = u_\alpha \boldsymbol{e}_\alpha$ (with $\alpha = r, z$) in the liquid and $\boldsymbol{f} = f_r \boldsymbol{e}_r + f_z \boldsymbol{e}_z = f_\alpha \boldsymbol{e}_\alpha$ on the liquid boundary then makes it possible to cast Eq. (14) into the following form:

Author complimentary copy. Redistribution subject to AIP license or copyright, see http://phf.aip.org/phf/copyright.jsp

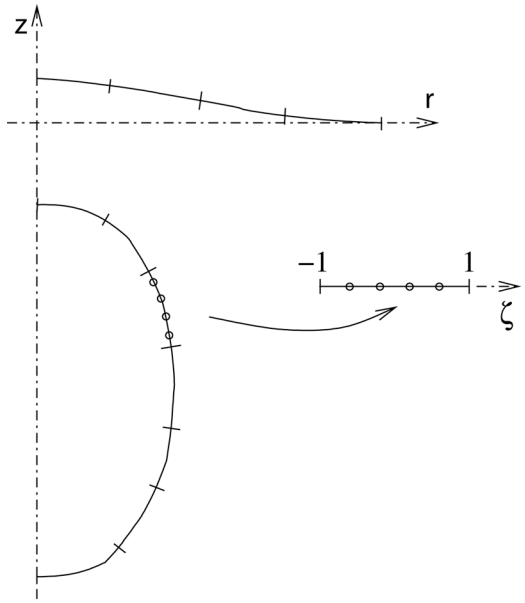

FIG. 2. Discretization and mapping of each element onto [− 1,1] with end points and collocation points are indicated by small segments or circles, respectively.

$$4\pi u_\alpha(\boldsymbol{x}_0) - \int_{\mathcal{L}} C_{\alpha\beta}(\boldsymbol{x},\boldsymbol{x}_0)u_\beta(\boldsymbol{x})dl(\boldsymbol{x}) = -\frac{1}{\mu}\int_{\mathcal{L}} B_{\alpha\beta}(\boldsymbol{x},\boldsymbol{x}_0)(\gamma\nabla_S\cdot\boldsymbol{n} - \rho g z)n_\beta(\boldsymbol{x})dl(\boldsymbol{x}), \quad (21)$$

where $\mathcal{L}_n$ is the trace of the surface S_n and $\mathcal{L} = \cup_{m=0}^{N}\mathcal{L}_n$ the entire contour. The quantity dl in the $\phi = 0$ half-plane (see also Fig. 2) is the differential arc length. The resulting 2×2 square matrices $B_{\alpha\beta}(\boldsymbol{x}, \boldsymbol{x}_0)$ and $C_{\alpha\beta}(\boldsymbol{x}, \boldsymbol{x}_0)$, called single-layer and double-layer and available in Pozrikidis,[20] are written in Appendix A.

IV. NUMERICAL IMPLEMENTATION

The boundary-integral equation (14) and the relations (7) are solved using a collocation method and a discrete Wielandt's deflation technique. The implemented steps are described below.

A. Employed boundary elements and discretized boundary-integral equation

Following Muldowney and Higdon's,[27] the liquid contour $\mathcal{L} = \cup_{m=0}^{N}\mathcal{L}_n$ is divided into N_e curved boundary elements arranged to preserve the $x \rightarrow -x$ symmetry. Each element has two end points, and N_c collocation points spread by a uniform or Gauss distribution. As seen in Fig. 2, the end point of an element can (i) belong to two elements located off the axis of symmetry, or (ii) either be on the symmetry axis or (iii) be completely free at the tip of the truncated contour $\mathcal{L}_0$ modeling the free surface.

Isoparametric interpolations are employed for the location of a point $\boldsymbol{x}^{i_e}$ belonging to the boundary element i_e and for the approximation of the associated velocity $\boldsymbol{u}(\boldsymbol{x}^{i_e})$ and surface traction $\boldsymbol{f}(\boldsymbol{x}^{i_e})$ with

$$\boldsymbol{x}^{i_e} = \sum_{i_c=1}^{N_c} L_{i_c}(\zeta)\boldsymbol{x}_{i_c}^{i_e},\ \boldsymbol{u}(\boldsymbol{x}^{i_e}) = \sum_{i_c=1}^{N_c} L_{i_c}(\zeta)\boldsymbol{u}_{i_c}^{i_e},\ \boldsymbol{f}(\boldsymbol{x}^{i_e}) = \sum_{i_c=1}^{N_c} L_{i_c}(\zeta)\boldsymbol{f}_{i_c}^{i_e}, \quad (22)$$

where L_{i_c} designates the employed $(N_c - 1)$-order Lagrangian interpolant polynomial and ζ the variable on the segment [− 1, 1] onto which each boundary element is mapped. The quantities $\boldsymbol{n}\cdot\boldsymbol{e}_z$, $\boldsymbol{n}\cdot\boldsymbol{e}_r$ and $\nabla_S\cdot\boldsymbol{n}$ are also expressed at the point $\boldsymbol{x}^{i_e}$ in Appendix B. Collecting at our N_eN_c nodal points the components $(\rho\boldsymbol{g}\cdot\boldsymbol{x} + \gamma\nabla_S\cdot\boldsymbol{n})\boldsymbol{n}\cdot\boldsymbol{e}_\alpha$ and $\boldsymbol{u}\cdot\boldsymbol{e}_\alpha$ for $\alpha = r, z$ in prescribed and unknown $2N_eN_c$ vectors $\boldsymbol{F}$ and $\boldsymbol{U}$ and exploiting Eq. (22) makes it possible to cast the boundary-integral equation (21) into the $2N_eN_c$-equation linear system

$$\boldsymbol{U} - \boldsymbol{C}\cdot\boldsymbol{U} = \boldsymbol{B}\cdot\boldsymbol{F}. \quad (23)$$

Matrices $\boldsymbol{B}$ and $\boldsymbol{C}$ are given in Appendix B as integrals over the segment [−1, 1] involving the quantities $B_{\alpha\beta}(\boldsymbol{x}, \boldsymbol{x}_0)$ and $C_{\alpha\beta}(\boldsymbol{x}, \boldsymbol{x}_0)$ defined in Appendix A and are here accurately computed, by exploiting the polynomial approximations given in Abramowitz and Stegun,[28] of the complete elliptic integrals of the first and second kind (see also[20])

$$F(k) = \int_0^{\pi/2} \frac{d\phi}{(1 - k^2\cos^2\phi)^{1/2}},\qquad E(k) = \int_0^{\pi/2} (1 - k^2\cos^2\phi)^{1/2}d\phi. \quad (24)$$

One should note that the velocity $\boldsymbol{u}$ is unknown at each nodal point of the truncated and discretized free-surface contour $\mathcal{L}_0$. Therefore, the tips of this truncated free-surface are not fixed in the numerical computations.

B. Computation of the matrices *B* and *C*

The components of the matrices $\boldsymbol{B}$ and $\boldsymbol{C}$ are reduced if necessary to regular integrals. They are accurately computed as explained in Appendix B by employing the self-adaptative method proposed by Voutsinas and Bergeles.[29] Here, we iteratively divide a segment $[a, b]$ into equal or inequal subsegments. The encountered regular integral over each subsegment is calculated by employing classical Gauss quadratures. The iterative procedure is stopped as soon as the computed value of the integral reaches a prescribed relative accuracy between 10^{-3} to 10^{-4} (obtained in practice using three or four iterations).

C. Discrete Wielandt's deflation

As previously explained in Sec. III B, the linear system (23) involves the matrix $\boldsymbol{C}$ with a discrete spectrum having a finite number of eigenvalues in the interval [− 1, 1] and the eigenvalues close to unity prevent one to accurately invert Eq. (23). Here we remove the eigenvalues of $\boldsymbol{C}$ close to unity without affecting the other eigenvalues by implementing a so-called Wielandt's deflation.[21] We compute the (discrete) spectrum of the $\boldsymbol{C}$ matrix by the QR method,[30] select n_{λ_1} eigenvalues close to unity with associated eigenvector $\mathbf{V}_n$ for the adjoint with eigenvalue λ_n and introduce the new matrix $\boldsymbol{C}'$ as

$$\boldsymbol{C}' = \boldsymbol{C} - \sum_{n=1}^{n_{\lambda_1}} \lambda_n \boldsymbol{Z}_n \otimes \boldsymbol{V}_n,\quad \boldsymbol{Z}_n = \boldsymbol{V}_n/||\boldsymbol{V}_n||^2, \quad (25)$$

with $||\boldsymbol{V}_n||$ the discrete norm of the vector $\boldsymbol{V}_n$ calculated using the entire discretized surface $S = \cup_{m=0}^{N} S_n$. Since the

Author complimentary copy. Redistribution subject to AIP license or copyright, see http://phf.aip.org/phf/copyright.jsp

eigenvector $\boldsymbol{V}_n$ must be collinear on $\boldsymbol{S}$ to the normal vector $\boldsymbol{n}$, the scalar product of $\boldsymbol{V}_n \cdot (\boldsymbol{B} \cdot \boldsymbol{F})$ must be practically equal to zero and therefore the linear system (23) is replaced with the well-posed one

$$\boldsymbol{U} - \boldsymbol{C}' \cdot \boldsymbol{U} = \boldsymbol{B} \cdot \boldsymbol{F}, \tag{26}$$

which is solved by *LU* decomposition.[31]

D. Fluid interfaces tracking

Each surface's shape is tracked in time by exploiting the conditions (6). In practice, the knowledge of the fluid velocity at each collocation point at time t is used to move between times t and $t+dt$ the position of each nodal point $\boldsymbol{x}_{i_c}^{i_e}$ by integrating the equation

$$\frac{d\boldsymbol{x}_{i_c}^{i_e}(t)}{dt} = \boldsymbol{u}_{i_c}^{i_e}(t). \tag{27}$$

This is numerically achieved by using a Runge-Kutta-Fehlberg method. The time step is adapted by controlling the numerical error between the computations at a second and a third Runge-Kutta algorithms. The new time step is determined following the relationship

$$dt_{\text{new}} = dt \sqrt[3]{3 \frac{\varepsilon}{||\overline{\boldsymbol{x}}_{i_c}^{i_e}(t+dt) - \hat{\boldsymbol{x}}_{i_c}^{i_e}(t+dt)||}}, \tag{28}$$

where[32] $\varepsilon > 0$ is a predefined accuracy, $\overline{\boldsymbol{x}}_{i_c}^{i_e}(t+dt)$ and $\hat{\boldsymbol{x}}_{i_c}^{i_e}(t+dt)$ are the computed locations at the second and third orders, respectively. The set of coefficients required in the Runge-Kutta algorithms are taken from the book of Stoer and Bulirsch.[30]

As time evolves, collocation points have been seen to concentrate near a stagnation area (a bubble rear) of the bubble(s), therefore, yielding stretched and thus unsuitable mesh(es) for the bubble(s). Such issues are circumvented by redistributing from time to time the collocation points. In addition, the typical length of the boundary elements is adequately reduced in the area where two interfaces are close by distributing elements nonuniformly, following a geometric sequence.

V. NUMERICAL RESULTS

This section presents and discusses our numerical results for a few suitable benchmark tests and for the time-dependent shapes of the free surface and one, two, or three bubble(s). We study bubble-surface and bubble-bubble interactions act, and the competition between such interactions.

A. Benchmark tests

Three tests have been performed for one bubble.

1. Integral identities

According to (13), (17), and (18) and the symmetries of the stress tensor $\boldsymbol{T}$ (recall (11)), the following identities hold for arbitrary point $\boldsymbol{x}_0$ located on the bubble surface S

$$\int_S G_{ij}(\boldsymbol{x}, \boldsymbol{x}_0) n_i(\boldsymbol{x}) dS(\boldsymbol{x}) = 0, \tag{29}$$

$$\int_S T_{ijk}(\boldsymbol{x}, \boldsymbol{x}_0) n_k(\boldsymbol{x}) dS(\boldsymbol{x}) = -4\pi\delta_{ij}. \tag{30}$$

In the axisymmetric formulation, the bubble has an associated contour $\mathcal{L}$ (the trace of its surface S in the $\phi = 0$ half-plane) and the previous relations then become

$$I_\alpha^s = \int_{\mathcal{L}} B_{\alpha\beta}(\boldsymbol{x}, \boldsymbol{x}_0) n_\beta(\boldsymbol{x}) dl(\boldsymbol{x}) = 0, \tag{31}$$

for $\alpha = r, z$, and

$$I_{zz}^d = \int_{\mathcal{L}} C_{zz}(\boldsymbol{x}, \boldsymbol{x}_0) dl(\boldsymbol{x}) = -4\pi, \tag{32}$$

$$I_{rz}^d = \int_{\mathcal{L}} C_{rz}(\boldsymbol{x}, \boldsymbol{x}_0) dl(\boldsymbol{x}) = 0. \tag{33}$$

Indeed, the introduction of the velocity and unit normal in the polar reference frame leads to a composition of the Cartesian components T_{ijk}. Using the definition of $\boldsymbol{C}$ easily shows that (30) yields only relations (32) and (33) for the components C_{zz} and C_{rz}. By contrast to the tridimensional formulation,[14] it is therefore not possible to regularize the double-layer potential in Eq. (21) by solely using the identities (32) and (33).

The computed average (over all collocation points) of the absolute value of the "single-layer" integral I_α^s arising in Eq. (31) is displayed in Table I using $N_e = 1$, 4, and 16 boundary elements on a sphere with unit diameter, $N_c = 4$, 6, and 8 collocation points on each element and 8 Gauss points to compute integrals over each partition.

Clearly, a good convergence is observed with, for N_e and N_c large enough, a $O(10^{-7})$ error comparable with the

TABLE I. Average of the absolute value of the integral (a) I_r^s and (b) I_z^s versus the numbers N_e and N_c of boundary elements and collocation points on each element, respectively.

		(a) I_r^s				(b) I_z^s		
		N_g				N_g		
		4	6	8		4	6	8
N_e	1	$4.8 \cdot 10^{-2}$	$1.9 \cdot 10^{-2}$	$5.6 \cdot 10^{-3}$	N_e	$5.7 \cdot 10^{-2}$	$2 \cdot 10^{-2}$	$4.6 \cdot 10^{-3}$
	4	$2.3 \cdot 10^{-4}$	$1.3 \cdot 10^{-5}$	$1.5 \cdot 10^{-5}$		$2.1 \cdot 10^{-4}$	$4.1 \cdot 10^{-6}$	$5.6 \cdot 10^{-6}$
	16	$2.6 \cdot 10^{-6}$	$1.3 \cdot 10^{-6}$	$3.6 \cdot 10^{-6}$		$6 \cdot 10^{-7}$	$2.9 \cdot 10^{-7}$	$7.1 \cdot 10^{-7}$

Author complimentary copy. Redistribution subject to AIP license or copyright, see http://phf.aip.org/phf/copyright.jsp

TABLE II. Average of the absolute value of the quantity (a) $I^d_{zz}/4\pi - 1$ and (b) integral I^d_{rz} versus the numbers N_e and N_c of boundary elements and collocation points on each element.

		(a) $I^d_{zz}/4\pi - 1$				(b) I^d_{rz}		
		N_g				N_g		
		4	6	8		4	6	8
N_e	1	$1\cdot10^{-3}$	$1.8\cdot10^{-5}$	$6.1\cdot10^{-6}$	N_e	$2.5\cdot10^{-2}$	$2.8\cdot10^{-3}$	$3.1\cdot10^{-5}$
	4	$4.9\cdot10^{-4}$	$1\cdot10^{-5}$	$5.1\cdot10^{-7}$		$2.3\cdot10^{-3}$	$1.8\cdot10^{-5}$	$2.7\cdot10^{-6}$
	16	$7.6\cdot10^{-6}$	$6\cdot10^{-7}$	$3.1\cdot10^{-7}$		$5.8\cdot10^{-5}$	$4.3\cdot10^{-6}$	$3.7\cdot10^{-5}$

obtained accuracy in computing the elliptic integrals of first and second kind given, respectively, by Eq. (24) using Abramowitz and Stegun.[28]

Similar results for the "double-layer" average values of the quantities $I^d_{zz}/4\pi - 1$ and I^d_{rz} are given in Table II for the same bubble and values of the integers N_e and N_c. Again, a very good agreement with the theory is found.

2. Ascending bubble

As pointed out by Taylor and Acrivos[33] and Pan and Acrivos,[34] within our assumption of negligible inertial effects, a bubble immersed in an *unbounded* liquid having uniform surface tension γ and spherical shape with radius a at initial time remains spherical with radius a when ascending under the action of a uniform gravity $\boldsymbol{g} = -g\boldsymbol{e}_z$. The bubble translates at the velocity $\boldsymbol{u} = U\boldsymbol{e}_z$ with $U = \rho g a^2/(3\mu)$ whatever the Bond number $\mathrm{Bo} = \rho g a^2/(3\gamma)$ and at its surface the velocity components u_r and u_z read (this is the so-called Hadamard-Rybczynski solution[35,36])

$$u_r = U\frac{\sin 2\theta}{4}, \tag{34}$$

$$u_z = U\left(1 - \frac{\sin^2\theta}{2}\right), \tag{35}$$

with θ the angle between the vector $\boldsymbol{e}_z$ and the radial direction. Computed values of u_r/U and u_z/U for $\mathrm{Bo} = 1000$ are compared against the analytical solutions (34)–(35) in Figs. 3 and 4.

Numerical results perfectly match the analytical ones even with the coarsest grid. Actually, the computed average relative error is order 0.1% when $N_e = 4$ and becomes order 10^{-3}% for refined meshes $N_e = 8, 20$.

3. Discrete spectrum of the discretized operator C

As mentioned in Sec. IV, a key step in accurately inverting the discretized system (23) is the computation of the eigenvalues λ of the linear operator $\boldsymbol{C}$. First, we consider a spherical bubble distant from the free surface. Using Lamb's solutions, Kim and Karrila[21] theoretically predicted these values to be

$$\lambda_n^- = \frac{-3}{(2n-1)(2n+1)}, \quad n = 1, 2, \ldots, \tag{36}$$

$$\lambda_n^+ = \frac{3}{(2n+1)(2n+3)}, \quad n = 0, 1, \ldots. \tag{37}$$

The computed values are compared with Eqs. (36)–(37) in Fig. 5 for different meshes of the bubble contour. For a given mesh, there is only one eigenvalue close to unity.

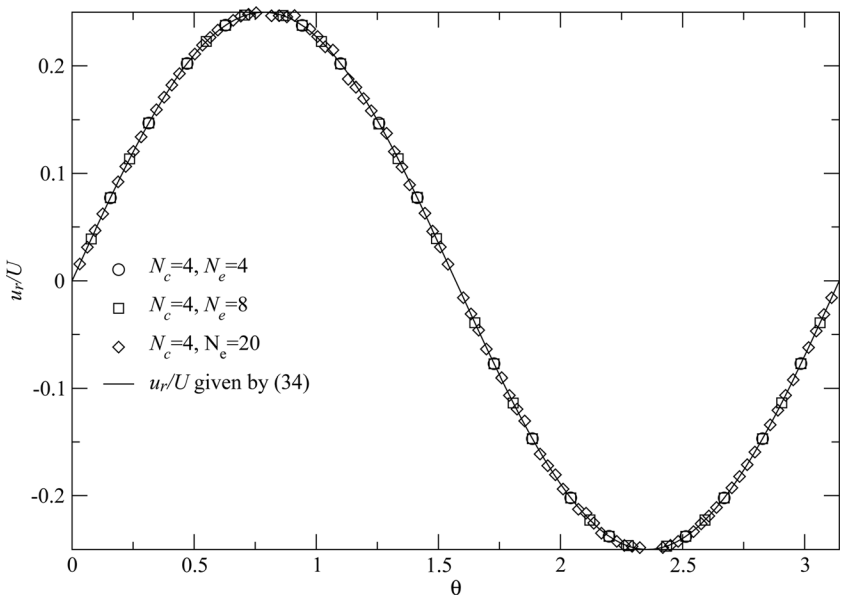

FIG. 3. Normalized velocity u_r/U velocity versus θ computed for $\mathrm{Bo} = 10^3$; $N_e = 4$, 8, 20; and $N_c = 4$. The analytical solution (34) is given by the solid line.

Author complimentary copy. Redistribution subject to AIP license or copyright, see http://phf.aip.org/phf/copyright.jsp

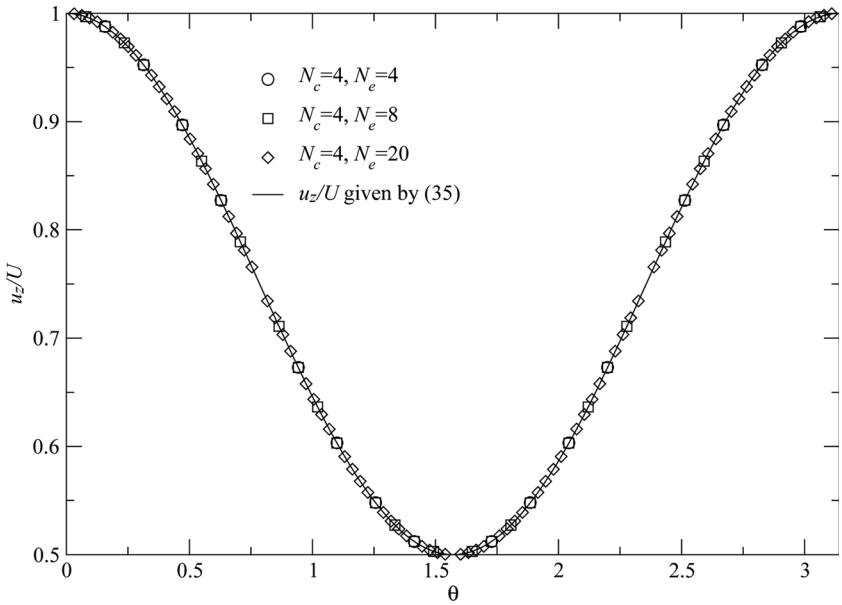

FIG. 4. Normalized velocity u_z/U velocity versus θ computed for $\mathrm{Bo} = 10^3$; $N_e = 4$, 8, 20; and $N_c = 4$. The analytical solution (35) is given by the solid line.

When the bubble approaches a free surface for a similar number of collocation points, there is a similar number of discrete eigenvalues, but these values tend to concentrate near the end point -1 and $+1$ as the gap between the free surface and the bubble decreases. This trend is clearly observed in Fig. 6 both for undeformed and deformed liquid surfaces. In such circumstances, one needs to apply Wielandt's deflation to all eigenvalues located close to unity.

B. Results for one bubble

Here, we consider the motion of one bubble toward a fluid interface under buoyancy effects. As mentioned in the Introduction, this case is encountered in various applications, such as in glass melting. For instance, the axisymmetric film drainage between a droplet and a free surface has been studied by Chi and Leal,[10] using a boundary integral formulation. However, Chi and Leal confined the investigations to droplets with a non-zero viscosity ratio between fluid inside the droplet and fluid outside. In the present work, the case of bubbles rising toward a fluid interface can be studied.

In practice, it is easier to work under dimensionless form. At initial time, the bubble is spherical with radius a. We henceforth take, respectively, $2a$, $U = \rho g a^2/(3\mu)$, and $2a/U = 6\nu/(ga)$ as length, velocity, and time scales. The normalized surface traction $\boldsymbol{f}$ using Eq. (5) and setting $p_1 = 0$ in the bubble then reads

$$\boldsymbol{f} = \left(\frac{\nabla_S \cdot \boldsymbol{n}}{\mathrm{Bo}} - 12z\right)\boldsymbol{n}, \tag{38}$$

with Bo, the Bond number, defined as

$$\mathrm{Bo} = \frac{\rho g a^2}{3\gamma}. \tag{39}$$

Here, we concentrate on the film drainage between the bubble and the free surface, which takes place after a pure rising regime of the bubble. Of course, both bubble and free

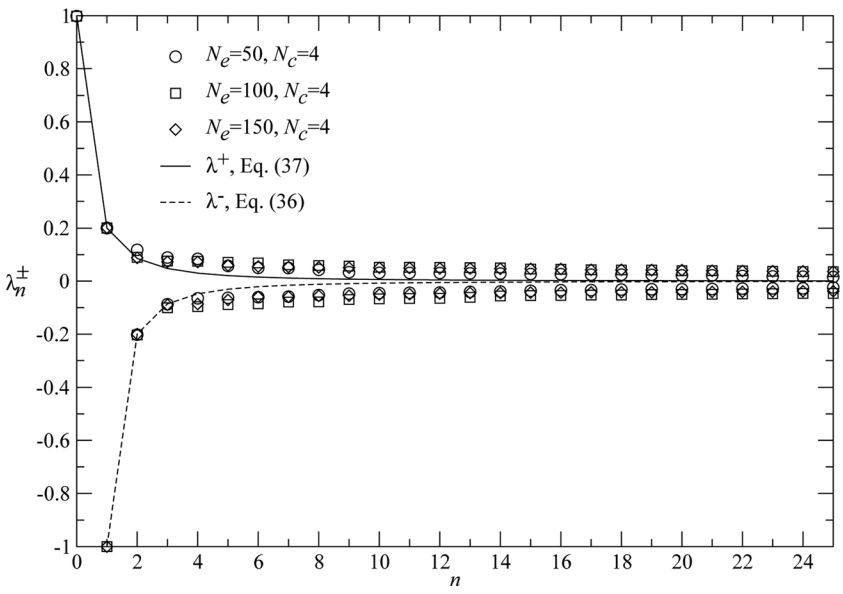

FIG. 5. Computed eigenvalues and analytical predictions (36)–(37) for a spherical bubble immersed in an unbounded liquid.

Author complimentary copy. Redistribution subject to AIP license or copyright, see http://phf.aip.org/phf/copyright.jsp

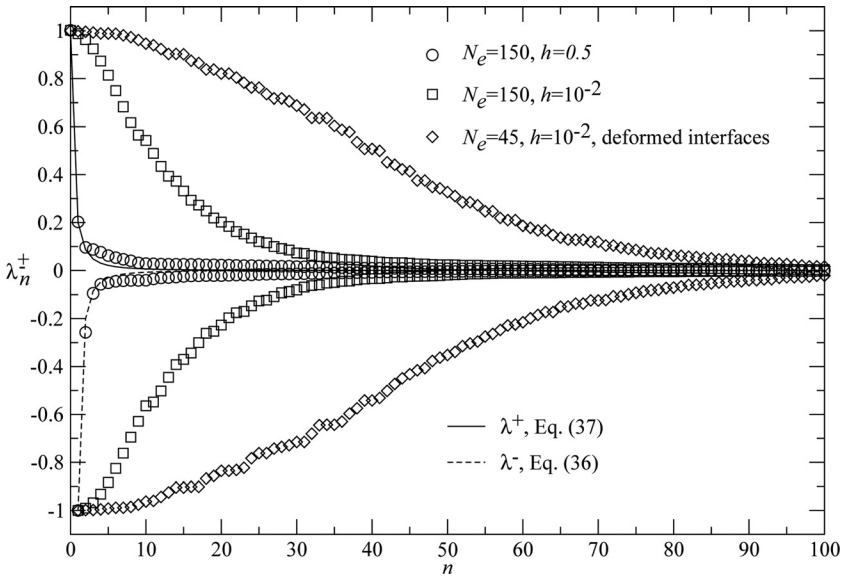

FIG. 6. Computed eigenvalues for a spherical or nonspherical bubble close to a free surface and comparisons with Eqs. (36)–(37) for a spherical bubble immersed in an unbounded liquid.

surface interfaces are likely to depend upon the initial location and shape of the bubble. In our numerical procedure, the free surface is moreover truncated and we therefore carefully investigate to which extent both the initial location of the bubble and the size of the truncated free surface affect the results.

Henceforth, the film thickness h designates the gap (normalized by $2a$) on the z-axis between the bubble surface and the free surface (note that $h = h_1/(2a)$ with h_1 shown in Fig. 1).

The bubble and free surface interfaces are tracked as explained in Sec. IV, using a self-adapted time step. More precisely, when the bubble is far from the interface, the time step is large and nearly constant between two time iterations. In contrast, when the bubble is very close to the free surface, the prescribed accuracy requires to decrease the time step. In practice, numerical computations are stopped as soon as the film thickness reaches a value of order 10^{-2}, or whenever the time step suitable to guarantee a prescribed accuracy becomes too small.

1. Sensitivity to the domain truncation

Numerical simulations[37] have been achieved at $\mathrm{Bo} = 10$, with initial gap between the spherical bubble and the flat (undeformed) interface equal to 1/2. The effect of the domain truncation has been first investigated by running simulations for a fluid interface extending over 5 and 10 bubble diameters using, respectively, 20 and 25 boundary elements on the bubble and on the free surface interfaces. The number N_c of collocation points (see Sec. IV) is equal to 4.

Fig. 7 presents for these numerical simulations both the film thickness h and the relative error $\Delta\mathcal{V}(t) = \mathcal{V}(t)/\mathcal{V}(0) - 1$ for the preserved bubble volume $\mathcal{V}(t)$, see Eq. (7).

Starting from a value equal to 0.5, h is seen to rapidly decrease at small time when the bubble is free to rise. For $t \gtrsim \mathcal{O}(1)$, the film thickness h slowly drops due to the drainage of the liquid between the very close interfaces of the bubble and of the free surface. The two numerical investigations clearly yield very close results. Therefore, truncating the free surface at a distance exceeding five bubble diameters appears to be sufficient.

2. Sensitivity to the bubble initial location

This time, numerical simulations are performed with two different initial locations of the bubble below the fluid interface, whereas the free surface is truncated at 5 bubble

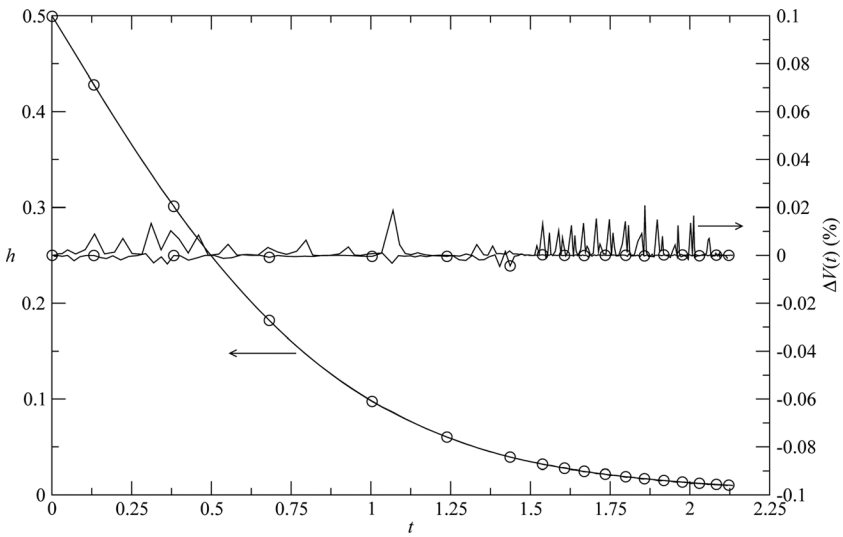

FIG. 7. Film thickness h and relative error of $\Delta\mathcal{V}(t)$ for the bubble volume as a function of time for a fluid interface truncated at a distance equal to 10 bubble diameters (—) and equal to 5 bubble diameters (○—○). Here, $\mathrm{Bo} = 10$ and the initial distance between the spherical bubble and the flat interface is 1/2.

Author complimentary copy. Redistribution subject to AIP license or copyright, see http://phf.aip.org/phf/copyright.jsp

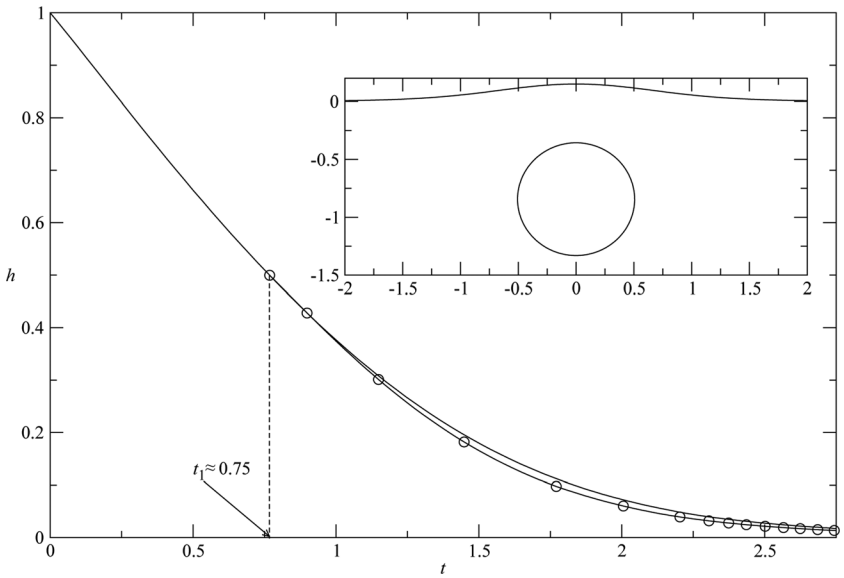

FIG. 8. Film thickness h versus time t for a bubble located initially at $h(0) = 1$ (—) and for a bubble located initially at $h(0) = 1/2$ (○—○) with $\mathrm{Bo} = 10$. The distant bubble is located at $h = 1/2$ at $t_1 \approx 0.75$ as depicted in the inset.

diameters. The numbers of boundary elements are identical to the previous calculations and again $N_c = 4$ and $\mathrm{Bo} = 10$.

Fig. 8 plots h versus time t for two bubbles: a distant one ($h = 1$ at $t = 0$) and another one starting from $h = 1/2$. More precisely, the distant bubble rises with $h = 1/2$ at time $t_1 \approx 0.75$, at which we let the other bubble start its motion (as illustrated in Fig. 8). The first stage of the bubble started from $h = 1/2$ with undeformed interfaces is slightly different from the case where the bubble is initially located at $h = 1$. Nevertheless, after the rising step, the two curves present the same trend.

The numerical value $t_1 \approx 0.75$ at which the distant bubble starting at $h = 1$ arrives at $h = 1/2$ is in good agreement with the typical rising velocity of a bubble. Indeed, as shown in Sec. V B 4, h obeys Eq. (41) for non-deformable interfaces. Solving Eq. (41) for weak hydrodynamic interactions then shows that the time to reduce h of 1/2 is 3/4, which is very close to t_1.

In view of the previous results, computations are henceforth achieved with an initial bubble-interface gap of one bubble radius and by truncating the interface beyond 5 bubble diameters.

3. *Bubble shape's sensitivity to the Bond number* Bo

As already pointed out, two different steps are observed in the bubble motion. The first one is the free rising of the bubble, which depends on its hydrodynamic interactions with the fluid interface. The second one is the key drainage step, in which the bubble is nearly at rest. In this second stage, the bubble's shape is driven by the competition between the buoyancy and surface tension forces. Consequently, the bubble's shape is a function of the Bond number. This shape has been determined by Princen[3] for a drop very close to the fluid interface by requiring the hydrostatic pressure balance.

Fig. 9 presents bubble's shapes when the bubble is nearly at rest for Bond numbers equal to 0.1, 1, and 10. Bubble's shapes predicted by the Princen's model are also drawn in Fig. 9 using dashed lines.

For the weak value of the Bond number, $\mathrm{Bo} = 0.1$, gravity effects are small compared with surface tension effects, and as seen in Fig. 9(a), the bubble remains nearly spherical when rising and the free surface is weakly deformed. By contrast, as Bo increases both the free surface and the bubble interface are affected and the bubble shape becomes non-spherical and evolves from a lens at $\mathrm{Bo} = 1$, see Fig. 9(b) to a quasi-hemispherical form at $\mathrm{Bo} = 10$, Fig. 9(c). In any case, the bubble however keeps its volume constant as retrieved by the numerics (see the given relative error volume given in Fig. 9 caption).

The area where the drainage is at play increases with the Bond number, and shrinks as the Bond number decreases. It tends to zero when $\mathrm{Bo} = 0$. A plateau is observed for the drainage area at very large Bo. From this variety of shapes of bubbles, we can expect to see the influence of the Bond number on the film drainage.

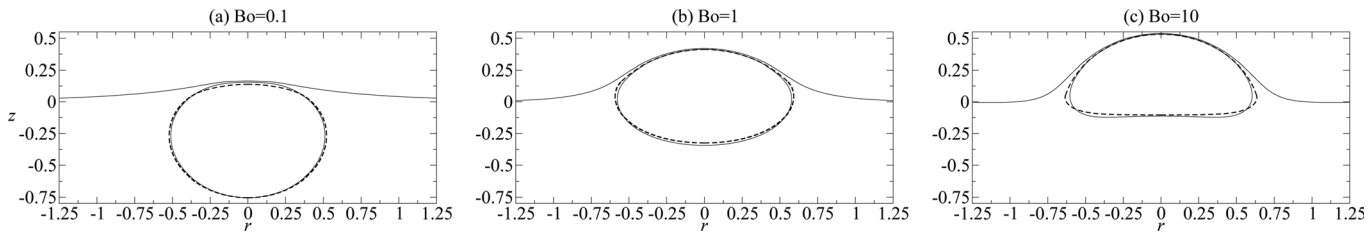

FIG. 9. Bubble shape close to the free surface at (a) $\mathrm{Bo} = 0.1$ with $\Delta\mathcal{V} = -1.1 \cdot 10^{-3}\%$, (b) $\mathrm{Bo} = 1$ with $\Delta\mathcal{V} = 1.7 \cdot 10^{-4}\%$ and (c) $\mathrm{Bo} = 10$ with $\Delta\mathcal{V} = 2.4 \cdot 10^{-5}\%$. Dashed lines indicate the bubble shapes predicted by Princen.[3]

Author complimentary copy. Redistribution subject to AIP license or copyright, see http://phf.aip.org/phf/copyright.jsp

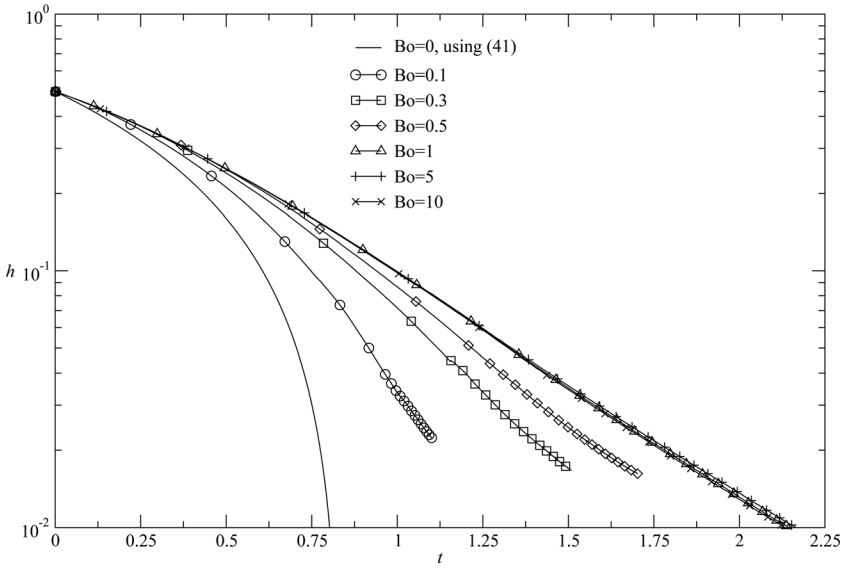

FIG. 10. Film thickness h versus time t at Bo = 0.1, 0.3, 0.5, 1, 5, 10. The solution for Bo = 0 is obtained by the integration of Eq. (41).

4. Dependence of the film drainage upon the Bond number

Additional calculations have been carried out for various Bond numbers in the range [0.1, 10], using the same initial position and identical discretization. Again, numerical simulations are performed until the dimensionless film thickness reaches a value of order 10^{-2} whenever possible. As seen in Fig. 10, where h versus t for various Bond numbers is plotted, it is easy to reach the thickness equal to 10^{-2} when $\mathrm{Bo} \gtrsim 1$. In contrast, for smaller Bond number, the 10^{-2} accuracy is difficult to reach. Consequently, the numerical computation is stopped before that h decreases below 10^{-2}.

The use of a log-scale on the h axis suggests that the film drainage behaves as an exponential function of time in the drainage regime, $t \gtrsim \mathcal{O}(1)$. This trend contrasts with the one observed on a viscous drop for which Chi and Leal[10] proposed a rapid drainage when the drop viscosity is small compared with the liquid viscosity, neutral drainage for equivalent viscosities, and slow drainage for highly viscous drops. Nevertheless, in this last situation, one observes an algebraic evolution of the film drainage as a function of time. For the bubble, the drainage is actually faster because the gas inside and above the fluid interface has no effect on the tangential stress balance. The drainage of a bubble in a highly viscous liquid has been experimentally investigated by Debrégeas *et al.*,[8] and these authors report an exponential behavior of the film drainage for a bubble suspended in a silicon oil.

As previously suggested, the Bond number has a strong influence on the drainage: the drainage rate increases when Bo decreases (see Fig. 10). When the Bond number is larger or equal to one, the film drainage is very similar. At a first glance, such a trend is amazing. However, since gas does not resist to the flow, the drainage is solely related to the flow in the film. As suggested by the exponential behavior of the film drainage, within the film the flow is a plug flow as it can be shown using lubrication arguments.[9] In this limit, the drainage is limited by the extensional viscous force, which is more important as the Bond number increases.

As Bo vanishes (for instance for high surface tension or a very small bubble), the fluid interfaces do not deform. In this limit, it is therefore possible to obtain h versus time by employing the exact Stokes flow solution established in Bart[38] by appealing to the bispherical coordinates procedure. For this purpose, the force balance applied on the bubble can be used. For a spherical bubble with a velocity $\boldsymbol{U}$ normal to the flat interface and a gap h, the experienced drag force reads

$$\boldsymbol{F}_d = -6\pi\mu a\lambda_d(h)\boldsymbol{U}, \tag{40}$$

where the drag coefficient λ_d describes the hydrodynamic interaction between the spherical bubble and the flat fluid interface. This quantity tends to 2/3 when h becomes large. In our axisymmetric case, the force balance between the drag and buoyancy forces, under the dimensionless form, yields

$$\lambda_d(h)\frac{dh}{dt} = -\frac{2}{3}. \tag{41}$$

The behavior of λ_d for h small can be obtained using the method proposed by Cox and Brenner.[39] Taking the drag coefficient given by Bart,[38] λ_d behaves as

$$\lambda_d = \frac{2}{3}\left(\gamma_E - \frac{\ln h}{2}\right), \tag{42}$$

with $\gamma_E \approx 0.57721$ the Euler's constant.[28] By virtue of Eq. (42), λ_d diverges as h tends to zero, but the occurring logarithmic singularity is soft. Moreover, the introduction of the last equation in Eq. (41) gives the following implicit equation for h:

$$\left(\gamma_E + \frac{1}{2}\right)h + h\ln h = \left(\gamma_E + \frac{1}{2}\right)h_0 + h_0\ln h_0 - t, \tag{43}$$

where h_0 is the film thickness for $t = 0$. This relationship predicts the film rupture in a finite time and mainly explains why the film drainage is faster when the fluid interfaces are undeformed.

Author complimentary copy. Redistribution subject to AIP license or copyright, see http://phf.aip.org/phf/copyright.jsp

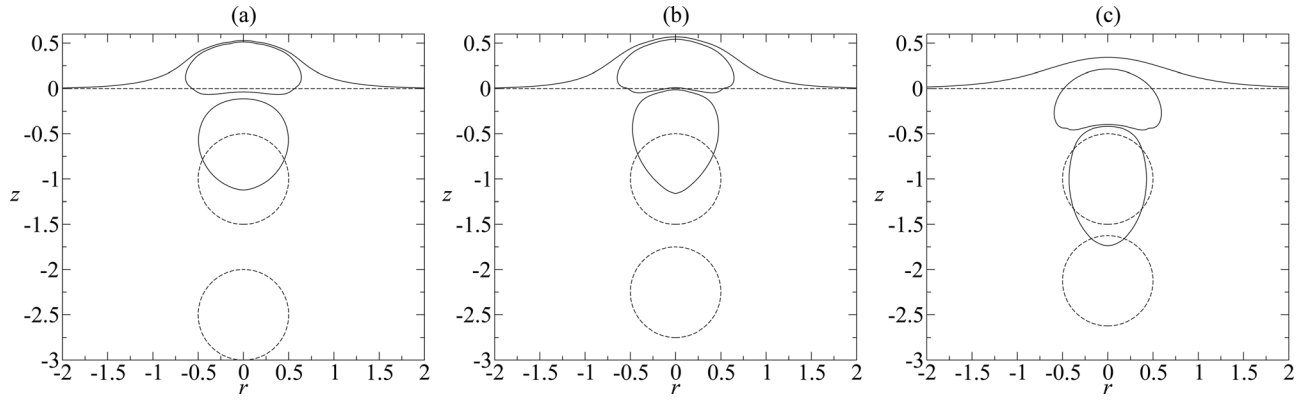

FIG. 11. Bubble shapes for (a) $h_2 = 1/2$, (b) $h_2 = 1/4$, and (c) $h_2 = 1/8$ at $t = 0$ and $\mathrm{Bo} = 1$. Solid lines represent the interfaces at the end of the computation. The dashed lines indicate each initial interface contour.

This conclusion contrasts with this one given by Howell,[9] who argued that the film behaves as an algebraic function of time when the Bond number is small considering that the gravity force is negligible. However, even if the Bond number is very small, the buoyancy term is still important as we can see in Eq. (41). Consequently, the drainage for a rising bubble takes place under a constant force corresponding to buoyancy effect. This conclusion should be different for a drainage obtained for constant velocity.

C. Results for two and three bubbles

So far, our attention has been restricted to the motion of one bubble moving toward a free surface. In this section, the proposed numerical method is used to investigate the axisymmetric drainage of two or three bubbles. Note that adding one or two bubble(s) however increases the number of involved parameters such as each bubble radius, and initial gaps between the bubbles. Whenever possible, each simulation is stopped as soon as the minimum normalized gap between bubbles is order 10^{-2}.

1. Sensitivity to the initial bubble-bubble gaps

The numerical procedure has been applied to the case of two bubbles rising toward a free surface. As depicted in Fig. 1, the bubble 1 is the closest one to the free surface. The film thickness between the free surface and the first bubble is denoted by h_1 whilst h_2 designates the gap between the two bubbles. The sensitivity to the initial gap between the two bubbles is addressed for identical bubbles and $\mathrm{Bo} = 1$. For each simulation, the initial value of h_1 is 1/2 and we use 20 and 25 boundary elements with 4 collocation points ($N_c = 4$) on each bubble and the free surface, respectively.

Fig. 11 shows each bubble shape when the initial distance between the two bubbles is (a) $h_2 = 1/2$, (b) $h_2 = 1/4$, and (c) $h_2 = 1/8$ at $t = 0$, respectively. As seen in Fig. 11(a), the first bubble is more deformed than when alone for an equivalent Bond number since the second bubble pushes it toward the free surface. In addition, the film drainage clearly acts between the free surface and the first bubble well before it takes place between the two bubbles.

These trends change when the initial gap h_2 decreases. For instance, Fig. 11(b) shows that for $h_2(t = 0) = 1/4$ the second bubble is this time more deformed and the drainage occurs almost simultaneously above and below the first bubble. As revealed by Fig. 11(c), for $h_2(t = 0) = 1/8$, the second bubble is more and more elongated as if it is sucked by the prior bubble, and the drainage occurs first between the two bubbles.

The film drainage is analyzed by plotting in Fig. 12 the film thicknesses h_1 and h_2 versus time for each addressed initial condition. As for a single bubble, the film drainage, h_1, decreases exponentially with time. For initial thickness $h_2(t = 0) = 1/2$ and 1/4, h_2 stays stable until a time approximately equal to 0.5 and further decreases with the same behavior as h_1. In Fig. 12(b), when $t \gtrsim 0.75$, the film thicknesses present a similar behavior.

2. Sensitivity to the bubble sizes

The influence of bubble sizes is investigated taking two unequal bubbles: a small one with radius $a/2$ and a big one

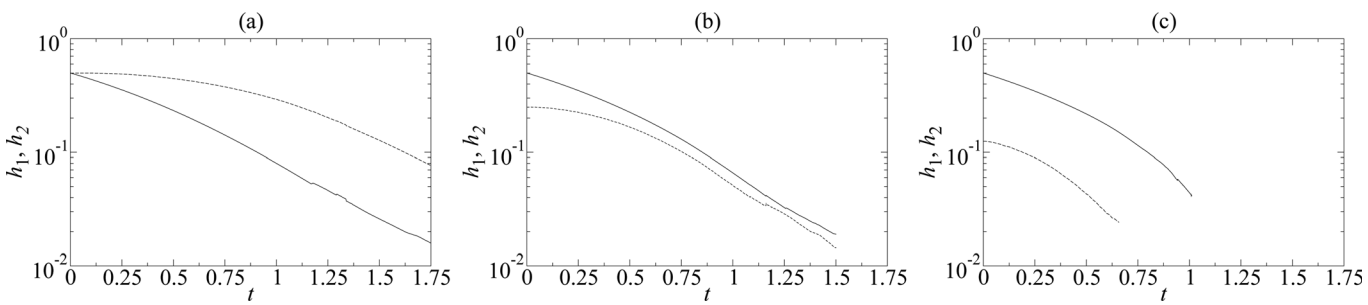

FIG. 12. Film thicknesses h_1 (solid line) and h_2 (dashed line) versus time for two bubbles when the initial distance between the two bubbles are (a) $h_2 = 1/2$, (b) $h = 1/4$, and (c) $h = 1/8$ and $\mathrm{Bo} = 1$.

Author complimentary copy. Redistribution subject to AIP license or copyright, see http://phf.aip.org/phf/copyright.jsp

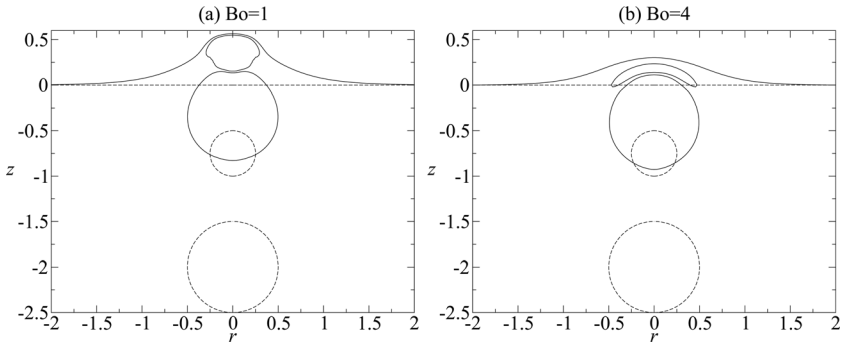

FIG. 13. Bubble shapes for Bo = 1 (a) and Bo = 4 (b). Solid lines indicate the interfaces at the end of the computation when $\min(h_1, h_2) \approx \mathcal{O}(10^{-2})$. The dashed lines are initial interfaces.

with radius a. One sets $\mathrm{Bo} = \rho g a^2/(3\gamma)$ and still takes $2a$, $U = \rho g a^2/(3\mu)$, and $2a/U$ as length, velocity, and time scales, respectively. Note that the Bond number based on the small bubble diameter is Bo/4. To study the influence of the Bond number, computations have been done for Bo = 1 and 4. The resulting interface shapes are given in Fig. 13. As seen in Fig. 13(a), bubbles are weakly deformed for Bo = 1, especially the (big) bubble 2. The small bubble 1 is found to exhibit two different curvatures: one on the top driven by the film drainage with the free surface and the second on the bottom due to the approaching second bubble. For Bo = 4, different shapes are obtained as seen in Fig. 13(b). For instance, observe that the big bubble is less deformed at Bo = 4 than at Bo = 1! The small bubble for Bo = 4 becomes thin and is stretched above and near the big bubble. It therefore screens the interactions between the free surface and the big bubble.

The film thicknesses h_1 and h_2 are given in Fig. 14 for these Bond numbers. For Bo = 1, the film thicknesses present similar behaviors. Observe that h_1 decreases faster than h_2 due to the pushing by the second bubble. When Bo = 4, the film drainage is smaller than the one observed when Bo = 1 both for h_1 and h_2. The sensitivity of the film drainage to Bo that we found for a single bubble is thus still valid for two bubbles.

3. Film drainage sensitivity to the number of bubbles and Bo

In this subsection, we consider three equal bubbles rising toward the free surface. The distance between successive bubbles is equal to 1/2 as well as the gap between the free surface and the first bubble. Again, computations are actually stopped here at time at which $\min(h_1, h_2, h_3) \approx 10^{-2}$. First, we examine the influence of the Bond number on the interface shapes by giving in Fig. 15 the free surface and bubble shapes for Bo = 0.1, 0.5, and 1.

For the smallest Bond number, all bubbles remain quasi-spherical, and the free surface is weakly deformed. As the Bond number increases, the first bubble is more and more deformed and takes a lens form. The second bubble is more and more deformed near its rear (lower side) whereas the last bubble undergoes the sucking of the previous bubble. This behavior is similar to the one observed for two bubbles. Actually, the last bubble is only sucked by the preceding bubble leading to the elongation.

The influence of the bubble number on the film drainage between the free surface and the first bubble is addressed by plotting in Fig. 16 for one, two, and three bubbles the film thickness h_1 versus time t still for Bo = 0.1, 0.5, and 1.

As observed for one bubble, and two and three bubbles, the film thickness h_1 exhibits an exponential decay beyond the free rising regime of the first bubble. Adding one bubble increases the film drainage as clearly shown in Fig. 16(a) when Bo = 0.1. Actually, at low Bond number, a second bubble has a very small influence on the shape of the first bubble located near the free surface but has a strong influence on the film drainage taking place between this first bubble and the free surface interface. This is because the second bubble pushes the first one toward the free surface, thereby initiating earlier the film drainage than in the case of a single bubble. In addition, the increase of the thinning rate with two bubbles is less pronounced when the Bond number increases, and the presence of a third bubble only weakly affects the thinning rate when the Bond number exceeds 0.5.

VI. CONCLUSIONS

This work examines the axisymmetric motion of a bubble chain rising toward a free surface. For this purpose, a relevant boundary-integral approach has been both proposed and carefully implemented. The numerical procedure is based on a discretization of boundaries, using discontinuous elements with variables interpolated using Lagrangian polynomials. Furthermore, a well-posed regular linear system is obtained by using a discrete Wielandt's deflation.

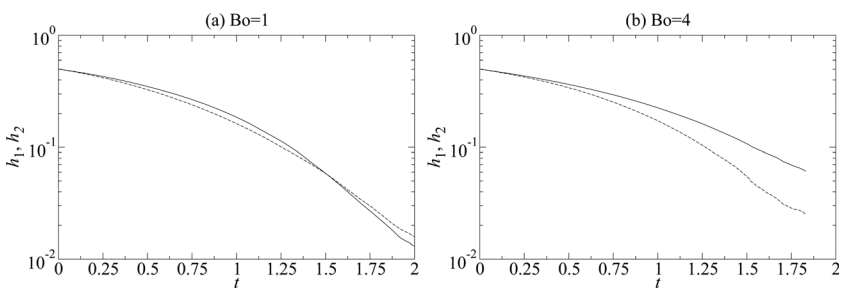

FIG. 14. Film thicknesses h_1 (solid line) and h_2 (dashed line) versus time for the two bubbles for Bo = 1 (a) and Bo = 4 (b).

Author complimentary copy. Redistribution subject to AIP license or copyright, see http://phf.aip.org/phf/copyright.jsp

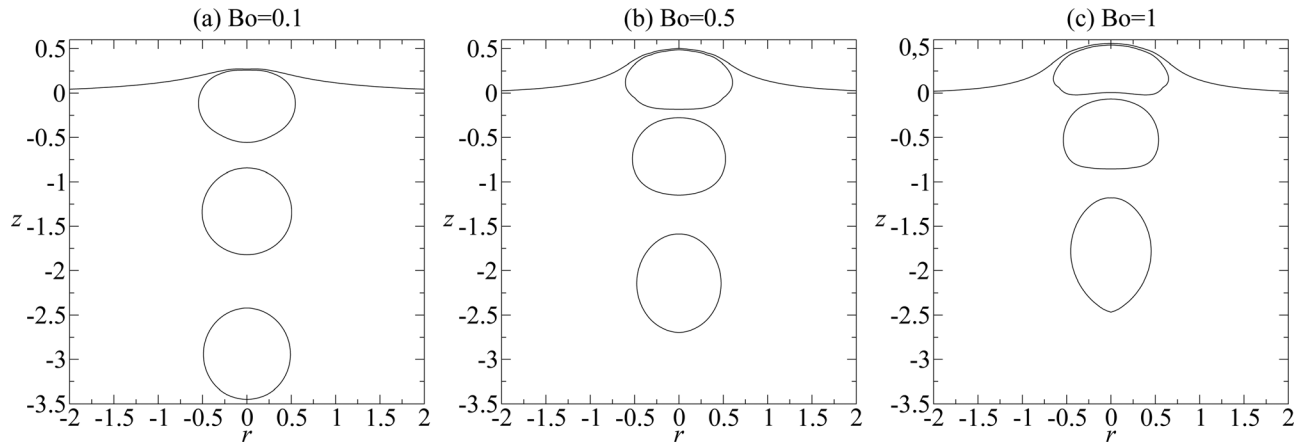

FIG. 15. Interface shapes for three rising bubbles at (a) Bo = 0.1 and (b) Bo = 0.5.

The numerical procedure has been tested against some integral identities verified by the Green functions, the rise of a bubble in an infinite media, and the computation of discrete eigenvalues of the double-layer potential of the Stokes equations.

The rise of a bubble toward a free surface has been investigated, with a special attention paid to the film drainage between the bubble interface and the free surface. When close to the free interface, the bubble is found to adapt a quasi-static shape. The obtained bubble shapes have been compared with the results given by Princen.[3] The thinning rate appears to behave as an exponential function of time, in agreement with prior experimental results obtained by Debrégeas *et al.*[8] The basic influence of the Bond number (ratio of the gravity force to the surface tension force) has been clearly revealed by the computation. More precisely, at small Bond number, the drainage is fast, mainly because of the weak deformation of fluid interfaces. For a sufficiently large Bond number (larger than 1 with a definition used in this article), the film drainage becomes independent of the Bond number.

Computations with one or two additional bubble(s) have also been performed. The initial distance between bubbles is found to affect mainly the deformation of the last bubble, because of the sucking of the first bubble. However, introducing one or two bubble(s) does not dramatically change the general behavior of the film drainage of the first bubble, which still exhibits an exponential thinning. Finally, the film drainage is seen to decrease with the Bond number.

As explained in this work, when the Bond number Bo is zero, the collapse of the liquid film between the bubble interface and the free surface occurs in a finite time obtained by solving Eq. (41). For a weak and non-zero Bond number, it is this time necessary to approximate the drag force exerted on the bubble for a slightly deformed bubble and fluid interface, in order to gain a modified equation (41) and the thin film collapse time. Such a challenging task is postponed to future investigations.

APPENDIX A: SIMPLE AND DOUBLE-LAYER OPERATORS IN AXISYMMETRIC FORMULATION

For $\boldsymbol{x}_0$ and $\boldsymbol{x}$ having cylindrical coordinates (r_0, z_0) and (r, z), respectively, one gets[20]

$$B_{zz}(\boldsymbol{x},\boldsymbol{x}_0) = r\left(I_{10} + \hat{z}^2 I_{30}\right), \quad B_{zr}(\boldsymbol{x},\boldsymbol{x}_0) = r\hat{z}(rI_{30} - r_0 I_{31}), \tag{A1}$$

$$\begin{aligned} B_{rz}(\boldsymbol{x},\boldsymbol{x}_0) &= r\hat{z}(rI_{31} - r_0 I_{30}),\\ B_{rr}(\boldsymbol{x},\boldsymbol{x}_0) &= r\left[I_{11} + (r^2 + r_0^2)I_{31} - r_0 r(I_{30} + I_{32})\right], \end{aligned} \tag{A2}$$

with $\hat{z} = z - z_0$ for the single-layer matrix and, setting $\boldsymbol{n}(\boldsymbol{x}) = n_r\boldsymbol{e}_r + n_z\boldsymbol{e}_z$, the relations

$$C_{zz}(\boldsymbol{x},\boldsymbol{x}_0) = -6r\hat{z}^2[\hat{z}I_{50}n_z + (rI_{50} - r_0 I_{51})n_r], \tag{A3}$$

$$\begin{aligned} C_{zr}(\boldsymbol{x},\boldsymbol{x}_0) = -6r\hat{z}[&\hat{z}(rI_{50} - r_0 I_{51})n_z\\ &+ (r_0^2 I_{52} + r^2 I_{50} - 2rr_0 I_{51})n_r], \end{aligned} \tag{A4}$$

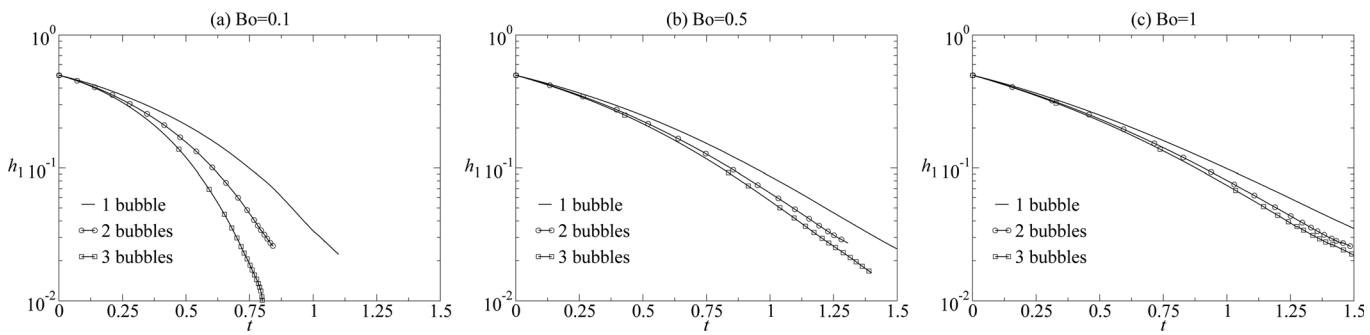

FIG. 16. Film thickness h_1 versus time for one, two, and three bubbles for Bo = 0.1 (a), 0.5 (b), and 1 (c).

Author complimentary copy. Redistribution subject to AIP license or copyright, see http://phf.aip.org/phf/copyright.jsp

$$C_{rz}(\boldsymbol{x},\boldsymbol{x}_0) = -6r\hat{z}\{\hat{z}(rI_{51} - r_0I_{50})n_z + [(r^2 + r_0^2)I_{51} - rr_0(I_{50} + I_{52})]n_r\}, \quad \text{(A5)}$$

$$C_{rr}(\boldsymbol{x},\boldsymbol{x}_0) = -6r\{\hat{z}[(r^2 + r_0^2)I_{51} - rr_0(I_{50} + I_{52})]n_z + [r^3I_{51} - r^2r_0(I_{50} + 2I_{52}) + rr_0^2(I_{53} + 2I_{51}) - r_0^3I_{52}]n_r\}, \quad \text{(A6)}$$

for the double-layer matrix with previous quantities I_{mn} defined as

$$I_{mn}(r,r_0,\hat{z}) = \frac{4k^m}{(4rr_0)^{m/2}}\int_0^{\pi/2}\frac{(2\cos^2\phi - 1)^n}{(1 - k^2\cos^2\phi)^{m/2}}d\phi, \qquad k^2 = \frac{4rr_0}{\hat{z}^2 + (r + r_0)^2}. \quad \text{(A7)}$$

APPENDIX B: MATERIAL FOR THE NUMERICAL IMPLEMENTATION

At a point $\boldsymbol{x}^{j_e}$ with coordinate ζ in the segment $[-1, 1]$ and located on the boundary element j_e, we denote by $l'_{j_e}(\zeta) = \{z'^2_{j_e}(\zeta) + r'^2_{j_e}(\zeta)\}^{1/2}$ the differential arc length where primes indicate differentiation. One then gets

$$n_z(\boldsymbol{x}^{j_e}) = -\frac{r'_{j_e}(\zeta)}{l'_{j_e}(\zeta)}, \quad n_r(\boldsymbol{x}^{j_e}) = \frac{z'_{j_e}(\zeta)}{l'_{j_e}(\zeta)}, \qquad \nabla_S\cdot\boldsymbol{n}(\boldsymbol{x}^{j_e}) = \frac{z'_{j_e}}{r_{i_e}\sqrt{z''_{j_e} + r''_{j_e}}} + \frac{r'_{j_e}z''_{j_e} - z'_{j_e}r''_{j_e}}{(z''_{j_e} + r''_{j_e})^{3/2}}. \quad \text{(B1)}$$

Furthermore, the matrices $\boldsymbol{B}$ and $\boldsymbol{C}$ occurring in Eq. (23) consist of $N_e \times N_e$ square block of order $2N_c \times 2N_c$ with coefficients

$$B^{i_ej_e}_{\alpha\beta;i_cj_c} = -\frac{1}{4\pi}\int_{-1}^{1} B_{\alpha\beta}(\boldsymbol{x}^{j_e},\boldsymbol{x}^{i_e}_{i_c})L_{j_c}(\zeta)l'_{j_e}(\zeta)d\zeta, \quad \text{(B2)}$$

$$C^{i_ej_e}_{\alpha\beta;i_cj_c} = \frac{1}{4\pi}\int_{-1}^{1} C_{\alpha\beta}(\boldsymbol{x}^{j_e},\boldsymbol{x}^{i_e}_{i_c})L_{j_c}(\zeta)l'_{j_e}(\zeta)d\zeta \quad \text{for } i_e \neq j_e, \quad \text{(B3)}$$

$$C^{i_ei_e}_{\alpha\beta;i_cj_c} = \frac{1}{4\pi}\int_{-1}^{1} C_{\alpha\beta}(\boldsymbol{x}^{i_e},\boldsymbol{x}^{i_e}_{i_c})L_{j_c}(\zeta)l'_{i_e}(\zeta)d\zeta, \quad \text{(B4)}$$

where $\boldsymbol{x}^{i_e}_{i_c}$ is the collocation point (with label i_c on the boundary element i_e) at which the discretized boundary-integral equation (21) is enforced. Two cases then occur when computing the integrals (B2)–(B4):

(i) Regular integrals: This is not only the case when $\boldsymbol{x}^{i_e}_{i_c}$ is not located on the boundary element j_e. Indeed, if $\boldsymbol{x}^{i_e}_{i_c}$ with intrinsic coordinate ζ_{ic} in the segment $[-1, 1]$, belongs to the boundary element j_e the off-diagonal components, $B_{zr}(\boldsymbol{x}^{i_e},\boldsymbol{x}^{i_e}_{i_c})$ and $B_{rz}(\boldsymbol{x}^{i_e},\boldsymbol{x}^{i_e}_{i_c})$ are regular[20] and, as $\zeta \to \zeta_{ic}$, one gets

$$C_{zz}(\boldsymbol{x}^{i_e},\boldsymbol{x}^{i_e}_{i_c}) = -\frac{8z'^2_{i_e}(\zeta_{i_c})}{l'^4_{i_e}(\zeta_{i_c})}\frac{z'_{i_e}(\zeta_{i_c})n_z + r'_{i_e}(\zeta_{i_c})n_r}{\zeta - \zeta_{i_c}}, \quad \text{(B5)}$$

$$C_{zr}(\boldsymbol{x}^{i_e},\boldsymbol{x}^{i_e}_{i_c}) = C_{rz} = -\left[\frac{8z'_{i_e}(\zeta_{i_c})r'_{i_e}(\zeta_{i_c})}{l'^4_{i_e}(\zeta_{i_c})}\right] \times \left[\frac{z'_{i_e}(\zeta_{i_c})n_z + r'_{i_e}(\zeta_{i_c})n_r}{\zeta - \zeta_{i_c}}\right], \quad \text{(B6)}$$

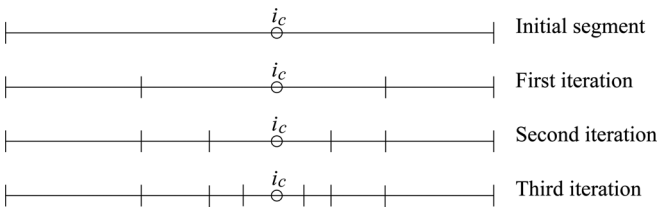

FIG. 17. Non-uniform refinement of the integration grid on the segment $[-1, 1]$ near the collocation point i_c when the number of partitions is equal to 2.

$$C_{rr}(\boldsymbol{x}^{i_e},\boldsymbol{x}^{i_e}_{i_c}) = -\frac{8r'^2_{i_e}(\zeta_{i_c})}{l'^4_{i_e}(\zeta_{i_c})}\frac{z'_{i_e}(\zeta_{i_c})n_z + r'_{i_e}(\zeta_{i_c})n_r}{\zeta - \zeta_{i_c}}. \quad \text{(B7)}$$

Exploiting (B1) then immediately shows that, as $\zeta \to \zeta_{ic}$,

$$z'_{i_e}(\zeta_{i_c})n_z + r'_{i_e}(\zeta_{i_c})n_r = \frac{r'_{i_e}(\zeta_{i_c})z''_{i_e}(\zeta_{i_c}) - r''_{i_e}(\zeta_{i_c})z'_{i_e}(\zeta_{i_c})}{l'_{i_e}(\zeta_{i_c})}(\zeta - \zeta_{i_c}). \quad \text{(B8)}$$

Accordingly, the integrals (B3)–(B4) are also regular ones.

(ii) Weakly singular integrals: This happens only for integrals (B2) when $\alpha = \beta$ and $\boldsymbol{x}^{i_e}_{i_c}$ is located on the boundary element j_e. This time

$$B_{rr}(\boldsymbol{x}^{i_e},\boldsymbol{x}^{i_e}_{i_c}) \sim B_{zz}(\boldsymbol{x}^{i_e},\boldsymbol{x}^{i_e}_{i_c}) \sim 2\ln\left[\frac{8r_{i_e}(\zeta_{i_c})}{l'_{i_e}(\zeta_{i_c})|\zeta - \zeta_{i_c}|}\right] \quad \text{as } \zeta \to \zeta_{i_c}, \quad \text{(B9)}$$

and we adopt the isolation and analytical integration of the above weakly singular logarithmic term as explained in Pozrikidis,[20] therefore, finally ending with the numerical evaluation of two regular integrals over the segments $[-1, \xi_{ic}]$ and $[\xi_{ic}, 1]$.

Each regular integral encountered in previous cases (i)–(ii) is iteratively computed by using the Voutsinas and Bergeles[29] procedure which here consists in dividing in case (i) the segment $[-1, 1]$ into equal or unequal subsegments when the point $\boldsymbol{x}^{i_e}_{i_c}$ is not too close or close the boundary element j_e and also using, as illustrated in Fig. 17, a non-uniform refinement of the segments $[-1, \xi_{ic}]$ and $[\xi_{ic}, 1]$ in case (ii).

[1]M. Manga, "The motion of deformable drops and bubbles at low Reynolds numbers: Application to selected problems in geology and geophysics," Ph.D. thesis, Harvard University, 1994.
[2]J. Kappel, R. Conradt, and H. Scholze, "Foaming behaviour on glass melts," Glastech. Ber. **60**, 189 (1987).
[3]H. M. Princen, "Shape of a fluid drop at a liquid-liquid interface," J. Colloid Interface Sci. **18**, 178 (1963).
[4]S. Hartland, "The coalescence of a liquid drop at a liquid-liquid interface. Part I: Drop shape," Trans. Inst. Chem. Eng. **45**, T97 (1967).
[5]S. Hartland, "The coalescence of a liquid drop at a liquid-liquid interface. Part II: Film thickness," Trans. Inst. Chem. Eng. **45**, T102 (1967).
[6]S. Hartland, "The profile of the draining film between a fluid drop and a deformable fluid-liquid interface," Chem. Eng. J. **1**, 67 (1970).
[7]A. F. Jones and S. D. R. Wilson, "The film drainage problem in droplet coalescence," J. Fluid Mech. **87**, 263 (1978).

Author complimentary copy. Redistribution subject to AIP license or copyright, see http://phf.aip.org/phf/copyright.jsp

[8]G. Debrégeas, P.-G. de Gennes, and F. Brochard-Wyart, "The life and death of 'bare' viscous bubbles," Science **279**, 1704 (1998).
[9]P. D. Howell, "The draining of a two-dimensional bubble," J. Eng. Math. **35**, 251 (1999).
[10]B. K. Chi and L. G. Leal, "A theoretical study of the motion of a viscous drop toward a fluid interface at low Reynolds number," J. Fluid Mech. **201**, 123 (1989).
[11]C. W. Hirt and B. D. Nichols, "Volume of fluid (VOF) method for the dynamics of free boundaries," J. Comput. Phys. **39**, 201 (1981).
[12]M. Sussman, P. Smereka, and S. Osher, "A level set approach for computing solutions to incompressible two-phase flow," J. Computat. Phys. **114**, 146 (1994).
[13]A. O. Unverdi and G. Tryggvason, "A front-tracking method for viscous, incompressible, multi-fluid flows," J. Computat. Phys. **100**, 25 (1992).
[14]M. Bonnet, *Boundary Integral Method for Solid and Fluid* (Springer, Berlin, 1995).
[15]H. A. Lorentz, "Ein allgemeiner Satz, die Bewegung einer reibenden Flüssigkeit betreffend, nebst einigen Anwendungen desselben," in *Abhandlungen über Theoretische Physik*, B. G. Teubner, Berlin, 1907, pp. 23–42.
[16]F. K. G. Odqvist, "Über die Randwertaufgaben der Hydrodynamik zäher Flüssigkeiten," Math. Z. **32**, 329 (1930).
[17]O. A. Ladyzhenskaya, *The Mathematical Theory of Viscous Incompressible Flow* (Gordon and Breach, New York, 1963).
[18]G. K. Youngren and A. Acrivos, "Stokes flow past a particle of arbitrary shape: A numerical method of solution," J. Fluid Mech. **69**, 377 (1975).
[19]J. M. Rallison and A. Acrivos, "A numerical study of the deformation and burst of a viscous drop in extensional flow," J. Fluid Mech. **89**, 191 (1978).
[20]C. Pozrikidis, *Boundary Integral and Singularity Methods for Linearized Viscous Flow* (Cambridge University Press, Cambridge, England, 1992).
[21]S. Kim and S. J. Karrila, *Microhydrodynamics. Principles and Selected Applications* (Dover, New York, 2005).
[22]R. Aris, *Vectors, Tensors and the Basic Equation of Fluid Mechanics* (Dover, New York, 1962).
[23]J. Hadamard, *Le problème de Cauchy et les équations aux dérivées partielles linéaires hyperboliques* (Hermann & Cie, Paris, 1923).
[24]V. D. Kupradze, *Dynamical Problems in Elasticity. In Progress in Solid Mechanics* (North-Holland, New York, 1963).
[25]M. Loewenberg and E. J. Hinch, "Numerical simulation of a concentrated emulsion in shear flow," J. Fluid Mech. **321**, 395 (1996).
[26]A. Z. Zinchenko, M. A. Rother, and R. H. Davis, "A novel boundary-integral algorithm for viscous interaction of deformable drops," Phys. Fluids **9**, 1493 (1997).
[27]G. P. Muldowney and J. J. L. Higdon, "A spectral boundary element approach to three-dimensional Stokes flow," J. Fluid Mech. **298**, 167 (1995).
[28]M. Abramowitz and I. A. Stegun, *Handbook of Mathematical Functions* (Dover, New York, 1965).
[29]S. Voutsinas and G. Bergeles, "Numerical calculation of singular integrals appearing in three-dimensional potential flow problems," Appl. Math. Model. **14**, 618 (1990).
[30]J. Stoer and R. Bulirsch, *Introduction to Numerical Analysis* (Springer-Verlag, New York, 1993).
[31]W. H. Press, B. P. Flannery, S. A. Teukolsky, and W. T. Vetterling, *Numerical Recipes in C. The Art of Scientific Computing* (Cambridge University Press, Cambridge, England, 1988).
[32]For our numerical computations, $\varepsilon = \mathcal{O}(10^{-5})$.
[33]T. Taylor and A. Acrivos, "On the deformation and drag of a falling viscous drop at low Reynolds number," J. Fluid Mech. **18**, 466 (1964).
[34]F. Y. Pan and A. Acrivos, "Shape of a drop or bubble at low Reynolds number," Ind. Eng. Chem. Fundam. **7**, 227 (1968).
[35]J. Hadamard, "Mouvement permanent lent d'une sphre liquide et visqueuse dans un liquide visqueux," C. R. Acad. Sci. Paris **152**, 1735 (1911).
[36]W. Rybczynski, "Über die fortschreitende Bewegung einer flüssigen Kugel in einem zähen Medium," Bull. de l'Acad. des Sci. de Cracovie, Ser. A **1**, 40 (1911).
[37]For $\mathrm{Bo} = \mathcal{O}(1)$, the surface tension is large enough so that the surfaces are weakly deformed. In contrast, for $\mathrm{Bo} = \mathcal{O}(10)$, the bubble and the free surface experience deformations that are more difficult to accurately compute. We thus propose computations for this regime.
[38]E. Bart, "The slow unsteady settling of a fluid sphere toward a flat fluid interface," Chem. Eng. Sci. **23**, 193 (1968).
[39]R. G. Cox and H. Brenner, "The slow motion of a sphere through a viscous fluid towards a plane surface. II. Small gap widths, including inertial effects," Chem. Eng. Sci. **22**, 1753 (1967).

Author complimentary copy. Redistribution subject to AIP license or copyright, see http://phf.aip.org/phf/copyright.jsp

Film drainage of viscous liquid on top of bare bubble: Influence of the Bond number

Helena Kočárková,[1] Florence Rouyer,[2] and Franck Pigeonneau[1]
[1)] *Surface du Verre et Interfaces - UMR 125 CNRS/Saint-Gobain*
39 Quai Lucien Lefranc - BP 135
93303 Aubervilliers Cedex, France
[2)] *Université Paris-Est, Laboratoire Navier (UMR CNRS 8205, Ecole des Ponts Paris Tech, IFSTTAR)*
5 bd Descartes, 77454 Marne-la-Vallée, France

(Dated: 26 March 2012)

We present experimental results of film drainage on top of gas bubbles pushed by gravity force toward a free surface of a liquid bath made of highly viscous Newtonian liquid with an uniform surface tension. The temporal evolution of the thickness of the film between a single bubble and the air/liquid interface is investigated *via* interference method under various physical conditions, range of viscosities and surface tension of the liquid, and bubble sizes. These experiments evidence the influence of the deformation of the thin film on the thinning rate and confirm the slow down of film drainage with Bond number as previously reported by numerical work of Pigeonneau and Sellier [Phys. Fluids, 23:092102, 2011]. A simple model that considered the liquid flow in the cap squeezed by buoyancy forces of the bubble is in good agreement with experimental and numerical data. Qualitatively, smaller is the area of the thin film compare to the surface of the bubble, faster is the drainage.

I. INTRODUCTION

Foam is a disperse system consisting of gas bubbles separated by liquid films. Its useful properties lead to a large range of applications in cosmetic, food, automotive, building materials and so on[1,2]. Nevertheless, foam can have a negative impact in various processes as for instance in glass melting[3,4]. Indeed, foam is a thermal insulator decreasing the energetic efficiency of glass furnaces. The conditions leading to the foam layer at the top of a glass bath is still scarcely understood requiring fundamental investigations. The stability of foams in high viscous fluid occurs also in lava flows[5] affecting the eruption mechanisms[6].

For such fluids that *a priori* do not contain any surfactant that might stabilized thin films and for which liquid flow are slow, the lifetime of foams is strongly dependent on the liquid drainage through films and Plateau borders. The first step in characterizing the liquid drainage is to determine the properties of the liquid flow confined by liquid-air interfaces. Practically, this can be achieved at the mesoscale by studying the drainage of thin film as it has been achieved in the book of Mysels *et al.*[7].

The study of thin film drainage gives information on the behavior of the liquid-air interface. With soap films attached to wire frames, Mysels *et al.*[7] pointed out that when the surfactant concentration is high, the film drainage is slow with interfaces behaving like immobile boundaries. By solving hydrodynamic equations with the no-slip conditions, Schwartz and Roy[8] found out an algebraic decay of the film thickness as a function of time. In contrary, with a relatively small concentration of surfactant, the film boundaries are mobile leading to a fast drainage. The lubrication models give an exponential decay of the film thickness with the time[8].

Equivalent experiments have been done on droplet at a liquid-liquid interface[9–11] or on bubble at a free surface[12,13]. As for vertical films, the mobility of the fluid interfaces has an influence on the dynamics of the film drainage. In absence of surfactant, mobility of the interface is associated to the viscosity ratio of the dispersed and the continuous phases. Fully mobile interfaces correspond to the case of bubbles whereas immobile interface correspond to viscous drop. Yiantsios and Davis[14] achieved a theoretical work to determine the motion of drop towards solid or deformable interfaces using the lubrication theory. They found that a pocket of fluid is trapped in the center of the film during its drainage (formation of a dimple), and that film thins according to a fractional powers of time. Nevertheless, this work is only valid for a small deformation of the interfaces (drop size smaller than capillary length) and for large ratio of viscosities of the inner and outer liquids. In case of viscosity ratio of the order of unity and for drop diameter comparable to the capillary length, recent experiments evidenced asymmetry of the dimple that would speed up the drainage compare to symmetric model prediction[15]. In the limit of bubble size larger than the capillary length with mobile interface (no surfactants), Debrégeas *et al.*[12] shown an exponential decay of the film as a

function of time and that the film thinning rate is proportional to radius of curvature of the film. Similarly, experiments with capillary force balance shown that curved film with immobile interfaces drains twice as slow as the plane-parallel film[16]. Recently, Pigeonneau and Sellier[17] studied by solving Stokes equations using a boundary integral formulation the migration of bubble with mobile interface and drainage of thin curved film on top of it close to a free surface. They pointed out the exponential decay of the thin liquid film. Moreover, they shown the strong influence of the bubble size on the thinning rate.

In spite of these contributions that evidence effect of film curvature and bubble size on drainage, the bubble size effect has not yet been observed experimentally over a large range of physical parameters. In fact, few attentions have been paid to the coalescence of bubbles at the top of a bath with mobile interfaces compared to the numerous studies of the coalescence between drops[18]. However, it is noteworthy that this step is crucial for the formation of a froth (foam layer) depending on the ratio of the production rate and death rate of bubbles at the surface. Thus, the present experimental work studies film drainage on top of a bubble at the free surface of a viscous liquid for different bubble diameters around the capillary length. In addition, we explore viscous and capillary forces by varying surface tension and viscosity over more than a decade in a regime where inertia is negligible (low Reynolds number and high Ohnesorge number) using oils (UCON$^{\mathrm{TM}}$ oil and Castor oil) and molten glasses (silicate melts). Moreover, molten glass studies require a specific experimental set-up working at high temperature which are always a big challenge. The secondary purpose of this investigation is to find a "liquid" to model molten glass in experiments carried out at room temperature.

First, the physical parameters and dimensionless numbers relevant for this problem considering capillarity, gravity, and viscous forces are recalled in section II. Then, the two experimental set-ups that allow measurements of film drainage on top of a bubble, over a wide range of physical parameters are presented in section III. Finally, the experimental results are developed in section IV. We quantitatively compare these results with previous works and recent numerical simulations and propose a simple model based on gravity driven flow and extensional viscous dissipation in the same section. Finally, conclusions are drawn in section V.

II. PHYSICAL PARAMETERS

When a bubble rises through a liquid toward a free surface, three steps emerge. The first is the rising of the bubble driven by the buoyancy forces where gradually the bubble velocity decreases with the distance between the bubble and the free surface[17]. In the second step corresponding to the drainage, a liquid film is created between the bubble interface and the free surface which thickness decreases with the time. The third step is the film rupture outside of the scoop of the present work. In the following, the parameters which control the shape and the drainage are detailed.

A. Asymptotic shape of a bubble at a liquid interface

The shape of the bubble is mainly controlled by the relative importance of the buoyancy forces given by $\rho g \pi D^3/6$ against the surface tension proportional to $D\sigma$ where ρ is the liquid density (the gas density is neglected), D the bubble diameter, σ the surface tension and g is the gravitational constant. The ratio of these two forces defines the Bond number given by:

$$\mathrm{Bo} = \frac{\rho g D^2}{\sigma}. \tag{1}$$

The careful determination of the bubble shape has been first described by Princen[19]. His model decomposes interfaces in three distinguishable parts: i) the interface between the interior of the bubble and the liquid bulk, ii) the liquid film and iii) the static meniscus of the free surface of the liquid. As it was pointed out by Princen, the liquid film in the limit of very thin layer forms a spherical cap. Even if the problem is easy to formulate the practical determination is not so easy. The bubble shape for the Bond number equal to 1 is shown in Figure 1 in which the three distinguishable parts are pointed out. The geometry of the spherical cap is characterized by the radius of curvature, R_{cap}, and the height of the cap, h_{cap} which set the diameter of the ring D_c at the base of the cap. As we will point out in the following, the relevant parameter to describe the film lubrication is the surface area of the spherical cap: $S_{\mathrm{cap}} = 2\pi R_{\mathrm{cap}} h_{\mathrm{cap}}$.

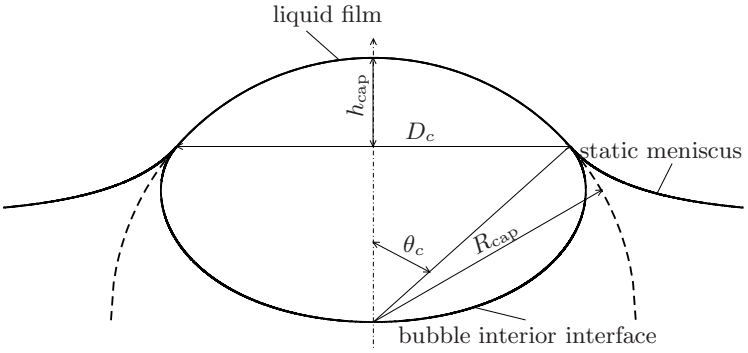

FIG. 1. Bubble shape at a free surface for Bo = 1.

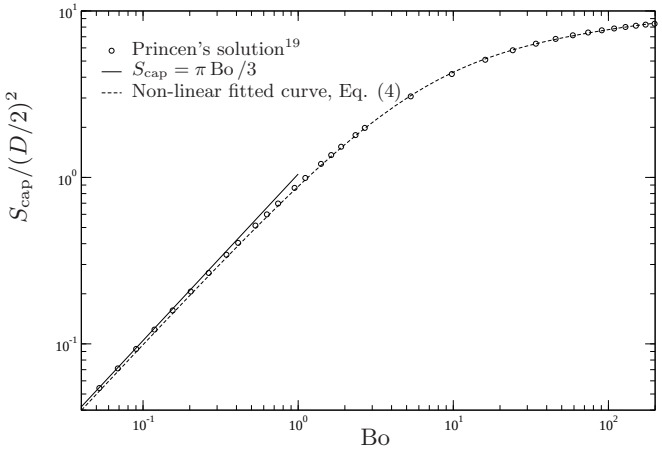

FIG. 2. $S_{\rm cap}/(D/2)^2$ versus Bo: circle points are determined according to Princen's model[19] and dashed line is the fit corresponding to equation 5. The solid line is the asymptotic behavior at small Bond number according to Howell's model[21].

The area of the spherical cap normalized by the square of bubble radius is given as a function of Bond number in Figure 2 determined according to Princen's model. This quantity has two asymptotic behaviors.

At small Bond number, corresponding to a bubble smaller than the capillary length defined by[20]

$$\kappa^{-1} = \sqrt{\frac{\sigma}{\rho g}}, \tag{2}$$

the interface above the bubble is slightly deformed and the bubble keeps the spherical shape. Howell[21] studied the bubble shape for small Bond number. Remark that the radius of curvature, $R_{\rm cap}$, is the twice of bubble radius when the Bond number goes to zero since the liquid film has two interfaces. Using the asymptotic solution given in[21], the area of the spherical cap normalized by the bubble radius squared is given by

$$\frac{S_{\rm cap}}{(D/2)^2} = \frac{\pi}{3}\,{\rm Bo} + \mathcal{O}({\rm Bo}^2). \tag{3}$$

Conversely, at large Bond number, corresponding to bubble size larger than the capillary length, the free surface is strongly deformed and the shape of bubble as well. In the limit of very high Bond number, the bubble at the free surface tends to a hemispherical cap of radius $R_{cap} = 2^{1/3}(D/2)$ leading to the following limit

$$\lim_{{\rm Bo}\to\infty} \frac{S_{\rm cap}}{(D/2)^2} = 2^{5/3}\pi \approx 9.974. \tag{4}$$

For intermediary values of Bond number, the bubble shape has to be determined numerically. The trend for a small Bo given by Eq. (3) is verified. For the large Bo, $S_{\rm cap}$ goes to the limit given by (4). In order

to evaluate easily $S_{\rm cap}$ which will be useful in § IV C, a non-linear fitted curve has been done using rational function for which the behaviors for small and large Bo are forced. This formula is given by

$$\frac{S_{\rm cap}}{(D/2)^2} = 2^{5/3}\pi \frac{94.7\,{\rm Bo} + {\rm Bo}^2}{902 + 142.5\,{\rm Bo} + {\rm Bo}^2}, \tag{5}$$

The value of $S_{\rm cap}$ versus Bo is compared to Princen's solution in Figure 2.

B. Characteristic time of drainage for bare bubble

During the film drainage, the bubble shape does not change with the time. Assuming the axisymmetry, the film thickness, h, is a function of time, t and the polar angle θ. The film thickness depends also on D, ρ, g, σ and μ. Dimensional analysis by taking ρ, D and μ as parameters with independent dimensions[22] gives that

$$\frac{h}{D} = f\left(\bar{t}, \theta, {\rm Bo}, {\rm Oh}\right), \tag{6}$$

where $\bar{t}$ is the dimensionless time given by

$$\bar{t} = \frac{tgD}{\nu}. \tag{7}$$

The quantity ν is the kinematic viscosity, μ/ρ. The dimensionless group, Oh, is the Ohnesorge number which compares viscous forces to intertia and capillary forces and is defined by

$${\rm Oh} = \frac{\mu}{\sqrt{\rho\sigma D}}. \tag{8}$$

In the previous works of Howell[21] and more recently of Pigeonneau and Sellier[17], the dependence on the Ohnesorge number does not appear in the formulation meaning that the film thickness is only a function of $\bar{t}$, θ and Bo.

The time scale, $\nu/(gD)$, found in the dimensional analysis can be established by a scaling analysis. Indeed, without surfactant on the interface or in other words with fully mobile interfaces, the shear stresses are free leading to diagonal stress tensor[23]. Consequently, the motion is a purely extensional flow: the velocity profile in the film is a plug flow[24]. As it has been already established for vertical film[8], the balance of gravity and viscous forces over a length scale equal to the diameter of the bubble D given by

$$\mu\frac{U}{D} \sim \rho g D, \tag{9}$$

defines the velocity scale:

$$U = \frac{gD^2}{\nu}, \tag{10}$$

and the time scale:

$$\tau = \frac{\nu}{gD}, \tag{11}$$

which is identical to the previous one introduced in the dimensional analysis.

Previous experimental work[12] shows that the time scale for film thinning on top of large bubble is varying as $1/R_{\rm cap}$. This scaling is based on the knowledge of the curvature of the film on top of the bubble which depends on the deformation of the bubble and characterized by the Bond number (see section II A). In most of the practical case $R_{\rm cap}$ can not be measured whereas the diameter of the initially spherical bubble is known. In the following, the time will be normalized by the time scale τ given by Eq. (11). According to the previous paragraph, the $R_{\rm cap}/D$ varies from 1 to 0.63 when Bo goes from zero the infinite. Thus, normalization of time based on D instead of $R_{\rm cap}$ would lead to small dependence with Bo.

Moreover, the independence on Oh will be verified.

III. EXPERIMENTAL SET-UP AND DETERMINATION OF THE PHYSICAL PARAMETERS

A. Experiment at room temperature with polymer liquid and mineral oil

Experiments are conducted in a room under air conditioning that fixes the atmospheric temperature at 20°C. Bubbles are observed from top and side at the center of the horizontal surface of the liquid that fills a cylindrical cell as it is illustrated in Figure 3-(a). The nature of liquids is described below in subsection III D. The cell is made of Teflon where its inner diameter and its height are respectively 3.4 and 3.5 cm. The top view is recorded by a AVT Marlin CCD video camera at a maximum frame rate of 60 images/s. The side view is recorded by a Photon video camera (Fastcam 1024PCI 100K) at a frame rate within 100 and 10,000 images/s depending on the velocity of the drainage. A powerful lighting (Dedolight 400D) is used in order to ensure a high rate recording with a low shutter time. Unfortunately, the device heats slightly the fluid up to 23 ± 1.4°C. Note that temperature measured at the liquid surface is uniform and it is controlled for each experiment. The bubbles are created by hand pushing air with a syringe through a needle placed vertically at the bottom of the cell. The bubble diameters range from 1 to 10 mm (cf. Table III) by varying the inner diameter of the needle from 0.4 to 1 mm.

The bubble diameter is determined from the image recording with the top view video camera at a time when the bubble moves toward the free surface of the liquid but does not deform the interface. Measurement uncertainty is less than 4 %, see Figure 3-(b).

Powerful white light illuminates from top side the surface of the liquid and many colored interference fringes are visible by eyes in the film on top of the bubbles. However, only the blue fringes are selected and recorded thanks to a blue filter placed in the front of the fast camera (see Figure 3-b).

B. Experiment at high temperature with molten glass

In order to perform a similar experiments on molten glasses, a laboratory furnace has been designed for which a sketch is given in Figure 4-(a). This furnace is closed and composed by a circular alumina tube filled of air atmosphere. The heating is done with electrodes around the alumina tube. The temperature is recorded thanks to a thermocouple in the heating space, noted T_F in Figure 4-(a). The molten glass is introduced in the platinum crucible which is placed at middle height of the furnace. The real temperature at this position is lower than the temperature given by T_F and has been calibrated previously, it is approximatively 65°C lower. Moreover, the thermal homogeneity has been verified showing that the thermal difference over the height of the crucible is not in excess of 5°C. The diameter and height of the crucible are 50 and 80 mm respectively but glass fills less than a half of the crucible (30 or 40 mm) to avoid the leakage of the melt in the furnace when creating bubbles. Gas is brought from N_2 bottle through plastic (outside of the furnace) and platinum tube (inside the furnace) to a small hole (100 μm) at the bottom of the crucible. The bubble inflation is controlled *via* a solenoid-valve that imposes periodically a pulse of pressure over an imposed time interval. The furnace allows visualization of the bubble only from the top through a silica window, see Figure 4-(b).

The optical set-up, localized above the furnace, consists of laser, silver mirror and CCD camera. Molten glass as well as refractories emit a thermal radiation in the infrared range of wavelength. Therefore, a green laser with wavelength at 532 nm is used in the experiment. The power of this laser is set to its maximum value at 150 mW. In the front of the video camera, a narrow filter ± 1 nm centered in the wavelength of 532 nm is introduced. Moreover, in order to remove the specular reflexion of light, the crucible has been scratched. The resolution of the CCD camera was 1392×1040 pixel^2 with a maximal rate of 20 full frames per second.

C. Interference analyses

The evolution of thickness is computed from an interference signal, which is obtained from the images recorded during the experiment, see Figure 5. The maximum and the minimum of the light intensity according to the classical theory of light interference[25] allows the determination of the film thickness as

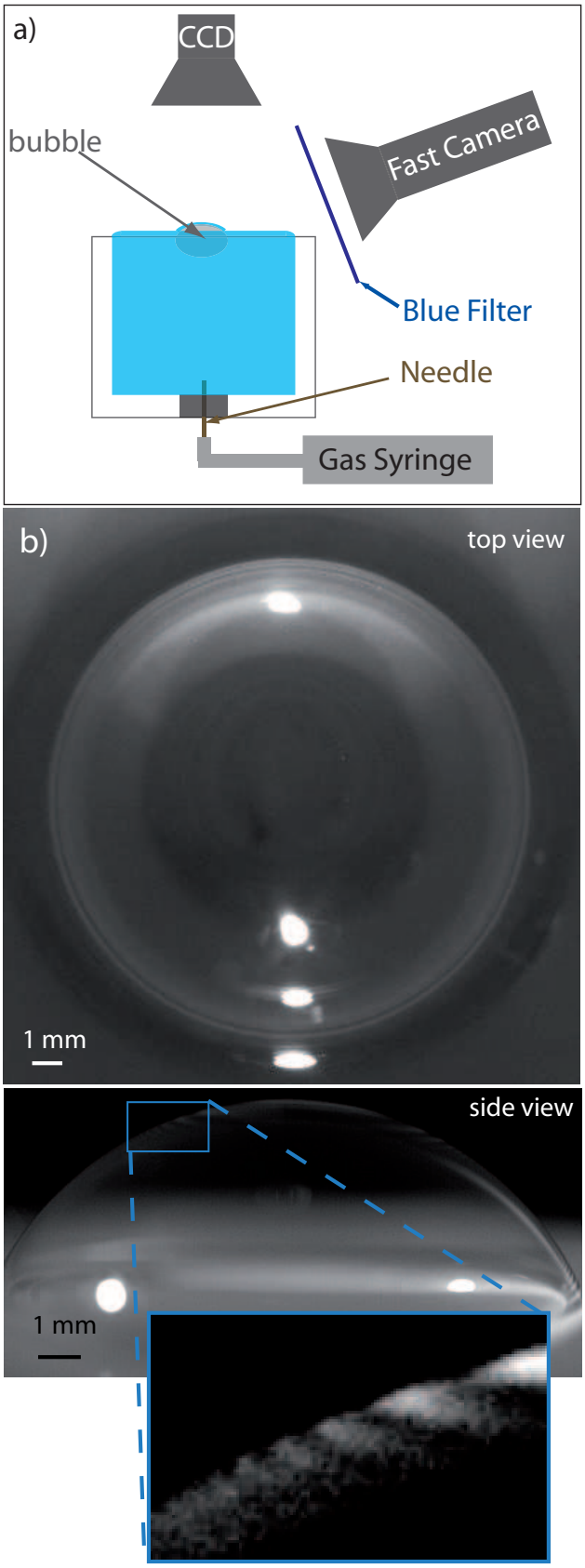

FIG. 3. a) Sketch of the experimental set-up at room temperature. b) Example of top and side views of a bubble at room temperature in UCON^{TM} oil.

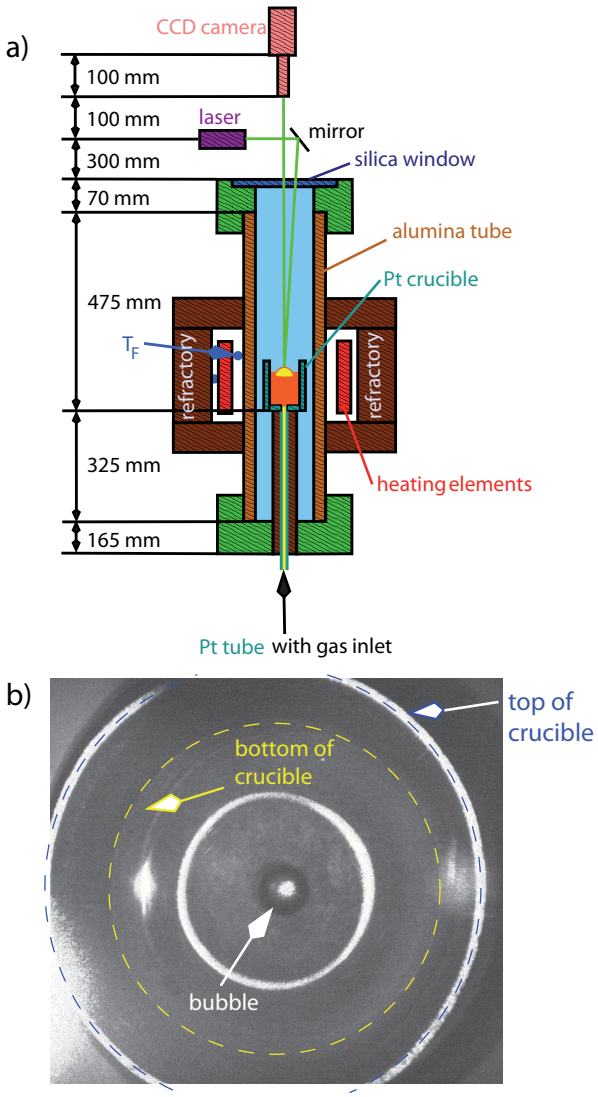

FIG. 4. a) Sketch of the experimental set-up designed for molten glass in a furnace. b) Example of top view of the platinum crucible with bubble (D= 6.8 mm) at 1044°C in molten window glass.

follows:

$$h_{I_{\max}} = \frac{\lambda(2k-1)}{4n}, \tag{12}$$

$$h_{I_{\min}} = \frac{\lambda k}{2n}, \tag{13}$$

where λ is the wavelength of the laser, n the refractive index and k the order of the interference. Note that these equations are obtained assuming that the incident light is perpendicular to the interface, which is approximatively the case close to the apex of the bubble.

D. Liquid properties and physical parameters

For the experiments achieved at room temperature, the liquids are either polymer fluid, UCON^{TM} 90,000, kindly provided by Dow Chemical or Castor oil purchased to Fischer Scientific. Physical properties of liquids are summed-up in Table I where the dynamic viscosity, the density, the surface tension and the refractive index are provided. The main difference between these two oils is the dynamic viscosity since the UCON^{TM}

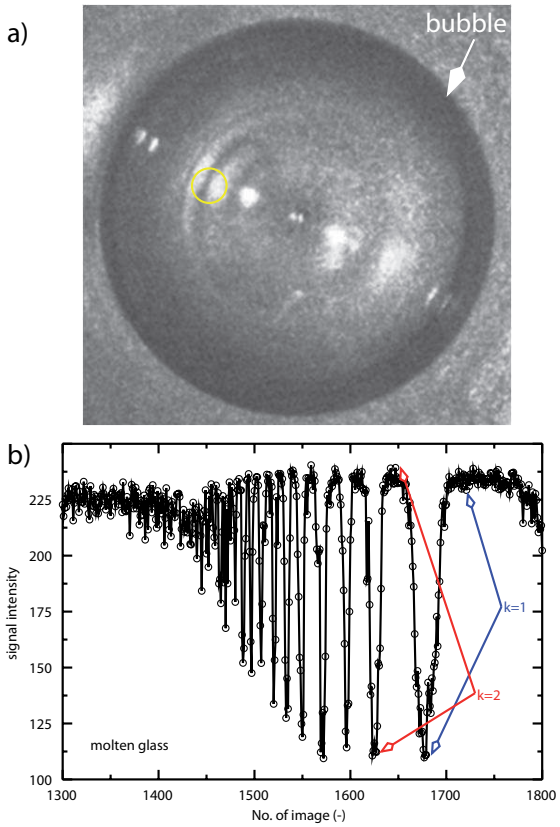

FIG. 5. a) Example of an interference pattern on the bubble, signal in figure b was obtained as an average intensity on time in yellow area. b) Example of an interference signal of molten glass.

	μ (Pa·s)	ρ (kg·m^{-3})	γ (mN·m^{-1})	n (–)
Castor oil	0.75 ± 0.05	957	33.8	1.46
UCON^{TM} oil	42 ± 5	1095	40.8	1.46
Glass 1	64 ± 7	2344	322	1.52
Glass 2	154 ± 13	2318	303	1.5

TABLE I. Dynamic viscosity, density, surface tension and refractive index of liquids explored in the experiments. The two first rows give the properties for liquids available at room temperature. The two last rows provide the properties for molten glasses determined for an operating temperature in the furnace equal to 1227°C.

oil has a dynamic viscosity 56 times greater than the Castor oil.

Surface tension of oils are measured in the lab with pendant drop method (TECLIS). Dynamic viscosities of oils are measured by bubble ascension inside the crucible as well as with cone plate rheometer over the temperature range 21-25°C. Error bars are related to temperature fluctuations from one experiment to another. Densities and refractive indexes of oil are taken from commercial data sheets provided by the suppliers.

For the experiments in the laboratory furnace at high temperature, two glasses are used. The compositions in main oxides are given in Table II. The Glass 1 is an oxide glass mainly composed of silica, soda ash and lime. The Glass 2 is also an oxide glass for which CaO has been substituted by K_2O. Its quantity of alumina is also more important. The properties of these two glasses given in Table I has been determined for an operating temperature equal to 1227°C in the furnace. The relative large content in alumina leads to an increase of the dynamic viscosity of Glass 2. The glass densities have been determined experimentally. Dynamic viscosities are determined from the glass composition according to the model of Lakatos *et al.*[26]. Surface tensions of glasses are also determined from their composition according to the computations provided by Dietzel[27], Lyon[28], Rubenstein[29] and Kucuk *et al.*[30]. The effect of the temperature on surface

	SiO_2	Na_2O	CaO	K_2O	MgO	Al_2O_3
Glass 1	72.3	13.5	9.6	-	4	0.6
Glass 2	61.8	12.6	0.5	9.4	7.6	8.1

TABLE II. Glass compositions given in weight percentage.

	D (mm)	Bo	Oh
Castor oil	$1.5 - 9.8$	$0.8 - 27$	$1.3 - 3.4$
UCON^{TM} oil	$1.5 - 10.5$	$0.6 - 32$	$61.3 - 162$
Glass 1	$3 - 23$	$6 - 32$	$15 - 23$
Glass 2	$8 - 23$	$5 - 40$	$38 - 64$

TABLE III. Ranges of bubble diameter investigated in the experiments. The corresponding Bond and Ohnesorge numbers are also summarized.

tension is estimated from the correction given by Scholze[31].

The ranges of bubble diameter investigated during experiments are given in Table III. The increase of viscosity and surface tension lead to an increase of the bubble size. We sum-up in Table III the Bond and Ohnesorge numbers where the range of Bond number does not change significantly from one liquid to another. Conversely, the range of Ohnesorge number is more important due to the large spread of dynamic viscosity.

IV. RESULTS AND DISCUSSION

A. Film drainage and influence of physical parameters

Once the shape of the bubble is stable at the surface of the bath, the motion of circular interference fringes is observed from the center to the periphery of the bubble. Fringes are scarcely centered at the apex of the bubble. These small decentering can be affected to a small misalignment of the optical set up compare to the vertical direction as well as a small asymmetric drainage. In this work, only results of circular fringes that encircled the top of the bubble are reported. A "black" film (no interference fringe) is observed all over the bubble just before its collapse. Thus, the last film thickness measured is estimated of the order of 200 nm, note that due to uncertainties of the angle of incidence of the light we can not give absolute values. The film thickness at its rupture is lower than this value.

From the interferometry, the film thickness is determined and plotted as a function of $\bar{t}$ defined by Eq. (7) in Figure 6 for (a) Castor oil, (b) UCON^{TM} oil, (c) Glass 1 and (d) Glass 2. For all liquids, three experiments with three different bubble diameters are provided and for which the corresponding Bond numbers are reported in Figure 6. The film thickness is normalized by its maximal measured value corresponding to the interference fringe observed at the first time.

For all liquids, the film thickness decays exponentially with time meaning that the dimensionless thickness, $\bar{h} = h(\bar{t})/h(0)$, can be written as follows:

$$\bar{h}(\bar{t}) = \exp(-a\bar{t}), \tag{14}$$

where the coefficient a can be seen as the logarithmic temporal derivative of $\bar{h}$ and thus the normalized thinning rate of the film. As previously pointed out by Schwartz and Roy[8] and Debrégeas *et al.*[12], the exponential behavior is the consequence of fully mobile interfaces. The liquid flow in the film is a purely extensional. These results then allow to conclude that none surface active agents affect the fluid interface for all liquids. Besides, normalized curves does not superimpose. Indeed, it appears from this graph that larger is the bubble diameter, slower is the decay of the thickness, *i.e.* lower is a.

The thinning rate is determined from the experimental data using a regression fitting assuming the exponential behavior. We thus plot the thinning rate, a, as a function of Bo for each liquid in Figure 7. Despite the scatter of the points, the trend of the decay of a with Bo is clearly identified for small Bond number (Bo ≤ 10) whatever the liquid nature. When the Bond number is larger than 10, the thinning rate reaches an asymptotic value around 0.1 for all liquids.

Errors bars of a due to uncertainties of physical parameters (viscosities and bubble diameters) do not seem to be enough to justify the spread of the data. Thus, in reference to a simple dimensional analysis

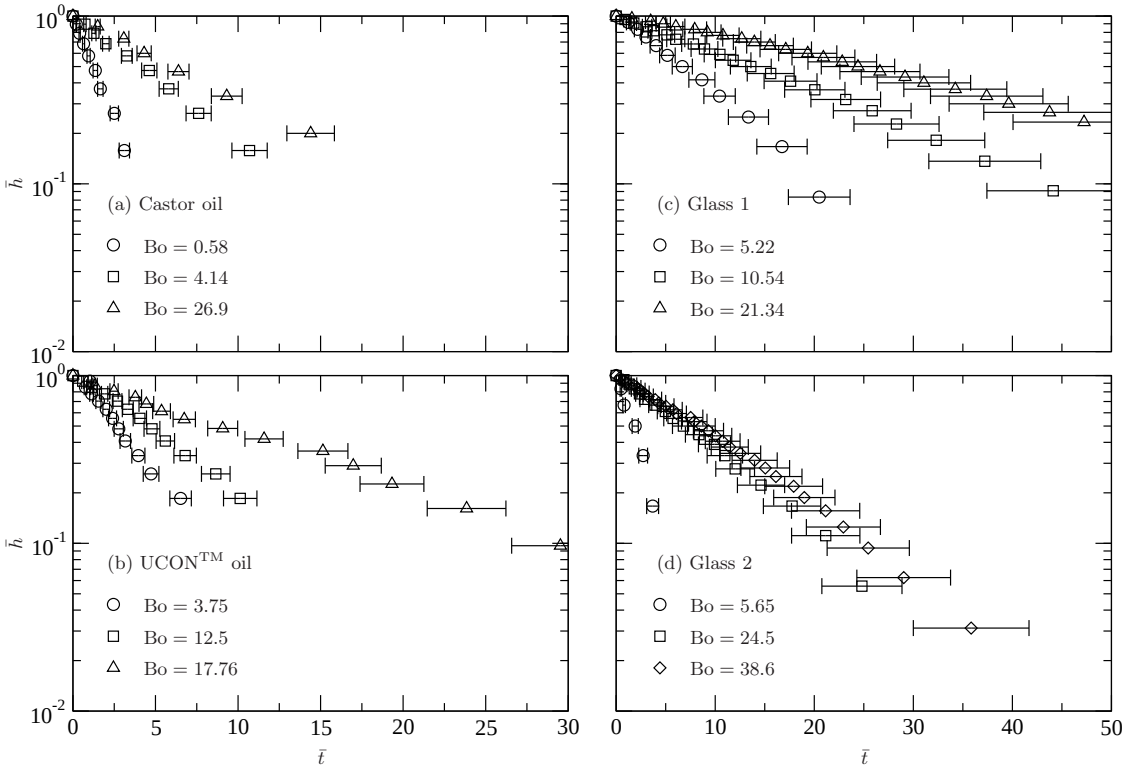

FIG. 6. Typical variation of the normalized thickness of the film as a function of dimensionless time.

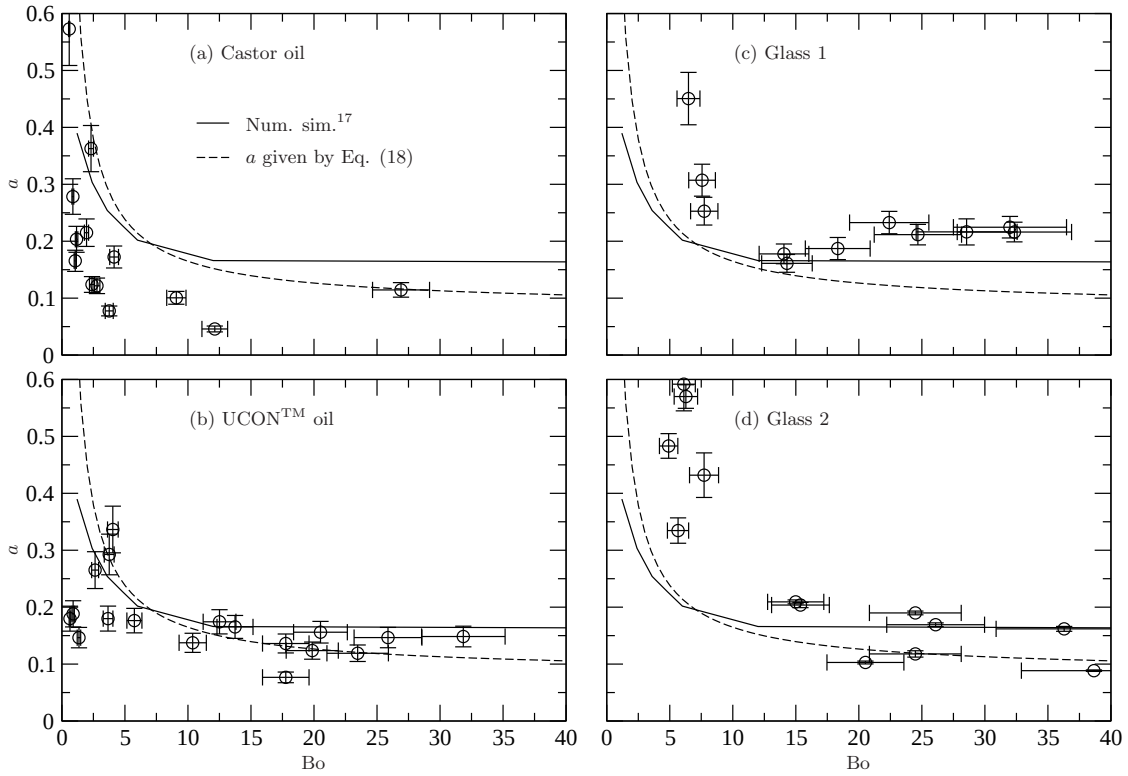

FIG. 7. Experimental results of normalized thinning rate versus Bond number obtaining for the four liquids.

	a	Oh
Castor Oil	0.1 ± 0.05	1.53 ± 0.03
UCON^{TM}	0.14 ± 0.04	65.7 ± 1.3
Glass 1	0.2 ± 0.05	18 ± 0.4
Glass 2	0.15 ± 0.02	44 ± 6

TABLE IV. Values of a and the corresponding Oh for the four liquids estimated Bo ≈ 20.

(see section II B), effects of viscous forces could be suspected as well. In aim to test this effect, we present in table IV the value of a and the Ohnesorge number estimated for bubbles for which the Bond number is close to 20 for the four liquids. No trend of variation of a as a function of Oh is observed as considered by previous theoretical and numerical works[17,21].

The scatter observed for the two glasses can be due to the underestimated uncertainties of the physical parameters for molten glass given by the literature. Moreover, the experiment at high temperature is not easy to do. The thermal field can perturb the drainage since the thermal gradient over the crucible which is relatively important, more than 500 K over few decimeters, can create a natural convection in the atmosphere. Similarly for experiments at room temperature, some air flow perturbation might occur above the bubble despite all precautions. Consequently, the drainage is not in a perfect axisymmetric and reproducible condition which can explain the observed scatter.

B. Comparison with previous works

An equivalent experiment has been previously done by Debrégeas *et al.*[12] in silicone oil at very high viscosity, 10^3 Pa·s. Debrégeas *et al.*[12] pointed out that the characteristic time from the bubble drainage depends on the radius of curvature of the cap. Their experimental work obtained for large bubble (limit of large Bond for which $R_{\text{cap}} \gg \kappa^{-1}$) shows that their thinning rate, $1/\tau_{\text{drainage}} = 1.63 R_{\text{cap}}$ ($\text{s}^{-1}\text{m}^{-1}$) which corresponds to a thinning rate $a = \tau/\tau_{\text{drainage}}$ equal to 0.104. Their experimental results is in good agreement with our experimental results for Bo larger than 20. However, their model based on gravity-driven plug flow in a hemispherical cap of radius R_{cap} predicts $1/\tau_{\text{drainage}} = (\rho g R_{\text{cap}})/\mu$ that corresponds to a variation of the thinning rate $a = R_{cap}/D$ from 1 to 0.63 for Bond number varying from zero to infinite. This analytical model qualitatively agrees with our experimental data as it predicts a decrease of the thinning rate with Bo. However, the decay is less important than the experimental one (lesser than a factor of two all over the range of Bo compare to a factor larger than 4 for the experiments). Moreover, the analytical value of a overestimates by a factor of 6 the experimental one at large Bond number. Thus, this "gravity-driven plug flow in hemispherical cap" model is not satisfactory to predict quantitatively our experimental results.

Howell[21] studied the drainage of bubble at the free surface using a lubrication model determining firstly the bubble shape according to the same principles of Princen[19]. The behavior of the film thickness is established in the limit of small Bond number. Howell[21] points out that the film thickness decays according to an algebraic function of time. Our experimental results show that we do not expect this trend. This disagreement suggests that the situation studied by Howell[21] does not correspond to the real observation done experimentally.

On the other hand, our experimental results confirm the recent numerical results based on the boundary-integral formulation of Stokes equations obtained by Pigeonneau and Sellier[17] pointing out an exponential behavior of the film thickness as a function of time. Quantitatively, the normalized thinning rate a is deduced from an exponential fit to the numerical values of $\bar{h}(\bar{t})$ at long time and presented in Figure 7 in solid line. The decay of a with Bo is clearly observed for the results obtained from the numerical method. Nevertheless, the thinning rate is underestimated for small Bond number due to a limitation of numerical method to compute accurately the drainage for a small Bond number as it is mentioned in[17]. For a large Bond number, the numerical simulations give the same thinning rate as it is also clearly observed experimentally.

Finally, we recall that previous experiments done with polydimethylsiloxane (PDMS) did not give the same behaviors[32] as the thinning rate was insensitive to the Bond number for the polymeric liquids. Different behavior might be artifacts due to the size of the polymeric chains but its understanding is still a challenge.

C. Model based on extensional flow in the cap

Even if our experimental results can be explained numerically we do not have a simple relationship to determine the thinning rate. Therefore, in this subsection, a simple model to find an estimation of the thinning rate a is proposed. In order to do that we first assume that the thinning of the thin film on top of the bubble is due to the pressure imposed by the rising bubble and by the top interface that resists further deformation, once the fluid surfaces remain in stationary shape. However, the buoyancy force pulls the bubble upward and the capillary force pushes the interface downward, consequently the fluid contained in the film is squeezed. For film thickness much smaller than the radius of curvature of the bubble and assuming axisymmetry along the vertical axis, the tangential and the azimuthal stress can be neglected compare to the radial stress and thus the flow in the film is similar to the squeeze between two disks of area equal to $S_{\rm cap}$. Then, assuming that the interfaces are fully mobile, the flow is a radial extension for which the tensile stress σ_T can be written as follows :

$$\sigma_T = 6\mu\dot{\epsilon}, \tag{15}$$

where the rate of strain, $\dot{\epsilon}$, is given by

$$\dot{\epsilon} = \frac{-1}{2h}\frac{dh}{dt}. \tag{16}$$

This tensile stress is thus opposed to the pressure imposed by the buoyancy force of the bubble that apply to the cap:

$$\sigma_T = 3\mu\frac{1}{h}\frac{dh}{dt} = -\frac{\rho g\frac{4\pi}{3}(D/2)^3}{S_{\rm cap}}, \tag{17}$$

from which, one can then deduce from the relationship given for $S_{\rm cap}$, Eq. (5), that the normalized thinning rate is :

$$a = \frac{2\pi}{9}\frac{(D/2)^2}{S_{\rm cap}} = \frac{1}{2^{2/3}9}\frac{902 + 142.5\,{\rm Bo} + {\rm Bo}^2}{94.7\,{\rm Bo} + {\rm Bo}^2}. \tag{18}$$

This model predicts the decrease of the normalized draining rate versus Bond number since the surface of the cap relative to the bubble size increases with Bond number (cf. Figure 1). The variation of a versus Bo according to equation (18) is plotted in dashed line in Figure 7. In the limit of large Bo, this law is in much better quantitative agreement with the experimental results that to the one given by Debrégeas *et al.*[12] presented in the previous paragraph. Moreover, it allows to predict the evolution of thinning rate of the thin film in the limit of intermediate Bond number when the interface is not fully deformed by the bubble.

It is noteworthy that for Bo goes to zero corresponding to the case of a spherical bubble approaching a flat interface, the analytical solution of the Stokes flow can determine the lubrication force as a function of the film thickness, see for instance[33]. According to the method proposed by Cox and Brenner[34] detailed in the book of Kim and Karrila[35], Pigeonneau and Sellier[17] point out that the lubrication force diverges following a logarithmic singularity leading to the collapse of the liquid film over a finite time. Thus, this asymptotic behavior is coherent with the divergence of (18) as well as the sharp increase of a observed experimentally in the limit of ${\rm Bo} \to 0$.

Finally, the disagreement in the limit of large Bo between the numerical simulation and the extensional flow model is explained by the fact that the capillary suction from the curved interface at the bottom of the film (Plateau border) is neglected in the model. Taking into account the capillary suction would increase the thinning rate.

V. CONCLUSION

Experiments of gas bubble pushed upward by gravity toward a free surface of a liquid with "bare" interface have been investigated. Four liquids are studied: the two firsts are synthetic and natural oils and the two lasts are molten glasses. Two specific experimental set-ups are developed working at room temperature for the investigations on oils and at high temperature for molten glasses. After the free rising of the

observed bubble, the liquid film between the bubble and the free surface of the liquid is determined by an interferometry method.

For both kinds of liquids, we show that the liquid drains exponentially with time. This result is important for molten glass as it shows that over the time where the drainage occurs the molten glass interfaces are totally mobile. Moreover, the thinning rate corresponding to the logarithmic temporal derivative of the film thickness is determined. This quantity is normalized by a time scale based on the balance of gravity and viscosity forces at the bubble scale. It is clearly established that the thinning rate is a function of the bubble size or more precisely function of the Bond number. As it has been observed on the numerical simulation provided in[17], the thinning rate increases when the Bond number decreases. In other words, small bubbles (or bubbles in high surface tension liquid) drain relatively faster than large bubble (or bubbles in low surface tension liquid).

It is noteworthy, that the relative surface of this cap compared to the surface of the bubble increases with Bond number. Thus, the pressure in the film squeezed by the buoyant force of the bubble decreases with Bond number. An analytical model based on extensional squeezed flow of the liquid within the cap describes quantitatively the experimental results.

Finally, finding a "liquid model" in agreement with the physics of molten glass has big consequences. Indeed, the experiments on molten glass are always a big challenge since they require high temperature leading to high energy consuming and difficulties to analyze the data as well. Moreover, many artefacts due to high temperature can increase the uncertainties. So, in conclusion, both Castor oil or UCON^{TM} oil can be used to study the film drainage in agreement with the physics of molten glass until any chemical effects play a role.

ACKNOWLEDGMENTS

We would like to thank M. Vignes-Adler for the helpful advices on the bubble experiment and discussion. We are grateful for the experimental work of S. Metallaoui during his Master Internship, who provides results of film thinning at ambient temperature. We are also indebted to P.-H. Guering and L. Canova working at Saint-Gobain Recherche (Aubervilliers, France) for the design of the optical set-up and G. Gauthier from FAST lab (Orsay, France) for viscosity measurements of oils.

[1] D. Weaire and S. Hutzler. *The physics of foams*. Clarendon Presss, Oxford, 1999.
[2] I. Cantat, S. Cohen-Addad, F. Elias, F. Graner, R. Höhler, O. Pitois, F. Rouyer, and A. Saint-Jalmes. *Les mousses. Structure et dynamique*. Editions Belin, Paris, 2010.
[3] J. Kappel, R. Conradt, and H. Scholze. Foaming behaviour on glass melts. *Glastech. Ber.*, 60:189–201, 1987.
[4] J. van der Schaaf and R. G. C. Beerkens. A model for foam formation, stability, and breakdown in glass-melting furnaces. *J. Colloid Interface Sci.*, 295:218–229, 2006.
[5] Both, glass and lava are silicates.
[6] A. A. Proussevitch, D. L. Sahagian, and V. A. Kutolin. Stability of foams in silicate melts. *J. Volcanol. Geotherm. Res.*, 59:161–178, 1993.
[7] K. Mysels, K. Shinoda, and S. Frankel. *Soap film. Studies of their thinning*. Pergamon, New York, 1959.
[8] L. W. Schwartz and R. V. Roy. Modeling draining flow in mobile and immobile soap films. *J. Colloid Interface Sci.*, 218:309–323, 1999.
[9] S. Hartland. The coalescence of a liquid drop at a liquid-liquid interface. Part I: Drop shape. *Trans. Instn Chem. Engrs*, 45:T97–T101, 1967.
[10] S. Hartland. The coalescence of a liquid drop at a liquid-liquid interface. Part II: Film thickness. *Trans. Instn Chem. Engrs*, 45:T102–T108, 1967.
[11] S. Hartland. The coalescence of a liquid drop at a liquid-liquid interface. Part III: Film rupture. *Trans. Instn Chem. Engrs*, 45:T109–T114, 1967.
[12] G. Debrégeas, P.-G. de Gennes, and F. Brochard-Wyart. The life and death of "bare" viscous bubbles. *Science*, 279:1704–1707, 1998.
[13] J. Senée, B. Robillard, and M. Vignes-Adler. Films and foams of Champagne wines. *Food Hydrocolloids*, 13:15–26, 1999.
[14] S. G. Yiantsios and R. H. Davis. On the buoyancy-driven motion of a drop towards a rigid surface or a deformable interface. *J. Fluid Mech.*, 217:547–573, 1990.
[15] R. Delfos G. Oldenziel and J. Westerweel. Measurements of liquid film thickness for a droplet at a two-fluid interface. *Phys. Fluids*, 24:022106, 2012.
[16] K. Kumar, A. D. Nikolov, and D. T. Wasan. Effect of film curvature on drainage of thin liquid films. *J. Colloid Interface Sci.*, 256:194–200, 2002.
[17] F. Pigeonneau and A. Sellier. Low-Reynolds-Number gravity-driven migration and deformation of bubbles near a free surface. *Phys. Fluids*, 23:092102, 2011.
[18] D. Y. C. Chan, E. Klaseboer, and R. Manica. Film drainage and coalescence between deformable drops and bubbles. *Soft Matter*, 7:2235–2264, 2011.
[19] H. M. Princen. Shape of a fluid drop at a liquid-liquid interface. *J. Colloid Interface Sci.*, 18:178–195, 1963.

[20]P.-G. de Gennes, F. Brochard-Wyart, and D. Quéré. *Gouttes, bulles, perles et ondes*. Belin, Paris, 2005.
[21]P. D. Howell. The draining of a two-dimensional bubble. *J. Eng. Math.*, 35:251–272, 1999.
[22]G. I. Barenblatt. *Scaling*. Cambridge University Press, Cambridge, 2003.
[23]C. J. S. Petrie. Extensional viscosity: A critical discussion. *J. Non-Newtonian Fluid Mech.*, 137:15–23, 2006.
[24]P. D. Howell. Models for thin viscous sheets. *Eur. J. Appl. Math.*, 7:321–346, 1996.
[25]C. Isenberg. *The science of soap films and soap bubbles*. Dover Pub., New-York, 1992.
[26]T. Lakatos, L.-G. Johansson, and B. Simmingsköld. Viscosity temperature relations in the glass system SiO_2-Al_2O_3-Na_2O-K_2O-CaO-MgO in the composition range of technical glasses. *Glass Technol.*, 13:88–94, 1972.
[27]A. Dietzel. Zusammenänge zwischen Oberflächenspannung und Struktur von Glasschmelzen. *Kolloid Z.*, 100:368–380, 1942.
[28]K. C. Lyon. Calculation of surface tension of glasses. *J. Am. Ceram. Soc.*, 27(6):186–189, 1944.
[29]C. Rubenstein. Factors for the calculation of the surface tension of glasses at 1200 C. *Glass Technol.*, 5:36–40, 1964.
[30]A. Kucuk, A. G. Clare, and L. Jones. An Estimation of the surface tension for silicate glass melts at 1400°C using statistical analysis. *Glass Technol.*, 40(5):149–153, 1999.
[31]H. Scholze. *Glass. Nature, Structures and Properties*. Springer-Verlag, Berlin, 1990.
[32]H. Kočárková, F. Pigeonneau, F. Rouyer, and M. Vignes-Adler. Film drainage between bubble and fluid interface. In *International Conference on Multiphase Flow 2010*, Tampa, Florida (USA), May 30-June 4 2010.
[33]E. Bart. The slow unsteady settling of a fluid sphere toward a flat fluid interface. *Chem. Eng. Sci.*, 23:193–210, 1968.
[34]R. G. Cox and H. Brenner. The slow motion of a sphere through a viscous fluid towards a plane surface - II Small gap widths, including inertial effects. *Chem. Eng. Sci.*, 22:1753–1777, 1967.
[35]S. Kim and S. J. Karrila. *Microhydrodynamics. Principles and selected applications*. Dover Publications, Inc., New-York, 2005.

Stability of vertical films of molten glass due to evaporation

F. Pigeonneau*,[a], H. Kočárková[a,1], F. Rouyer[b]

[a] *Surface du Verre et Interfaces, UMR 125 CNRS/Saint-Gobain, 39 quai Lucien Lefranc – BP 135, 93303 Aubervilliers cedex, France*

[b] *Université Paris-Est, Laboratoire Navier (UMR CNRS 8205, Ecole des Ponts Paris Tech, IFSTTAR), 5 bd Descartes, 77454 Marne-la-Vallée, France*

Abstract

First, we report observations achieved on a gravitationally-driven film drainage with molten glass pointing out a stabilizing effect when temperature is larger than 1250°C. A model to describe the change of surface tension with the film thickness due to the evaporation of oxide species is proposed. A lubrication model is derived taking into account the gradient of surface tension. The final system of equations describing the mass and the momentum conservations is numerically solved by an implicit time solver using a finite difference method at a second order scheme in time and space.

The numerical procedure is applied to study a film drainage of molten soda-lime-silica glass. The effect of the surface tension gradient is investigated pointing out that with an increase of 0.5 % of the surface tension over the spread of the film which is order of few centimeters, the liquid film reaches an equilibrium thickness in agreement with previous experimental work.

Key words: foam, film drainage, Marangoni effect, glass, stability, evaporation

1. Introduction

Foams are dispersions of gas bubbles in a liquid matrix. Foams have several very interesting and unusual properties which make them possible candidates for use in many industrial applications. In most of cases, the stability of foam is a required property. Today, many investigations are devoted to the creation of stable foams [7]. Nevertheless, in glass melting process in particular, foam can be a nuisance. Most of glass furnaces are heated by a combustion chamber above the glass bath. Consequently, if a large part of the bath surface is covered with foam, heat transfer, mainly radiative due to the high temperature, decreases due to the thermal insulator property of glass foam [38]. Consequently, the optimization of the industrial plants needs to improve the knowledge of the physical grounds playing an important role in the foam stability.

*Corresponding author: Tel. +33 (1) 48 39 59 99, Fax +33 (1) 48 39 55 62.

Email addresses: franck.pigeonneau@saint-gobain.com (F. Pigeonneau), helena@ecoglass.cz (H. Kočárková), florence.rouyer@univ-mlv.fr (F. Rouyer)

[1] Present address: EcoGlass, a.s., Arbesova 66a, 466 04 Jablonec nad Nisou (Czech Republic)

Glass melting is a chemical process for which glass is made in most of cases with silica, soda ash, and lime [33]. The raw materials are generally carbonaceous elements giving a carbon dioxide release. The low solubility of CO_2 leads to a creation of large quantity of bubbles entrapped in a molten glass. To remove these gaseous inclusions, sulfate compounds are added to raw materials. Thus gases released by sulfate decomposition lead to a bubble growth. Due to buoyancy forces, larger bubbles can escape from bath surface more rapidly [33].

The onset of glass foaming has been studied by Kim and Hrma [16]. From a knowledge of chemical reactions produced by sulfate species, they determined the foaming temperature. Pilon [24] developed a model to study the foam formation by bubbling and established a relationship between foam layer and physical properties of liquid using a dimensional analysis. Foams in the glass melting process have been recently reviewed by Pilon [23] giving a large overview where many references can been found.

Foam aging is related to the liquid film stability formed between bubbles. A liquid film can be created under various size, shape and spatial orientation as it has been reviewed by Exerowa and Kruglyakov [11]. Initiated by the work of Mysel *et al.* [20], a liquid film formed on a vertical frame has been extensively studied. The influence of surfactants in aqueous solutions has been experimentally investigated by studying the film thickness as a function of the velocity at which the film is pulled out in [19, 8, 3] and more recently by Saulnier *et al.* [29]. Mathematical models to describe the two-dimensional draining film have been studied by various authors as for instance Schwartz and Roy [32] investigating mobile and immobile soap films. Howell [14] presented a general method to obtain lubrication model of thin film in various situations with free shear stresses on interfaces. An important contribution has been done by the team of Braun [5, 4, 21] studying the drainage of vertical film taking into account the Marangoni stress and the transport of surfactant agent. The law describing the film thickness as a function of the pulling-out velocity and physical properties including surface rheology has been studied by van Nierop *et al.* [36, 37]. The role played by thermal gradient on the surface tension has been recently studied by Scheid *et al.* [30]. They shown that it is possible to form a stable liquid film controlled by a surface tension gradient.

Kappel *et al.* [15] achieved an experimental study about film drainage on molten glass. They found that the film thickness decreases exponentially with time. They observed a stabilization state leading to a film thickness around one hundred nanometers. Laimböck [18] did a similar experiments where film thicknesses were determined by electric resistivity. He found that glass film can reach a stabilized thickness in the same order of magnitude found by Kappel *et al.* [15]. Laimböck proposed a model to explain the film stability. He pointed out an adsorption of sodium oxide at the free surfaces of the liquid film. After a simple model to explain the change of surface tension, a static equilibrium between the gravity and surface tension forces is written over the length of the liquid film. As we will see later our observations invalidate the adsorption of sodium oxide.

Despite these contributions, investigations have seldom been done on the mathematical model to describe the stabilization of the vertical molten glass film. So, the purpose of this work is to study the drainage of a vertical film dynamically. Based on experimental observations, the feature of surface tension as a function of the film thickness is proposed. A lubrication model in which the surface tension gradient is introduced according to the prior developments of Howell [14] and Breward [6].

The section 2 reports an experiment achieved on a vertical film drainage where a

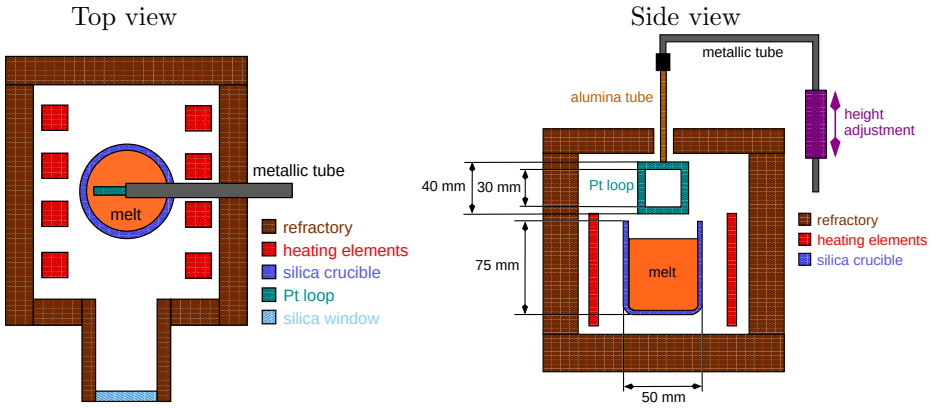

Figure 1: Experimental set-up for vertical film in molten glass (top and side views).

SiO_2	Na_2O	CaO	K_2O	MgO	Al_2O_3
72.1	13.3	9	0.1	3.6	0.8

Table 1: Composition given in weight percentage of glass used in the film drainage experiments.

stability of molten glass film has been observed. Section 3 is devoted to the modeling of the evolution of the surface tension as a function of the film thickness due to evaporation of surface active species. The lubrication model is presented in section 4. Numerical results including the two previous developments and discussion are detailed in section 5 before to conclude.

2. Experiment of vertical film drainage of molten glass

We performed a gravitationally-driven film drainage experiment achieved on molten glass film created with a squared frame of 3 cm side and 1 mm thick made of an alloy of Platinum and Rhodium. A top and side views of the sketch of the laboratory furnace are shown in Figure 1. Observation of the experiment is enabled *via* silica window, which is placed in the front part of the furnace, see the top view of Figure 1. Molten glass is introduced in a transparent silica crucible enabling the controlled motion of the Platinum-Rhodium loop inside the pool. Experiments are done in the temperature range from 1100 to 1300°C. Due to this high temperature surrounding and great difficulties to control film position, the thickness measurement by an optical method was not achieved. However, throughout the experiment, a recording with CCD video camera is done in which a narrow band filter is added in the optical objective to remove the thermal radiation. This recording allows to determine the film lifetime as well as to observe flow patterns in the film.

A commercial oxide glass has been studied: its composition in term of main oxides is given in Table 1. The main applications of this glass are in habitat and in automotive.

The lifetimes of the liquid film have been recorded for five temperatures for which the experiment is repeated four times. The lifetime, t_{life}, as a function of temperature is given in Figure 2. Since the lifetime is mainly controlled by the viscous drainage driven by

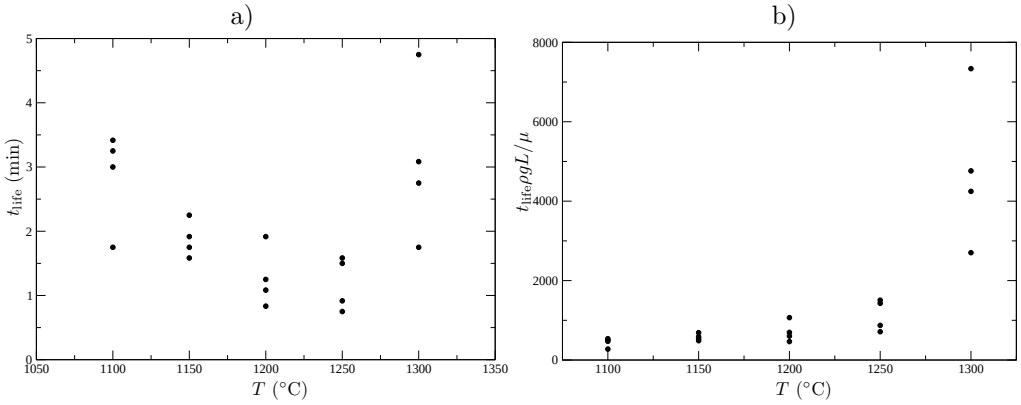

Figure 2: a) Lifetime of the vertical molten glass film versus temperature inside the furnace. b) Normalized lifetime of the vertical molten glass film versus temperature inside the furnace.

the gravity, we expect that the lifetime decreases with temperature because the viscosity decreases with temperature. This is verified while temperature is smaller than 1250°C in Figure 2-a. However, for temperature larger than 1250°C, the lifetime increases with the temperature. In aim to quantify this unexpected behavior, we compare the lifetime measured experimentally to the time scale based on a lubrication model of gravitational drainage for a 2D film with free surfaces that will be explained in details in § 4. Thus, the lifetime is normalized by $\rho gL/\mu$ where ρ is the liquid density, g the gravitational constant, L the height of the liquid film and μ the dynamic viscosity. The film thickness does not appear in this time scale because the interfaces are shear free meaning that the flow in the film liquid is a pure extensional flow. As it is well-known in this situation, the time scale arises from the balance of the gravity and extensional viscosity forces for which the film thickness is an irrelevant quantity [14]. However the lifetime of the film depends on initial thickness and critical thickness at rupture that are both assumed to be independent of temperature. Indeed, the initial thickness would depend essentially on frame thickness when the film is pulled slowly. The critical thickness at rupture would depend on the film size, the Hamaker constant and the surface tension [39, 26]. In case of molten glass, this thickness is reported of the order of 100 nm [35]. Figure 2-b shows that the normalized lifetime does not change significantly with temperature and that it is equal to few hundreds while temperature is less than 1150°C. However, for larger temperature, the normalized lifetime increases strongly with the temperature. At $T = 1300$°C, the lifetime is very important since it is larger than 2500 times the time scale of drainage.

These experimental results show that a physical mechanism, occurring at temperature larger than 1150°C, is able to slow down the film drainage or stabilize the film and that its effect increases with temperature. Figure 3 is a serial of snapshots taken every 20 seconds with a black background. The bright part around the liquid film is the Platinum-Rhodium loop. On the bottom of each picture, the white part is the top of the crucible. Moreover, fringes on the film surface shown in Figure 3 appear and move with time[2].

[2]The supplementary materials can be downloaded in the website of the journal to see a movie of an experiment.

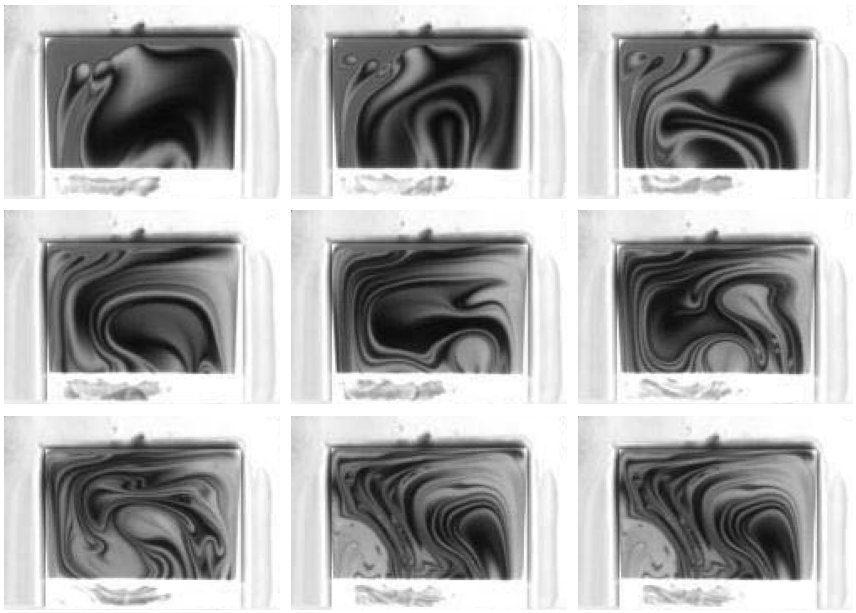

Figure 3: Snapshots of a glass film during an experiment achieved at $T = 1300°C$. Snapshots are spaced of 20 seconds. The chronometric order is from left to right and from top to bottom.

The film thickness stabilization and the motions can be due to a variation of the surface tension. The thermal homogeneity in the furnace over the length of the Platinum-Rhodium loop used in the experiment is well controlled to ensure that the motion is not driven by a heat phenomena. We argue that the surface tension changes due to a chemical process and is dominant compared to thermal effect.

In order to confirm the last assertion, experiments which pull a thin film out of the molten glass bath has been repeated but the molten glass film has been taken out before its rupture, and quenched. After annihilation of the mechanic stresses in the film, an analysis has been achieved using a Secondary Ion Mass Spectrometry (SIMS) technique. In this method, a focused primary ions beam are launched onto the surface of the sample. The analysis thanks to a mass spectrometer of the ejected secondary ion gives the composition of the surface of the sample, see for more details [40]. Depth profiling is done by use of two ion beams that operate simultaneously. While the first beam is sputtering a crater, the second beam is progressively analyzing the crater bottom. Our spectrometer works with either a cation of Bi^+ or a cluster of Bi^+ as primary ion and has been purchased from ION-TOF GmbH. Figure 4 presents the Na_2O content through the film obtained at 1200 and 1400 °C after a calibration of the intensity recorded by the spectrometer (details of the determination of Na_2O content can be found in [17]). The content of Na_2O is smaller at the interface meaning an evaporation of this oxide. The content at the interface decreases with the temperature. Furthermore, the typical scale over which the Na_2O changes is more important at high temperature. The scale over which Na_2O changes is noted δ as represented in Figure 4. The decrease of Na_2O close to the interfaces is followed by an increase of SiO_2 and CaO over the same depth.

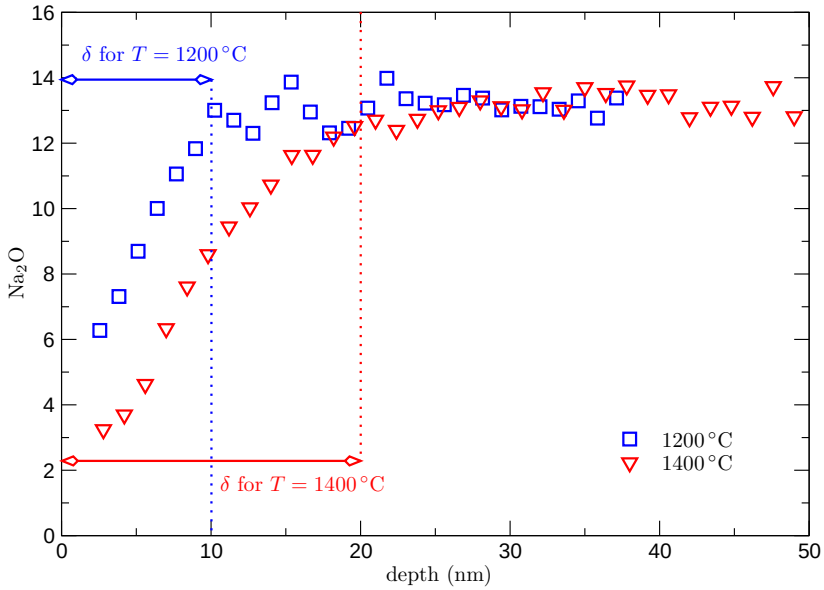

Figure 4: Na_2O content as a function of the depth in the film for two temperature.

The noteworthy point is that our measurements are in disagreement with the one reported by Laimböck [18]. Indeed, using XPS technique with an ion gun, Laimböck [18] observed that the glass composition over the film thickness changes significantly: the Na_2O content increases strongly at the film interface while the SiO_2 content decreases. This disagreement can be due to the glass nature. In the current study, the industrial glass is used whilst Laimböck [18] studied a ternary glass. The other source of disagreement could come from the analysis techniques which are different.

However, recall that Na_2O is known to be a volatile species [28, 1]. The evaporation of Na_2O leads to a modification of the glass composition at the interface. The evaporation of Na_2O is generally explained by a heterogeneous chemical reaction between water vapor and sodium oxide giving sodium hydroxide, NaOH. Consequently, it is expected to observe a positive gradient of Na over the depth of the film as it is measured in our chemical analysis.

The evaporation of chemical species leading to a Marangoni phenomena has been previously studied by Berg *et al.* [2] to investigate the patterns observed in horizontal liquid layers heated from below. The evaporating or condensing films have been also reviewed by Oron *et al.* [22]. The climbing films occurring for instance in the evaporative alcohol solutions have been also studied experimentally and theoretically by Hosoi and Bush [13].

The evaporation of Na_2O leads to a change in the nature of glass and in consequence of what the surface tension does not stay uniform in space. This phenomena can explain the increase of the lifetime of the liquid film. The following of this article is devoted to the demonstration of the effect of the evaporation process of Na_2O on the film stability thanks to a simple model to describe the surface tension changes with film thickness.

3. Surface tension in molten glass and variation with the film thickness

The volatilization of sodium oxide involves a heterogeneous chemical reaction with non-linear behaviors of mass fluxes. Moreover, the full problem implies transient diffusion process with a mass transfer coefficient between the film and the atmosphere difficult to evaluate. So, the aim of this section is to provide a simple model to describe the variation of the surface tension as a function of film thickness.

According to an additivity principle, Scholze [31] writes the surface tension of glass as follows:

$$\gamma = \sum_{i=1}^{N} \gamma_i y_i, \tag{1}$$

where γ is the surface tension, N is the number of oxides in the glass composition, y_i the mass fraction of the oxide i and γ_i is a factor corresponding to the contribution of the oxide i in the surface tension given in N/m.

Since the surface tension is determined from the bulk quantities and that Na_2O evaporate, we consider the volatilization of Na_2O to describe the change of surface tension. When the film is pulled out, the volatilization occurs leading to a decrease of Na_2O concentration. To determine this quantity for a portion of film of volume V and constant thickness h, the mass balance before and after the evaporation is given by

$$\rho_{Na_2O,0} V = \rho_{Na_2O} V + 2\frac{dm_{Na_2O}}{dS} S, \tag{2}$$

in which $\rho_{Na_2O,0}$ is the mass concentration of Na_2O in the bulk and ρ_{Na_2O} the mass concentration in the liquid film, V the volume of the film and S the area of each interface. Finally, dm_{Na_2O}/dS is the mass loss by unit surface. Since the ratio of S over V is directly the film thickness, h, the last equation can be written as follows

$$\rho_{Na_2O,0} h = \rho_{Na_2O} h + 2\frac{dm_{Na_2O}}{dS}. \tag{3}$$

This equation is similar in appearance to the one used to describe the soap films just after the pulling out but with different physics [10]. To close this equation, we assume that the loss of mass is proportional to ρ_{Na_2O} inside the portion of film of thickness h and to the size δ over which the volatilization occurs as introduced in the previous section:

$$\frac{dm_{Na_2O}}{dS} = \delta \rho_{Na_2O}. \tag{4}$$

This assumption is similar to the Langmuir isotherm used by Ruckenstein and Jain [26] to study the rupture of thin liquid film with a soluble surface active agents. Remark that Laïmbock [18] took the same approximation assuming the the sodium oxide is adsorbed whereas we argue that the sodium oxide is evaporated. By combining Eqs. (3) and (4), the mass concentration of Na_2O in a portion of film of thickness h is given by

$$\rho_{Na_2O} = \frac{\rho_{Na_2O,0}}{1 + 2\delta/h}. \tag{5}$$

So, this phenomenological relationship leads to a closed equation to describe the mass

concentration of Na_2O as a function of the film thickness. Finally, the difference of mass concentration of Na_2O in a film of thickness h and the bulk that will be used to describe the change of surface tension, is given by

$$\rho_{Na_2O} - \rho_{Na_2O,0} = -\frac{\rho_{Na_2O,0}}{1 + h/(2\delta)}. \tag{6}$$

This last equation can be used to evaluate the feature of surface tension as a function of film thickness. Indeed, if we assume that the surface tension changes only due to the mass concentration of Na_2O, SiO_2 and CaO which are the main oxides in the glass, the difference between the surface tension for a very thin film, γ, and a surface tension of bulk glass, γ_0, is given according to (1) by

$$\gamma - \gamma_0 = \gamma_{Na_2O}(y_{Na_2O} - y_{Na_2O,0}) + \gamma_{SiO_2}(y_{SiO_2} - y_{SiO_2,0}) + \gamma_{CaO}(y_{CaO} - y_{CaO,0}). \tag{7}$$

By assuming that the decrease of the concentration of Na_2O is compensated by the increase of SiO_2 and CaO proportionally to their mutual initial weight ratio, the surface tension becomes

$$\gamma = \gamma_0 + \delta\gamma f_\gamma(h/2), \tag{8}$$

where $\delta\gamma$ is given by

$$\delta\gamma = \left(\gamma_{SiO_2}\frac{y_{SiO_2,0}}{y_{SiO_2,0} + y_{CaO,0}} + \gamma_{CaO}\frac{y_{CaO,0}}{y_{SiO_2,0} + y_{CaO,0}} - \gamma_{Na_2O}\right) y_{Na_2O,0}, \tag{9}$$

and $f_\gamma(\chi)$, where $\chi \in [-h/2; h/2]$, is an even function given by

$$f_\gamma(\chi) = \frac{1}{1 + |\chi|/\delta}. \tag{10}$$

From the factors γ_{SiO_2}, γ_{CaO} and γ_{Na_2O} provided in [31, 25] and with the glass composition given in Table 1, $\delta\gamma$ is a positive quantity meaning that the surface tension given by (8) increases when the film thickness decreases. While the scale, δ, over which the sodium oxide evaporates depends on temperature, the quantity $\delta\gamma$ is only a function of the glass nature. Its value is equal to $4.2 \cdot 10^{-2}$ N/m whilst the surface tension γ_0 is equal to $3.2 \cdot 10^{-1}$ N/m for the largest temperature $T = 1400°C$. According to this modeling, the relative increase of surface tension is at the maximum equal to 1.5% for $h \to 0$ and of the order of 0.5% for $h \simeq 5\delta$. This last value seems appropriate for quantifying the Marangoni stress due to evaporation for thin film whose thickness $h \sim 100$ nm and whose Na_2O variation is observed over a depth equal to 20 nm.

4. Extensional flow model of 2D-Cartesian film

The situation addressed in this section is shown in Fig. 5 where a vertical film is attached to a horizontal wire in $x = 0$. The quantity x represents the longitudinal direction relative to the height of the film while y is the transversal coordinate relative to its thickness. Moreover, the vertical axis ($y = 0$) is axis of symmetry. Under the gravity force, directed along x, the film thickness, h is a function of the time t and of position

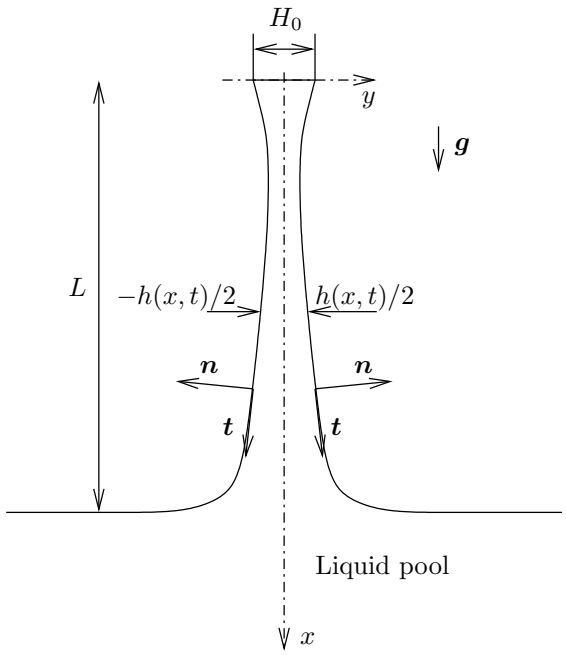

Figure 5: Liquid film draining under the gravity force. Figure is not on scale.

x. The film has a height equal to L and falls in a liquid pool. In the following, the film thickness H_0 on $x = 0$ is assumed to be very small compare to the height L.

A lubrication model is used to study the drainage of the liquid film under the assumption that the interface behaves as a free surface. The derivation of the lubrication model has been done by different authors starting by the first study achieved by Trouton [34]. In the situation of 2D-Cartesian film, two unknowns are involved: $h(x,t)$, the film thickness, and $u(x,t)$, the cross-sectionally averaged velocity. The two equations describing the mass and the momentum are [14, 6, 22]

$$\frac{\partial h}{\partial t} + \frac{\partial (hu)}{\partial x} = 0, \tag{11}$$

$$\rho h \left(\frac{\partial u}{\partial t} + u u_{,x} \right) = 4\mu \frac{\partial (h u_{,x})}{\partial x} + \frac{\gamma h h_{,xxx}}{2} + \delta\gamma \frac{df_\gamma}{d\chi} h_{,x} + \rho g h, \tag{12}$$

where ρ is the liquid density, μ the dynamic viscosity, g is the gravitational constant and the subscript $,x$ denotes the partial derivative over x. The left hand side of the momentum equation is the inertia term. The first term of the right hand side of (12) is the viscous force in which the factor 4 is the Trouton coefficient [34] for the 2D plane situation, the second term is the force due to the curvature gradient, the third is the contribution due to the surface tension gradient where $\delta\gamma$ and f_γ have previously been introduced. Finally, the last term is the gravity force.

The equations are normalized by assuming that the driven forces are the gravity and viscous terms. In this case, the characteristic velocity is $U_0 = \rho g L^2/\mu$. The dimensionless

variables are written as follows

$$\overline{x} = \frac{x}{L},\ \overline{h} = \frac{h}{H_0},\ \overline{u} = \frac{u}{U_0},\ \overline{t} = \frac{tU_0}{L}. \tag{13}$$

Eq. (12) becomes

$$\mathrm{Re}\,\overline{h}\left(\frac{\partial \overline{u}}{\partial \overline{t}} + \overline{u}\overline{u}_{,\overline{x}}\right) = 4\frac{\partial(\overline{h}\overline{u}_{,\overline{x}})}{\partial \overline{x}} + \frac{\overline{\gamma}\overline{h}\overline{h}_{,\overline{x}\overline{x}\overline{x}}}{2\,\mathrm{Bo}} + \mathrm{Ma}\,\frac{df_{\overline{\gamma}}}{d\chi}\overline{h}_{,\overline{x}} + \overline{h}, \tag{14}$$

where the Reynolds, Bond and Marangoni numbers are respectively given by

$$\mathrm{Re} = \frac{\rho U_0 L}{\mu},\ \mathrm{Bo} = \frac{\rho g L^3}{\gamma_0 H_0},\ \mathrm{Ma} = \frac{\delta\gamma}{\mu U_0}. \tag{15}$$

The dimensionless surface tension, $\overline{\gamma}$, is given by

$$\overline{\gamma} = 1 + \overline{\delta\gamma} f_\gamma(\overline{h}/2), \tag{16}$$

where

$$\overline{\delta\gamma} = \frac{\delta\gamma}{\gamma_0} \tag{17}$$

and $f_{\overline{\gamma}}(\chi)$ is a dimensionless even function defined according to the development detailed in § 3 and given by:

$$f_{\overline{\gamma}}(\chi) = \frac{1}{1 + |\chi|/\overline{\delta}}, \tag{18}$$

where $\overline{\delta} = \delta/H_0$.

Eqs. (11), and (14) must be completed by boundary conditions. At the top of the film, the thickness and the velocity are specified (Dirichlet conditions):

$$\overline{h}(0,\overline{t}) = 1, \tag{19}$$

$$\overline{u}(0,\overline{t}) = 0. \tag{20}$$

Since the purpose is to determine the film thickness profile of the entire film, the matching with the liquid pool must be described thanks to the boundary conditions written on the bottom of the film. As already shown in [27, 41], it is possible to match with the pool by assuming that the equation of the static meniscus

$$\overline{\kappa}_{,\overline{x}} = \frac{1}{\overline{l_c}^2} \tag{21}$$

is verified. The reduced capillary length, $\overline{l_c}$, is defined by

$$\overline{l_c} = \frac{1}{L}\sqrt{\frac{\gamma_0}{\rho g}}, \tag{22}$$

and the curvature, $\overline{\kappa}$, by

$$\overline{\kappa} = -\frac{\epsilon \overline{h}_{,\overline{x}\overline{x}}}{2(1+\epsilon^2 \overline{h}_{,\overline{x}}^2/4)^{3/2}}, \tag{23}$$

in which ϵ is the aspect ratio equal to H_0/L.

By multiplying Eq. (21) by $\overline{\kappa}$ and integrating over $\overline{x}$, the following relationship is obtained

$$\overline{\kappa}^2 = -\frac{\epsilon \overline{h}_{,\overline{x}}}{\overline{l_c}^2 \sqrt{1+\epsilon^2 \overline{h}_{,\overline{x}}^2/4}} + \frac{A}{\overline{l_c}^2}, \tag{24}$$

where A is an integration constant.

For a film falling in a large pool, the free surface can be considered as flat meaning that $\overline{h}_{,\overline{x}}$ goes to infinity when $\overline{x} \to 1$. Since the curvature must be equal to zero when $\overline{x} \to 1$, A must be equal to 2 [27, 5, 4].

According to the previous works of Braun *et al.* [5, 4], a matching between the liquid film described by the momentum equation (14) and the static meniscus can be achieved by specifying the first and the second derivatives of $\overline{h}$. We specify the first derivative of $\overline{h}$ at the bottom of the film as

$$\overline{h}_{,\overline{x}}(1,\overline{t}) = \alpha. \tag{25}$$

According Eqs. (23) and (24), the second derivative is given by

$$\overline{h}_{,\overline{x}\overline{x}}(1,\overline{t}) = \beta = \frac{2}{\epsilon \overline{l_c}} \sqrt{\left(2 - \frac{\epsilon\alpha}{\sqrt{1+\epsilon^2\alpha^2/4}}\right)(1+\epsilon^2\alpha^2/4)^3}. \tag{26}$$

These two relationships are used as boundary conditions at the bottom.

This is an asymptotic patch since by imposing $\overline{h}_{,\overline{x}}$ and $\overline{h}_{,\overline{x}\overline{x}}$, the matching occurs only at a single point localized in the area close to the "real" free surface of the pool. The distance from the free surface for which the matching occurs could be approximated by the position where the slope of the static profile is equal to α. According to Heller [12] who determined the profile of a static vertical film, the matching distance, $\overline{x}_* = 1 - \overline{x}$, is given by the relationship:

$$\overline{x}_* = \sqrt{2\overline{l_c}} \sqrt{1 - \frac{\alpha\epsilon}{\sqrt{4+(\alpha\epsilon)^2}}}, \tag{27}$$

This distance is proportional to the capillary length and would be smaller and smaller when the product $\alpha\epsilon$ is larger and larger. In the numerical applications provided latter, $\overline{x}_*$ will be equal to few percent of the film length. Note that neither a value, nor a flux for the velocity are imposed on the bottom of the film.

At the initial time, $\overline{h}$ is imposed equal to one where the matching with the static meniscus is achieved using

$$\overline{h}(\overline{x},0) = 1, \tag{28}$$

for $\overline{x} \in [0; \overline{x}_c]$ and

$$\overline{h}(\overline{x}, 0) = 1 - (\alpha - \beta)\overline{x}_c - \frac{\beta \overline{x}_c^2}{2} + (\alpha - \beta)\overline{x} + \frac{\beta \overline{x}^2}{2}, \tag{29}$$

for $\overline{x} \in]\overline{x}_c; 1]$ where α and β are the coefficients used in the boundary conditions on $\overline{x} = 1$ given previously and $\overline{x}_c$ is equal to

$$\overline{x}_c = 1 - \frac{\alpha}{\beta}. \tag{30}$$

The velocity $\overline{u}$ is assumed to be equal to zero at $\overline{t} = 0$.

The coupled equations (11) and (14) are solved numerically using a finite difference method. The spatial derivatives are determined by the second order schemes given in [9] using unsymmetric schemes close to the top and the bottom for the second and third derivatives. The nonlinear system is solved using a Newton-Raphson algorithm.

5. Numerical results and comparison to experiments

This section is devoted to the results obtained for the numerical simulations applied on the drainage of vertical film connected to the liquid pool.

The drainage of vertical film is investigated by solving the coupled equations (11) and (14) with the conditions given by Eqs. (19), (20), (25) and (26). The physical properties are taken from data corresponding to the glass composition given in Table 1. The density is equal to 2350 kg/m^3, the dynamic viscosity is equal to 50 Pa·s, corresponding to molten glass at 1240 °C. The surface tension, γ_0 is equal to 0.32 N/m using the correlation factors given by Rubenstein [25]. The length and the initial thickness of the liquid film are respectively $L = 3 \cdot 10^{-2}$ m and $H_0 = 10^{-3}$ m. With these characteristic values, the Bond number is equal to $1.94 \cdot 10^3$ and the Reynolds number to $5.85 \cdot 10^{-1}$.

Since the connection to the liquid pool is achieved artificially using the boundary conditions (25) and (26), we first present a study on the influence of α on the drainage in § 5.1. The second part of this section will be devoted to the contribution of the surface tension gradient on the vertical drainage.

5.1. Effect of the boundary conditions at the bottom

In this subsection, the surface tension is assumed uniform but the boundary conditions at the bottom of the film (parameter α) is varied in aim to study its influence on the evolution in space and time of the film thickness.

Figure 6 represents the minimum of $\overline{h}$ in the liquid film as a function of time for three value of α. The film thickness decreases rapidly in the first times ($\overline{t} < 50$). For long times ($\overline{t} > 50$) the thinning rate is slower than at first times. The first decrease is mainly due to the initial condition assuming the uniform thickness. Close to the top of the liquid film a meniscus appears as soon as the drainage starts as it is shown in Figure 7. The second part of the thinning process is a properly speaking due to the drainage. As expected, the film thickness decreases exponentially with the time due to the pure extensional flow in a film with stress free surfaces. The effect of the boundary conditions at the bottom has a small influence on the drainage of the liquid film at its minimal thickness. The thinning rates for the three values of α are similar.

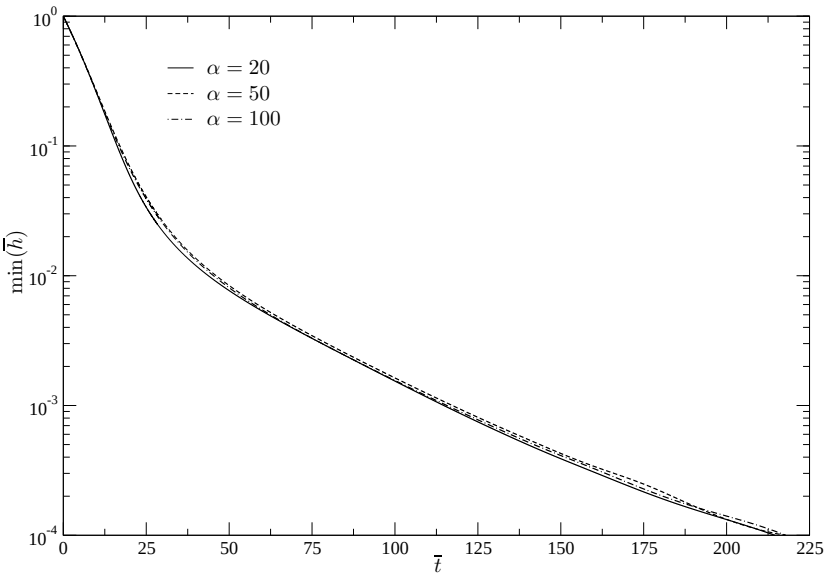

Figure 6: Minimum of $\overline{h}$ in the liquid film as a function of time for $\alpha = 20$, 50, and 100.

In Figure 7, the film thickness is plotted versus $\overline{x}$ for the three values of α and four times. Close to the top, the profiles of $\overline{h}$ are similar whatever the value of α. The main differences appear close to the bottom of the liquid film. The spread of the liquid film increases obviously with α. Nevertheless, the difference between the results obtained with $\alpha = 50$ and 100 are not very large for all times. Since except on top and bottom parts, the film thickness becomes small when $\overline{t} = 40$, $\overline{h}$ has been rescaled for $\overline{x} \in [0.1; 0.6]$ and plotted in the insert of Figure 7-(d).

Figure 8 gives the velocity profile for the three values of α and the same times used in Figure 7. The main advantage of the boundary conditions (25) and (26) is that the velocity is not specified at the bottom but is a solution of the problem. Since the spread of the liquid film increases with α, the velocity at the bottom is overestimated when α is small as a result of the mass conservation. The result is particularly true when $\alpha = 20$ and $\overline{t} = 20$. On the contrary, the velocity profiles are quasi-similar for $\alpha = 50$ and 100. The velocity calculated at the bottom are very similar for these two values of α. Nevertheless, when $\alpha = 100$, a shoulder is observed for both times.

Finally, remark as it can be seen in Insert of Figure 8 when $\overline{t} = 40$, the velocity is slightly negative close to the top of the liquid film as a consequence of the suction of the boundary where the liquid film is thicker than the film thickness far away from the top boundary.

The results show that the boundary conditions given by Eqs. (25) and (26) are relevant to describe numerically the matching with the liquid pool and that drainage can be assumed independent on the boundary conditions parameter α once this parameter is larger than 50. In the following, numerical computations are done with $\alpha = 100$.

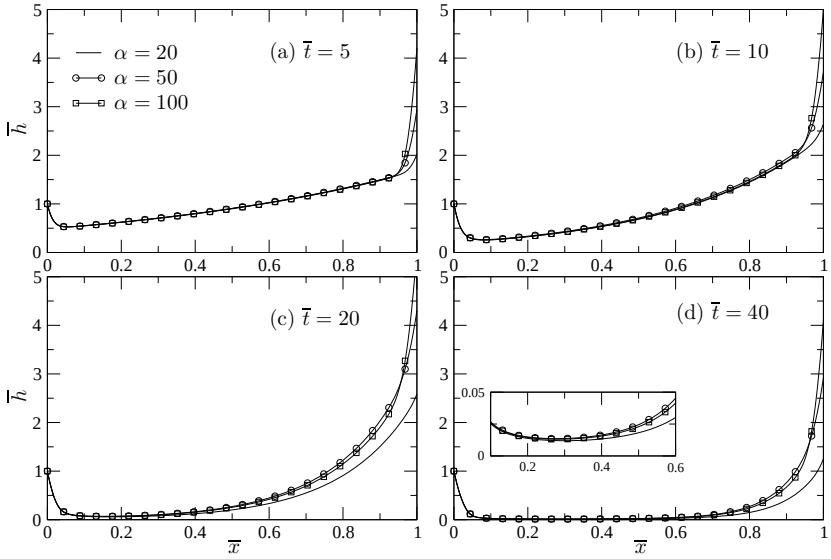

Figure 7: Film thickness, $\overline{h}$, as a function of $\overline{x}$ for $\alpha = 20$, 50, and 100 and for (a) $\overline{t} = 5$, (b) 10, (c) 20 and (d) 40.

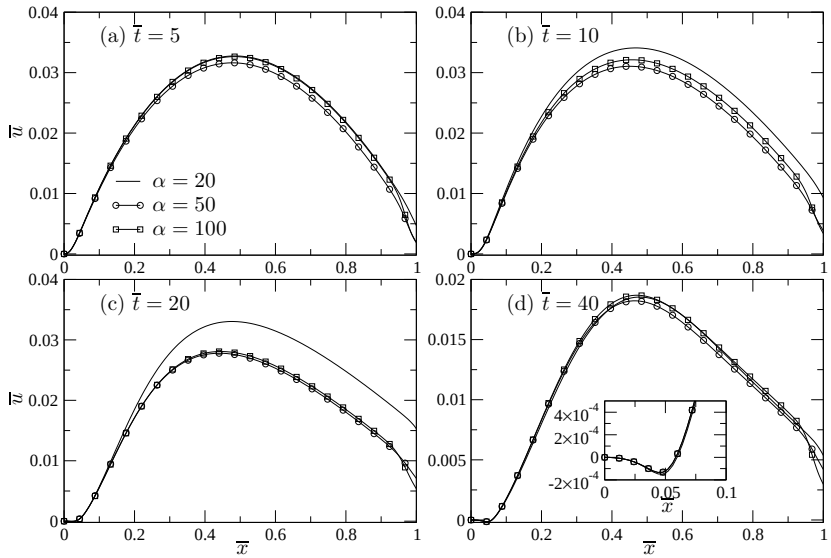

Figure 8: Film velocity, $\overline{u}$, as a function of $\overline{x}$ for $\alpha = 20$, 50, and 100 and for (a) $\overline{t} = 5$, (b) 10, (c) 20 and (d) 40.

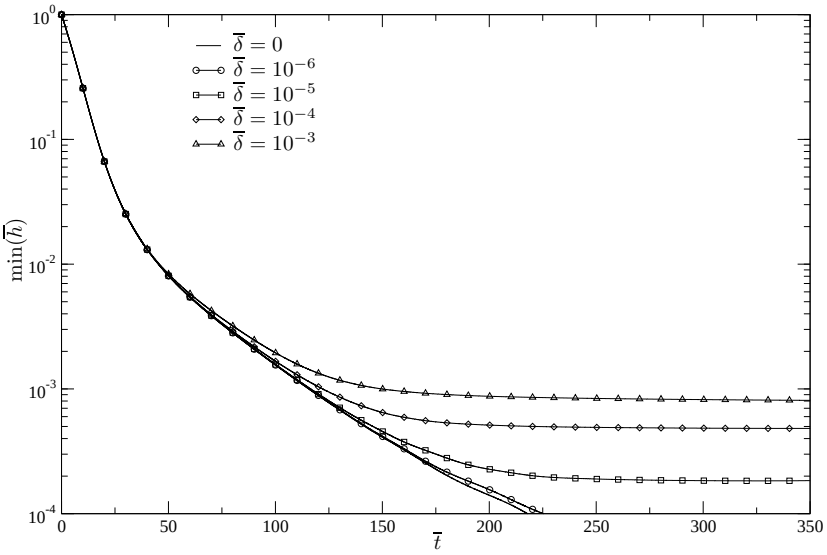

Figure 9: Minimum of $\overline{h}$ in the liquid film as a function of time for $\overline{\delta} = 0$, 10^{-6}, 10^{-5}, 10^{-4} and 10^{-3}.

5.2. Effect of the surface tension gradient

The surface tension and its gradient are determined for the same glass used in the previous subsection. The quantity $\delta\gamma$ given by (9) is equal to $4.2 \cdot 10^{-2}$ N/m using the coefficient factors given by Rubenstein [25]. The conditions used in the numerical simulations are identical to these used in the previous subsection. The Marangoni number is equal to $2.02 \cdot 10^{-3}$.

First, the effect of $\overline{\delta}$ is addressed by plotting the minimum of $\overline{h}$ as a function of time. The numerical computations are operated until the minimum of $\overline{h}$ reaches the dimensionless value equal to 10^{-4} corresponding to a thickness around 100 nm for an initial thickness H_0 equal to 1 mm. We assume that these dimensioned quantities are approximatively the maximum and minimum of thickness of the film during the experiment. Recall that the thickness of the frame is 1 mm and that film rupture for glass is around 100 nm. Figure 9 shows the behavior of the minimum of the film thickness versus time for five values of $\overline{\delta}$. The case of $\overline{\delta} = 0$ means that the surface tension gradient is equal to zero. When $\overline{\delta} = 10^{-6}$, the surface tension gradient is too small to see an effect on the drainage for a typical thickness of 10^{-4}. On the contrary, when $\overline{\delta}$ is larger than 10^{-6}, the behavior of the film thickness changes strongly when $\overline{h}$ is sufficiently small. Indeed, a steady-state regime is observed after drainage. The asymptotic film thickness increases with $\overline{\delta}$ due to the surface tension gradient that acts sooner in time when $\overline{\delta}$ is larger.

It is noteworthy that, according to these numerical simulations, film thickness decreases by a factor 10^4 over a dimensionless time approximatively equal to 220. The experimental measurements for temperature lower than 1150°C (see Figure 2-a) give a lifetime around 500 in the same unit. Even if the disagreement between the experimental and the numerical results seems important, these first numerical analysis and experimental measurements are promising. Indeed, the experiences are difficult to control. We do not know accurately the pulling-out velocity and the initial thickness profile.

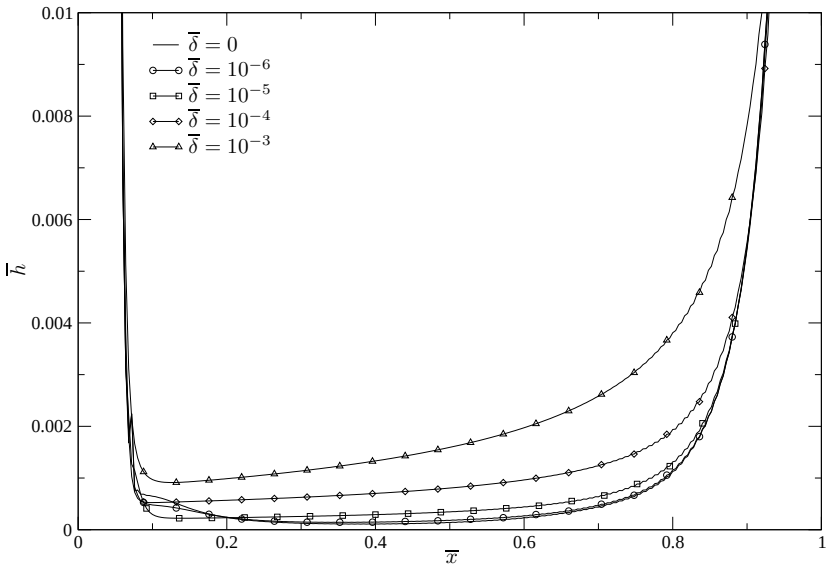

Figure 10: Film thickness, $\overline{h}$, as a function of $\overline{x}$ for $\overline{\delta} = 0$, 10^{-6}, 10^{-5}, 10^{-4} and 10^{-3} when $\overline{t} = 200$.

Film thickness profiles for $\overline{t} = 200$ for the five values of $\overline{\delta}$ are plotted in Figure 10. The film profile does not change for $\overline{\delta}$ equal to 0 and 10^{-6}. For $\overline{\delta} = 10^{-5}$, the film thickness is slightly thicker in the middle of the liquid film than for $\overline{\delta} < 10^{-5}$. Close to the top and the bottom, the film thickness is very similar to the profiles obtained with $\overline{\delta} = 0$ and $\overline{\delta} = 10^{-6}$. For $\overline{\delta} > 10^{-5}$, the shapes of the film profile are compared to the one computed for $\overline{\delta} = 10^{-5}$, but with larger values.

The main differences are significant on the film velocity as it can be seen in Figure 11 where $\overline{u}$ is plotted versus $\overline{x}$ for the five values of $\overline{\delta}$. The typical velocity decreases by a factor 3 when $\overline{\delta}$ increases from 0 to 10^{-5}. Remark, all profiles are close together near the bottom. The velocity profile observed for $\overline{\delta} = 10^{-5}$ and $\overline{\delta} = 10^{-4}$ does not change a lot apart from the top and the bottom. For the highest value of $\overline{\delta}$ (10^{-3}, the velocity decreases from the top to the bottom due to the largest heterogeneities in the film thickness observed in Figure 10, with a value less than the one obtained for $\overline{\delta} = 10^{-4}$ close to the bottom.

With $\overline{\delta} = 10^{-5}$, the film thickness reaches an asymptotic value equal to $1.8 \cdot 10^{-4}$. We note that this dimensionless depth and thickness correspond respectively to dimension values around 10^{-8} m, which is close to the depth over which Na_2O concentration varies according to SIMS analysis, and around 180 nm for asymptotic film thickness. Quantitatively as presented in section 2 this means that the surface tension varies in the range of $[1; 1.005]$. So, an increase of 0.5 % is enough to stabilize the film thickness. Moreover, the equilibrium thickness found with this value are close to the experimental value given by Laïmbock [18] who found a value equal to 200 nm. Kappel *et al.* [15] pointed out a value smaller (100 nm) but they did not measure the film thickness carefully. When $\overline{\delta}$ is larger than 10^{-5}, the equilibrium thicknesses seem too large compared to the previous results given in [18, 15].

The experiments done in [18, 15] and the present one were achieved in laboratory

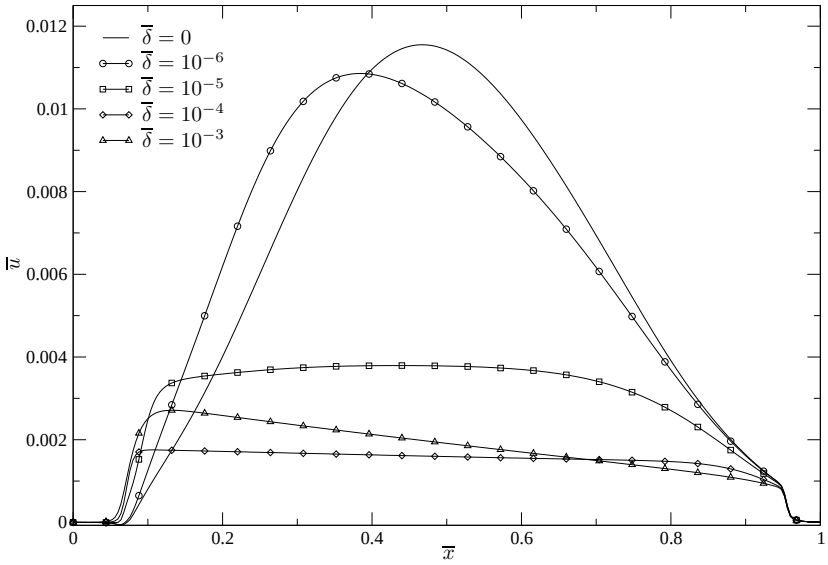

Figure 11: Film velocity, $\overline{u}$, as a function of x for $\overline{\delta} = 0$, 10^{-6}, 10^{-5}, 10^{-4} and 10^{-3} when $\overline{t} = 200$.

furnaces where the thermal homogeneities must be controlled. Indeed, a thermal gradient can also changes the surface tension. Scholze [31] indicates a coefficient of surface tension thermal gradient equal around $4 \cdot 10^{-5}$ N/(m·K) meaning that to have an increase of 0.5 % of the surface tension, the difference of the temperature must be equal to 40 K. This thermal difference must be appeared over the liquid length, typically few centimeters, which is too large with laboratory furnaces in which the thermal heterogeneities are usually less than 10 K in the area of working space. So, the stabilization of the liquid film must be mainly due to the chemical effect.

6. Conclusion

Drainage of vertical film of molten glass is investigated by reporting an experiment achieved at high temperature in a laboratory furnace. As expected, the observed lifetime decreases when temperature rises from 1100 to 1250°C because of a faster drainage due to decrease of bulk viscosity. However, we make evidence of an increase of lifetime for temperature larger than 1250°C that is correlated with the observation of patterns motion in the film. These motions are very similar to previously reported unstable motion generated by upward stresses that oppose regular gravitational drainage. We argue that these two phenomena are the consequence of the evaporation of surface active species like Na_2O confirmed by a decrease of Na_2O at proximity of the air/liquid interface measured by SIMS analysis. The evaporation has larger effect on surface tension in the area where the liquid film is thin than at the surface of the deep bath and thus generate upward Marangoni stresses. We quantitatively model the evolution of surface tension with film thickness by assuming that surface tension is the sum of the contribution of all chemical components present in volume and that mass loss per unit surface is function of film thickness.

A lubrication model is introduced to study the drainage of vertical liquid films. A surface tension gradient is introduced similarly to desorption/adsorption isotherm of thin film. The lubrication model coupled with surface tension variation is numerically solved with a finite difference method with an implicit time solver. The numerical procedure is applied to study the drainage of molten glass with a composition close to a window glass. We show that the chemical effect leading to the surface tension gradient can stabilize the liquid film at a thickness in agreement with observed results achieved by Laïmbock [18].

These results point out that even if a molten glass is usually considered as interface without "surfactant agents" (no amphiphilic molecules), the evaporation of oxides like Na_2O from interface can lead to a stabilization of gravitational drainage of vertical film. This effect is very important for applications because it can explain why a significant foam layer appears in glass furnaces. Indeed, if the temperature for which the gas release in the bulk of molten glass is in the range where the evaporation of Na_2O is significant to stabilize the liquid film, a foam layer can appear when the bubble flux coming from the glass bath is sufficiently important.

References

[1] R. G. C. Beerkens. Modeling the kinetics of volatilization from glass melts. *J. Am. Ceram. Soc.*, 84:1952–1960, 2001.

[2] J. C. Berg, A. Acrivos, and M. Boudart. Evaporative convection. In *Advances in Chemical Engineering*, volume 6, pages 61–123. Academic Press Inc., New York, 1966.

[3] S. Berg, Z. A. Adelizzi, and S. M. Troian. Experimental study of entrainment and drainage flows in microscale soap films. *Langmuir*, 21:3867–3876, 2005.

[4] R. J. Braun, S. A. Snow, and S. Naire. Models for gravitationally-driven free film drainage. *J. Eng. Math.*, 43:281–314, 2002.

[5] R. J. Braun, S. A. Snow, and U. C. Pernisz. Gravitational drainage of a tangentially immobile thick film. *J. Colloid Interface Sci.*, 219:225–240, 1999.

[6] C. J. W. Breward. *The mathematics of foam*. PhD thesis, University of Oxford, 1999.

[7] I. Cantat, S. Cohen-Addad, F. Elias, F. Graner, R. Höhler, O. Pitois, F. Rouyer, and A. Saint-Jalmes. *Les mousses. Structure et dynamique*. Editions Belin, Paris, 2010.

[8] S. Cohen-Addad and J.-M. di Meglio. Stabilization of aqueous foam by hydrosoluble polymers. 2. Role of polymer/surfactant interactions. *Langmuir*, 10:773–778, 1994.

[9] L. Collatz. *The numerical treatment of differential equations*. Springer-Verlag, Berlin, 1960.

[10] P.-G. de Gennes. "Young" soap films. *Langmuir*, 17:2416–2419, 2001.

[11] D. Exerowa and P. M. Kruglyakov. *Foam and foam films. Theory, experiment, apllication*. Elsevier, Amsterdam, 1998.

[12] M. Heller. *Numerical study of free surfaces and particle sorting in microfluidic systems*. PhD thesis, Technical University of Denmark, 2008.

[13] A. E. Hosoi and J. W. M. Bush. Evaporative instabilities in climbing films. *J. Fluid Mech.*, 442:217–239, 2001.

[14] P. D. Howell. Models for thin viscous sheets. *Eur. J. Appl. Math.*, 7:321–346, 1996.

[15] J. Kappel, R. Conradt, and H. Scholze. Foaming behaviour on glass melts. *Glastech. Ber.*, 60:189–201, 1987.

[16] D.-S. Kim and P. Hrma. Foaming in glass melts produced by sodium sulfate decomposition under ramp heating conditions. *J. Am. Ceram. Soc.*, 75:2959–2563, 1992.

[17] H. Kočárková. *Stabilité des mousses de verre : Expériences à l'échelle d'une bulle ou d'un film vertical (in English)*. PhD thesis, Université Paris-Est, Marne la Vallée, 2011.

[18] P. Laimböck. *Foaming of glass melts*. PhD thesis, Technische Universiteit Eindhoven, 1998.

[19] S. Lionti-Addad and J.-M. di Meglio. Stabilization of aqueous foam by hydrosoluble polymers. 1. Sodium dodecyl sulfate-ply(ethylene oxide) system. *Langmuir*, 8:324–327, 1992.

[20] K. Mysels, K. Shinoda, and S. Frankel. *Soap film. Studies of their thinning*. Pergamon, New York, 1959.

[21] S. Naire, R. J. Braun, and S. A. Snow. An insoluble surfactant model for a vertical draining free film. *J. Colloid Interface Sci.*, 230:91–106, 2000.
[22] A. Oron, S. H. Davis, and S. G. Bankoff. Long-scale evolution of thin liquid films. *Rev. Mod. Phys.*, 69:931–980, 1997.
[23] L. Pilon. Foams in glass manufacture. In P. Stevenson, editor, *Foam engineering: Fundamentals and Aplications*.
[24] L. Pilon. *Interfacial and transport phenomena in enclosed cell foam*. PhD thesis, Purdue University, 2002.
[25] C. Rubenstein. Factors for the calculation of the surface tension of glasses at 1200 C. *Glass Technol.*, 5:36–40, 1964.
[26] E. Ruckenstein and R. K. Jain. Spontaneous rupture of thin liquid films. *J. Chem. Soc., Faraday Trans. 2*, 70:132–147, 1974.
[27] K. J. Ruschak. Flow of a falling film into a pool. *AIChE J.*, 24:705–709, 1978.
[28] D. M. Sanders and W. K. Haller. Effect of water vapor on sodium vaporization from two silica-based glasses. *J. Am. Ceram. Soc.*, 60:138–141, 1977.
[29] L. Saulnier, F. Restagno, J. Delacotte, D. Langevin, and E. Rio. What is the mechanism of soap film entraintment? *Langmuir*, 27:13409–2011.
[30] B. Scheid, E. A. van Nierop, and H. A. Stone. Thermocapillary-assisted pulling of thin films: Application to molten metals. *Appl. Phys. Lett.*, 97:171906–1–3, 2010.
[31] H. Scholze. *Glass. Nature, Structures and Properties*. Springer-Verlag, Berlin, 1990.
[32] L. W. Schwartz and R. V. Roy. Modeling draining flow in mobile and immobile soap films. *J. Colloid Interface Sci.*, 218:309–323, 1999.
[33] J. E. Shelby. *Introduction to Glass Science and Technology*. The Royal Society of Chemistry, Cambridge, 1997.
[34] F. T. Trouton. On the coefficient of viscous traction and its relation to that of viscosity. *Proc. R. Soc. London, Ser. A*, 77:426–440, 1906.
[35] J. van der Schaaf and R. G. C. Beerkens. A model for foam formation, stability, and breakdown in glass-melting furnaces. *J. Colloid Interface Sci.*, 295:218–229, 2006.
[36] E. A. van Nierop, B. Scheid, and H. A. Stone. On the thickness of soap films: an alternative to Frankel's law. *J. Fluid Mech.*, 602:119–127, 2008.
[37] E. A. van Nierop, B. Scheid, and H. A. Stone. On the thickness of soap films: an alternative to Frankel's law - CORRIGENDUM. *J. Fluid Mech.*, 630:443, 2009.
[38] M. J. Varady and A. G. Fedorov. Combined radiation and conduction in glass foams. *J. Heat Transfer*, 124:1103–1109, 2002.
[39] A. Vrij. Possible mechanism for the spontaneous rupture of thin, free liquid films. *Discuss. Faraday Soc.*, 42:23–33, 1966.
[40] R. G. Wilson, F. A. Stevie, and C. W. Magee. *Secondary ion mass spectrometry: a practical handbook for depth profiling and bulk impurity analysis*. John Wiley and Sons Inc, Hoboken (USA), 1989.
[41] S. D. R. Wilson and A. F. Jones. The entry of a falling film into a pool and the air-entrainment problem. *J. Fluid Mech.*, 128:219–230, 1983.

Annexe C

Reproduction d'articles relatifs au chapitre 3

Concernant les travaux sur les mouvements de convection naturelle appliqués aux fours verriers, trois articles sont également reproduits. Le premier traite d'une approche systémique pour décrire un four verrier. Les deux suivants ont trait aux régimes de convection dans des cavités allongées. Les références de ces articles sont les suivantes :

- A. Ponsich, C. Azzaro-Pantel, S. Domenech, L. Pibouleau and F. Pigeonneau. A systemic approach for glass manufacturing process modeling. *Chemical Engineering and Processing*, 48 :1310-1320, 2009.
- J.-M. Flesselles and F. Pigeonneau. Kinematic regimes of convection at high Prandtl number in a shallow cavity. *C. R. Mécanique*, 65 :3158-3168, 2004.
- F. Pigeonneau and J.-M. Flesselles. Practical laws for natural convection of viscous fluids heated from above in a shallow cavity. *Int. J. Heat Mass Transfer*, 55 :436-442, 2012.

Chemical Engineering and Processing 48 (2009) 1310–1320

Contents lists available at ScienceDirect

Chemical Engineering and Processing: Process Intensification

journal homepage: www.elsevier.com/locate/cep

A systemic approach for glass manufacturing process modeling

A. Ponsich [a], C. Azzaro-Pantel [a,*], S. Domenech [a], L. Pibouleau [a], F. Pigeonneau [b]

[a] Laboratoire de Génie Chimique, UMR5503 CNRS/INP/UPS, 5 rue Paulin Talabot F-BP1301, 31106 Toulouse cedex 1, France
[b] Laboratoire Surface du Verre et Interfaces, UMR125 CNRS/Saint-Gobain 39, Quai Lucien Lefranc, BP 135, F-93303 Aubervilliers cedex, France

ARTICLE INFO

Article history:
Received 31 January 2008
Received in revised form 4 June 2009
Accepted 6 June 2009
Available online 16 June 2009

Keywords:
Glass manufacturing
Reactor networks
Mathematical programming optimization

ABSTRACT

Due to the difficulty in defining accurate models to represent the physical phenomena in glass furnaces, a large number of studies consider the process as a *black-box* system. The systemic approach proposed in this paper relies on a decomposition of the furnace into two entities, i.e. the combustion chamber and the glass bath. Next, a reactor network structure is automatically designed to reproduce the hydrodynamic features in the considered zone. These computations are based on the minimization of the quadratic difference between the network output and Residence Time Distributions (RTDs) obtained through CFD simulations.

The optimization results provide a network structure showing good agreement with the RTDs computed by CFD. In addition, they highlight, in both furnace zones, some *useless* volumes that do not participate to the global flow. These results stand as a good basis to extend the study to the computations of kinetics, energy or environmental criteria, which in turn may be optimized.

© 2009 Elsevier B.V. All rights reserved.

1. Introduction

During the last decades, glass industry has gained a great experience in the operating mode of glass melting furnaces, thus leading to the implementation of accurate and efficient processes. The study of such furnaces has constituted a major research activity of many companies. However, the extreme temperature conditions existing within the furnaces make it very difficult to observe and understand the occurring physico-chemical phenomena. Consequently, only a few models have been developed to understand the global behavior of the furnace and to interpret the process trends.

The main purpose of this study is to present a functional analysis of some glass manufacturing processes, particularly focusing on a description of the furnaces. In a more general and long-term perspective, the underlying idea consists in proposing generic models that would fit very well with the furnace behavior, in such a way that some performance criteria, defined according to the glass industry needs, could be optimized. These criteria might be oriented, for instance, towards technico-economic, environmental or energy requirements. In this context, the present study only constitutes a feasibility analysis, in order to lay the foundations of a more complete work. The paper is organized as follows: in the second section, a synthesis of the literature devoted to glass processes is proposed. This preliminary analysis leads to the definition of the chosen methodology, i.e. a systemic approach based on reactor networks modeling in Section 3. Section 4 shows the first results of the work, while some conclusions and perspectives are drawn in the last section.

2. Literature review

This literature review gives a global roadmap of the various works dedicated to the representation of glass manufacturing furnaces and their behavior. It is worth mentioning that even if the number of research works dealing with the physical phenomena occurring in the glass furnace is important, the variety of studies is quite few diversified. Indeed, it appeared that the mathematical modeling of these phenomena is based on two kinds of representation modes. The former, which constitutes the great majority of them, lies on fluid dynamics computations. The second research domain does not aim at accurately describing the involved internal mechanisms, but mostly views the furnaces as 'black-box' systems and only analyses inputs and outputs, leading to either learning/training techniques, or reactor network approaches.

2.1. Computational fluid dynamics (CFDs)

Most published works on glass manufacturing furnaces modeling deal with CFD techniques, developed in order to represent locally and globally the hydrodynamics, heat or mass transfer phenomena taking place in the furnaces. For instance, studies such as in [1] try to model and optimize the chemical development of NOx pollutants, emitted in the laboratory smokes, in the combustion chamber. The optimization variables are the combustible

* Corresponding author.
E-mail address: Catherine.AzzaroPantel@ensiacet.fr (C. Azzaro-Pantel).

0255-2701/$ – see front matter © 2009 Elsevier B.V. All rights reserved.
doi:10.1016/j.cep.2009.06.001

composition, the air pre-heating conditions (combustive) and the combustion reaction stoichiometry. In [2], convection models are adopted to represent the convection intensity in the glass bath, while the effect of the addition of elements to the furnace structure.

In the CFD simulation framework, the furnace geometry, the melted glass physical properties, the influence of spatial temperature distribution and many other factors constitute parameters. However, the use of CFD techniques to represent the involved physical and chemical phenomena with both a good accuracy and acceptable computational times, is currently a challenging issue. Thus, the aim of our study is to propose an alternative computational strategy that would avoid such CFD calculations.

In spite of the improvements both in discretization methods (finite volume/finite elements) and computational powers, the main drawback of the CFD approach still lies in the computational times, which may be, in some cases, prohibitive. In that context, it is difficult to consider some phenomena such as, for instance, the kinetics of the chemicals involved in the process. The models then have to be simplified in order to integrate them in the CFD computations.

2.2. Learning methods

In a great variety of research areas, several methods were developed to improve the understanding of systems viewed as 'black-box' systems. The learning methods are based on the availability of data measured on real systems and then use inference mechanisms to build rules extrapolating the observed trends. In the literature devoted to the study of glass manufacturing systems, the learning methods result mainly from the Artificial Intelligence area.

- Artificial Neural Networks (ANNs) consist in generating analytical expressions of the system outputs according to the input data. These analytical expressions may be linear or not, and lead to the formulation of predictive models. In [3], neural networks are implemented to compute the weekly production of a glass furnace according to the production planning. Several tools are used (linear or non-linear regressions, ANNs systems with retro-propagation algorithms, etc.), as well as a 175 elements database, to accurately predict the furnace output for a given input. Even though the mentioned project does not exactly aim at the description of the physical phenomena inside a furnace, it shows that possible applications can be reached; some precisions will be given on this point in the next section.
- Expert systems methodology is to reproduce the cognitive mechanisms of an expert in a particular area. It lies on a database of facts and rules, and on an inference motor, using the database to produce new facts and thus providing a decision-support tool.
- Fuzzy-logic-based learning methods present some similarities with expert systems. They are based on a fuzzy partition of the definition ranges of the input parameters and on inference processes that allow the generation of extrapolated system responses, in a similarly fuzzy-partitioned output domain. These methods were mainly applied to the case of control systems of the furnaces. The control parameters are then tuned through an optimization step carried out with genetic algorithms, considering the following criteria: energy (fuel consumption), quality (number of bubbles or of not-melted elements in the resulting glass production) (see [4,5]). The details of the fuzzy-logic approach and of the used genetic algorithm are fully explained in [6].

Learning method class is obviously quite attractive since system outputs can be obtained without an accurate knowledge of the physics of the involved phenomena (of course, the knowledge of system outputs can constitute the real challenge). Nevertheless, its inherent drawback is the necessary availability of databases related to the studied problem: the database size will then condition the quality of the resulting inference model. It is worth recalling that, moreover, the database will be used not only to build and train the model, but also to validate later its behavior and evaluate the accuracy of the proposed extrapolation.

2.3. Reactor network models

Reactor network modeling is a commonly used technique in chemical engineering, to model various kinds of flows inside a closed container. In a way similar to the learning techniques, it does not require an accurate physical understanding of the involved phenomena. Unitary operating items from the chemical engineering area, such as Continuous Stirred Tank Reactors (CSTRs), plug-flow reactors (PRs), idle zones, bypass or recycling streams, etc., are organized in a stream network, in such a way that the experimental output of the real system is reproduced. According to the information found in a literature overview, two types of approach are possible:

- *The systemic approach* relies on the knowledge of experimental input and output signals. From the formulation of mass balance equations for each unit or node in the network, an optimization problem is generally deduced involving two objectives: (i) minimizing the gap (quadratic difference) between the model and the experiment; (ii) designing a model that is as simple as possible, i.e. including the lowest number of elementary items. A key-point of the application of this method is of course the choice of an appropriate solution technique. Two kinds of variables are involved, either structural (existence of an element of the network) or parametrical (size of the reactors, flow-rates of the internal streams) characteristics of the network. There are two classes of experimental signals, either static or dynamic:
  - *Static case*: the input stream has known and fixed flow-rates and concentrations. The reactor network thus tries to approximate the output concentration value, assuming a steady state for the whole system. This kind of study was illustrated in [7] with the modeling of a fluidized bed used for the cleanup of aqueous effluents and in [8] with the representation of a decantation bed and of a natural gas distribution network. The used optimization methods were respectively a hybrid technique (genetic algorithm and sequential quadratic programming) and a Mathematical Programming technique (Branch & Bound) implemented in the SBB solution module, integrated within the GAMS environment [9].
  - *Dynamic case*: the signal is subjected to a variation of the input concentration of any tracer. Dirac pulse and step injection are usually used to obtain the Residence Time Distributions, which are typical of each type of input variation. This kind of studies thus focuses on transient state analysis, which involves the formulation of differential mass balances. These models were used in [10](simulated annealing) and [8](GAMS-SBB) for the representation of flows in a ventilated room. The experimental signals are actually outputs obtained by CFD calculations, or arbitrarily designed to solve academic examples.
- *The topological approach* is mainly related to the gas flows due to combustions, which typically take place in the combustion chamber of the furnace, above the glass bath ("laboratory") (see [11,12]). The development of this approach is based on the observation that the CFD methods are computationally very greedy. Particularly, they prevent from considering, in addition to the hydrodynamic aspects, the chemical kinetics of combustion in a way different from extremely simplified models, which do not provide satisfying results (as compared with the experimental trends). The main idea of this method then consists in decoupling both phenomena by representing, in a first step, the flows

characteristics by a reactor network, and then by applying to this latter the realistic and complex chemical kinetics of contaminant production, such as NOx [13]. To find the reactor network corresponding to the studied system, the methodology first determines a mapping of the combustion chamber, focusing particularly on the spatial distributions of some parameters that perform a key-role in the above-mentioned chemical kinetics: the temperature (T) and the combustion air/fuel stoichiometry (σ). The hydrodynamics computed by CFD thus enables to generate (T)-fields and σ-fields. Then, a group of zones is determined within the combustion chamber, where the key-parameters (T) and σ present homogeneous values. This operation is manually initialized and is then run automatically in such a way that both mean and standard deviation values of (T) and σ within each zone do not exceed a maximal allowed variation (see [12]). Finally, these homogeneous zones can be represented as ideal reactors: the nature of each reactor (CSTR or PR) is deduced from an analysis of velocity fields inside the corresponding zone. A uniform velocity distribution is interpreted as a continuous stirred tank reactor (CSTR) while an unidirectional velocity field typically represents a plug-flow reactor (PR). Besides, the determined zones are composed of the elementary volumetric cells that were initially used for the space discretization during the CFD calculations. An analogy can then be empirically established between the combustion chamber mapping and the reactor network, in order to complete the definition of this latter:

- Each zone volume corresponds to the associate reactor volume.
- The mass exchanges between each zone, computed as the sum of the mass exchanges between cells belonging to different zones, correspond to the flow-rates of the network streams.
- The mean values (computed through the formula proposed in [12]) of temperature and stoichiometry on each zone correspond to the temperature and the composition in each ideal reactor, thus allowing to carry out the kinetics computations of NOx production.

The numerical results provided in [14] highlighted the validity of the kinetics calculated following this methodology, which proved to be in agreement with the experimental data available for real combustion chambers.

Both of the above-mentioned reactor network strategies seem relevant, but they differ on two particular issues. First, the topological approach has the advantage to associate each homogeneous zone to a physical region in the furnace, and therefore to the operating parameters (temperature and composition) that are necessary for the kinetics computations. Second, [14] showed that the topological method is more accurate to predict the combustion kinetics, when the number of reactors in the network is high: this involves high computational times to determine a sufficiently extended network and then to carry out the kinetics calculations over it. In comparison, even if the systemic approach does not focus on the operating parameters of each reactor, it considers the network simplicity as an important aspect, which renders easier the following kinetics calculations. Thus, a reliable method, associating operating parameters to the reactors, would guarantee a large efficiency to the systemic approach.

3. Preliminary analysis

A soda-lime-silica glass is obtained by heating raw materials composed mainly by silica, SiO_2 and carbonated elements, Na_2CO_3, and $CaCO_3$. Thermal energy comes from combustion chamber just above the glass bath and in a least part from electric energy directly in the glass bath. The bubbling device is generally used to increase locally the heat flux (see for more details [15]). This chemical process leads to a huge production of bubbles. The quality requirements need to remove this bubble population by a chemical process activated by temperature [16,17]. So, the size and number of bubbles at the end of the furnace and the quantity of unmelted particles as well are important to know. The environmental requirements need also to know the quantity of pollutant elements as SO_x, NO_x, and CO_2.

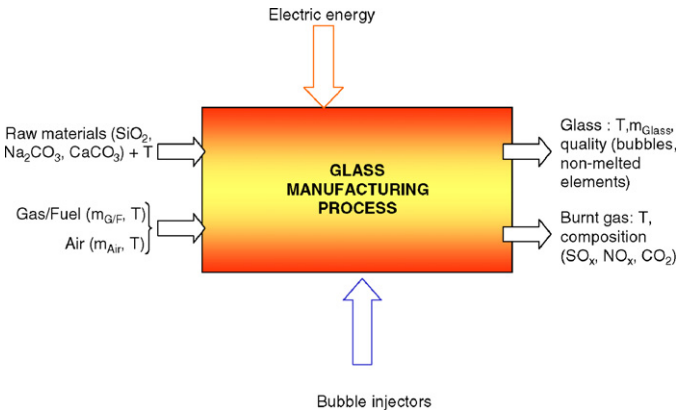

Fig. 1. Global description of the glass manufacturing furnace.

In this study, two accuracy levels were considered. On the one hand, the furnace is viewed as a single "black-box" system: the input and output of the system are defined such as illustrated in Fig. 1. For this type of representation, the learning methods seem to be the only ones that can be applied. The drawback, already mentioned in the previous section, is the requirement of gathering a sufficient data number to create a reliable database on which the training may be carried out. This involves a large experimental campaign, performed on many real glass manufacturing plants, including the determination of ways of measuring the variables and criteria defined in Fig. 1, which is not a simple task under the extreme conditions governing the furnaces.

On the other hand, within the perspective of applying a reactor network modeling approach, a more accurate decomposition of the whole system is proposed in Fig. 2. The glass manufacturing process is decoupled into two entities, i.e. glass bath and combustion chamber. This decomposition would then allow taking advantage of the CFD simulations. These are carried out separately on each part of the system, imposing particular boundary conditions to the interface glass bath–combustion chamber. Therefore, the objective would be to generate two reactor networks, each one dedicated to the representation of a furnace section. This methodology would require, in order to model a whole furnace, the availability of data obtained from CFD simulations carried out on both zones of a same furnace.

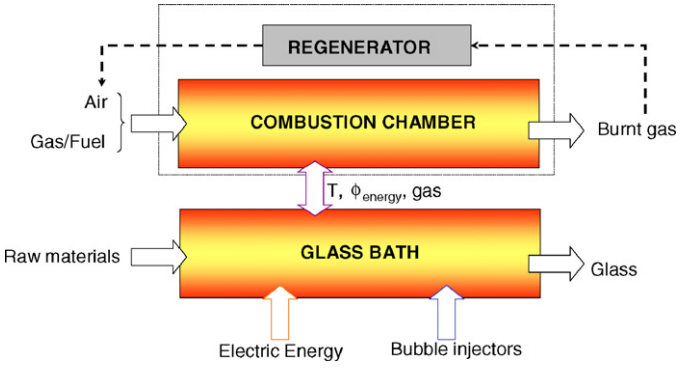

Fig. 2. Decoupling the glass manufacturing furnace.

As a result, the systemic approach seems to be a promising strategy to solve this kind of problems. In this framework, this paper constitutes the first step of the global methodology. Such as mentioned in the previous section, it is necessary to integrate kinetics or energy aspects to the network obtained from the CFD computations, which constitutes long-term research perspectives. The preliminary step which is presented here, has the objective to validate the feasibility of this strategy, by determining reactor networks by specific Residence Time Distributions, obtained by simulations carried out in Saint-Gobain Recherche Center. The numerical computations have been performed by use of a commercial CFD software tool. The glass is assumed as an incompressible fluid where the buoyancy force due to the thermal dilatation is taken into account under Boussinesq approximation [18]. The heat and mass transfer is mainly produced by the free convection due to the large scale thermal gradient occurring on the top surface of the bath (see for more details [19]). The thermal dependence of the dynamical viscosity is taken into account using an exponential behavior as a function of temperature [20]. The radiative process is also very important in the glass industry since temperature reaches 1600 ° C in the glass bath. A glass is a semitransparent material where the radiative transfer is treated as a diffusion process for which the radiative conductivity is a function of the cube of temperature [21]. The thermal boundary conditions between the glass and furnace walls are determined by the knowledge of the design of furnace. The raw material is seen as a thermal sink and a mass inlet. The computation is carried out by a specific fitting of temperature obtained numerically and in the industrial plant. The Residence Time Distribution is achieved after the CFD calculation. The RTD is determined by looking the answer of Heaviside function. The time derivative gives directly the RTD.

4. Systemic approach implementation

The set of the following computations presented in this section aims at validating the systemic approach by reactor networks implemented in this study. The objective is to show that a structure of reactor network and the associated parameters can be derived from the experimental signal corresponding to the hydrodynamics phenomena in the glass manufacturing furnaces. This experimental signal was obtained by CFD simulations that were carried out, for both combustion chamber and glass bath, by the 'Glass Melting' research team of Saint-Gobain Recherche.

4.1. Details of the method

The main principles of the flow model identification were briefly recalled in the bibliography review section. All the aforementioned studies deal with dynamic case, i.e. the (CFD-based) experimental signal is a Residence Time Distribution (RTD) resulting from a classical input variation (Dirac pulse or step injection): it is thus necessary to reproduce, with an adapted model, the output signal evolution throughout time. It is worth noting that, despite the existence of various chemical compounds in the furnace (in both combustion chamber and glass bath, such as exhibited in Fig. 1), only one is considered in the framework of this study. This chemical is thus viewed as a tracer (involving no chemical reaction) for which concentration variations are observed in order to get the Residence Time Distributions used for the following computations.

As it was mentioned previously, the model equations represent the mass balances at each node of the network and for each ideal reactor involved in the structure. However, because of the dynamic nature of the problem, the considered mass balances imply differential formulations: of course, the time scale discretization results in a number of equations that must be verified at each instant $t = t_1, \ldots, t_F$. The method begins defining a superstructure, which gathers all the elementary operations likely to constitute a final network that accurately models the studied flow. Binary variables y_i are associated to each potential unit: they are equal to 1 if the unit exists, and to 0 otherwise. The variables representing the flow-rate and concentration in each stream (resp. Q_j and C_j), as well as the ones associated to the reactor volumes (V_i) are real variables. For the sake of illustration, Fig. 3 provides a hypothetical superstructure.

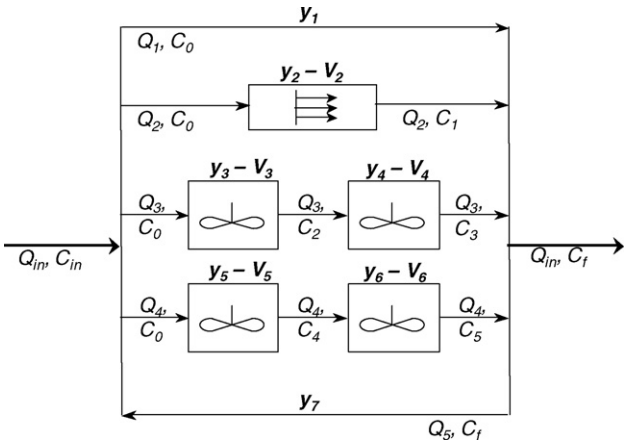

Fig. 3. Superstructure example.

Therefore, the optimizing tool will have to modify and schedule the initial superstructure in order to minimize a criterion that takes into account: (i) on the one hand, for each time discretization slot, the distance between the CFD output concentration Cf_{exp} and the modeled one Cf_{mod}; (ii) on the other hand, the structure complexity, i.e. the number of elementary units belonging to the final network. This objective can thus be formulated such as the following equation:

$$\min Z = k \left[\sum_{t=t_1}^{t_F} (Cf_{\text{exp}}(t) - Cf_{\text{mod}}(t))^2 \right] + \sum_{j=1}^{nj} y_j \quad (1)$$

In this equation, k is a constant scalar balancing the relative weights of each term within the global criterion. For instance, the higher k, the greater the importance given to the model-experiment distance minimization; in the same time, the optimization tool will disregard the structure complexity reduction. For the following computations, the k value was determined after a preliminary sensitivity analysis study which showed very clear variations (between a very simple network that did not optimize well the quadratic difference criterion and complex solutions that did not bring significant improvements of the quadratic difference criterion) and allowed an easy choice of the coefficient: the k value is taken equal to 5×10^3.

Besides, the model is submitted to equality constraints that consist of differential mass balances on the network (a complete description of the equations is available in Appendix A). It must be pointed out that some variables and constraints are subjected to the existence of the element (stream or reactor) they are associated with: this requires a dynamic constraint handling and a valid bounding technique for the real variables within the optimization problem.

The resulting problem is of Mixed Integer Non-Linear Programming (MINLP) nature since it involves both binary and continuous variables, with non-linear equations. This kind of problem is of the most complex ones because of the discretization of the search space due to the integer variables. At the same time, non-linearities may cause local optima in non-convex cases. It was shown in [8] that the most efficient solution technique is a Mathematical Programming Branch & Bound procedure (implemented in the SBB module of the GAMS environment [9]). This method was therefore chosen for this study.

The structural and parametric identification of a network requires the following data:

- Global reactor volume (i.e. the sum of the ideal reactor volumes in the network is equal to the real container volume simulated by CFD).
- Flow-rate (static) and concentration (dynamic) of the input and output streams.
- Residence Time Distribution on the considered tank (combustion chamber or glass bath).

It must be pointed out that the RTD curves provided by the CFD simulations correspond to a Dirac pulse. However, the mass balance differentiation for Dirac pulses involves complex mathematical formulations. Since the Dirac pulse corresponds to the step injection derivative, the response (output signal) is obtained by a simple integration of the former signal response over time. Thus, for the following calculations, the output signal was integrated in order to get a response to a step injection, whose magnitude is equal to 1. This results in a simpler model formulation.

Necessarily, the RTD curves computed from CFD computations have a large number of points corresponding to the time discretization (about 20,000 points for each RTD). Yet, the chosen formulation leads to write the mass balance equations for each time slot in the model. Thus, to avoid a huge number of constraints that would heavily penalize the solution procedure, the interval between each time slot was increased in order to finally use only 100 points for the time discretization (sensitivity tests that are not presented here showed that this number allowed a correct solution accuracy without slowing down the computations).

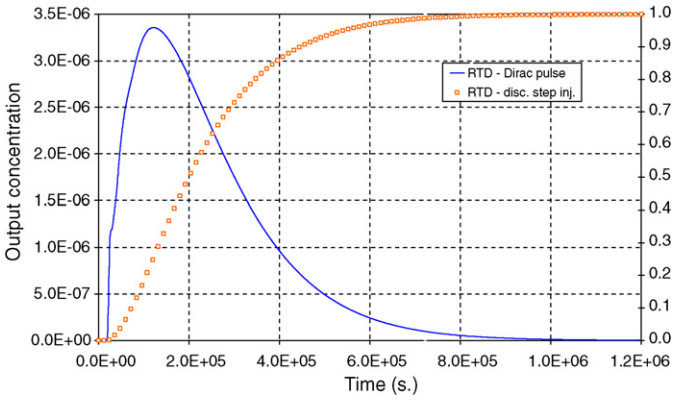

Fig. 4. Glass bath (initial and integrated) RTD.

The two next subsections present the computational results obtained on the glass bath and the combustion chamber, respectively.

4.2. Computations on the glass bath

Fig. 4 shows the RTD associated to the glass bath in its both initial (Dirac pulse) and integrated (step injection) form. The value of the glass bath total volume is 798.05 m^3, and the input flow-rate is equal to 12.18 m^3/h.

Table 1
Glass bath results, according to the initial superstructure.

Used superstructure	Solution	Q.D.
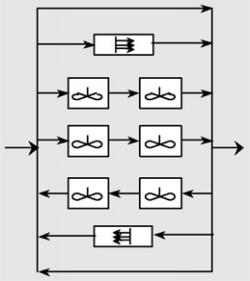	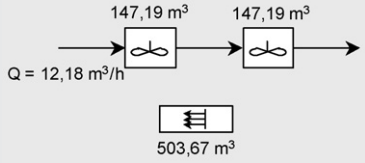	2.79×10^{-3}
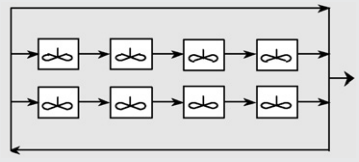		2.09×10^{-3}
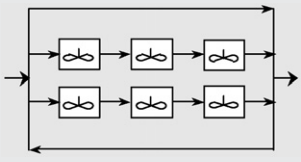	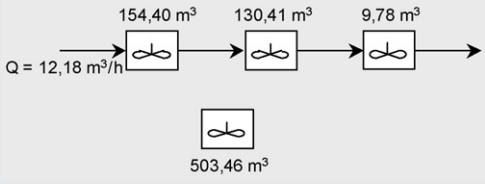	5.73×10^{-6}
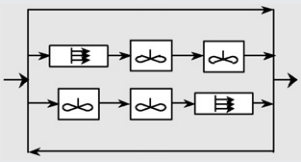	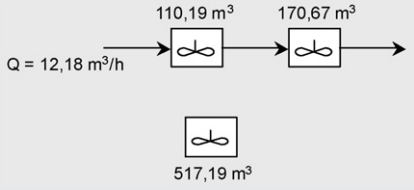	2.60×10^{-4}

Table 1 sums up the superstructures tested to reproduce the flow associated to the above RTD, as well as the corresponding solutions and the quadratic distance between model and CFD-based data. The curves for these models are available in Appendix B. It appears that superstructure 3 is the most adapted to provide a modeled output similar to the simulated one, with a quadratic difference approximately equal to 10^{-6}.

An immediate comment is that, whatever the initial used superstructure, the solutions propose a separate reactor (CSTR or PR), without any stream to feed it, characterized by a volume varying from 501 to 517 m^3. This volume is commonly called 'idle' volume, or 'useless' volume. It is worth underlying that this volume is not likely to represent a particular unique zone in the glass bath, but more certainly a set of regions, spread over the whole volume, where local dynamic behaviors (for instance, very local recirculation streams) do not participate to the global flow.

Nevertheless, even though it is commonly admitted by glass manufacturing experts that there exists some zones that are no involved in the global flow, the 'useless' volume highlighted by these computations fills a large part of the total volume (between 63 and 65 percent, depending on the considered solution). Moreover, the repeatability of this result, obtained independently from the initial superstructure, seems to confirm the trend. Two additional analyses were carried out in order to justify it.

The former study aims at proving that this is not a numerical problem that constrained the optimizing procedure to keep trapped on this solution. Thus, similar computations are carried out, only by modifying the global reactor volume: 500 m^3 instead of the initial value of 798.05 m^3. The result is identical to the previous one (structure and volumes of the ideal reactors), except for the 'useless' volume that is equal to 205.46 m^3: the difference between the two obtained 'useless' volumes is thus equal to the difference between the two global volumes ($798.05 - 500 = 298.05\ m^3$). This confirms the purpose of the 'useless' volume, which can be seen as a slack variable for the global volume constraint:

$$\sum_{j=1}^{nj} V_j = V_T \tag{2}$$

This former step validates the existence of a 'useless' volume. The latter study focuses on the physical meaning of this trend. Two simulations are now carried out (with any spreadsheet software) in order to observe the response of a single CSTR reactor. Its volume is chosen equal to 800 m^3 (the global volume) and 300 m^3 (the 'useful' volume) successively. Fig. 5 gives an illustration of both outputs, compared to the CFD simulation: it clearly shows that, even if the curve corresponding to the 300 m^3 reactor does not exactly fit the curve obtained by CFD, it constitutes a much better approximation than the 800 m^3 reactor curve. Thus, the 'useless' volume determined by network identification is justified.

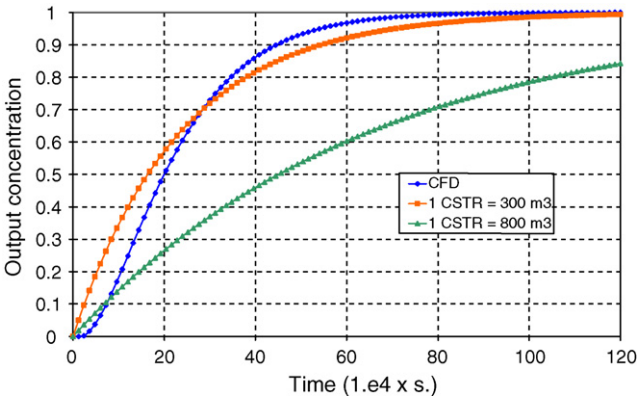

Fig. 5. CSTR simulations with $V = 300\ m^3$ and $V = 800\ m^3$.

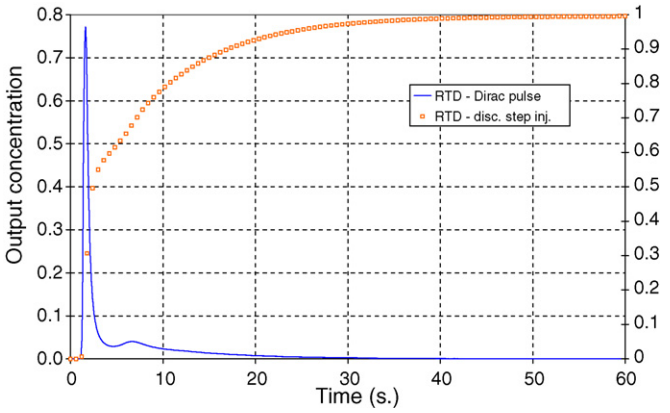

Fig. 6. Combustion chamber (initial and integrated) RTD.

The solutions obtained from the different superstructures have various reactors arranged in series. Additional computations (not presented here) were performed to verify that the order of the CSTRs does not have any effect on the output concentration.

4.3. Combustion chamber

The RTD used in this section is not associated to the whole combustion chamber but to a cross-section (perpendicular to the glass flow in the below bath) that includes one of the fuel-air injector of the considered 'float' furnace: the zone in front of this injector is the location where the flame develops, up to the smoke outlets towards the corresponding regenerator. Fig. 6 presents the RTD curve associated to this combustion chamber section in its both initial (Dirac pulse) and integrated (step injection) form. The total section volume is equal to 90.63 m^3 and the flow-rate is equal to 1.942 m^3/s. This flow-rate is higher than in the glass bath case, which will imply lower characteristic residence times.

Just in the same way as for the glass bath study, various initial superstructures were tested and their respective solutions are presented in Table 2. The quadratic differences shown in Table 2 highlight that the first solution is undoubtedly the best one. Furthermore, the curves showing CFD simulation vs. model curves are available in Appendix C and confirm the low consistency of the other solutions (2–4) towards the 'experimental' curve.

The second 'swelling' observable in the original Dirac pulse RTD reproduces an important recirculation stream, which is identified whatever the used superstructure. However, this trend causes a sudden change in the slope of the integrated RTD curve, which is not reproduced by superstructures 2 and 3. Besides, the slight response time-shift with respect to the input injection time (minimum residence time) can be easily assimilated to a plug-flow effect, and can only be modeled by at least 3 CSTRs set up in series (this explains why superstructure 4 is unable to reproduce this effect).

Moreover, a second trend that is similar in all four determined solutions is the existence of an almost zero flow-rate stream (direct way for structures 2 and 3 and in reverse way for structures 1 and 4). This stream passes through various CSTRs that fill a global volume of between 76 and 79 m^3. Once more, this observation indicates that a 'useless' volume can be considered, with a very important relative size towards the global volume (about 85 percent). A more accurate analysis of the first superstructure solution will prove it and lead to further network simplifications.

Firstly, a simulation is carried out to determine the response of solution 1 when the weak flow-rate stream and the two associated CSTRs are removed. This leads to consider an 'idle' volume

Table 2
Combustion chamber results, according to the initial superstructure.

Used superstructure	Solution	Q.D.
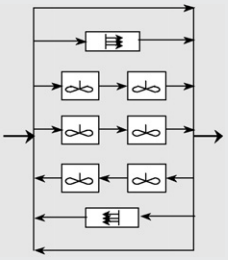	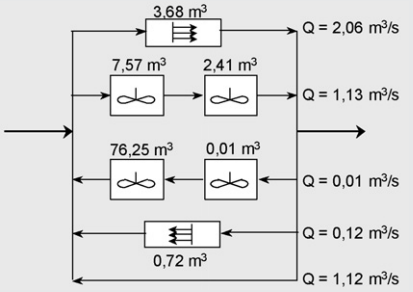	6.75×10^{-5}
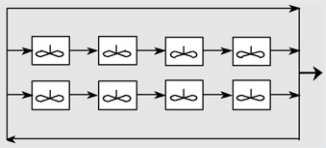	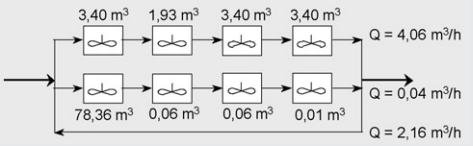	1.69×10^{-1}
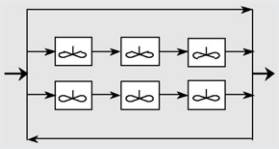	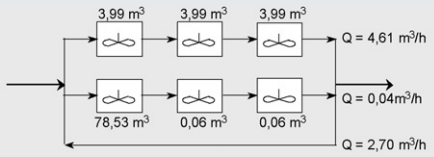	6.86×10^{-2}
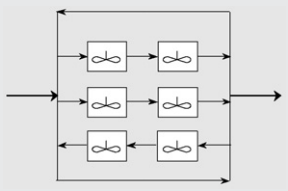	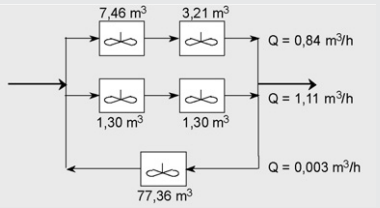	3.13×10^{-2}

equal to 76.26 m^3, and the 0.01 m^3/s stream is added to the recycling stream ($Q = 1.12 + 0.01 = 1.13\ m^3/s$). The simulation then provides a quadratic difference value equal to 2.09×10^{-3} (instead of the initial 6.75×10^{-6}). Even though the accuracy loss seems quite important, the response curve given in Fig. 7 proves that the main features of the experimental output signal are respected (minimum residence time, slope variation). This confirms the 'useless' volume existence. Besides, the magnitude of this useless volume towards the global volume can be explained more easily than in the glass bath case: the studied flow is a flame development flow, which does not necessarily fill a large volume since the main energy transfer occurs through radiation. The large size of the 'useless' volume is therefore less surprising here.

Moreover, a second simplification can also be proposed: since the second plug-flow reactor volume is very low with respect to the global container one (0.72 m^3), this reactor can also be removed, adding the 0.72 m^3 to the 'useless' volume and the corresponding stream flow-rate to the recycling stream (now equal to 1.25 m^3/s) The quadratic difference in the resulting solution is equal to 2.27×10^{-3}, which represents an insignificant increase (and the response curve is almost identical to that shown in Fig. 7). A second simplified structure of solution 1, illustrated in Fig. 8, is thus obtained. This former provides a very satisfactory output. This

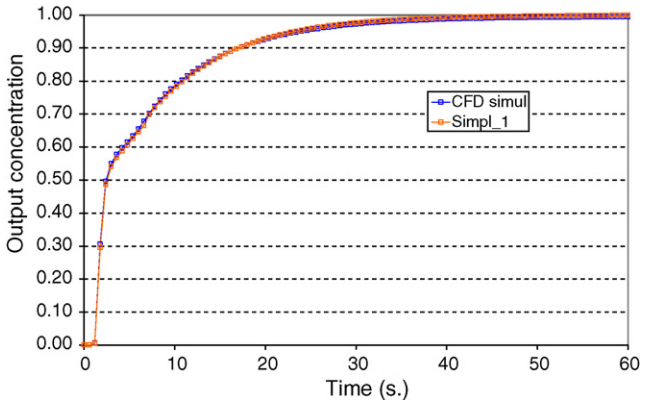

Fig. 7. Response for solution 1 first simplification ($Simpl_1$).

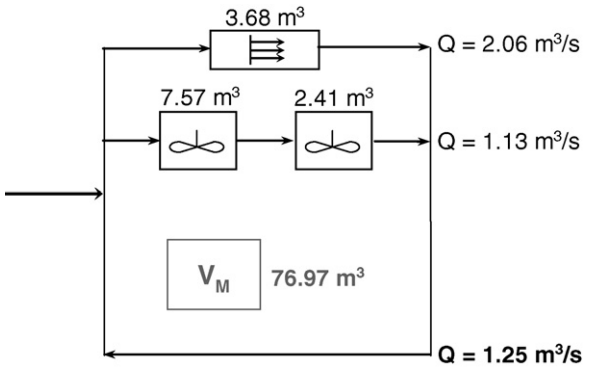

Fig. 8. Final structure, after simplifying solution 1.

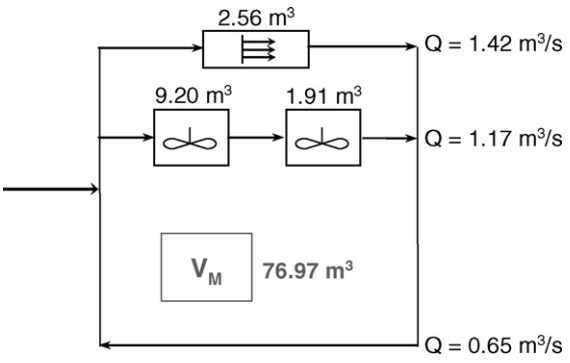

Fig. 9. Final solution after optimization.

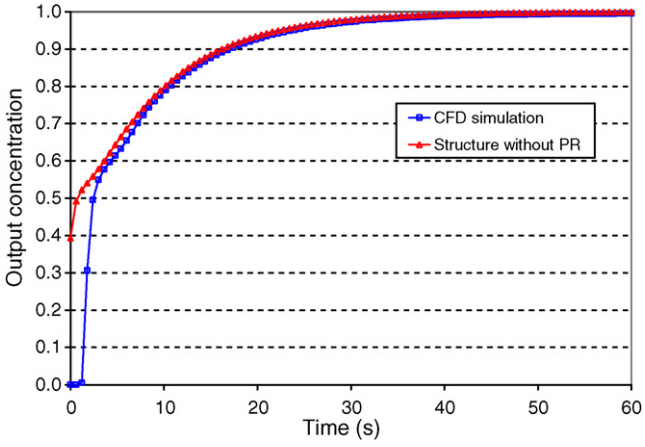

Fig. 10. Proof of the necessary presence of the PR in the final structure.

network was not found by the optimization module because of the higher quadratic difference, but it may be obtained by increasing the weight associated to the structure complexity reduction in the optimization criterion, i.e. decreasing the k factor in Eq. (1).

Finally, in order to confirm the validity of the found solution, an optimization step is carried out, using the final determined solution as the initial superstructure. The same solution structure is found, which thus confirms the optimality of the resulting network. Only the parametrical variables (volumes and flow-rates) are modified, to obtain a solution (Fig. 9) that slightly improves the quadratic difference (1.09×10^{-3}).

A last simulation was run to show that the plug-flow reactor is necessary. Fig. 10 then proves that, by removing the PR and the associated stream, the output curve does not reproduce the minimum residence time, which is one of the main features of the experimental response. The above-mentioned plug-flow effect is thus demonstrated.

5. Conclusions and perspectives

This study presents a new way of modeling glass manufacturing processes, based on a systemic approach commonly used in Process Systems Engineering. The involved processes exhibit complex phenomena occurring in the glass manufacturing system. The lack of sufficient experimental data renders difficult the use of learning methods. Thus, the proposed methodology first relies on the decomposition of the whole furnace in two entities, i.e. the combustion chamber and the glass bath. Then, it uses simulations carried out by CFD tools as experimental data to optimize a reactor network to obtain a simplified representation of the hydrodynamics in each furnace zone.

The proposed framework is an alternative computational strategy to design-oriented CFD computations: the system representation is a "black-box" model, where physical and chemical phenomena occurring inside the furnace (which have an obvious influence on the fluid dynamics) are not taken into account explicitly. The advantage of the proposed method is that it only considers input/output informations in order to build a model that reproduces faithfully the Residence Time Distribution. The presented study validates this first step, while future work must be devoted to the extension of the model and to the consideration of kinetics computations. More precisely, the following steps have been taken into account:

- The optimization step consists in representing the mass balances over a predefined superstructure and in differentiating the equations to get a dynamic model that can fit with the Residence Time Distributions provided by CFD simulations. The resulting Mathematical Programming formulation then minimizes the quadratic distance between model and CFD simulation outputs, and is solved through a Branch & Bound procedure.
- The preliminary computations provided very satisfactory results, since in furnace region cases, a reactor network giving an output similar to the experimental response can be identified. This proves the method ability to reliably modeling the hydrodynamics phenomena in the glass bath or over a section of the combustion chamber. Moreover, the obtained results exhibit some trends proper to the glass manufacturing furnace, and, more particularly, the existence of 'useless' volumes that do not participate to the global flow. These numerical trends were confirmed by further studies, and therefore, they should lead glass manufacturing experts to go into the details of the physical reasons of the mentioned behavior (strong recirculation streams, particular flows local to narrow zones, etc.).
- Besides, the literature review developed in Section 2 showed that a quite similar methodology was used in the dedicated literature: the reactor network representing the flow in the considered container was yet derived from a topological approach. This strategy is particularly useful to carry out detailed and complex kinetics computations to study the contaminant production (particularly the NOx species that appear in the combustion chamber). In this sense, the systemic approach drawback is clearly the issue of associating operating parameters to the reactors in the network, in order to perform the above-mentioned kinetics computations in a second step. The clear advantage of the systemic approach over the topological one is the complete automation of the modeling and solution process: only rough data (global volume and inlet flow-rate) are needed, as well as an adapted initial superstructure. Neither variable initialization nor preliminary manual design of the possible network are necessary and the final reactor network is automatically generated by the optimization process. Moreover, the computational time necessary to find a solution (a few seconds) with the proposed method is much lower than the times reported in the studies applying the topological methodology (several minutes). Finally, the systemic approach guarantees an optimal solution in terms of similarity between model and (CFD-based) experimental data, and furthermore includes the concept of model simplicity that might be useful and CPU-time saving for further computations (such as, for instance, the previously mentioned kinetics calculations).

The perspectives of this work should particularly focus on the following points:

- In addition to the mass balances formulated on the reactor network, energy balances should be also written in order to identify the temperatures associated to each reactor. In this sense, exper-

imental verification of energy balances, available for some real furnaces, would lead to a more complete structural and parametrical identification (over either the glass bath or the combustion chamber).
- Another way to produce this kind of structure would be to apply a temperature variation (Dirac pulse or step injection) on the furnace input. The CFD simulations of the output temperature would then provide another signal on which to carry out new model identification by systemic approach.
- Besides, it is worth noting that energy balances formulated on the reactor network require some knowledge about chemistry compositions, and thus about the kinetics (to determine the reaction enthalpies). A first step could thus use simplified kinetics mechanisms (for instance, the Zeldovich mechanisms in the combustion case). In a second step, a more complex kinetics mechanisms could be integrated to the reactor network (see [13]).

Finally, even though the application zone of the mentioned perspectives seems to be mostly the combustion chamber, the ultimate objective is to build a global representation of the glass manufacturing furnaces, by associating the reactor network to both furnace entities. The critical point of this strategy would then be located on the glass bath–combustion chamber interface.

Appendix A. MINLP formulation for reactor network modeling

The initial data necessary to generate a reactor network that fits the experimental-CFD output curve over a discretized time period $\{t_1, \ldots, t_F\}$ are the following ones:

- the volume of the considered container V_T,
- the inlet flow-rate Q_{tot} and concentration C_{in} for each instant t (here, $C_{in}(t) = 1$, $t = t_1, \ldots, t_F$),
- the outlet concentrations $Cf_{exp}(t)$, $t = t_1, \ldots, t_F$ (obtained by CFD simulation),
- an initial superstructure.

The above-mentioned superstructure involves the unitary elements that will be characterized by the equations of the model. In addition, general constraints such as the upper bound of the container volume, as well as the inlet and outlet mass balances, have to be defined whatever the superstructure. Finally, a dynamic bounding for reactors volume and streams flow-rate variables must be implemented, in order to set the associated values equal to zero when the considered items do not exist (i.e. the corresponding binary variables are equal to 0).

The used variables are:

- y_j is a binary variable denoting the existence of an item ($j = 1, \ldots, nj$),
- V_j is a continuous variable representing the volume of item j ($j = 1, \ldots, nj$),
- Q_k is a continuous variable representing the flow-rate of stream k ($k = 1, \ldots, nk$),
- $C_i(t)$ is a continuous variable representing the concentration at instant t ($t = t_1, \ldots, t_F$) and at a specific point of the superstructure named i ($i = 1, \ldots, ni$),
- $Cf_{mod}(t)$ is a continuous variable representing the output concentration at instant t ($t = t_1, \ldots, t_F$), generated by the model.

The objective function accounts for: (i) the minimization of the model-experimental quadratic distance, for each instant t; and (ii) the complexity of the resulting network, calculated as the sum of items involved in the final structure:

$$\min Z = k \left[\sum_{t=t_1}^{t_F} (Cf_{exp}(t) - Cf_{mod}(t))^2 \right] + \sum_{j=1}^{nj} y_j. \tag{3}$$

The constraints are described straightforward:

- Constraint on the global container volume:

$$\sum_{j=1}^{nj} V_j = V_T \tag{4}$$

- Global mass balance at the inlet node:

$$Q_{tot} + \sum_{k_{in}} Q_k = \sum_{k_{out}} Q_k \tag{5}$$

where k_{in}/ k_{out} represent the indexes for streams entering/leaving the inlet node, apart from the inlet stream.
- Partial mass balance on the inlet node:

$$\forall t \in \{t_1, \ldots, t_F\}, Q_{tot} C_{in} + \sum_{k_{in}} Q_k C_{i'}(t) = \sum_{k_{out}} Q_k C_{i''}(t) \tag{6}$$

where k_{in}/k_{out} represent the indexes for streams entering/leaving the inlet node, apart from the inlet stream. i' and i'' represent the points in the superstructure associated with the streams entering (k_{in}) or leaving (k_{out}) the inlet node.
- Partial mass balance on the outlet node:

$$\forall t \in \{t_1, \ldots, t_F\}, \sum_{k_{in}} Q_k C_{i'}(t) = Q_{tot} Cf_{mod}(t) + \sum_{k_{out}} Q_k C_{i''}(t) \tag{7}$$

where k_{in}/ k_{out} represent the indexes for streams entering/leaving the outlet node, apart from the outlet stream. i' and i'' represent the points in the superstructure associated with the streams entering (k_{in}) or leaving (k_{out}) the outlet node.
- Mass balance on a CSTR module:

$$\forall t \in \{t_1, \ldots, t_F\}, \forall j \in \{1, \ldots, nj\}, C_{i''}(t) = \frac{hQ_k}{z_1 + V_j}(C_{i'}(t-1) - C_{i''}(t-1)) + C_{i''}(t-1) \tag{8}$$

where k represent the index of the stream passing through the CSTR module j; i' is a superstructure point before the CSTR module and i'' is a superstructure point after the CSTR module; h is a small time slot used for differentiation and z_1 is a small constant.
- Mass balance on a plug-flow module:

$$\forall t \in \{t_1, \ldots, t_F\}, \forall j \in \{1, \ldots, nj\}, C_{i''}(t) = C_{i'}(t) sigmoid\left(z_2\left(t - \frac{V_j}{z + Q_k}\right)\right) \tag{9}$$

where k represent the index of the stream passing through the plug-flow module j; i' is a superstructure point before the plug-flow module and i'' is a superstructure point after the plug-flow module. Function sigmoid is used for the representation of a plug-flow effect when a step injection is used as an input signal. z_2 is constant used to tune the sigmoid function.
- Dynamic bounding of the items volume:

$$\forall j \in \{1, \ldots, nj\}, V_j \le y_j V_T \tag{10}$$

- Dynamic bounding of the stream flow-rates:

$$\forall k \in \{1, \ldots, nk\}, Q_k \le M \sum_{j_k} y_j \tag{11}$$

where j_k represent the indexes of the items that are crossed by stream k. The parameter M is that of the classical big-M technique, used to define an upper bound on a variable while avoiding the formulation of bilinear constraints (which strongly penalize the solution process).

Appendix B. Computations on the glass bath

See Figs. B.1–B.4 .

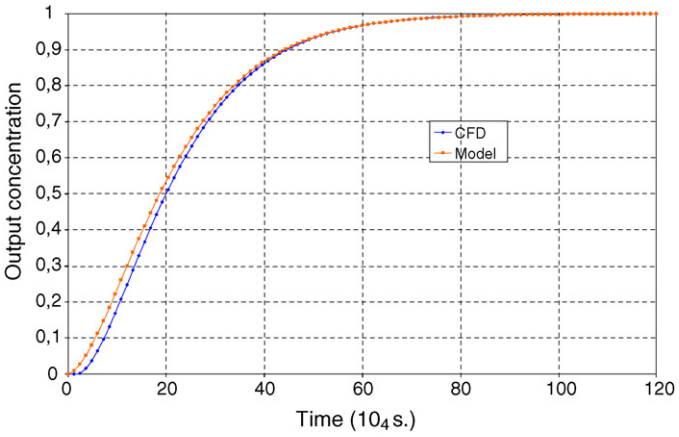

Fig. B.1. Comparison between CFD and model results for superstructure 1, glass bath.

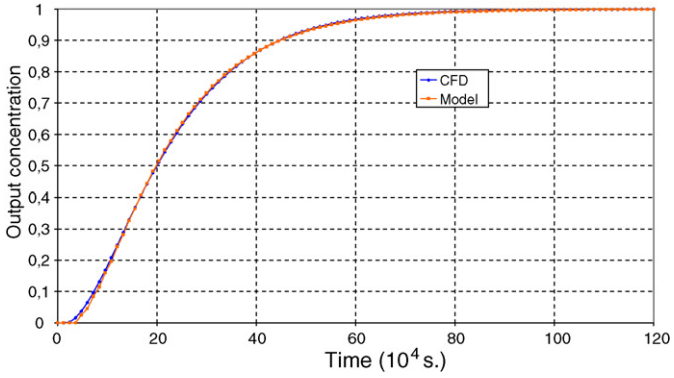

Fig. B.2. Comparison between CFD and model results for superstructure 2, glass bath.

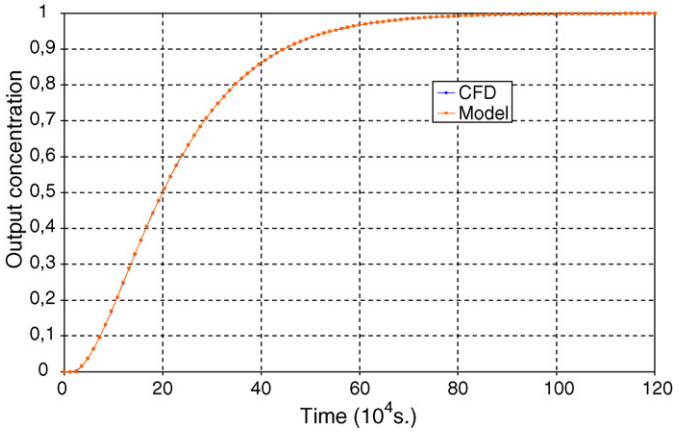

Fig. B.3. Comparison between CFD and model results for superstructure 3, glass bath.

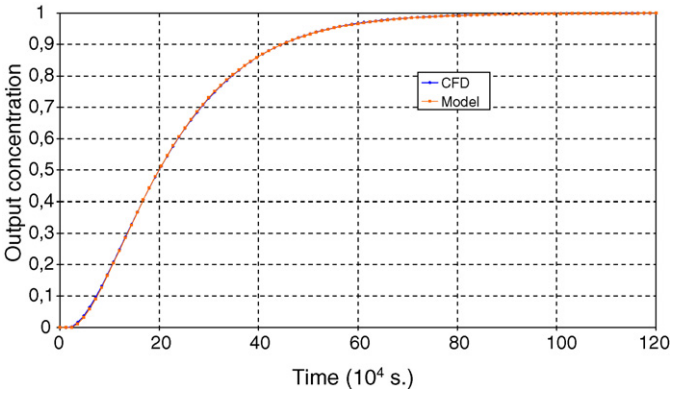

Fig. B.4. Comparison between CFD and model results for superstructure 4, glass bath.

Appendix C. Computations on the combustion chamber

See Figs. C.5–C.8 .

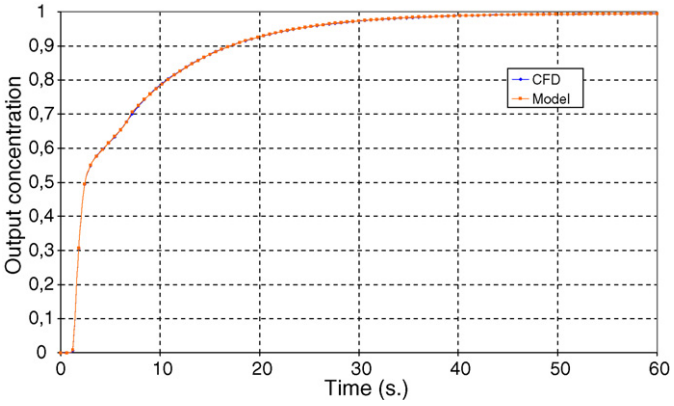

Fig. C.5. Comparison between CFD and model results for superstructure 1, combustion chamber.

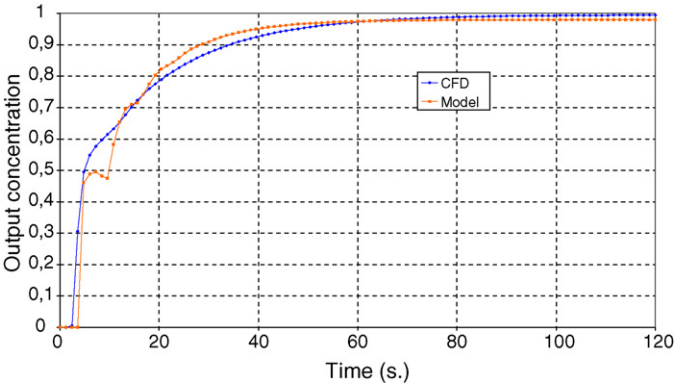

Fig. C.6. Comparison between CFD and model results for superstructure 2, combustion chamber.

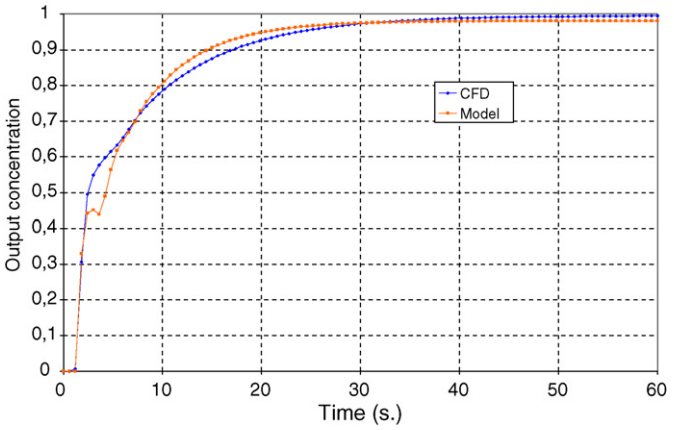

Fig. C.7. Comparison between CFD and model results for superstructure 3, combustion chamber.

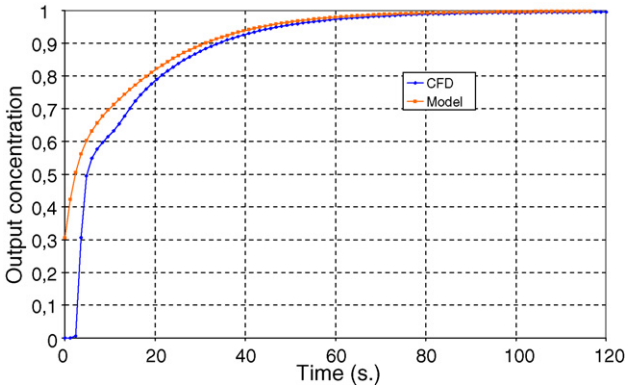

Fig. C.8. Comparison between CFD and model results for superstructure 4, combustion chamber.

References

[1] M. Carvalho, V. Semiao, P. Coelho, Modelling and optimization of the no formation in an industrial glass furnace, Journal of Engineering for Industry 114 (1992) 514–523.
[2] J.-M. Flesselles, Phénomènes de transferts dans les fours de verrerie industriels, in: Congrès Français de Thermique, SFT 2004, Presqu'Ile de Giens, 2004.
[3] B. Carnahan, R.C. Warner, B. Bidanda, K.L. Needy, Predicting glass furnaces output using statistical and neural computing methods, International Journal of Production Research 38 (2000) 1255–1269.
[4] J. Pina, P. Lima, An operation system for industrial processes: application to a glass furnace, 9–12 juillet, in: Actes de 10th Mediterranean Conference on Control and Automation—MED 2002, Lisbon, Portugal, 2002.
[5] J. Pina, P. Lima, A glass furnace operation system using fuzzy modelling and genetic algorithms for performance optimisation, Engineering Applications of Artificial Intelligence 16 (2003) 681–690.
[6] P. Costa, J. Dente, The application of fuzzy-logic in automatic modelling of electromechanical systems, Fuzzy Sets and Systems 95 (1998) 273–293.
[7] L. Montastruc, Modélisation et optimisation d'un réacteur en lit fluidisé de déphosphatation d'effluents aqueux. PhD thesis, INPT (2003).
[8] S. Hocine, Identification de modèles de procédés par programmation mathématique déterministe. PhD thesis, INPT (2006).
[9] A. Brooke, D. Kendrick, A. Meeraus, R. Raman, GAMS User's Guide, GAMS Development Corporation, Washington, DC, 1998.
[10] C. Laquerbe, Modélisation des écoulements dans un local ventilé par une approche systémique. PhD thesis, INPT (1998).
[11] T. Faravelli, L. Bua, A. Frassoldati, A. Antifora, L. Tognotti, E. Ranzi, A new procedure for predicting NOx emissions from furnaces, Computers and Chemical Engineering 25 (2001) 613–618.
[12] M. Falcitelli, S. Pasini, L. Tognotti, Modelling practical combustion systems and predicting NOx emissions with an integrated CDF based approach, Computers and Chemical Engineering 26 (2002) 1171–1183.
[13] T. Faravelli, A. Frassoldati, E. Ranzi, Kinetic modelling of the interactions between no and hydrocarbons in the oxydation of hydrocarbons at low temperatures, Combustion and Flame 132 (2003) 188–207.
[14] A. Frassoldati, S. Frigerio, E. Colombo, F. Inzoli, T. Faravelli, Determination of NOx emissions from strong swirling confined flames with an integrated CFD-based procedure, Chemical Engineering Science 60 (2005) 2851–2869.
[15] W. Trier, Glass furnaces, design construction and operation, Society of glass technology, Sheffield, 1984.
[16] F. Pigeonneau, Coupled modelling of redox reactions and glass melt fining processes, Glass Technology: European Journal of Glass Science and Technology A 48 (2) (2007) 66–72.
[17] F. Pigeonneau, Mass transfer of rising bubble in molten glass with instantaneous oxidation–reduction reaction. Part 1. Determination of Sherwood number, Chemical Engineering and Science 64 (13) (2009) 3120–3129.
[18] D.G. Gray, A. Giorgini, The validity of the Boussinesq approximation for liquids and gases, International Journal of Heat Mass Transfer 19 (1976) 545–551.
[19] F. Pigeonneau, J.-M. Flesselles, 2009. Natural convection of a high Prandtl number fluid in a long cavity heated from above, International Journal of Heat Mass Transfer, submitted for publication.
[20] H. Scholze, Glass. Nature, Structures and Properties, Springer-Verlag, Berlin, 1990.
[21] R. Viskanta, E.E. Anderson, Heat transfer in semitransparent solids, Advances in Heat Transfer 11 (1975) 317–441.

Available online at www.sciencedirect.com
SCIENCE DIRECT®
C. R. Mecanique 332 (2004) 783–788
COMPTES RENDUS MECANIQUE

Kinematic regimes of convection at high Prandtl number in a shallow cavity

Jean-Marc Flesselles *, Franck Pigeonneau

Saint-Gobain Recherche, 39, quai Lucien Lefranc, 93303 Aubervilliers, France

Received and accepted 21 June 2004

Available online 10 August 2004

Presented by Patrick Huerre

Abstract

We consider free convection in a horizontal shallow cavity with different end temperatures, filled with a high Prandtl number fluid. From scaling analysis, we find two kinematic regimes resulting from the competition of heat transfer by conduction and by convection. Numerical simulations realized for a large range of Rayleigh number and aspect ratio confirm the phenomenological analysis and provide the threshold between the two regimes. The conductive and convective regimes occur at $Ra\,A^2$ smaller and larger than 443 respectively, where Ra is the Rayleigh number and A is the aspect ratio. In the convective regime, the characteristic velocity is independent of depth of the cavity. ***To cite this article: J.-M. Flesselles, F. Pigeonneau, C. R. Mecanique 332 (2004).***

© 2004 Académie des sciences. Published by Elsevier SAS. All rights reserved.

Résumé

Régimes cinématiques de la convection à haut nombre de Prandtl dans une cavité allongée. Nous traitons de la convection naturelle dans une cavité horizontale allongée différentiellement chauffée selon les parois verticales, emplie d'un fluide à grand nombre de Prandtl. L'analyse d'échelles fait apparaître deux régimes cinématiques résultant de la compétition entre transfert de la chaleur par conduction et par convection. Des simulations numériques faites dans une large gamme de nombre de Rayleigh et de facteur de forme confirment l'analyse phénoménologique. Le régime conductif (resp. convectif) apparaît pour $Ra\,A^2$ inférieur (resp. supérieur) à 443, où Ra est le nombre de Rayleigh et A le facteur de forme. La loi d'échelle du régime convectif donne une vitesse caractéristique indépendante de la hauteur de la cavité. ***Pour citer cet article : J.-M. Flesselles, F. Pigeonneau, C. R. Mecanique 332 (2004).***

© 2004 Académie des sciences. Published by Elsevier SAS. All rights reserved.

Keywords: Fluid mechanics; Natural convection; High Prandtl number

Mots-clés : Mécanique des fluides ; Convection naturelle ; Haut nombre de Prandtl

* Corresponding author.
E-mail addresses: jean-marc.flesselles@saint-gobain.com (J.-M. Flesselles), franck.pigeonneau@saint-gobain.com (F. Pigeonneau).

1631-0721/$ – see front matter © 2004 Académie des sciences. Published by Elsevier SAS. All rights reserved.
doi:10.1016/j.crme.2004.06.003

Version française abrégée

Nous considérons une cavité allongée bidimensionnelle de hauteur H et de longueur L emplie d'un fluide incompressible de viscosité cinématique ν, de diffusivité thermique κ et de coefficient de dilatation volumique β avec $Pr = \nu/\kappa \gg 1$. Le champ de gravité est noté g. Les deux parois verticales sont placées respectivement à des températures fixes T_- et T_+. On note $\Delta T = T_+ - T_-$ et $A = H/L$.

Par une analyse phénoménologique réalisée dans le cadre de l'approximation de Boussinesq, nous montrons qu'il n'existe que deux régimes cinématiques selon la valeur de $Ra\,A^2$. Cette quantité correspond au rapport du temps caractéristique de diffusion de la chaleur suivant la verticale au temps d'advection longitudinale.

Dans le régime conductif obtenu à faible valeur de $Ra\,A^2$, la vitesse caractéristique est donnée par

$$u_0 \sim Ra\,\frac{\kappa}{L} \quad \text{avec } Ra = \frac{g\beta\Delta T H^3}{\nu\kappa} \tag{1}$$

Dans le régime convectif, observé à grand $Ra\,A^2$, la vitesse caractéristique a pour expression

$$u_0 \sim (Ra\,A^2)^{-3/5} Ra\,\frac{\kappa}{L} \sim (g\beta\Delta T/\nu)^{2/5}\kappa^{3/5}L^{1/5} \tag{2}$$

Cette analyse confirme celle précédemment faite par Boehrer [2] car nous retrouvons que le paramètre de contrôle est la quantité $Ra\,A^2$. Par contre, nous concluons qu'il n'y a que deux régimes cinématiques alors qu'une analyse basée sur la thermique montrait trois régimes. Dans le régime convectif, la vitesse caractéristique ne dépend plus de la hauteur, et augmente avec la longueur de la cavité.

Nous avons réalisé plusieurs simulations numériques du problème considéré dans cette note en faisant varier le nombre de Rayleigh de 1 à 10^9 et le facteur de forme de $1/2$ à $1/20$. La représentation de la composante longitudinale de la vitesse obtenue numériquement en fonction de $Ra\,A^2$ confirme les prédictions théoriques. La transition entre les deux régimes est assez franche. Elle est observée pour $Ra\,A^2 \simeq 443$.

1. Introduction

Despite the amount of work devoted to natural convection, the subject is not yet exhausted because of the variety of situations of interest, the number of possible control parameters and the subtlety of the effects at play. The purpose of this Note is to determine the different kinematic regimes that occur in a two-dimensional cavity with end walls kept at fixed temperature and filled with a high Prandtl number fluid.

The side-heated cavity is an academic model for many realistic situations of natural or technological flows. It has first been introduced by Batchelor [1] to study air circulation in buildings. In this case, the geometry – a tall and thin cavity – is characterized by a large aspect ratio A and the fluid, namely air, is characterized by a Prandtl number of order 1. The situation of a shallow cavity (with a small aspect ratio) also received much attention since it applies to a large number of geophysical flows, such as estuaries or waste heat disposal. Studies concentrated on low Prandtl number fluids like air ($Pr = 0.7$) or water ($Pr = 7$) which are most commonly encountered, but a few authors have also studied high Prandtl number flows.

Boehrer published [2] a comprehensive analysis of all available experimental data as well as possible theoretical scalings for the flow of a fluid in a two-dimensional shallow cavity with end heated walls, within the Boussinesq approximation. He deplored that no clear understanding of the various regimes that may occur in such an apparently simple flow had yet emerged and suggested a global picture of the convection regimes as well as the relevant control parameters.

According to him, his analysis applies to long cavities ($0 < A < 0.25$), provided the Rayleigh number is not excessively high ($Ra < A^{-12}$), and filled with any fluid such that the Prandtl number is larger than unity. His main results are the following: the relevant control parameter is $Ra\,A^2$, where Ra is the Rayleigh number; there exist

three regimes, called conductive regime, transition regime and convective regime, the boundaries of which are at $Ra\,A^2 \simeq 10^2$ and $Ra\,A^2 \simeq 10^4$. He also provides estimates for the temperature gradient in the core of the cavity.

Boehrer's analysis is based on a comparison of published data, together with a physical analysis of the different scaling, and a systematic re-plotting of all data according to the different hypothesis. However, Boehrer's emphasis is essentially put on the temperature gradient within the core of the cavity.

Following Boehrer, we have reconsidered the case of high Prandtl number fluids. Our analysis is based on a physical analysis of the scaling laws and extensive computational fluid dynamics simulations. We deduce that, from a kinematic point of view, only two regimes exist. We provide the threshold between them and the laws for the velocity scale in each regime.

2. Formulation

We consider a two-dimensional rectangular shallow cavity of height H and length L filled with an incompressible fluid of constant kinematic viscosity ν and constant heat diffusivity κ. The heat expansion coefficient of the fluid is β. The cavity is in the gravity field g. One vertical side of the cavity is kept at a hot fixed temperature T_+ and the opposite side is kept at a cold temperature T_-. The temperature difference is $\Delta T = T_+ - T_-$. Top and bottom sides are adiabatic. The fluid velocity vanishes on all sides. The Boussinesq approximation is assumed.

The continuity equation can be written:

$$\frac{u_0}{L}\frac{\partial u}{\partial x} + \frac{v_0}{H}\frac{\partial v}{\partial y} = 0 \tag{3}$$

where $x = \bar{x}/L,\ y = \bar{y}/H,\ u = \bar{u}/u_0,\ v = \bar{v}/v_0$ and overlines indicate dimensional variables. The scaling variables $u_0,\ v_0$ for horizontal and vertical velocity scales are still unknown. Eq. (3) sets the relation between them:

$$v_0 \sim (H/L)u_0 \tag{4}$$

Since the aspect ratio $A = H/L$ is very small, v_0 is much smaller than u_0: the flow is parallel (except near the lateral walls). With the use of Eq. (4), the equations of motion are:

$$St\frac{\partial u}{\partial t} + u\frac{\partial u}{\partial x} + v\frac{\partial u}{\partial y} = -\frac{\delta P}{\rho_0 u_0^2}\frac{\partial P}{\partial x} + \frac{\nu}{u_0 L A^2}\left[A^2\frac{\partial^2 u}{\partial x^2} + \frac{\partial^2 u}{\partial y^2}\right] \tag{5}$$

$$A^2\left(St\frac{\partial v}{\partial t} + u\frac{\partial v}{\partial x} + v\frac{\partial v}{\partial y}\right) = -\frac{\delta P}{\rho_0 u_0^2}\frac{\partial P}{\partial y} + \frac{\nu}{u_0 L}\left[A^2\frac{\partial^2 v}{\partial x^2} + \frac{\partial^2 v}{\partial y^2}\right] + \frac{\beta\Delta T g H}{u_0^2}\theta \tag{6}$$

$$St\frac{\partial \theta}{\partial t} + u\frac{\partial \theta}{\partial x} + v\frac{\partial \theta}{\partial y} = \frac{\kappa}{u_0 L A^2}\left[A^2\frac{\partial^2 \theta}{\partial x^2} + \frac{\partial^2 \theta}{\partial y^2}\right] \tag{7}$$

in which the Strouhal number St is defined by $St = L/(u_0 t_0)$. In Eqs. (5)–(7), new unknown scaling variables for time, density and pressure have been introduced with the corresponding nondimensional variables: $t = \bar{t}/t_0$, $\rho = \overline{\rho}/\rho_0,\ P = \overline{P}/\delta P$. The nondimensional temperature is $\theta = (T - T_-)/(T_+ - T_-)$.

The scaling variables correspond to the maximum values attained within the domain where the scaling applies: it is the central region where the flow is parallel. In the next section, we determine these variables by a phenomenological analysis [3]. It relies on the least degeneracy principle, according to which the largest possible number of terms should be kept (see [4,5]).

3. Phenomenological analysis

From Eq. (7), one deduces that

$$\kappa/(u_0 L A^2) \sim \max(St, 1) \tag{8}$$

We first consider the case where $St \gg 1$, which means that the typical horizontal advection distance is much smaller than the length of the cavity. In this case, Eq. (8) yields the time scale:

$$t_0 \sim H^2/\kappa \tag{9}$$

It is a characteristic thermal diffusion time over height H. When inserted into Eq. (5), with the assumption of large Prandtl number ($Pr \gg 1$), this yields a relation between pressure and velocity scales:

$$\delta P/(\rho_0 u_0^2) \sim \nu/(u_0 L A^2) \tag{10}$$

This, with Eq. (6), sets the u_0 velocity as proportional to the H based Rayleigh number:

$$u_0 \sim Ra\,\frac{\kappa}{L} \quad \text{with } Ra = \frac{g\beta\Delta T H^3}{\nu\kappa} \tag{11}$$

This equation may be written in a nondimensional way by introducing the Péclet number:

$$Pe \sim Ra \quad \text{with } Pe = \frac{u_0 L}{\kappa} \tag{12}$$

It is easily checked that the $St \gg 1$ condition also gives $Ra\,A^2 \ll 1$.

The Strouhal number may also be seen as the ratio of the horizontal advection time scale to the vertical thermal diffusion time scale. Hence we call this low Rayleigh number regime the *conductive* regime since the motion is controlled by the (long) thermal time scale. A temperature perturbation has time to equilibrate vertically because of thermal diffusion before being advected along the length of the cavity: isotherms are essentially vertical, which corresponds to a conductive solution.

On the other hand, if the Strouhal number becomes small enough, hence at large Rayleigh number, a thermal perturbation will travel along the cavity. This means that a horizontal boundary layer of thickness δ has appeared, within which the fluid moves to the vertical walls. This thickness is such that the Strouhal number associated to it is equal to unity:

$$\kappa L/(\delta^2 u_0) \sim 1 \tag{13}$$

Vertical length scales should be rescaled with δ instead of H. A similar analysis to the previous one may be performed. One finds that the Péclet number is no more equal to the Rayleigh number:

$$Pe \sim Ra(\delta/H)^3 \tag{14}$$

The size of the boundary layer is found by inserting Eq. (14) in Eq. (13). Finally one gets the final expression of the (nondimensional) velocity in the *convective* regime:

$$Pe \sim Ra(Ra\,A^2)^{-3/5} \tag{15}$$

The previous analysis sets on firm grounds the analysis and hypothesis of Boehrer: we recover the role of the quantity $Ra\,A^2$ as the control parameter and we derive rigorously the relevance of the conductively controlled boundary layer, based on the advection time scale. In addition, we show that there exists only two kinematic convection regimes, whereas the current understanding focuses on the thermal field, and leads to a three regime classification.

4. Comparison with numerical data

In order to check the theoretical predictions (12) and (15), we have performed extensive numerical simulations of the problem expressed in the appropriate nondimensional variables. In a permanent state, the equations of motion can be written:

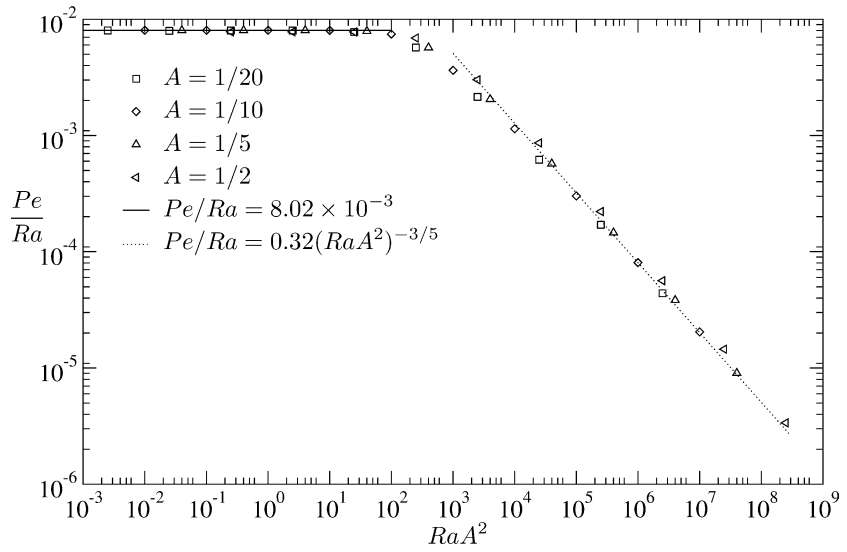

Fig. 1. Nondimensional maximum value of the x-velocity component in shallow cavities of various aspect ratios A versus $Ra\,A^2$ for a high-Prandtl number fluid.

Fig. 1. Valeur maximale de la composante x de la vitesse adimensionnée dans des cavités de différents facteurs de forme A en fonction de $Ra\,A^2$ pour un fluide de haut nombre de Prandtl.

$$\frac{\partial u}{\partial x} + \frac{\partial v}{\partial y} = 0 \tag{16}$$

$$u\frac{\partial u}{\partial x} + v\frac{\partial u}{\partial y} = -\frac{\partial P}{\partial x} + \frac{Pr}{Ra\,A}\nabla^2 u \tag{17}$$

$$u\frac{\partial v}{\partial x} + v\frac{\partial v}{\partial y} = -\frac{\partial P}{\partial y} + \frac{Pr}{Ra\,A}\nabla^2 v + \frac{Pr}{Ra\,A^2}\theta \tag{18}$$

$$u\frac{\partial \theta}{\partial x} + v\frac{\partial \theta}{\partial y} = \frac{1}{Ra\,A}\nabla^2 \theta \tag{19}$$

where velocities are normalized by $Ra\,\kappa/L$, and lengths by H. Eqs. (16)–(19) are solved with a commercial CFD code in a rectangular box of height 1, and length $1/A$, filled with a fluid of viscosity $Pr/Ra\,A$, of thermal conductivity $1/Ra\,A$, and of thermal expansion coefficient $Pr/Ra\,A^2$.

About 40 cases have been calculated, where the aspect ratio A was varied between $1/20$ and $1/2$ and the Rayleigh number Ra was varied in the range 1 to 10^9. The Prandtl number was fixed, and equal to 1000. With the considered nondimensional variables, the maximum value of the x component of the velocity is equal to Pe/Ra. Its value is shown a function of $Ra\,A^2$ on Fig. 1. In accordance with the phenomenological analysis Pe/Ra is constant at low $Ra\,A^2$, i.e. in the conductive regime. This constant value is easily calculated in the $Ra \to 0$ limit. It is equal to $1/72\sqrt{3} \simeq 8.02 \times 10^{-3}$ [6]. At high $Ra\,A^2$, i.e. in the convective regime, $Pe/Ra = 0.32\ (Ra\,A^2)^{-3/5}$, where the proportionality constant comes from a fit. The intersection between the two scalings provides the regimes boundary. It is rather sharp and occurs at $Ra\,A^2 \simeq 443$.

5. Conclusion

The numerical data are in perfect agreement with our phenomenological analysis. These results both confirm and extend Boehrer's analysis: the relevant control parameter for natural convection of a high-Prandtl number fluid

in a shallow box is indeed $Ra\,A^2$, which is the ratio of the heat diffusion time scale to the convection time scale. There are only two kinematic regimes, and the only condition lies on $Ra\,A^2$, provided $Pr > 1$.

In the convective regime, that occurs when $Ra\,A^2 \gtrsim 443$, a boundary layer develops. As this new length scale sets in the problem, the velocity scale changes. When expressed in dimensional quantities, the velocity coming from Eq. (15) is written:

$$u_{\max} = 0.32\left(\frac{g\beta\Delta T}{\nu}\right)^{2/5}\kappa^{3/5}L^{1/5} \tag{20}$$

Hence, contrary to the intuitive understanding, the velocity no longer depends on depth and increases with the length of the cavity, in full agreement with theoretical prediction and numerical results.

Acknowledgement

We thank X. Chavanne for numerous and fruitful discussions.

References

[1] G.K. Batchelor, Heat transfer by free convection across a closed cavity between vertical boundaries at different temperatures, Q. Appl. Math. 12 (1954) 209–233.
[2] B. Boehrer, Convection in a long cavity with differentially heated end walls, Int. J. Heat Mass Transfer 40 (1997) 4105–4114.
[3] A. Bejan, Convection Heat Transfer, Wiley, New York, 1995.
[4] P. Germain, Méthodes asymptotiques en mécanique des fluides, in: Fluid Dynamics, Gordon and Breach, London, 1977, pp. 1–147.
[5] R.K. Zeytounian, Modélisation asymptotique en mécanique des fluides newtoniens, Springer-Verlag, 1994.
[6] D.E. Cormack, L.G. Leal, J. Imberger, Natural convection in a shallow cavity with differentially heated end walls. Part 1. Asymptotic theory, J. Fluid Mech. 65 (1974) 209–229.

Author's personal copy

International Journal of Heat and Mass Transfer 55 (2012) 436–442

Contents lists available at SciVerse ScienceDirect

International Journal of Heat and Mass Transfer

journal homepage: www.elsevier.com/locate/ijhmt

Practical laws for natural convection of viscous fluids heated from above in a shallow cavity

F. Pigeonneau [a,*], J.-M. Flesselles [b]

[a] Surface du Verre et Interfaces, UMR 125, CNRS/Saint-Gobain, 39 quai Lucien Lefranc, BP 135, 93303 Aubervilliers Cedex, France
[b] Saint-Gobain Recherche, 39 quai Lucien Lefranc, BP 135, 93303 Aubervilliers Cedex, France

ARTICLE INFO

Article history:
Received 31 January 2011
Received in revised form 12 September 2011
Accepted 14 September 2011
Available online 12 October 2011

Keywords:
Natural convection
Glass furnace
Nusselt number
Shallow cavity
Asymptotic analysis
Numerical simulation

ABSTRACT

Industrial production of glass involves natural convection of viscous fluids heated from above in shallow cavities. This problem is revisited by means of extensive numerical simulations and analytical expansions for a 2D configuration.

This approach yields exact and approximate analytical expressions that can be practically used to evaluate the convective intensity and the heat flux in the different regimes.

These results also confirm that the control parameter for this problem is the product of the Rayleigh number, based on the height of the enclosure, by the cavity aspect ratio squared whatever the top boundary conditions.

© 2011 Elsevier Ltd. All rights reserved.

1. Introduction

Although generally poorly known to the general public, industrial glassmaking involves multiple heat and mass transfer phenomena. Glass furnaces are essentially made up of a combustion system and a tank within which raw materials undergo a series of high temperature chemical reactions, finally producing a homogeneous glass. Within these long and shallow tanks, convective motion driven by controlled temperature gradients move the liquid "uphill". The magnitude of the velocity sets the residence time distribution and the mixing intensity, both of which impact the power needed to make glass, i.e. the eventual energy consumption of an industrial plant. Although velocity and temperature fields in glass furnaces can be computed using various numerical tools, the understanding of heat and mass transfer phenomena is still partial. Furnace design should be improved through better knowledge of the key parameters driving natural convection inside the glass bath.

The purpose of this paper is to give a physical insight to the phenomena at play and provide analytical "ready to use" formula on natural convection.

At high temperature, molten glass is a Newtonian fluid: its mechanical properties are properly described by a scalar viscosity, that, depends on temperature [16]. In large window glass furnaces, where the melt temperature varies from 1200 to 1500 °C, viscosity ranges over about one order of magnitude. Molten glass being also a semi-transparent media, heat transfer is not only conductive but also radiative. However, for most common glasses, including ordinary transparent window glass, the absorption length is such that radiation can be approximated by a conductive model [9,17] where the equivalent heat conductivity varies like T^3 (Rosseland approximation). As a consequence the Prandtl number based on the effective conductivity and the viscosity ranges from 2×10^3 to 2×10^4. Detailed calculations outside the scope of the paper show that the actual impact of these variations does not bring any new phenomena.

Since furnaces are generally longer and wider than they are high (for a precise description of technology see Ref. [19]), main flow structures take place in the longitudinal plane. The problem can thus be studied in a long 2D cavity. To mimic the fact that glass is heated by gas flames from above and cooled by raw materials floating on the surface next to where they are charged, an uneven temperature profile is applied on the upper boundary. The presence of raw materials and sometime foam floating at the surface of a glass furnace make it difficult to describe the kinematic conditions for the liquid. It is known in this kind of convection problems [4] that the choice of slip or no slip does not modify the fluid physics at play in the bulk nor the scaling laws for the overall motion. For our goal, we do choose the simplest case for our model, i.e. an all no-slip condition enclosure. Although a number of authors have recently studied similar problems [4,10], none has yet pro-

* Corresponding author. Tel.: +33 1 48 39 59 99; fax: +33 1 48 39 55 62.
E-mail addresses: franck.pigeonneau@saint-gobain.com (F. Pigeonneau), jean-marc.flesselles@saint-gobain.com (J.-M. Flesselles).

0017-9310/$ - see front matter © 2011 Elsevier Ltd. All rights reserved.
doi:10.1016/j.ijheatmasstransfer.2011.09.042

Author's personal copy

Nomenclature

Roman symbols

A	aspect ratio, $=H/L$ (–)
$\mathcal{A}_0$	function of $\bar{y}$ in the zero order asymptotic solution (–)
$\mathcal{A}_1$	function of $\bar{y}$ in the first order asymptotic solution (–)
$\mathcal{B}_1$	function of $\bar{y}$ in the first order asymptotic solution (–)
$\mathcal{C}_1$	function of $\bar{y}$ in the first order asymptotic solution (–)
$\mathcal{D}_1$	function of $\bar{y}$ in the first order asymptotic solution (–)
$\mathbf{e}_x$	unit vector along the x coordinate (–)
$\mathbf{e}_y$	unit vector along the y coordinate (–)
g	gravity constant (m s^{-2})
H	cavity height (m)
L	cavity length (m)
Nu	Nusselt number, $=(\partial T/\partial n)/(\Delta T/H)$ (–)
$\langle Nu\rangle$	average Nusselt number based on L_2 norm of Nu (–)
$P, \bar{P}$	dimensionless pressure (–)
Pe	Péclet number, $=u_0 L/\kappa$ (–)
Pr	Prandtl number, $=\nu/\kappa$ (–)
Ra	Rayleigh number based on height H (–)
T	temperature (K)
$u, \bar{u}$	dimensionless longitudinal velocity component (–)
$v, \bar{v}$	dimensionless vertical velocity component (–)
$x, \bar{x}$	dimensionless longitudinal coordinate (–)
$y, \bar{y}$	dimensionless vertical coordinate (–)

Greek symbols

β	heat expansion coefficient (K^{-1})
ΔT	temperature difference, $=T_+ - T_-$ (K)
κ	heat diffusivity (m^2 s^{-1})
ν	kinematic viscosity (m^2 s^{-1})
θ	dimensionless temperature, $=(T - T_-)/(T_+ - T_-)$ (–)

Subscripts

0	characteristic scale or zeroth order asymptotic solution
1	first order asymptotic solution
+	cold temperature
–	hot temperature

vided a set of laws that could be used by a practitioner to design such a convection tank and control the flow structure.

In the following, a sinusoidal temperature profile is imposed along the top of the cavity like already done by Somerville [18]. Such a choice brings numerous benefits: it allows for a regular solution at the corners and makes some analytical calculations possible. That does not restrict the generality of the analysis since it is the first term of a Fourier development of any similar, realistic, imposed temperature profile. Finally, in the following analysis, the Prandtl number is assumed to be large in order to mimic glass properties.

This situation is not far from the case where the cavity is heated along its side walls. In both cases, convection occurs without threshold and is mainly driven by the longitudinal thermal gradient. As it has been shown in [7], scaling laws can be obtained by balancing terms in the equations of motions, without involving the actual boundary conditions. For the cavity heated along its side walls, Böhrer [3] compiled a large amount of numerical and experimental data. He studied kinematic and thermal structures and suggested that the governing parameter is the product of the Rayleigh number by the aspect ratio squared,[1] $Ra\,A^2$. Later, Flesselles and Pigeonneau [7] presented a scale analysis to explain why $Ra\,A^2$ is the governing parameter. That is compatible with the results of Chiu-Webster et al. [4], where a linear profile was applied to the upper limit, but analyzed with a different set of variables (although with similar notations).

The problem is presented in Section 2, where cavity geometry and boundary conditions are defined. Section 3 is devoted to the presentation of the numerical results and their analysis. Conclusions are given in Section 4. Appendix A details the asymptotic solution of heat and mass transfer in the enclosure when the aspect ratio is small.

2. Problem statement

We consider a two-dimensional rectangular shallow cavity of height H and length L placed within the gravity field g. It is filled with an incompressible fluid, the kinematic viscosity, ν, and the heat diffusivity, κ, of which are constant. Fig. 1 gives the kinematic and thermal boundary conditions. The following temperature profile is imposed along the upper boundary:

$$T(x) = T_- + \frac{\Delta T}{2}\left[1 - \cos\left(\pi\frac{x}{L}\right)\right]. \tag{1}$$

The temperature difference is defined by $\Delta T = T_+ - T_-$ where $T_+ > T_-$. Adiabatic conditions are applied along the other walls. Eq. (1) ensures continuity with the vanishing heat flux along the left and right sides. No-slip conditions are used along all boundaries.

The problem is governed by three dimensionless numbers (see [1]) viz. the Prandtl number Pr, the aspect ratio A, and the Rayleigh number Ra given respectively by

$$Pr = \frac{\nu}{\kappa}, \tag{2a}$$

$$A = \frac{H}{L}, \tag{2b}$$

$$Ra = \frac{g\beta\Delta T H^3}{\nu\kappa}, \tag{2c}$$

where, in Eq. (2c), β is the heat expansion coefficient. The Prandtl number Pr depends only on the fluid's physical properties. Previous work of Rossby [15], Lim et al. [13] and Gramberg et al. [10] has shown that heat and mass transfer are insensitive to the Prandtl

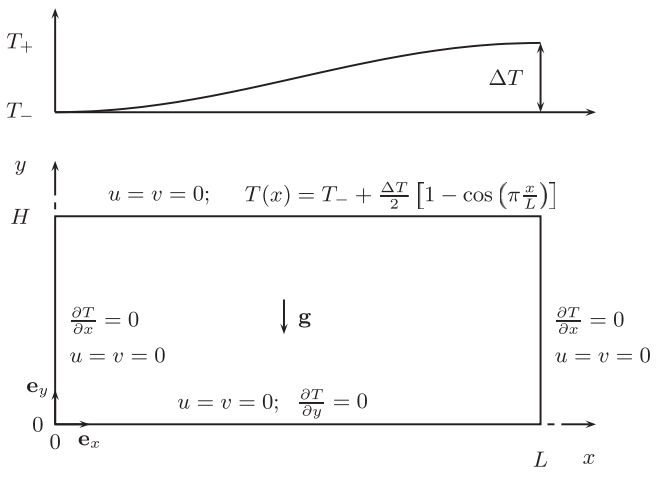

Fig. 1. Rectangular cavity with kinematic and thermal boundary conditions.

[1] Definitions of these quantities will be given below and can also be found in the Nomenclature.

Author's personal copy

number if the latter is large enough. Consequently, Pr is henceforth taken as constant and equal to 10^3. In the following, the aspect ratio A is less than unity. The Rayleigh number, Ra, controls heat and mass transfer.

In articles [5,7], the authors showed that the longitudinal velocity scales as $Ra\kappa/L$ for small aspect ratios and small Rayleigh numbers. This velocity is used to normalize balance equations. All spatial coordinates are normalized by the height, H. Dimensionless equations written within the framework of the Oberbeek –Boussinesq approximation are:

$$\frac{\partial u}{\partial x}+\frac{\partial v}{\partial y}=0, \tag{3a}$$

$$u\frac{\partial u}{\partial x}+v\frac{\partial u}{\partial y}=-\frac{\partial P}{\partial x}+\frac{Pr}{Ra\,A}\left(\frac{\partial^2 u}{\partial x^2}+\frac{\partial^2 u}{\partial y^2}\right), \tag{3b}$$

$$u\frac{\partial v}{\partial x}+v\frac{\partial v}{\partial y}=-\frac{\partial P}{\partial y}+\frac{Pr}{Ra\,A}\left(\frac{\partial^2 v}{\partial x^2}+\frac{\partial^2 v}{\partial y^2}\right)+\frac{Pr}{Ra\,A^2}\theta, \tag{3c}$$

$$u\frac{\partial \theta}{\partial x}+v\frac{\partial \theta}{\partial y}=\frac{1}{Ra\,A}\left(\frac{\partial^2 \theta}{\partial x^2}+\frac{\partial^2 \theta}{\partial y^2}\right). \tag{3d}$$

The horizontal and vertical velocity components are, respectively, u and v where P is the pressure. The dimensionless temperature is:

$$\theta=\frac{T-T_-}{T_+-T_-}. \tag{4}$$

We present herewithin a numerical solution obtained using a commercial CFD software based on the finite volume method. A segregated solver is used to solve iteratively each equation. Pressure and velocity fields are decoupled *via* the semi-implicit method for pressure linked equation (SIMPLE), [8]. The convective term gradients are determined by a third-order QUICK scheme introduced by Leonard [12]. About hundred cases have been run for which A varies between 1/50 and 1/5 and Ra from 1 to 10^9. The domain is meshed with a mapped grid using a square finite volume. The mesh size is equal to 2×10^{-2} regardless of the Rayleigh number, so that the largest number of finite volumes is 125000 obtained for A equal to 1/50. This spatial resolution is enough to capture the boundary layer that is observed in the numerical solution and that follows the scaling established in the next section. The steady state solution is obtained when the residuals on the continuity and energy equations are equal to 10^{-8}. For the momentum equations, the residuals are 10^{-6}.

3. Results

Previous results [3,4,7] suggest that two kinds of flow emerge. The first one, observed at small Rayleigh numbers, is dominated by thermal conduction and is called the *conductive* regime. The second kind of flow is obtained at large Rayleigh numbers and is characterized by a boundary layer below the upper boundary. This second regime is driven by convection and is therefore called the *convective* regime.

The typical thermal and kinematic patterns for (a) a small Rayleigh number, (10^{-3}), and (b) a large Ra, (10^6), in a cavity with $A=1/5$ are shown in Fig. 2. When $Ra=10^{-3}$, the flow is in the conductive regime. The main thermal gradient is along the longitudinal coordinate. The streamlines present a pointwise symmetry around the center of the cavity. In the convective regime (see Fig. 2(b)), the symmetry is broken both on isotherms and streamlines. The thermal field is mainly driven by convection, which leads to the boundary layer just below the top boundary and a strong stratification in the bulk of the cavity. As seen in the streamline pattern, the flow is shifted toward the cold side (to the left of the enclosure). Close to the top left corner, the fluid falls down in the form of a plume.

In the following, the convective intensity and the heat flux on the upper limit are successively studied. The numerical results are compared to the asymptotic solution, given in Appendix A, obtained when A and Ra are small.

3.1. Péclet number in the enclosure

The maximum of the x-velocity sets the velocity scale in the enclosure and characterizes the convective intensity. The Péclet number is defined as:

$$Pe=\frac{|u|_{\max}L}{\kappa}, \tag{5}$$

where $|u|_{\max}$ is the maximum of the longitudinal velocity in physical dimensions. With the normalization used to numerically solve the problem, the x-velocity maximum is equal to the ratio Pe/Ra.

In order to investigate the convective intensity, $Pe\,A^2$ versus $Ra\,A^2$ is plotted in Fig. 3 for seven aspect ratios and Ra ranging from 1 to 10^9. The merging of all numerical data onto a single curve confirms that $Ra\,A^2$ remains the control parameter whatever the boundary conditions: differentially heated end walls [3,7] or an uneven top temperature profile. In both situations, convection occurs without threshold. It follows from the criteria pointed out by Joseph [11], i.e. the non zero value of the cross product of the thermal gradient and the gravity vector. So, the observed scaling is the consequence of the balance between the vorticity and the thermal gradient.

In summary, for the convective intensity:

For $Ra\,A^2\leqslant 10$:

$$Pe\,A^2=\frac{\pi\sqrt{3}}{432}Ra\,A^2\approx 1.26\cdot10^{-3}Ra\,A^2, \tag{6}$$

and for $Ra\,A^2\geqslant 10^4$:

$$Pe\,A^2=4.6\cdot10^{-1}(Ra\,A^2)^{2/5}, \tag{7}$$

Eq. (6), plotted as a solid line in Fig. 3, comes from the asymptotic analysis. In that regime, $Pe\,A^2$ is proportional to $Ra\,A^2$. Eq. (7) is plotted as a dashed line in Fig. 3. The coefficient comes from fitting numerical data to $(Ra\,A^2)^{2/5}$, where the 2/5 exponent is explained in [7].

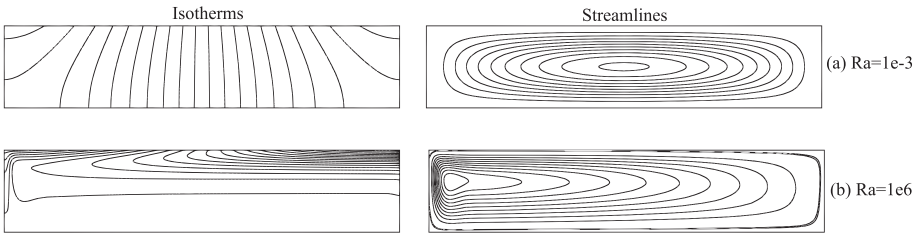

Fig. 2. Isotherms and streamlines in a cavity with aspect ratio equal to 1/5 for $Ra=10^{-3}$ (first row) and $Ra=10^6$ (second row).

Author's personal copy

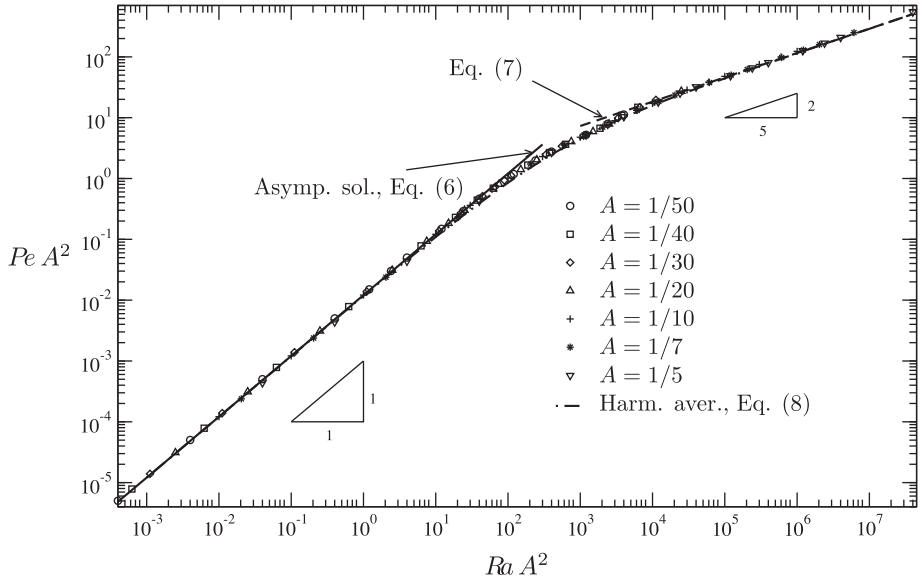

Fig. 3. $Pe\,A^2$ as a function of $Ra\,A^2$ for cavities with aspect ratios of 1/50, 1/40, 1/30, 1/20, 1/10, 1/7 and 1/5.

Finally, in order to obtain a practical estimate of the convective intensity, a harmonic average of Eqs. (6) and (7), written as follows, can be used:

$$Pe\,A^2 = \left\{ \left(1.26\cdot 10^{-3} Ra\,A^2\right)^{-1} + \left[4.6\cdot 10^{-1}\left(Ra\,A^2\right)^{2/5}\right]^{-1} \right\}^{-1}. \quad (8)$$

The dotted-dashed line in Fig. 3 represents this solution. It is close to all numerical data with an error smaller than 15%.

3.2. Nusselt number on the upper limit

The Nusselt number represents the normalized heat flux. With our normalization, it can be defined locally as follows:

$$Nu(x) = \frac{\partial\theta(x,1)}{\partial y}. \quad (9)$$

From the asymptotic solution given in Appendix A, the Nusselt number in the conductive regime is given by

$$Nu(x) = -\frac{\pi^2 A^2}{2}\left(1 - A^2\frac{\pi^2}{3}\right)\cos(\pi Ax) + \frac{Ra\,A^4\pi^4\cos(2\pi Ax)}{1920} - \frac{(Ra\,A^2)^2\pi^4\cos(\pi Ax)\sin^2(\pi Ax)}{967680} + \mathcal{O}\left(A^6, (Ra\,A^2)^3\right). \quad (10)$$

For small Rayleigh numbers, the leading term of Nu is proportional to A^2. Higher order terms are proportional to powers of A^2 and $Ra\,A^2$. Eq. (10) is compared to numerical results on Fig. 4. When $Ra\,A^2$ is sufficiently small (typically less than 10^2), the Nusselt number follows the sinusoidal function as predicted by (10): the local Nusselt number reaches its maximum at the top corners of the enclosure. As $Ra\,A^2$ increases, the convective transfer leads to a qualitative change of behavior in the Nusselt number along the longitudinal axis: the local maxima move from the vertical sides to the interior of the enclosure. The asymptotic solution reproduces this trend.

A global expression of the Nusselt number is needed to study the heat flux over the entire range of Rayleigh numbers. Since

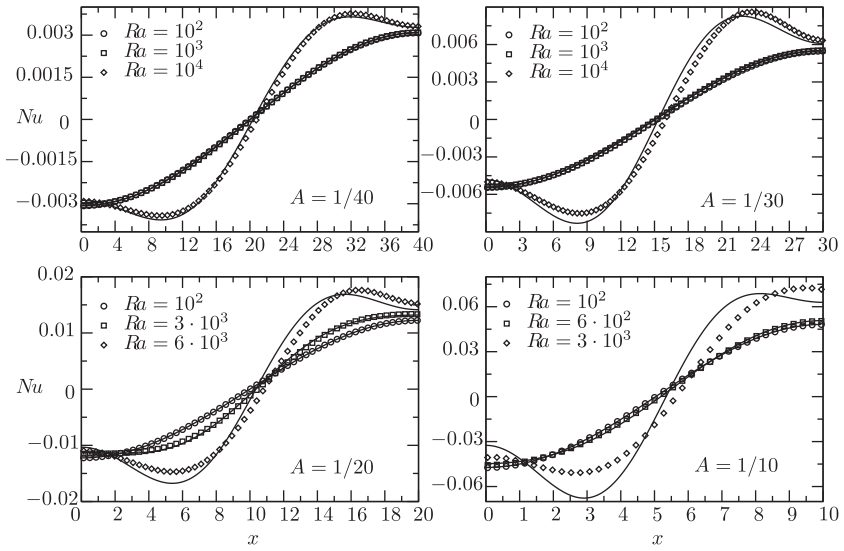

Fig. 4. Nu as a function of x for aspect ratios equal to 1/40, 1/30, 1/20 and 1/10. Solid lines represent the Nusselt number obtained from Eq. (10).

Author's personal copy

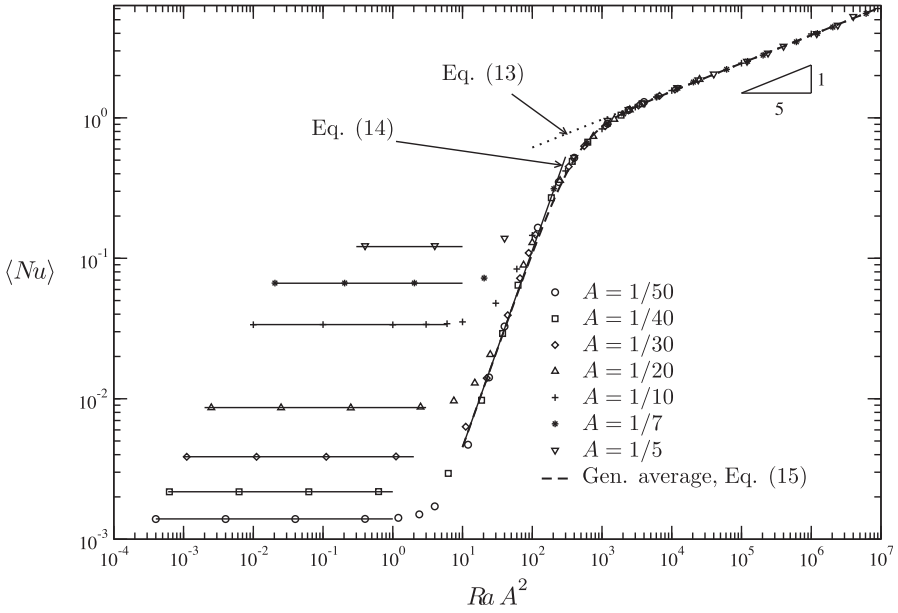

Fig. 5. $\langle Nu \rangle$ as a function of $Ra\,A^2$ for cavities with aspect ratios of 1/50, 1/40, 1/30, 1/20, 1/10, 1/7 and 1/5.

the average heat flux is null, we take the L_2 norm of $Nu(x)$ defined by

$$\langle Nu \rangle = \sqrt{A \int_0^{1/A} Nu^2(x)dx}. \tag{11}$$

$\langle Nu \rangle$, obtained from numerical simulations, is plotted as a function of $Ra\,A^2$ in Fig. 5. Once again, $Ra\,A^2$ appears as a relevant quantity. The results can be summed up as follows:

For $Ra\,A^2 \leqslant 10$:

$$\langle Nu \rangle = \frac{\pi^2 A^2}{2\sqrt{2}}\left(1 - A^2\frac{\pi^2}{3}\right), \tag{12}$$

and for $Ra\,A^2 \geqslant 10^3$:

$$\langle Nu \rangle = 0.245\left(Ra\,A^2\right)^{1/5}. \tag{13}$$

Eq. (12) corresponds to the conductive regime represented by horizontal lines in Fig. 5. The Nusselt number is independent of $Ra\,A^2$ and depends only on the aspect ratio squared. Eq. (13) is a consequence of the scaling law for the convective regime whose the coefficient is a fit of numerical data. In this regime, the heat flux is driven by the boundary layer occurring just below the upper limit of the cavity.

The scaling obtained in the convective regime can be easily recovered using a simple argument. Under the convective regime, cavity height is irrelevant to scale the boundary layer thickness and dimensional analysis shows that the only possible length scale is $[\kappa\nu\, L^2/(g\beta\Delta T)]^{1/5}$. Consequently, the laws for the Nusselt number in the convective regime should hold no matter what temperature profile is applied to the upper boundary of a long cavity filled with a high Prandtl number fluid.

Between these two asymptotic regimes, i.e. for $Ra\,A^2 \in]10; 10^3[$, the Nusselt number rises sharply due to the contribution of convection. Heat flux must be a function of $Ra\,A^2$ when convection becomes predominant. A fit in this intermediate region is:

$$\langle Nu \rangle = 1.8 \cdot 10^{-4}(Ra\,A^2)^{1.4}. \tag{14}$$

The approximation (14), represented by solid line in Fig. 5, accurately represents the transition regime.

As for convective intensity, a generalized average of (14) and (13) is obtained by

$$\langle Nu \rangle = \left\{\left[1.8 \cdot 10^{-4}(Ra\,A^2)^{1.4}\right]^{-3/2} + \left[0.245(Ra\,A^2)^{1/5}\right]^{-3/2}\right\}^{-2/3}. \tag{15}$$

This gives a practical estimate of the Nusselt number for the transition and convective regimes as is shown by the dashed line in Fig. 5.

3.3. Comparison with previous results

The results obtained in this article can be compared to previous works. As already pointed out by Böhrer [3], the $Ra\,A^2$ parameter is the control parameter even if the temperature is imposed on the upper limit. The agreement is the consequence of the meaning of the quantity $Ra\,A^2$. This product can be seen as the ratio of thermal diffusion time over H to the advection time over the length L. Low values of $Ra\,A^2$ mean that thermal diffusion is efficient. When $Ra\,A^2$ is high, thermal advection is the relevant phenomena that controls the thermal field.

In Ref. [4], Ra is based on the cavity length. So A^5Ra, against which Pe is plotted for $A < 1$, is equivalent to our expression $Ra\,A^2$. Moreover, the Péclet number in [4] is defined as the maximum of the stream function, i.e. the integral of the velocity field. In the conductive regime, the scaling obtained in [4] is equivalent to our result where the Péclet number is proportional to the Rayleigh number. In the convective regime, the Péclet number scales as $(Ra\,A^2)^{1/5}$ according to Chiu-Webster et al. whilst our results show that $Pe\,A^2$ is proportional to $(Ra\,A^2)^{2/5}$. The apparent discrepancy is a consequence of the definition of Pe. Indeed in the convective regime, the derivative along the y-axis of the stream function scales like $1/\delta$ where δ is the scale of the boundary layer below the upper limit. As pointed out in [7], $\delta \propto 1/(Ra\,A^2)^{1/5}$. Consequently, the expression found in [4] is in agreement with our scaling.

As for the Péclet number, the comparison of the Nusselt number with the previous work of Chiu-Webster et al. [4] has to be carefully studied. In [4], the Nusselt number is taken as the average of the absolute value of the thermal gradient and based on the longitudinal dimension. In the conductive regime, Chiu-Webster et al. show that the Nusselt number is proportional to the aspect ratio

Author's personal copy

whereas our results give a scaling in A^2. These two results are in fact in perfect agreement if the same spatial scale is used. In the convective regime, our results agree with ones given in [4]. Note that this scaling has been already pointed out by Rossby [14].

4. Conclusion

In this article, the problem of natural convection in a shallow enclosure is investigated, where a sinusoidal temperature profile is applied to the upper boundary, while the side and bottom walls are adiabatic. With this choice, it is shown that $Ra\,A^2$ (see definition in Nomenclature) remains the control parameter. Two main regimes emerge: the first one, observed for $Ra\,A^2 < 10$, is dominated by conduction whereas the second, for $Ra\,A^2 > 10^3$, is driven by convection. Analytical laws for convective intensity and heat flux are derived that are based on an analytical asymptotic expansion and on extensive numerical calculations. Under the convective regime, numerical coefficients for these laws come from fitting numerical data, their functional form relying on analytical expansions.

An expression for convective intensity is given over the whole range of $Ra\,A^2$ based on a harmonic average. When $Ra\,A^2$ belongs to $[10;10^2]$, an approximate relationship is proposed to describe the sharp increase in heat flux. Finally, a generalized average describes the heat flux in both the transition, when $Ra\,A^2 \in [10;10^2]$, and the convective regimes. The choice of variables makes these expressions directly applicable to practical situations.

From these developments, the characteristic velocity under the conductive regime is shown to be proportional to $Ra\,\kappa/L = \beta g \Delta T H^3/(\nu L)$. This parameter is highly sensitive to cavity height and depends also on length and dynamic viscosity but not on heat conductivity. In the convective regime, characteristic velocity is *independent* of enclosure height since it can be written as $u_0 \sim (\beta \Delta T g/\nu)^{2/5}\kappa^{3/5}L^{1/5}$ but increases with length and thermal conductivity. Viscosity's importance is reduced since it appears with a 2/5 exponent. These results provide physically grounded answers to the empirical suggestions given by Trier [19].

Regarding heat transfer, the conductive regime leads to a thermal flux on the upper boundary, $\partial T/\partial n$, proportional to enclosure height and inversely proportional to length squared. Under the convective regime, heat flux becomes independent of enclosure height: as with characteristic velocity it is completely driven by the boundary layer below the upper limit.

These results serve as guides to analyze heat and mass transfer in more complex situations closer to those experienced in industrial plants.

Appendix A. Asymptotic solution for small aspect ratio

In the conductive regime, flow develops in the whole cavity. Therefore, spatial length scales are proportional to enclosure size and spatial coordinates are normalized as follows[2]:

$$\bar{x} = \frac{x}{L}, \tag{16}$$

$$\bar{y} = \frac{y}{H}. \tag{17}$$

The results obtained in [7] are used to normalize velocity in the conductive regime. The scaling of u and v is:

$$\bar{u} = \frac{u}{\kappa Ra/L}, \tag{18}$$

$$\bar{v} = \frac{v}{\kappa RaH/L^2}. \tag{19}$$

With this scaling, balance equations are written:

$$\frac{\partial \bar{u}}{\partial \bar{x}} + \frac{\partial \bar{v}}{\partial \bar{y}} = 0, \tag{20a}$$

$$A^2\frac{Ra}{Pr}\left(\bar{u}\frac{\partial \bar{u}}{\partial \bar{x}} + \bar{v}\frac{\partial \bar{u}}{\partial \bar{y}}\right) = -\frac{\partial \bar{P}}{\partial \bar{x}} + A^2\frac{\partial^2 \bar{u}}{\partial \bar{x}^2} + \frac{\partial^2 \bar{u}}{\partial \bar{y}^2}, \tag{20b}$$

$$A^4\frac{Ra}{Pr}\left(\bar{u}\frac{\partial \bar{v}}{\partial \bar{x}} + \bar{v}\frac{\partial \bar{v}}{\partial \bar{y}}\right) = -\frac{\partial \bar{P}}{\partial \bar{y}} + A^4\frac{\partial^2 \bar{v}}{\partial \bar{x}^2} + A^2\frac{\partial^2 \bar{v}}{\partial \bar{y}^2} + \theta, \tag{20c}$$

$$Ra\,A^2\left(\bar{u}\frac{\partial \theta}{\partial \bar{x}} + \bar{v}\frac{\partial \theta}{\partial \bar{y}}\right) = A^2\frac{\partial^2 \theta}{\partial \bar{x}^2} + \frac{\partial^2 \theta}{\partial \bar{y}^2}. \tag{20d}$$

Eqs. (20a)–(20d) are similar to those used by Bejan [2] (Chapter 5) and can be used to find the perturbation solution expanded in terms of A^2 at small Rayleigh numbers. From Eq. (20d), the expansion in terms of A^2 is valid when $Ra\,A^2 \ll 1$. Note that the problem is singular [6] since all x-derivatives disappear if A is taken equal to zero. Actually, the form (20a)–(20d) corresponds to an external solution valid in the enclosure's core.

To find the asymptotic solution, all quantities are developed as (see [2]):

$$f = f_0 + A^2 f_1 + A^4 f_2 + \cdots + A^{2i} f_i + \cdots. \tag{21}$$

At zeroth order, the solution is[3]:

$$\bar{u}_0(\bar{x},\bar{y}) = \pi \sin(\pi\bar{x})\mathcal{A}_0'(\bar{y}), \tag{22a}$$

$$\bar{v}_0(\bar{x},\bar{y}) = -\pi^2 \cos(\pi\bar{x})\mathcal{A}_0(\bar{y}), \tag{22b}$$

$$\theta_0(\bar{x},\bar{y}) = \frac{1}{2}[1 - \cos(\pi\bar{x})], \tag{22c}$$

with

$$\mathcal{A}_0(\bar{y}) = \frac{\bar{y}^2(\bar{y}-1)^2}{48}. \tag{22d}$$

At first order, the solution is:

$$\bar{u}_1(\bar{x},\bar{y}) = \frac{Ra\ \pi^3}{2304}\sin(2\pi\bar{x})\left[\mathcal{A}_1'(\bar{y}) + \frac{\mathcal{B}_1'(\bar{y})}{Pr}\right] + \frac{\pi^3}{24}\sin(\pi\bar{x})\mathcal{C}_1'(\bar{y}), \tag{22e}$$

$$\bar{v}_1(\bar{x},\bar{y}) = -\frac{Ra\ \pi^4}{1152}\cos(2\pi\bar{x})\left[\mathcal{A}_1(\bar{y}) + \frac{\mathcal{B}_1(\bar{y})}{Pr}\right] - \frac{\pi^4}{24}\cos(\pi\bar{x})\mathcal{C}_1(\bar{y}), \tag{22f}$$

$$\theta_1(\bar{x},\bar{y}) = \frac{Ra\ \pi^2 \sin^2(\pi\bar{x})}{96}\mathcal{D}_1(\bar{y}) - \frac{\pi^2}{4}\cos(\pi\bar{x})(\bar{y}^2-1), \tag{22g}$$

with

$$\mathcal{A}_1(\bar{y}) = \frac{\bar{y}^9}{630} - \frac{\bar{y}^8}{140} + \frac{\bar{y}^7}{105} - \frac{\bar{y}^4}{30} + \frac{16\bar{y}^3}{315} - \frac{3\bar{y}^2}{140}, \tag{22h}$$

$$\mathcal{B}_1(\bar{y}) = -\frac{\bar{y}^9}{252} + \frac{\bar{y}^8}{56} - \frac{\bar{y}^7}{30} + \frac{\bar{y}^6}{30} - \frac{\bar{y}^5}{60} + \frac{\bar{y}^3}{252} - \frac{\bar{y}^2}{840}, \tag{22i}$$

$$\mathcal{C}_1(\bar{y}) = \frac{\bar{y}^6}{20} - \frac{\bar{y}^5}{10} - \frac{\bar{y}^4}{6} + \frac{13\bar{y}^3}{30} - \frac{13\bar{y}^2}{60}, \tag{22j}$$

$$\mathcal{D}_1(\bar{y}) = \frac{\bar{y}^5}{5} - \frac{\bar{y}^4}{2} + \frac{\bar{y}^3}{3} - \frac{1}{30}. \tag{22k}$$

At zeroth order, the temperature is similar to the boundary condition on $\bar{y} = 1$. The function $\mathcal{A}_0(\bar{y})$ is identical to the one obtained by Cormack et al. [5]. Function $\bar{u}_0$ differs from the Cormack et al. solution by the quantity $\pi\sin(\pi\bar{x})/2$. The velocity solution at zeroth order is derived from the purely conductive temperature field. The function $\bar{u}_0$ is minimum and maximum for $\bar{y}$ equal to $(3+\sqrt{3})/6$ and $(3-\sqrt{3})/6$, respectively. At first order, the thermal solution has two terms: the first linked to convection and the second to conductive transfer.

[2] In this appendix, the bar is used over dimensionless variables.

[3] The symbol $'$ corresponds to differentiation with respect to $\bar{y}$.

Author's personal copy

To determine the local Nusselt number in the conductive regime, the integral form of energy Eq. (20d) is used. Indeed, integration over the vertical direction with boundary conditions gives the local Nusselt number:

$$Nu(\bar{x}) = -A^2 \frac{d^2}{d\bar{x}^2} \int_0^1 \theta(\bar{x},\bar{y}) d\bar{y} + Ra\, A^2 \frac{d}{d\bar{x}} \int_0^1 \bar{u}\theta d\bar{y}. \quad (23)$$

By taking the two first orders of the asymptotic solution, Eq. (10) is found. The integro-differential Eq. (23) is useful to determine the local Nusselt number since the term proportional to A^4 is obtained without the solution at second order.

References

[1] G.K. Batchelor, Heat transfer by free convection across a closed cavity between vertical boundaries at different temperatures, Q. Appl. Math. 12 (1954) 209–233.
[2] A. Bejan, Convection Heat Transfer, John Wiley & Sons, New York, 1995.
[3] B. Böhrer, Convection in a long cavity with differentially heated end walls, Int. J. Heat Mass Transfer 40 (1997) 4105–4114.
[4] S. Chiu-Webster, E.J. Hinch, J.R. Lister, Very viscous horizontal convection, J. Fluid Mech. 611 (2008) 395–426.
[5] D.E. Cormack, L.G. Leal, J. Imberger, Natural convection in a shallow cavity differentially heated end walls. Part 1. Asymptotic theory, J. Fluid Mech. 65 (1974) 209–229.
[6] M. Van Dyke, Perturbations Methods in Fluid Mechanics, The Parabolic Press, Stanford, California, 1975.
[7] J.-M. Flesselles, F. Pigeonneau, Kinematic regimes of convection at hight Prandtl number in a shallow cavity, C.R. Mécanique 332 (2004) 783–788.
[8] C.A.J. Fletcher, Computational Techniques for Fluid Dynamics, Specific Techniques for Different Flow Categories, vol. II, Springer-Verlag, Berlin, 1991.
[9] R. Gardon, A review of radiant heat transfer in glass, J. Am. Ceram. Soc. 44 (1961) 305–312.
[10] H.J.J. Gramberg, P.D. Howell, J.R. Ockendon, Convection by a horizontal thermal gradient, J. Fluid Mech. 586 (2007) 41–57.
[11] D.D. Joseph, Stability of Fluid Motions II, Springer-Verlag, Berlin, 1976.
[12] B.P. Leonard, A stable and accurate convective modelling procedure based on quadratic upstream interpolation, Comput. Methods Appl. Mech. Eng. 19 (1) (1979) 59–98.
[13] K.-O. Lim, T.-H. Song, K.-S. Lee, Patterns of natural convection driven by the free surface temperature distribution in a glass melting furnace, Glass Technol. 39 (1998) 27–31.
[14] H.T. Rossby, On thermal convection driven by non-uniform heating from below: an experimental study, Deep-Sea Res. 12 (1965) 9–16.
[15] H.T. Rossby, Numerical experiments with a fluid heated non-uniformly from below, Tellus 50A (1998) 242–257.
[16] H. Scholze, Glass. Nature, Structures and Properties, Springer-Verlag, Berlin, 1990.
[17] R. Siegel, J. Howell, Thermal Radiation Heat Transfer, Taylor & Francis, Levitown, 2002.
[18] R.C.J. Somerville, A nonlinear spectral model of convection in a fluid unevenly heated from below, J. Atmos. Sci. 24 (1967) 665–676.
[19] W. Trier, Glass Furnaces, Design Construction and Operation, Society of Glass Technology, Sheffield, 1984.

Annexe D

Curriculum Vitae

Cette annexe présente mon parcours professionnel, mes diplômes, la liste de mes publications, mes stages pré et post-doctoraux, l'encadrement d'étudiants et les responsabilités de recherche et d'enseignement.

Franck PIGEONNEAU Né le 27 janvier 1969 (43 ans)
Surface du Verre et Interface, UMR 125 CNRS/Saint-Gobain
39 quai Lucien Lefranc - BP135
93303 Aubervilliers cedex
Tél. 01 48 39 59 99. Fax 01 48 39 55 62
Courriel franck.pigeonneau@saint-gobain.com

DOCTEUR DE L'UNIVERSITÉ P. ET M. CURIE – INGÉNIEUR E.S.E.M.

Expérience professionelle

Depuis 2007 Chercheur associé au sein du laboratoire Surface du Verre et Interface, UMR 125 CNRS/Saint-Gobain.

2000–2007 Ingénieur de recherche au sein du service Elaboration du Verre de Saint-Gobain Recherche.

1998–2000 Post-doctorat au Commissariat à l'Energie Atomique, Département de Mécanique et Technologie, Saclay.

1995–1998 Doctorat au Laboratoire de Physique et de Mécanique des Milieux Hétérogènes, UMR 7636, ESPCI, Paris.

Diplômes

1998 Docteur en mécanique de l'université Pierre et Marie Curie : **Modélisation et calcul numérique des collisions de gouttes en écoulements laminaires et turbulents**.

1993 D.E.A. de Conversion d'Énergie, option : système de propulsion et aérodynamique externe.

1990–1993 Ingénieur généraliste de l'Ecole Supérieure de l'Energie et des Matériaux (ESEM, Orléans), option : aérodynamique et structure.

1988–1990 D.U.T. en Génie Mécanique et Productique (Orléans).

Références

Articles dans des journaux avec comité de lecture

[1] F. Feuillebois, A. Lasek, P. Creismeas, F. Pigeonneau, and A. Szaniawski. Freezing of a subcooled liquid droplet. *J. Coll. Interface Science*, 169 :90–102, 1995.

[2] F. Pigeonneau and F. Feuillebois. Drag forces on two drops embedded in a general linear flow field. *Z. Angew. Math. Mech.*, 78(S2) :S665–S666, 1998.

[3] F. Pigeonneau and F. Feuillebois. Collision and size evolution of drops in homogeneous isotropic turbulence. *J. Aerosol Sci.*, 29 :S1279–S1280, 1998.

[4] F. Pigeonneau and F. Feuillebois. Collision of drops with inertia effects in strongly sheared linear flow fields. *J. Fluid Mech.*, 455 :359–386, 2002.

[5] X. Chavanne, J.-M. Flesselles, and F. Pigeonneau. Bubbling laws in a glass furnace. *Verre*, 9(2) :6–8, 2003.

[6] F. Pigeonneau and J.-M. Flesselles. Convection laws for glass furnaces revisited. *Verre*, 9(2) :14–16, 2003.

[7] F. Pigeonneau and F. Feuillebois. Test-case no 16 : Impact of a drop on a thin film of the same liquid (pe,pa). *Multiphase Science and Technology*, 16(1-3) :105–109, 2004.

[8] F. Pigeonneau and F. Feuillebois. Test-case no 23 : Relative trajectories and collision of two drops in a simple shear flow (pa). *Multiphase Science and Technology*, 16(1-3) :133–139, 2004.

[9] J.-M. Flesselles and F. Pigeonneau. Kinematic regimes of convection at hight Prandtl number in a shallow cavity. *C. R. Mécanique*, 332 :783–788, 2004.

[10] F. Pigeonneau. Coupled modelling of redox reactions and glass melt fining processes. *Glass Technol. : Eur. J. Glass Sci. Technol. A*, 48(2) :66–72, 2007.

[11] A. Ponsich, C. Azzaro-Pantel, S. Domenech, L. Pibouleau, and F. Pigeonneau. A systemic approach for glass manufacturing process modelling. *Chem. Eng. Process.*, 48 :1310–1320, 2009.

[12] F. Pigeonneau. Mass transfer of rising bubble in molten glass with instantaneous oxidation-reduction reaction. *Chem. Eng. Sci.*, 64 :3120–3129, 2009.

[13] F. Pigeonneau, D. Martin, and O. Mario. Shrinkage of oxygen bubble rising in a molten glass. *Chem. Eng. Sci.*, 65 :3158–3168, 2010.

[14] F. Pigeonneau. Mechanism of mass transfer between a bubble initially composed of oxygen and molten glass. *Int. J. Heat Mass Transfer*, 54 :1448–1455, 2011.

[15] F. Pigeonneau and A. Sellier. Low-Reynolds-Number gravity-driven migration and deformation of bubbles near a free surface. *Phys. Fluids*, 23 :092102, 2011.

[16] F. Pigeonneau and J.-M. Flesselles. Practical laws for natural convection of viscous fluids heated from above in a shallow cavity. *Int. J. Heat Mass Transfer*, 55 :436–442, 2012.

[17] H. Kočárková, F. Rouyer, and F. Pigeonneau. Film drainage of viscous liquid on top of bare bubble : Influence of the Bond number. *Phys. Fluids*, under consideration, 2012.

[18] F. Pigeonneau, H. Kočárková, and F. Rouyer. Stability of vertical films of molten glass due to evaporation. *Colloids Surf., A*, under consideration, 2012.

Actes de congrès

[19] F. Pigeonneau and F. Feuillebois. Détermination des forces d'interactions sur deux gouttes de rayons différents dans un écoulement linéaire quelconque. In *12ème Journée d'Etudes et de Recherches sur les Aérosols*, pages 51–56, Paris, 4 et 5 décembre 1996.

[20] F. Pigeonneau and F. Feuillebois. Evolution du spectre de gouttes en écoulement turbulent homogène et isotrope. In *13ème Congrès Etudes et de Recherche sur les Aérosols*, pages 71–76, Paris, 2-3 décembre 1997.

[21] F. Pigeonneau and F. Feuillebois. Trajectoires et collision de gouttes dans un écoulement à taux de déformation constant. In *13ème Congrès Français de Mécanique*, volume 1, pages 305–308, Poitiers-Futuroscope, 1-5 septembre 1997.

[22] F. Dabbene, S. Gounand, J. P. Magnaud, F. Pigeonneau, and E. Studer. Modelling and simulation of convection flows with large temperature difference : a benchmark problem for low mach number solvers. In *12ème séminaire de mécanique des fluides numérique*, CEA Saclay, 25-27 janvier 2000.

[23] F. Pigeonneau and P. G. Ferreira. A physicist's approach of batch blanket modelling. In *Sixth European Society of Glass Science and Technology Conference*, Montpellier, France, June 2002.

[24] F. Lopépé, J.-M. Flesselles, and F. Pigeonneau. Train of bubbles in a viscous fluid. In *XX International Congress on Glass*, Kyoto, Japan, Sep. 27th-Oct. 1st 2004.

[25] N. McDonald and F. Pigeonneau. In-situ measurements of the effect of sulphate on bubble growth rate and gas emissions during fining. In *XXIst International Congress on Glass*, Strasbourg, France, July, 1-6 2007.

[26] V. Vincent, O. Caballina, F. Pigeonneau, and M. Souhar. Experimental study of the hydrodynamic interactions between two spherical bubbles in a solid-body rotation flow. In *International Conference on Multiphase Flow*, Leipzig, Germany, July, 9-13 2007.

[27] M. Perrodin, V. Sarrot, E. Climent, and F. Pigeonneau. Hydrodynamique, transfert de matière et réactions chimiques autour d'une bulle de gaz en ascension dans du verre fondu. In *19ème Congrès Français de Mécanique*, Marseilles, 24-28 Août 2009.

[28] H. Kočárková, F. Pigeonneau, F. Rouyer, and M. Vignes-Adler. Film drainage between bubble and fluid interface. In *International Conference on Multiphase Flow 2010*, Tampa, Florida (USA), May 30-June 4 2010.

[29] M. Perrodin, E. Climent, E. Brunet, and F. Pigeonneau. Coupling chemical reactions with mass transfer around a bubble rising in molten glass. In *International Conference on Multiphase Flow 2010*, Tampa, Florida (USA), May 30-June 4 2010.

[30] F. Pigeonneau. Mass transfer of a rising bubble in a molten glass. In *International Conference on Multiphase Flow 2010*, Tampa, Florida (USA), May 30-June 4 2010.

[31] F. Pigeonneau. Mass transfer of a rising bubble in a molten glass. In *International Conference on Glass 2010*, Salvador de Bahia, Brazil, September 20-25 2010.

[32] F. Pigeonneau and A. Sellier. Low-Reynolds-Number gravity-driven migration and deformation of bubbles near a free surface. In *20ème Congrès Français de Mécanique*, Besançon, 29 août au 2 septembre 2011.

Stages pré-doctoraux

1994–1995 Ingénieur de calcul à la Société d'Étude et de Recherche en Mécanique Aérotechnique (SERMA, Orléans) : Réalisations des dossiers de calculs aérodynamiques et de structures dans le cadre de la certification d'avions légers.

1993 (mars à septembre) Stage de D.E.A. réalisé au Centre d'Essais des Propulseurs (C.E.Pr, Saclay) : Modélisation eulérienne-eulérienne des écoulements diphasiques et conception d'un code de calcul de congélation de gouttelettes en surfusion.

Stages post-doctoraux

1998-2000 Post-doctorat au Laboratoire de Thermique et Mécanique des Fluides au Département de Mécanique et Technologie du C.E.A. Saclay : Evaluation des possibilités de stratification d'hydrogène émis dans une enceinte d'un réacteur en cas d'accident grave.

Encadrements

Etudiants en thèse

1. Helena Kočárková, «Stabilité des mousses de verre : Expériences à l'échelle d'une bulle ou d'un film vertical», Université Paris-Est, Marne la Vallée. Coencadrement avec Florence Rouyer (MdC, Univ. Paris-Est). Thèse soutenue le 14 novembre 2011.
2. Marion Perrodin, «Modélisation et simulation numérique du couplage entre hydrodynamique et réactions chimiques dans du verre fondu peuplé en microbulles», Université de Toulouse. Coencadrement avec Eric Climent (Prof. INP de Toulouse). Thèse soutenue le 15 novembre 2011.
3. Erdem Uguz, "Development of Navier-Stokes solver with a spectral method. Application to the natural convection in an enclosure". Coencadrement avec Gérard Labrosse (Prof. Univ. Paris-Sud, Orsay). Thèse en cours et en cotutelle entre l'université Paris-Sud, Orsay et l'université de Floride (Gainesville, USA).
4. Marine Guémas, «Hydrodynamique de bulles dans un liquide visqueux et mélange induit», Ecole Polytechnique. Coencadrement avec Antoine Sellier (Prof. Ecole Polytechnique). Thèse en cours débutée en octobre 2011.

Etudiants en stage de Master 2 ou équivalent

1. Jérémie Tâche, «Ecoulement dans les fours verriers. Simulation et comparaison à des résultats expérimentaux». DESS de mathématiques appliquées Université Pierre et Marie Curie Paris VI, mars-août 2002.
2. Mohamed Boutajar, «Simulation numérique de fours verriers et caractérisation des mouvements de convection par trajectographie». Stage de troisième année de Poly-Tech'Orléans, mars-août 2003.
3. Yassine Chagraoui, «Simulation numérique de fours verriers et caractérisation des mouvements de convection par trajectographie». DESS de mathématiques appliquées Université Pierre et Marie Curie paris VI, mars-août 2004.
4. Eric Fallas, «A propos de l'élaboration du verre. Étude de mélangeurs dynamiques et statiques et recherche de grandeurs qualificatives». Stage de deuxième année de l'école Polytechnique, avril-juillet 2006.
5. Malek Mebazaa, «Modélisation numérique d'écoulement diphasique à bulles». Stage de troisième année d'ENSEM Nancy, mars-août 2006.
6. Nicolas Champagne, «Etude de la Stabilité des Films de Verre». Master 2 Concepts Fondamentaux de la Physique, parcours : Physique des Liquides et Matière Molle, Université Pierre et Marie Curie, janvier-juillet 2008.

7. Nicolas Riefle, «Mécanismes d'oxydation des silicates liquides ferrifères». Master Physique et sciences pour l'ingénieur. Parcours matériaux avancés et de haute technologie de l'université d'Orléans, février-juillet 2010.
8. Jaouad Bahadi, «Interaction hydrodynamique d'une inclusion proche d'une interface fluide faiblement déformée». Master de Physique spécialité système complexe naturels et industriels. Parcours fluide et matières complexes. Université de Rennes 1, mars-juillet 2010.

Etudiants en stage de Master 1

1. Salahedine Metallaoui, «Etude expérimentale du drainage et éclatement d'une bulle à la surface d'un liquide». Master 1 de Sciences et Technologies de l'Université Pierre et Marie Curie, Mention Sciences de l'Ingénieur, mai-août 2011.

Responsabilités de recherche

- Organisation d'un minicolloque sur «Mélange chaotique de fluides à petite échelle» lors des $10^{\text{èmes}}$ journées de la matière condensée, Toulouse, 2006.
- Participant au projet ANR jeune chercheur porté par Eric Climent (Institut de Mécanique des Fluides de Toulouse) «Génération, mouvement et croissance de bulles dans les solides en fusion», acronyme «DyBuMelt», 2007-2011.
- Membre du programme international PIRE intitulé "Collaborations with France and Japan on complex and multiphase fluid technologies" porté par le Prof. Ranga Narayanan, Department of Chemical Engineering of University of Florida.
- Membre élu du bureau de la division physique de la matière condensée de la Société Française de Physique depuis 2011.
- Membre du comité scientifique du GDR Verres porté par Lionel Montagne, Unité de Catalyse et de Chimie du Solide, université de Lille 1.
- Participant au GDR Mousses et Emulsions porté par Cyprien Gay, Matières et Systèmes Complexes, université Paris-Diderot.
- Organisateur des séminaires de recherche de Saint-Gobain Recherche (un par semaine) depuis 2008.
- Comité d'organisation des $13^{\text{èmes}}$ Journées de la Matière Condensée qui auront lieu à Montpellier fin août 2012.

Responsabilités d'enseignement

- Intervention dans le DESS mathématiques appliquées de l'université Pierre et Marie Curie sur les «Problèmes de modélisations dans l'élaboration et le travail du verre», (année univ. 2002/2003).
- Intervention dans le master 2 de Physique spécialité système complexe naturels et industriels de l'université de Rennes 1 sur «Recherche et développement dans le cadre de l'élaboration du verre», (années univ. 2009/2010, 2010/2011).
- Cours intituté «Ouverture aux Domaines aux Aplications des Industrielles» sur «les phénomènes de transfert dans l'élaboration des verres» au Master de Science de l'ingénieur de l'université Pierre et Marie Curie (6 heures), années universitaires 2010/2011 et 2011/2012.

– Cours sur la «Simulation numérique à l'échelle macroscopique par la méthode des éléments finis» de l'école «Modélisations des verres : de la structure aux propriétés» réalisée dans le cadre du GDR Verres (8 heures), mai 2011.